Scan Time Reduction and Scatter Rejection in Dual Modality Breast Tomosynthesis

Tushita Patel
Charlottesville, Virginia

Bachelor of Science in Physics and Bachelor of Science in Astronomy & Astrophysics,
Pennsylvania State University, 2008

A Dissertation presented to the Graduate Faculty
of the University of Virginia in Candidacy for the Degree of
Doctor of Philosophy

Department of Physics

University of Virginia
December 2015

ABSTRACT

The dual modality tomosynthesis (DMT) system is an investigational scanner that combines x-ray breast tomosynthesis (DBT) and gamma ray emission breast tomosynthesis (MBT) in a single gantry. In breast tomosynthesis, several two-dimensional (2D) images are taken at varying angles over a circular arc within a limited angular range and combined together by a reconstruction algorithm to create a three-dimensional (3D) reconstructed volume of the breast. A combination of the modalities that are employed in the DMT reveal the anatomy of the breast (DBT), which can be correlated with a map of the molecular activity within the breast (MBT). Despite the success of the DMT pilot study in illustrating the benefit of combining both modalities for improving cancer detection, DMT DBT, as it currently stands, must be optimized.

DMT x-ray images are acquired through the step-and-shoot (SNS) method where the gantry comes to a complete stop between projection angles. The resulting DBT scan time can take up to two minutes, a long process that raises the probability of patient discomfort and motion artifacts in the x-ray images. In addition to long scan times, as in the case of most clinical DBT systems, there is currently no method for rejecting scattered x-rays from DMT DBT images. Scattered radiation introduces errors in the estimated attenuation coefficients of breast structures, represented by voxels in the reconstructed images. These errors degrade DBT image quality by reducing lesion detectability and contrast. Quantification of scattered radiation relative to primary rays in DMT DBT emphasizes the need for x-ray scatter rejection. The geometry of the DMT systems raises the possibility of implementing an anti-scatter grid for removing scattered x-rays.

The objectives of this work were to reduce the DBT scan time and to introduce a method for removing x-ray scatter from DBT images. To reduce scan time, a hybrid motion profile was developed where the gantry moves continuously for a portion of the scan and uses a slightly modified version of SNS for the remainder of the scan. For more efficient scatter removal, a novel method of reciprocating a 2D focused anti-scatter grid is presented.

The effects on image quality under conditions of fixed radiation dose resulting from the implementation of a hybrid motion profile and a reciprocating grid are discussed. Modification of the gantry motion profile made it possible to reduce the total DMT DBT scan time to 20 seconds. Finally, inclusion of the reciprocating grid improved lesion contrast of phantoms images under conditions of fixed radiation dose, which is conventionally raised for grid-in full-field digital mammography (FFDM) acquisitions. These adjustments will be incorporated for future DMT human subject clinical trials.

ACKNOWLEDGEMENTS

There are so many to whom I am grateful for helping me get to where I am today. First and foremost, I would like to thank my adviser Dr. Mark Williams for giving me the opportunity to learn so much by making me a part of the lab and giving me this project. I am thankful to all of my committee members (Dr. Craig Dukes, Dr. P.Q. Hung, and Dr. Heather Peppard) for keeping me on track with my thesis, especially Dr. Heather Peppard who has been such a great mentor and cheerleader. Thank you to all of the current and former students in the lab, including Dr. Patricia Judy who showed me the ropes. Many thanks to the guys in the machine shop, the clinical research team members, and all of the inspiring people I have been so fortunate to meet and work with in the UVa Breast Care Center. Finally, I would like to thank my family and friends outside of the lab. I am especially grateful to my mom, my grandmom, and my sister for their loving encouragement and ever-present support.

TABLE OF CONTENTS

Chapter 1: Introduction

Chapter 2: Scan Time Reduction (STR)

Chapter 3: Impact of STR on Image Quality

Chapter 4: Scatter in DMT DBT

Chapter 5: Anti-scatter Grid Reciprocation

Chapter 6: Assessment of Scatter Rejected Images

Chapter 7: Conclusions

LIST OF FIGURES

LIST OF TABLES

LIST OF ABBREVIATIONS

2D – two-dimensional

3D – three-dimensional

AGD – average glandular dose

AOR – axis of rotation

APS – active pixel sensor

BB – ball-bearing

BSGI – breast-specific gamma imaging

CEM – contrast-enhanced mammography

CMOS – complementary metal-oxide semiconductor

CT – computed tomography

CTBI – computed tomography breast imaging

DBT – digital breast tomosynthesis

DMT – dual modality tomosynthesis tomosynthesis

DQE – detective quantum efficiency

FFC – flat-field correction

FFCI – flat-field correction image

FFDM – full field digital mammography

FFT – fast Fourier transform

FOM – figure of merit

FOV – field of view

GFP – grid focal point

GLA – grid line artifact

HDR – high dynamic range

HMP – hybrid motion profile

HS – high-sensitivity

HVL – half value layer

L(R)CC –left (right) craniocaudal

L(R)MLO – left (right) mediolateral oblique

MBT – molecular breast tomosynthesis

MRI – magnetic resonance imaging

MTF – modulation transfer function

NPS – noise power spectrum

PET – positron emission tomography

PMMA - polymethyl methacrylate

PS – power spectrum

ROI – region of interest

SD – signal difference

SDNR – signal difference to noise ratio

SID – source to imager distance

SNS – step-and-shoot

SPECT – single photon emission computed tomography

SPR – scatter-to-primary ratio

ST – shift-and-twist

STR – scan time reduction

US – ultrasound

XFS – x-ray focal spot

Chapter 1

Introduction

The human breast goes through many changes throughout the course of a woman's lifetime. As part of the natural process, cells reproduce by dividing to make new replacements for the older cells that die [1]. When the signals for regulating the reproduction and death cycles of these cells goes unheeded due to defects in their genetic material, proliferation of these cancerous cells can accelerate [2]. Their spread to other parts of the body will eventually inhibit proper functioning of vital organs, making it deadly when undetected and left untreated [2]. Despite being one of the most publicized cancers, with so many dedicated to its awareness, breast cancer is still the second most common cause of cancer death among women in the United States [3]. Approximately 40,290 women are estimated to die in 2015 from this disease [3]. In light of a better understanding of breast cancer risk factors and the availability of better treatment options, the mortality rate for breast cancer has been declining [3, 4]. However, early detection is pivotal to a higher probability of survival.

1.1 Breast Cancer Screening

1.1.1 Mammography

The Society of Breast Imaging (SBI) and the American College of Radiology (ACR) recommend annual screening mammograms for women starting from 40 years of age [4] for detecting the presence of cancer. Screening mammography is believed to have played a major role in the nearly 30% decrease in breast cancer mortality seen since 1990 [4]. Mammography is an imaging modality that uses x-rays to allow radiologists to see the internal structures of the breast. A schematic of a typical mammography scanner is shown in Figure 1-1 in which the breast is compressed by a flat compression paddle between an x-ray tube and an x-ray detector.

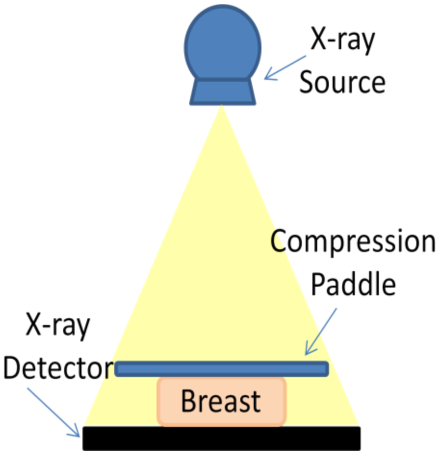

Figure 1-1: Schematic of a clinical mammography scanner

In a standard screening mammogram, each breast is imaged in two configurations called the craniocaudal (CC) view and the mediolateral oblique (MLO) view [5]. For the CC view, the breast is compressed vertically, parallel to the direction from the head towards the foot [5]. The MLO compression looks at the breast at an oblique angle with respect to the center of the chest to the outside, or lateral, side of the body [5]. The MLO view provides the most information since the most tissue can be imaged in this view [6].

However, not enough information can be inferred from this view alone [6]. A combination of the CC view with the MLO view allows the radiologist to estimate the position of any suspicious findings and reveals any findings that may otherwise be obscured in one of the views [6].

A compressive force between 40 to 180 Newtons [7, 8] is applied to reduce the compressed thickness as much as possible and to keep the breast immobilized during the x-ray exposure. The Beer-Lambert law in Equation (1-1) is the principle behind how the image is generated through the varying attenuation properties of different types of breast tissue and partially explains why large compressive forces are applied.

$$\frac{I}{I_0} = e^{-\mu x} \tag{1-1}$$

This law states that the fraction of an incident beam with initial intensity I_0 that will transmit through a particular substance with linear attenuation coefficient μ decreases exponentially with increasing thickness x of that substance. An x-ray image is created when different parts of the breast attenuate the incident x-ray beam intensity I_0 by varying degrees so that the detector sees intensity I after transmission through the breast. Higher radiation doses would be required to compensate for the effects of too much attenuation and scattered radiation. Compressing the breast as much as possible decreases the probability of absorption and scatter of the incident rays, limiting the necessary radiation dose.

Medical x-ray imaging provides structural information by exploiting the differing x-ray attenuation properties of various tissue types with the goal of differentiating between abnormal and healthy tissue. Image formation and analysis relies upon the assumption that x-rays travel in straight lines from the cone beam x-ray source to the x-ray detector. However, when x-rays scatter due to interactions with the breast, the attenuation properties of different structures inferred from the detected radiation can be incorrectly estimated. Scattered radiation in projection x-ray imaging increases strongly with object thickness and can reduce lesion contrast and detectability. To minimize the negative effects of scatter in mammography, anti-scatter grids are routinely placed between the breast and the detector to block a portion of the scatter that would otherwise reach the detector. Anti-scatter grids consist of strips of high atomic number material, such as lead, separated by less attenuating material, such as a carbon fiber or air. In modern mammography, anti-scatter grids have been shown to improve contrast by anywhere from ~15% to over 70%, depending upon the thickness and composition of the breast, thereby improving the accuracy of the estimated attenuation properties [9, 10, 11].

Linear attenuation coefficients are functions of the beam energy, which is within the range of 12 – 40 keV in mammography [12]. A continuous spectrum of bremsstrahlung x-rays are produced when electrons accelerate from a cathode towards a rotating anode inside the x-ray tube [13]. A generator supplies the voltage to the cathode and anode, setting the energy of the electrons, which, in turn, determines the peak energy of the output spectrum of photons [13]. The energy for an average photon in this spectrum is typically one-third to one-half of the energy peak [13]. Many of the lowest energy x-rays have a high probability of absorption by the breast without adding any useful information to the image [14]. Filters are used to cut out a majority of these lower energy photons that would unnecessarily add to the radiation dose [14].

Digital detectors in full field digital mammography (FFDM) are now replacing the screen-films that were used to capture images of these transmitted rays [15]. Digital imagers can either be direct or indirect. Indirect detectors consist of scintillators that convert incident x-ray light into a lower frequency of light that then gets converted into an electrical signal [16]. Finally, the electrical signal is converted again into a digitized pixel value [16]. Direct detectors, such as the amorphous selenium detector, convert incident x-ray radiation directly into an electrical signal [17]. Both systems are integrating detectors, where the pixel values are directly proportional to the total energy deposit of the incident radiation over the exposure time. For mammograms, the exposure time is on the order of a second.

Because an essential part of catching cancers early is the ability to detect them when they are small in size, mammography requires high spatial resolution detectors [18]. FFDM systems typically have spatial resolutions of 5-6 line pairs/mm (lp/mm), allowing for visualization of features on the order of a few hundred microns [18]. Among the many complicated structures in the breast as seen in Figure 1-2(a), the two main types are glandular tissue and adipose (fat) tissue [19]. Glandular tissue has a higher value of μ than adipose tissue, whereas cancerous tissue has slightly higher attenuation than glandular tissue as illustrated by their absorption spectra in Figure 1- 2(b). The percent composition of glandular and adipose tissues varies from one woman to the next [19]. Denser breasts have a higher composition of glandular tissue, and studies have shown that for breast cancer, breast density is one of the strongest risk factors [20].

An example of a breast with slightly more glandular tissue than adipose is shown in Figure 1-3 in an (a) MLO view and (b) a CC view of the same breast with an obvious cancer circled in red. This breast also exhibits the presence of many calcifications (arrows in Figure 1-3(a)), which are small calcium deposits within the breast [21] that can be an early and, at times, the only indicator for the presence of cancer [22]. While not cancerous themselves, tight clusters of small calcifications, as those seen in the dashed circle of Figure 1-3(b), can be of concern [21] and require further investigation.

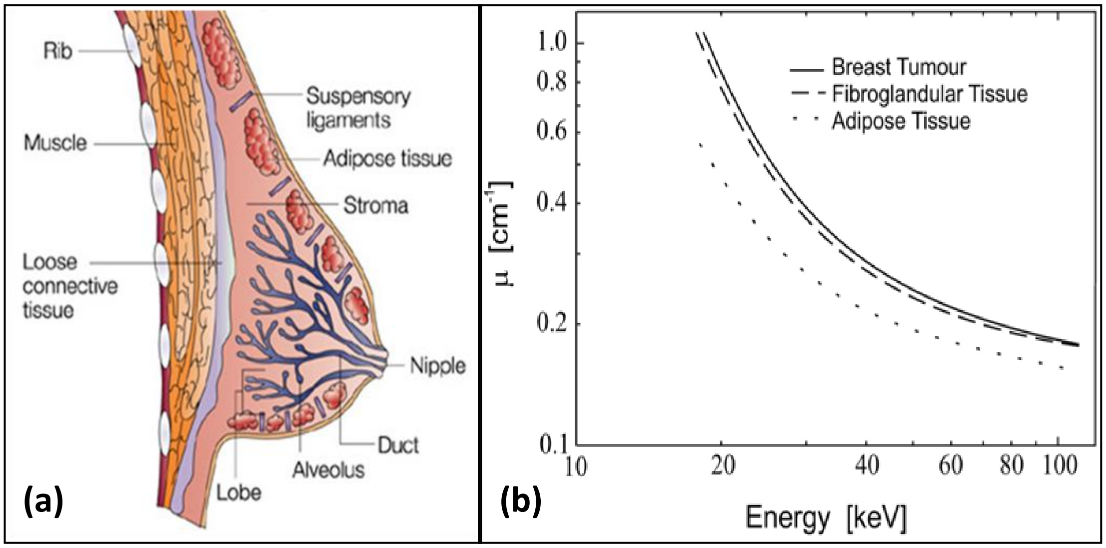

Figure 1-2: (a) Anatomy of a human breast. (b) Absorption spectra of the two main types of healthy tissue, adipose tissue and glandular tissue shown with absorption spectrum of cancerous

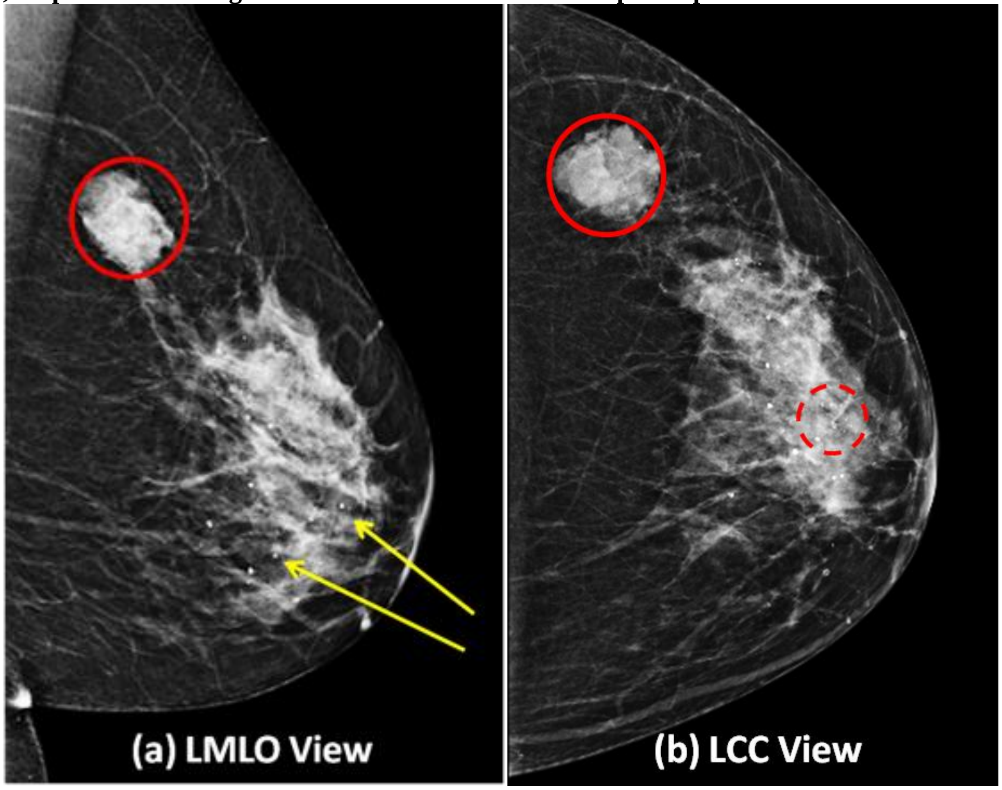

Figure 1-3: (a) Mediolateral oblique view of a left breast (LMLO) with an obvious cancerous mass circled in red. Arrows point to calcifications, which can be indicators of cancer. (b) Craniocaudal (LCC) view of the same left breast as shown in (a) with the same cancer circled in red. A tight group of calcifications is shown in a dashed circle.

Mammography is used for screening because of its high overall sensitivity between 78-85% and specificity of 99% [23, 24], where sensitivity is the percentage of suspicious findings that are correctly identified and specificity is the percentage of negative results that are correctly assessed as negative. Kolb et al. found that the sensitivity of mammography drops to 48% for dense breasts [23]. Denser breasts with higher percentages of glandular tissue can have hidden cancers under overlapping tissue. Alternatively, overlapping structures can also look like cancerous masses in the mammogram [25]. Though the US Preventive Services Task Force (USPSTF) suggest that screening mammograms have a high certainty of a moderate to substantial net benefit [26], mammography alone has its shortcomings in finding and diagnosing all types of cancers. Additional workup of suspicious findings is done in conjunction with other imaging modalities, and efforts are being made to include developing technologies as more is learned about the behavior and causes of breast cancer.

1.1.2 Digital Breast Tomosynthesis (DBT)

A relatively new modality approved for screening is digital breast tomosynthesis (DBT). DBT imaging is performed by using the same equipment and scanner configuration as FFDM. Instead of a single exposure, in DBT, multiple low-dose x-ray images are taken at various angles along a circular arc relative to the direction of compression. A reconstruction algorithm combines these images to create a three-dimensional (3D) image of the breast, which consists of slices or sections of the breast [27]. The issue of missed cancers arising from obscuration by surrounding tissue in mammography is alleviated by some degree by the reduction of tissue overlap in DBT reconstructed slices. Another advantage of DBT is the possibility of depth localization of findings within the reconstructed volume, which is not possible from a single projection image.

DBT, in conjunction with FFDM, has been shown to reduce recall rates [28, 29]. Rose et al. found that cancer detection rates increased and recall rates that arise from lacking information in screening mammograms fell from 8.7% to 5.5% when DBT was introduced as a screening modality [30]. Figure 1-4(a) shows an MLO view mammogram of a right breast. Figure 1-4(b) shows a reconstructed slice from the DBT acquisition of the same breast where the cancer (circled in red) is focused, has more contrast, and is more visible after the superimposition of tissue is reduced.

Even though DBT improves detectability of obscured masses, there is generally no form of scatter rejection in most clinical DBT units. Because the x-ray source moves with respect to the x-ray detector, the anti-scatter grids that are used in FFDM cannot easily be implemented for clinical DBT scans. Although, there is less overlap of tissue, the loss of contrast between cancers and background tissue due to scatter is still a possibility in DBT.

X-ray imaging techniques alone have their shortcomings in finding and diagnosing all types of cancers. Currently, the only definitive way of determining whether a finding is malignant is by performing a biopsy, which is the process of taking a small tissue sample of the feature in question. Further investigation of suspicious mammogram findings is done in conjunction with other imaging modalities to try to avoid unnecessary biopsies, which can cause patient anxiety due to the invasive nature of the procedure [31].

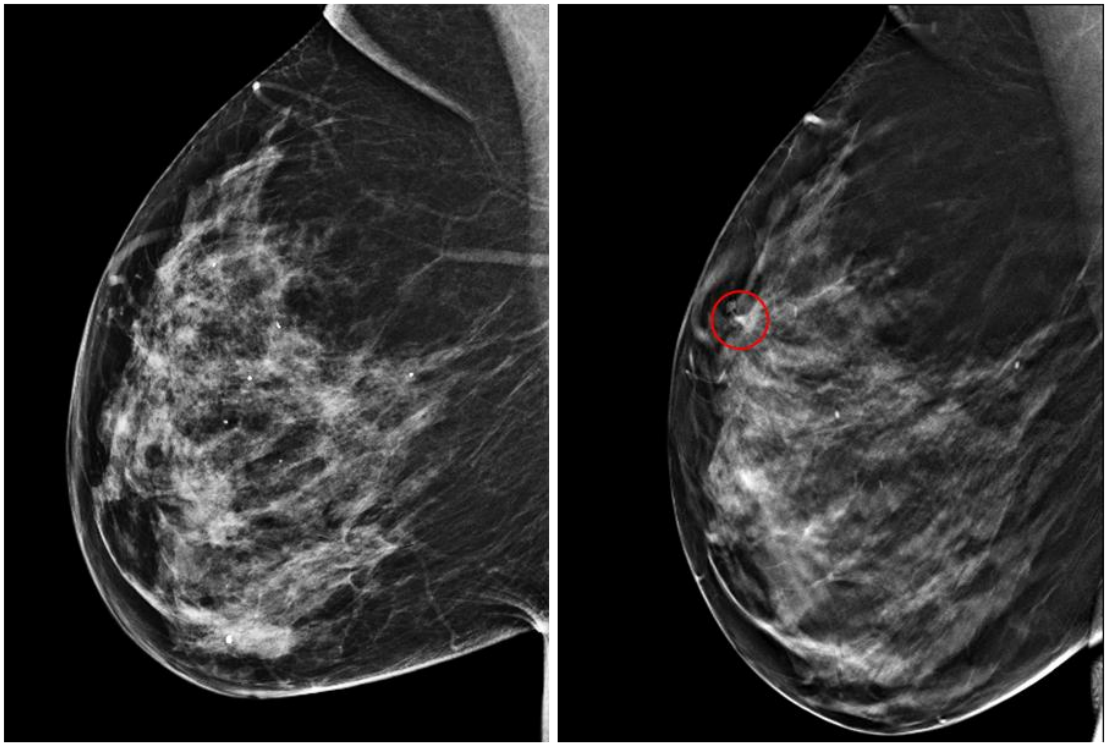

(a) RMLO Mammogram (b) RMLO DBT Slice

Figure 1-4: (a) Clinical mammogram of right breast in MLO (RMLO) view (b) Reconstructed slice of the same breast in an RMLO view. Solid circle shows where cancer is located and has more contrast in focal DBT slice than in the mammogram in (a).

1.2 Diagnostic Imaging Modalities

1.2.1 Contrast-Enhanced X-ray Imaging

Contrast-enhanced mammography (CEM) is an x-ray imaging modality that has been recently approved by the FDA for diagnostic tests [32]. CEM is performed with the same type of hardware that is used for FFDM and DBT. The intravenous injection of an iodine contrast agent by a power-injector is one of the features that differentiates CEM from conventional mammography [14]. When administered through the vein, the iodine contrast agents flows through blood vessels to the regions that are being supplied by the vessels [33], with a tendency to be taken up more by vessels feeding cancers, which require more fuel to sustain proliferation. With a K-edge at 33.169 keV [34], iodine will absorb a large portion of incident photons with approximately this same K-edge energy. When imaged using x-rays, iodine will appear as regions of higher attenuation than breast tissue [14].

Enhancement of the vasculature and the regions supplied by these vessels is accomplished by either temporal subtraction or by the dual-energy method [14]. Temporal subtraction is carried out by acquiring the first set of images of the breast before the iodine is injected and a second set of images after the contrast is administered [14]. Subtraction of these two image sets yields an image of the iodine distribution within the breast [14]. On the other hand, the dual energy technique involves acquiring two types of images in quick succession after the contrast agent is injected. The first is a low-energy image, only showing the structures of the breast as in a typical mammogram, and the second is a high energy image using x-ray techniques that would cause a high rate of absorption around the K-edge of iodine [14]. By subtracting the two images, breast structure from the low energy image is removed from the higher energy image, leaving just the regions of higher absorption by the iodine in the final difference image [14].

Figure 1-5 shows an example of CEM images produced by the dual energy method of the same breast shown in Figure 1-3. The first panel (a) shows the low energy image, which looks like a regular mammogram. (b) and (c) are the high energy and difference images, respectively. Significant reduction in contrast can be seen in the high energy image (b) where most of the higher energy x-rays transmit through the breast. The contrast enhanced image in (c) provides high resolution structural and functional information of the vasculature of the breast, at times uncovering structures that would may otherwise be indiscernible in conventional mammography.

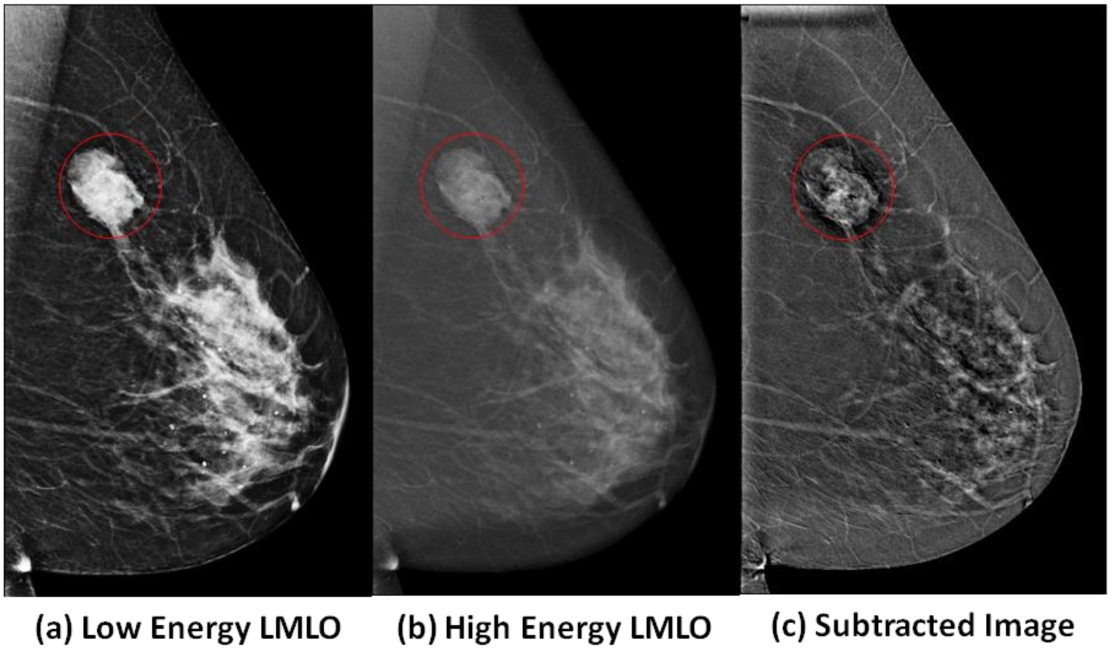

Figure 1-5: Contrast-enhanced mammography (CEM) images of the same left breast as shown in Figure 1-3. (a) is the low energy image, (b) is the high energy image, and (c) is the resulting difference image after subtraction of (a) from (b). Enhancement of the mass is seen in (c) in the solid circle.

Jochelson et al. found that CEM had higher sensitivity than conventional FFDM in a study of 52 women with newly diagnosed cancers [35]. In spite of its advantages over mammography and DBT, allergies to iodine contrast, diabetes, and renal insufficiency are major contraindications for the use of the iodine contrast agents essential for CEM [36], excluding many from being eligible for this procedure.

1.2.2 Ultrasound (US)

A less expensive alternative [37] for further work-up of suspicious features that look like masses in the mammogram is ultrasound (US) [6]. Instead of photons, US imaging is performed through the use of a transducer that emits high frequency sounds waves through the breast [38]. The reflected sound waves that travel back with different amplitudes and at different times are the signals used to produce a real-time image of internal structures of the breast [38]. The resolution of the images depends upon the frequency of the sound waves used, with higher frequency waves producing higher resolution images [37]. Although lower frequency sound waves provide lower resolution images, these waves can penetrate deeper since they are less likely to be absorbed as the higher frequency waves [37]. Despite lower resolution than mammography, US has higher sensitivity in women with dense breasts [4]. In a study of 455 palpable lesions performed by Soo et al., the negative predictive value (NPV) when mammography was followed by US was found to be 99.8% [39]. However, US alone cannot be used for screening for cancer since the region of interest must be known for visualization [4].

1.2.3 Breast Specific Gamma Imaging (BSGI)

Another alternative imaging modality for breast cancer imaging is scintimammography, or breast specific gamma imaging (BSGI). For BSGI, a radiotracer is intravenously administered to the patient. Technetium-99m (Tc-99m), a radioisotope with a half-life of 6 hours, emits photons with energy of 140 keV and is typically attached to a ligand to create a cationic complex [40]. The most common form of this radiotracer used for BSGI is sestamibi, which tends to have a higher uptake and retention in regions of higher negative mitochondrial potential, such as cancers [41]. Areas of focal uptake in the breast emit more gamma rays than areas of less uptake.

A gamma camera is used for imaging the distribution of the radiotracer within the breast. Gamma cameras are photon counting detectors consisting of scintillators that convert incident gamma rays to a lower frequency of light [42]. These lower energy rays are then converted to voltage signals, conventionally by photomultiplier tubes (PMTs) [42]. Finally, these voltage signals are converted into digital pixel values that are proportional to the number of detected photons [42]. Unlike x-ray imaging, detected gamma rays must be within a very specific energy range to be considered as a gamma event used for image production. Furthermore, since sestamibi tends to be taken up by other organs besides the breast [41], all gamma rays would not provide information within just the breast in the planar image formation of the tracer distribution. A collimator, which is an array of holes made of a highly attenuating material, such as lead, is necessary for rejecting gamma rays that do not come from a desired direction [43]. As a result, longer acquisition times ~5-10 min are required for BSGI image acquisition for which the patient is seated throughout the scan [43].

This imaging modality provides functional information of the breast at a molecular level [43]. Brighter regions within the image where more photons are detected are more likely to be cancerous than areas of less uptake. For BSGI, the breast can compressed in the same configurations as those used for mammography [44]. Figure 1-6 shows BSGI images of the (a) LMLO and (b) LCC views of the same breast seen in Figures 1-3 and 1-5. In the color scheme used for these images, darker pixel values represent higher photon counts. Higher uptake can be seen in the cancer circled in red.

In contrast to mammography, the sensitivity of BSGI is independent of breast density [45, 46, 47], making it advantageous for detecting cancers in dense breasts. Brem et al. performed a study of 146 patients and found BSGI to have a sensitivity of 96.4% and a specificity of 59.5% [48]. Despite a higher sensitivity, one disadvantage of BSGI is the planar nature of the images, which does not account for attenuation of the gamma rays as they travel through the breast to the detector [43]. Similar to mammography, there is an overlap of features over the depth that gets imaged, which reduces contrast between areas of higher uptake and surrounding healthy tissue [43]. Finally, BSGI suffers not only from overlapping features, but also from lower spatial resolution. Detection of cancers smaller than the order of a few millimeters is especially hindered with increasing distance between the camera and the breast [49].

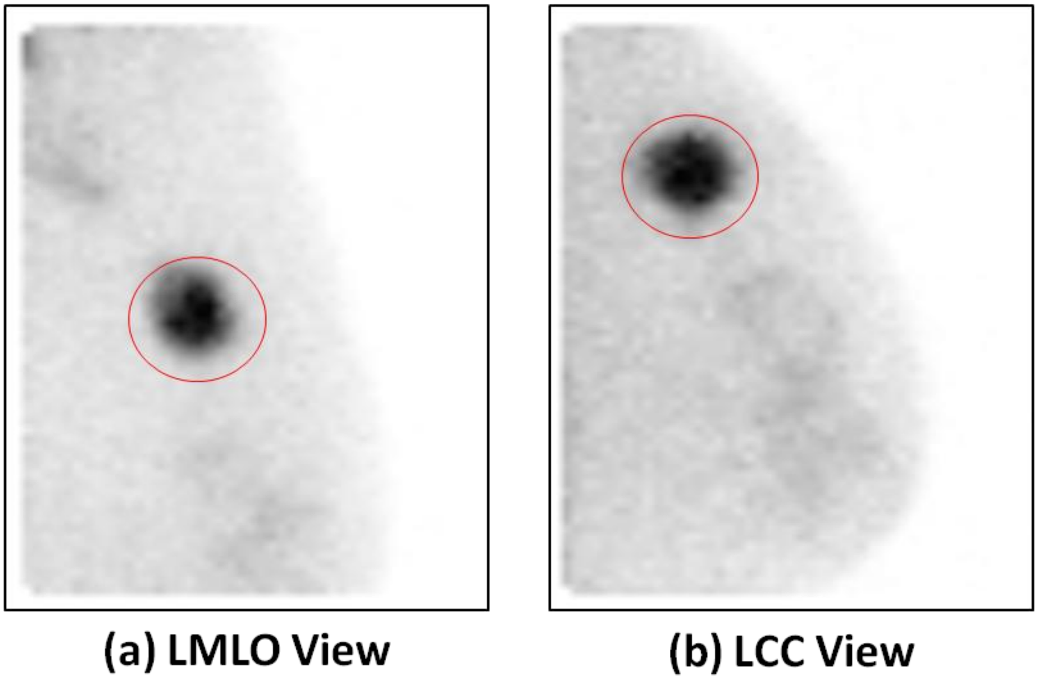

Figure 1-6: BSGI image of left breast in (a)MLO view and (b) CC view. This breast is the same as shown in Figures 1-3 and 1-5. A solid circle shows where the cancer is.

1.2.4 Magnetic Resonance Imaging (MRI)

Rather than using ionizing radiation as in diagnostic mammography or nuclear medicine, magnetic resonance imaging (MRI) is accomplished by the application of magnetic fields and radiofrequency pulses to manipulate the spin alignments of protons in various tissues [50]. The relaxation of these protons creates voltage signals in a radio antenna that are used to create an image [50]. Variations in the relaxation time found in different tissue types allows for the distinction between soft tissues with better contrast than that of radiography [50]. Contrast agents can also be used in MRI to enhance images, which, similar to the iodine contrast agent of CEM, tend to be taken up in specific regions, such as cells within and surrounding cancerous regions [51].

In a study performed by Warner et al., MRI had 77% sensitivity and 95% specificity [52], where the sensitivity was found to be higher than mammography, but specificity was lower than mammography or US. Because of its high sensitivity, breast MRIs have been recommended by the SBI and the ACR as a screening modality for women at high risk of breast cancer [4]. However, because of the high rate of false positives and the high cost of breast MRI, this imaging modality is mostly used for diagnostic purposes when available [53, 54, 55, 56, 57].

1.3 Investigational Scanners

1.3.1 Dedicated Breast Single Photon Emission Computed Tomography (SPECT)

Dedicated breast single photon emission computed tomography (SPECT) provides a three-dimensional (3D) image of a radiotracer within the breast, solving the problems associated with lesion localization and contrast reduction in BSGI. Breast SPECT scans require gamma cameras to acquire images over an angular range of at least a 180º around the breast [43]. For these scans, the patient lays prone, face down, on a table with the breast hanging pendant through an opening in the table [49]. A camera beneath the table surface then rotates about a vertical axis that runs parallel through the pendant breast [49]. A reconstruction algorithm creates a 3D volume of the breast from the images acquired. However, just as in BSGI, a major shortcoming to SPECT is its low spatial resolution [49].

1.3.2 Breast Positron Emission Tomography (PET)

Positron emission tomography (PET) is another nuclear medicine imaging modality that works similar to SPECT. PET uses ^{18}F-FDG, which is a radioisotope that emits positrons instead of photons. In contrast to SPECT, PET scanners must detect, simultaneously, the two 511 keV photons that result from the annihilation of positrons with electrons to deem an event as usable for image reconstruction [49]. Dedicated breast PET systems have been configured in essentially the same way as dedicated breast SPECT with the prone patient’s breast hanging pendant, the main difference being a ring of detectors setup for coincidence imaging [49].

Because of the tendency of ^{18}F-FDG to accumulate in primary breast cancer as well as regions to where cancer has spread, PET is used to monitor the efficacy of various treatment methods that are applied for reducing the size of cancers before they are surgically removed [49]. PET also provides slightly better spatial resolution than conventional gamma cameras [49].

Despite the advantages of higher sensitivity associated with molecular imaging modalities such as PET, SPECT, and BSGI, the radiation dose and relatively lower spatial resolution still remain major concerns that inhibit their wide-spread use as diagnostic tools in the clinic [49]. However, improvements in gamma camera technology have made it possible to reduce the radiation dose by a factor of over three times that initially used in scintimammography [58, 59].

1.3.3 Dedicated Breast Computed Tomography (CT)

Though not used in the clinic, dedicated breast computed tomography (CT) is currently under investigation for its potential use as a screening or diagnostic imaging modality

[60]. In dedicated breast CT, the patient is again prone and the breast is kept pendant [60]. Patient studies performed by Lindfors et al. used a cone beam x-ray source and indirect x-ray detector that rotated through an angle of 360º, taking 500 projection images within 16.6 seconds [60]. A 3D image is reconstructed from these projections. They found that while visualization of microcalcifications in CT was inferior to that of mammography for the same dose as 2-view mammography, CT provided improved visibility of masses [60].

Because CT provides a full data set, spatial resolution is nearly equivalent in all three dimensions of the reconstructed image [61]. This is unlike DBT where depth resolution is diminished due to data undersampling [62]. Even though breast CT can potentially provide superior visualization of tissues in 3D in comparison to DBT, patient positioning in CT is not ideal for catching cancers that are located close to the chest wall, which typically does not get imaged due to the presence of the table upon which the patient lays prone [63].

1.3.4 Dual Modality Tomosynthesis (DMT)

The DMT system is an investigational device that was built at the University of Virginia [64]. This unique system combines DBT with molecular breast tomosynthesis (MBT) in a single gantry. In the DMT system, the DBT portion of the scan is equivalent to limited angle breast CT in which both source and detector rotate together around a common axis of rotation (AOR). DMT MBT is a limited angle version of dedicated breast SPECT, in which gamma images of a radiotracer are acquired at multiple angles over a limited circular arc. Figure 1-7 shows a photograph of the scanner. The DMT scanner consists of a gamma camera, an x-ray tube, and an x-ray detector rigidly attached to a C-arm gantry.

In contrast to breast SPECT and breast CT, the gantry is an upright system where the patient is seated for the scan. Since a table does not separate the subject from the detectors, better access to the chest wall edge is possible with upright systems.

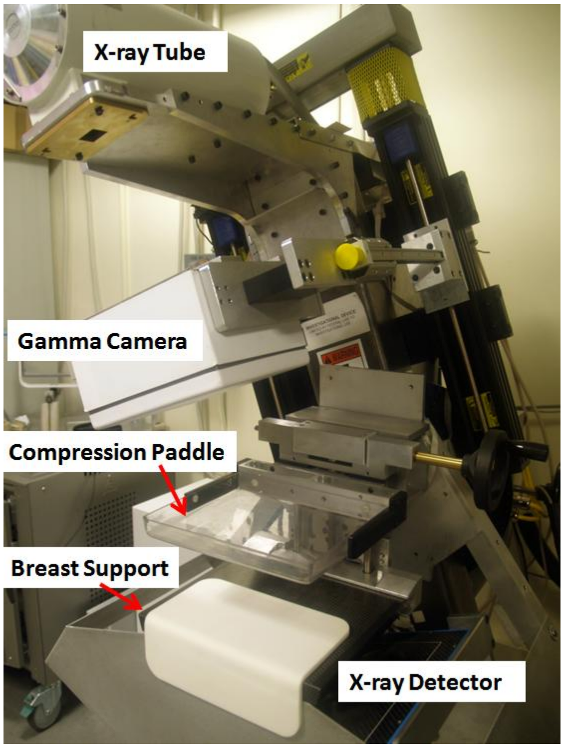

Figure 1-7: Dual modality tomosynthesis (DMT) scanner built at the University of Virginia. X-ray tube, gamma camera, and x-ray detector all rotate together around a breast placed on the breast support that is immobilized by a flat compression paddle.

For a typical DMT scan, the patient is injected with Tc-99m sestamibi, the same radiotracer as described for BSGI. After injection of the radiotracer, the breast is placed on a breast support that is independent of the gantry arm. A flat paddle compresses the breast onto a breast support, using just enough compressive force to immobilize the breast. Once the desired tissue is confirmed to be within the field of view (FOV) of the x-ray detector, the full DBT scan is performed by acquiring thirteen x-ray images over a 24 degree angular. The duration of the DBT scan is approximately two minutes, and the exposure for a single scan is targeted to be equivalent to the subject’s most recent two-view clinical mammogram [64]. It is then followed by a ten minute MBT scan. Instead of a single 10 minute gamma image as in BSGI, five 2-minute images are collected by the gamma camera within an angular span of $-20°$ to $+20°$relative to the direction of compression. A full DMT scan of a single breast can take up to 15 minutes to complete. The process is then repeated on the other breast.

Once both image sets have been collected, each set is reconstructed separately. Since the breast is in the same configuration for both scans, findings in the MBT scan can be correlated with the structures seen in the DBT reconstruction. Alternately, suspicious findings in the DBT image can more likely be assessed as benign if there is no evidence of uptake in the corresponding region of the gamma reconstruction. An example of the reconstructed slices from each image set are shown in Figure 1-8 for the same breast seen in Figures 1-3, 1-5, and 1-6. The focal slice of the obvious cancer circled in red in the DBT image is shown in (a) and the corresponding slice in the MBT reconstruction is shown in (b).

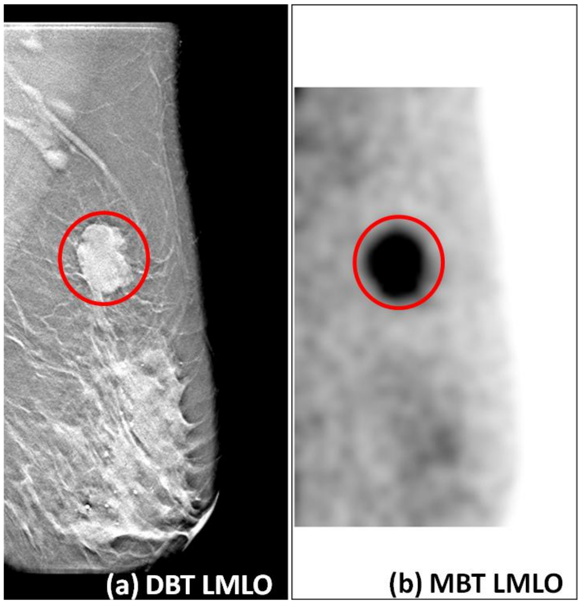

Figure 1-8: Images acquired by the DMT system of the same left breast shown in Figures 1-3, 1-5, and 1-6. (a) Reconstructed slice from DBT LMLO. (b) Corresponding slice of MBT reconstruction

1.4 Purpose

The DBT portion of a DMT scan resolves the problem of tissue overlap witnessed with FFDM alone. The addition of MBT would, in theory, increase the sensitivity of detecting cancers in dense breasts. DMT offers a more affordable, less time-consuming option over MRI. In addition, both modalities allow for the visualization of the chest wall edge, a capability that is not currently available in dedicated breast CT and dedicated breast SPECT [63]. By combining the relatively high spatial resolution of DBT with the sensitivity of molecular imaging, DMT could potentially provide both structural and functional information for all breast types. Pilot study data from the DMT system showed promising results with a sensitivity of 86% and a specificity of 100% [64]. Since this preliminary study included a small number of participants, clinical studies are currently underway with the DMT system to assess whether it can be used as another adjunct to mammography for the diagnosis of breast cancer. Despite the success of the pilot study, DMT, as it currently stands, must be optimized for it to be eventually implemented in the clinic.

Modern day clinical DBT scans can take anywhere from a few seconds up to ~30 seconds [65]. The DBT portion of the DMT scan can take up to two minutes. Even though only mild compression is applied, such a long scan time increases the likelihood of patient discomfort and patient motion. Motion blur creates unacceptable artifacts in the x-ray images, which demand high resolution for resolving sub-millimeter structures. Depending upon its extent, this motion can also lead to inaccurately co-registered images, diminishing the reliability in the correlation of a suspicious finding in one modality to the corresponding location in the other.

Another disadvantage of the DMT DBT system is that there is no form of scatter rejection as there is for cone-beam CT. In tomographic x-ray imaging, such as CT, scatter produces cupping and streak artifacts and causes errors in the estimated x-ray attenuation coefficients represented by image voxels. As in CT, DBT images consist of voxels whose values are ideally linearly related to the linear attenuation coefficient μ of the tissue within the voxel. However, the limited angular range of DBT does not provide a complete tomographic data set. Therefore, the estimate of μ for a given voxel is affected by artifacts arising from structures in nearby slices. Scatter in DBT introduces additional errors in the form of cupping artifacts and attenuation quantitation errors, similar to those in CT [66, 67, 68, 69]. Moreover, scatter increases strongly with increasing object thickness [70]. As less compression is applied for DMT scans, the average breast compressed thickness of ~8 cm seen in DMT clinical studies is significantly higher than the 5.3 cm U.S. average in mammography [71, 72], emphasizing the importance of some form of scatter rejection.

The purpose of this work is to reduce the scan time of the DBT portion of DMT scans and to introduce an x-ray scatter rejection method for improving lesion detectability. Ramifications of the required changes are analyzed to ensure that the applied patient radiation dose is not raised from the current levels used in human subject clinical trials.

Chapter 2

Scan Time Reduction

2.1 X-ray Tomosynthesis

The most simplified form of tomosynthesis was first described in early works by David Grant in which an x-ray source and film cassette move in opposite directions in planes above and below an object being imaged [73]. Figure 2-1(a) shows two circles, one solid and one dotted, being imaged by a parallel x-ray source and cassette that are moved from position 1 to position 2 over the scan. Grant explained that a single plane, called the tomographic plane as determined by the scanning geometry, can be resolved from within the object, while features outside of the plane are blurred as more views are acquired [73]. Figure 2-1(b) shows a plane containing a solid circle whose image from both positions 1 and 2 overlap in the same location on the film. Because of its location, the dotted circle's image is distributed over the film rather than summed in one location, and its image is blurred on the film. The configuration of the source and detector is chosen such that motion is centered on the desired plane. As the detector and source move from position 1 to position 2, the solid circle is projected in the same location on the film throughout the motion while the dotted circle is blurred by the motion of the film [73].

This geometry allows for the multiple projections of the solid circle located at the tomographic plane to be superimposed on the film, making the solid circle image more focused in comparison to those of structures above and below this plane [73]. The extent to which the tomographic plane comes into focus depends upon the degree to which the other planes are blurred [73]. The tomography example presented by Grant used the same exposure level as a single radiograph [73].

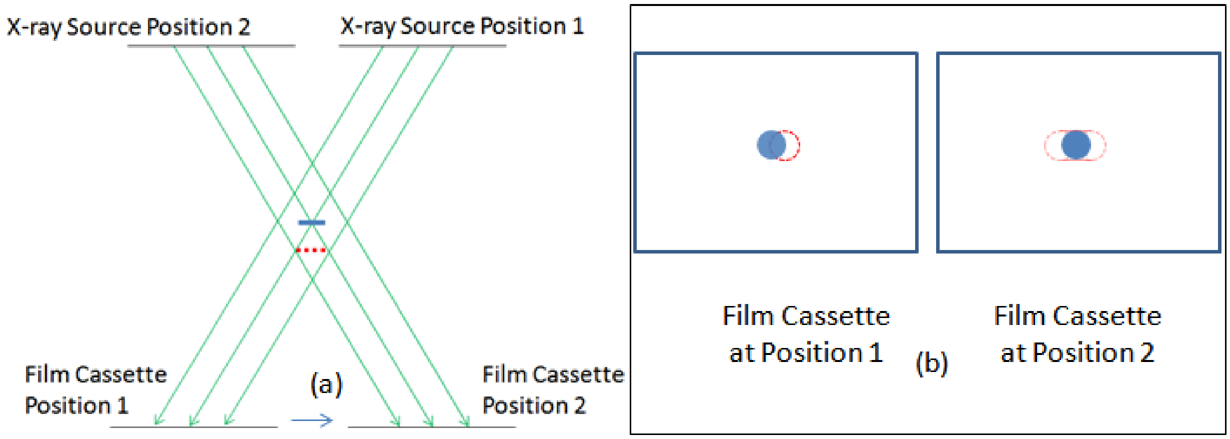

Figure 2-1: (a) Parallel x-ray source and cassette move in opposite directions from position 1 to position 2, imaging 2 circles in each configuration. The resulting images are shown in (b). The film cassette in position 2 has the summed image where the dashed circle is blurred out in comparison to the solid circle, which is located at the tomographic plane and is focused in the image.

Coining the term tomosynthesis for describing this process, Grant then went on to explain that all object planes can be resolved by summing multiple separate images rather than integrating over a single film [73]. Figure 2-2 is a simplified schematic of how images are acquired separately on individual films, which are stacked with offsets respect to each other that are chosen to align the images of a particular plane. The advantage of this process is that each plane could then be visualized separately, irrespective of its positions relative to the source and detector [73]. In contrast to the case where only a single film is used and only a single tomographic plane is resolved based upon the specific source-detector geometry, all planes can be resolved individually without having to center source and detector motion about the desired plane [73].

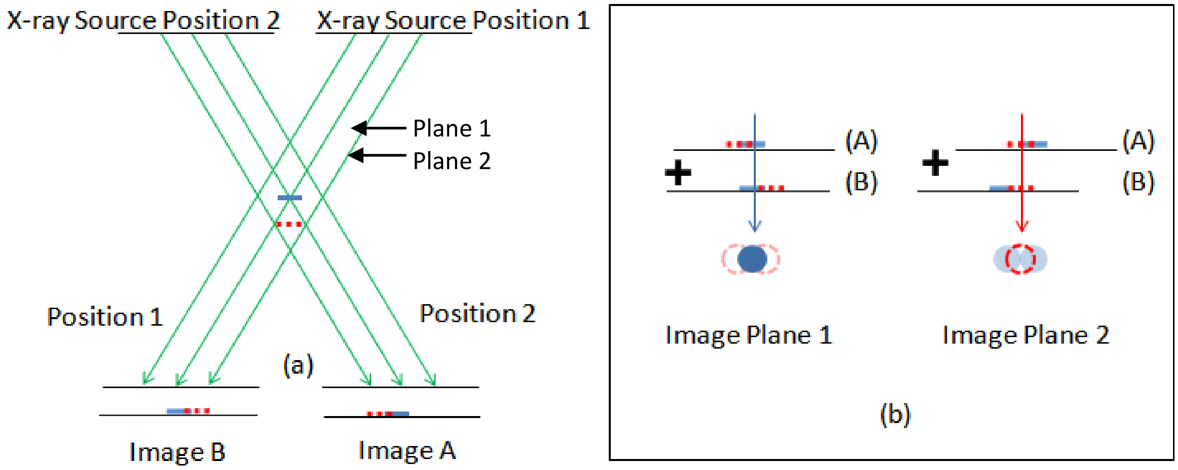

Figure 2-2: (a) Parallel x-ray source and detector move in opposite directions from position 1 to position 2, imaging 2 circles in two individual projection images. The plane of each circle can be resolved individually by shifting and summing the images based upon the geometry and the desired plane as shown in (b). Plane 1 shows the focal plane of the solid circle where its projections overlap while those of the dashed circle are distributed over the plane in different locations. Plane 2 has the summed image where the solid circle is faint and the dashed circle is in focus.

Grant described a system for generation of a 3D image volume using a circular geometry scan where both source and detector moved in circles that were in separate, parallel planes above and below the object being imaged as shown in Figure 2-3 [73].

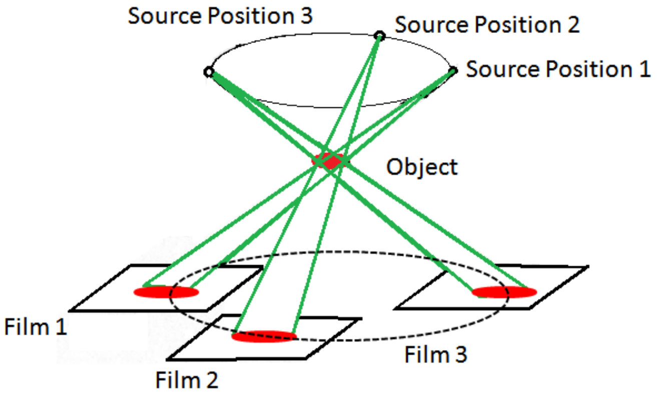

Figure 2-3: Circular geometry scan where both source and detector move in circles within parallel planes above and below the object being imaged.

The desired plane could be resolved by shifting and summing the films based upon the scanning radius selected [73]. Grant proposed multiple methods for summing images, which included using a computer to sum images that were digitized from the films, using contact prints, or using video disk recorders [73]. In the system that Grant described, 20 separate radiographs were acquired using the circular scan geometry where views were uniformly distributed over an angular range of 360º [73]. These were then photoreduced onto films. All reduced images were illuminated to project their images using a wide-angle lens onto individual mirrors spaced with the same angular separation as the radiographs [73]. The mirrors then reflected the projections into a display volume [73]. Individual planes of the volume were produced by summation of the projections onto a viewing screen, allowing for the visualization of any single plane by orienting the viewing screen within the display volume to match the orientation of the desired plane within the object [73].

Screen-film mammography (SFM), once the standard modality of breast cancer screening, is now being replaced with full-field digital mammography (FFDM) [15] due to the many advantages that come with digital detectors. These detectors provide digital images of the total fluence of x-rays incident on the detector, the resolution of which depends in part upon the detector element size [15]. Even though SFM has much higher spatial resolution, the much higher dynamic range of FFDM detectors compared to film offers improved visualization of structures in dense breasts [74]. Also, digital readout and storage of images provides the ability to post-process the image after acquisition, and image display on acquisition workstation monitors provides the ability to almost immediately view the image after exposure [15] rather than waiting for the film to be processed. The advent of digital systems made acquisitions of multiple images over a short period time possible [75], leading the way for DBT.

The use of digital detectors in breast imaging made it possible to visualize multiple planes within the object with a single tomosynthesis scan during which individual projection views are acquired and stored [73]. Three-dimensional (3D) representations of the breast could be computed from DBT projection images using reconstruction algorithms. These algorithms attempt to take the information in the projections and provide a map of the attenuation for each plane of the imaged breast within a reconstructed volume. Mathematically, this principle can be written as a linear system where a 3D matrix $\boldsymbol{x}$ consists of linear attenuation coefficients that are projected onto the detector at a given projection angle using the projection matrix operator $\boldsymbol{A}$, which results in the pixel values $\boldsymbol{y}$ seen in the projection image as shown in Equation (2-1).

$$\boldsymbol{A}\boldsymbol{x} = \boldsymbol{y} \tag{2-1}$$

The goal of most reconstruction algorithms is to solve for voxels in $\boldsymbol{x}$, or the matrix elements within the 3D reconstruction volume [76]. Back-projection (BP), transform algorithms, and iterative algorithms are three common types of reconstruction algorithms [77].

The simplest algorithm of the three categories is back-projection as it is the most similar to the shift-and-add (SAA) method described by Grant. Instead of a single film, multiple projections are backprojected through the matrix $\mathbf{x}$ using the known values of the source and detector locations with respect to the object for every projection view [77]. The summed backprojections provide the 3-D estimate of the attenuation distribution in the object. Therefore, fluence information from pixels in the projections, which are proportional to line integrals of the attenuation that x-rays experience along the paths from the source to each detector element [78], can be used to estimate linear attenuation coefficients in the voxels [76].

Though BP can be used for any source-detector configuration, this method introduces strong interplane artifacts as a result of projecting each pixel value back through the reconstruction volume [76]. Transform algorithms, such as the commonly used filtered back-projection (FBP) in computed tomography (CT) and the Feldkamp or FDK algorithm in conebeam breast tomosynthesis, make use of the Fourier central slice theorem [76]. This theorem states that the Fourier transform of a projection image at viewing angle θ is equal to a slice in frequency space through the Fourier transform of the attenuation distribution within the object at that same angle θ. [79]. For a parallel beam geometry, the rays through the object are oriented at the same angle θ and thus all correspond to the same linear slice in frequency space. [77]. However, direct implementation of the central slice theorem for DBT image reconstruction is not straightforward for the cone beam geometry of DBT [77]. In addition, frequency space is severely undersampled when only a limited angular range typical of DBT is available [77, 76].

To overcome the issues created by the geometry of DBT, iterative reconstruction algorithms have been proposed for reconstructing DBT images. These algorithms check the forward projection of the reconstructed volume against the original projections and update the reconstruction volume iteratively until the error between the unknown linear coefficients $\boldsymbol{x}$ from Equation (2-1) and the apparent attenuation, as determined from the projection image, is sufficiently minimized [77]. Since the success of this type of algorithm does not require a mathematically complete projection data set, it can be applied to incomplete tomographic data such as that in DBT [76]. An iterative algorithm provided by Dexela/Perkin-Elmer (London), the manufacturer of the DMT x-ray detector is used for reconstructing DMT DBT images.

2.2 DMT Digital Breast Tomosynthesis (DBT)

2.2.1 Step-and-Shoot (SNS) in DMT

Modern day clinical DBT scans can take anywhere from a few seconds, when imaging is done while the x-ray source is moving continuously, up to ~30 seconds when using the step-and-shoot (SNS) method [65]. During a human subject DMT DBT scan, the x-ray images are taken in a SNS fashion over a 24° angular range. In this method of acquisition, the gantry is first put into motion. When it reaches the desired projection angle, the tube motion is stopped and several seconds elapse before the detector integration window is turned on. Because the exact time of triggering the x-ray tube has some uncertainty, the detector integration window is set to a slightly larger value than the exposure time of the x-ray source. Once the x-ray source has been triggered and the exposure is completed, the gantry is put into motion again. The reason for the use of SNS acquisition among early DBT systems was in part the older CCD detectors used for earlier DMT studies, which required longer pauses between exposures for image readout. Another reason for the pause of several seconds between projections is the necessity to wait for gantry arm oscillations to damp out when the gantry comes to a stop for the exposure.

Using the SNS method, the DMT DBT scan can take up to two minutes to complete, greatly increasing the total time that the patient is in compression compared to 2-D mammography (~1-2 seconds). Longer scan times increase the likelihood of patient motion, which create motion artifacts in the images [80, 81].

2.2.2 Scan Time Reduction (STR) of DMT DBT Scans

An alternative to SNS acquisition is continuous tube motion [82, 83]. With continuous tube motion, the gantry is moving, typically at a constant angular speed [83], during imaging to reduce the amount of time required for the initiation and termination of motion between projections in the SNS method [81]. Hologic, Inc., a manufacturer of mammography scanners has been able to reduce their DBT scan time from 18 seconds down to less than 4 seconds using continuous tube motion during imaging [84]. This reduction in scan time has been shown to significantly reduce the incidence of patient motion [81, 84]. Continuous tube motion is investigated here for scan time reduction (STR) of DMT DBT acquisitions.

STR involves shortening the duration of the DBT scan by introducing gantry arm motion during imaging to reduce the likelihood of patient motion artifacts. Therefore, in addition to minimizing overall DMT DBT scan time, motion artifacts caused from gantry arm motion during x-ray exposures must be minimized so that high resolution and contrast are maintained in the projection images. Besides tube motion, there are multiple factors that cause image blurring, which include geometric unsharpness, blurring caused by the detector, and patient motion. Geometric unsharpness is the blurring created by the non-zero width of the x-ray source. Because the x-ray source is not a true point source, the shadows cast by objects onto the detector will have an umbra and a penumbra, creating a broadening of features in the image [85]. The detector itself will also cause image blurring through all of the processes that are required to convert the input signal into an image, including the conversion of x-ray light into visible light by a scintillator. If the angular speed of the tube is optimized, blurring caused by tube motion could potentially be negligible in comparison to patient motion and the other sources of blurring.

2.2.3 Angular Range and Projection Angles for STR

In tomosynthesis imaging, artifacts in the reconstructed image are inevitable due to the blurring of out-of-plane features within the focal slice [73]. Unlike CT reconstructions where a complete data set provides uniform transaxial resolution within slices taken from the reconstructed volume [61], the resolution of DBT reconstructions in the undersampled dimension is not as high as the in-plane resolution [62]. Depth resolution refers to how accurately two overlapping structures in the undersampled z-direction can be resolved in the reconstructed volume where the z-direction is along the direction of breast compression, or depth, in DBT. Depth resolution of the DBT reconstructions is not as high as the in-plane resolution because the breast is not imaged over a 360º angular range [81]. For example, if one of the images of the two circles in Figures 2-1(a) and 2-2(a) were acquired at a wider 90º angle with the source on the left side of the figure and the detector on the right (rather than with the source on top and the detector on the bottom), there would be no overlap of the circles in this projection. The two circles would be resolved better in the reconstructed volume because of less out-of-plane artifacts and more information about their dimensions along the z-direction. Similarly, if images of the breast were acquired at wider angles, depth resolution would be improved [86, 87].

Improvement in depth resolution can be seen in increased in-plane contrast-to-noise ratio (CNR) because of the decrease in the extent of the spread of the out-of-plane artifacts [88]. CNR is the contrast between the target (i.e. breast lesion) and background voxel values in an image divided by an estimate of the normalized noise in which the signal is embedded as shown in Equation (2-2) [88].

$$CNR = \frac{\frac{V_{lesion} - V_{background}}{V_{background}}}{\frac{\sigma}{V_{background}}} \tag{2-2}$$

In the equation above, V_{lesion} is the mean voxel value in the lesion, $V_{background}$ is the mean voxel value in a region of interest (ROI) drawn within the background outside of the lesion, and σ is the standard deviation of voxels within a background ROI. This provides an estimate of how well the target can be detected. When the z-direction is better sampled, a more accurate estimate of the size of features along the z-direction can be obtained, leading to less spread of the signal over multiple slices in the reconstructed volume [88]. A smaller angular range typically results in lower depth resolution and lower in-plane CNR because of more smearing of the structures throughout the reconstructed volume along the undersampled depth direction [62, 89, 90].

There are many acquisition variables that affect reconstructed image quality including number of projection images, angular range, and selected projection angles. There is no universally accepted set of imaging parameters [91], and the choice of angular range, projection angles, and number of views is system-specific [84]. The viewing angles used in DMT SNS acquisitions were recommended by the manufacturer of the x-ray detector and projection views are acquired at the following angles relative to the direction of breast compression: $\pm 12°, \pm 8°, \pm 5°, \pm 3°, \pm 2°, \pm 1°,$ and $0°$.

Studies have consistently shown that tomosynthesis images acquired over angular ranges of ~60º have superior in-plane CNRs and better depth resolution over those acquired over ~10º ranges [89, 88, 62]. Readers preferred reconstructed images of a 5 cm thick breast-like phantom obtained from tomosynthesis acquisitions over a 60º angular range over acquisitions performed using a 16º angular range in a reader study performed by Goodsitt et al [62]. Also, CNRs of the details within phantoms used in that study and also in a study performed by Zhang et al. were highest for the wider-angle acquisitions tested than for the lower angular range acquisitions [62, 88].

Despite an increase in the in-plane CNR and depth resolution, wider angles decrease in-plane resolution [88, 62, 92, 93]. Visualization of small features that are ~100 microns in size, such as microcalcifications, requires superior in-plane resolution. Hu and Zhao have found that conspicuity of small calcifications was improved by clustering views more tightly around the 0º view, with the angular separation of adjacent views increasing with the angle away from the z-axis. [94].

Though DMT DBT scans may benefit from angular ranges wider than the current 24º range used, the following hardware constraints limit the use of wider angles. In contrast to many clinical systems in which the breast is compressed directly on top of the x-ray detector, the x-ray detector used in DMT DBT rotates with the x-ray source. Because of this motion and the proximity of the detector to the breast support structure, the detector would hit the breast compression mechanism or the patient’s arm (in MLO image acquisition) for angles greater than ±20º with respect to the direction of compression. Therefore despite the potential improvements in image quality available with larger angular range, in the work described in this thesis we have chosen to limit the angular range to its current value of ±12º while exploring methods for reducing overall scan time.

2.2.4 Minimizing Gantry Motion Artifacts

In the DMT system, immediately after the gantry arm is repositioned during SNS acquisition, the abrupt deceleration of the tube, x-ray detector, and gamma ray detector results in damped oscillation of the arm around the desired position. One reason for this oscillation is the jerk of the system, which is the rate of change in acceleration. When the change in acceleration is large over a small amount of time, ringing can occur in mechanical systems [95]. Another source of oscillatory motion is the gearhead to which the gantry arm is attached. Backlash from the gearhead also creates jerky motion. If an exposure were made immediately after the arm was rotated, this damped oscillatory motion would create blur artifacts [81]. Therefore, a relatively long pause of 3 seconds is inserted after motion execution to wait for the ringing motion to damp out.

Ringing motion can be limited by reducing the rate of deceleration of the gantry just before the image is acquired. Lowering the jerk would decrease the amplitude of the tube and detector oscillations and thus reduce the length of the required pause before the image is captured. Additionally, if continuous motion acquisition were used, the total acquisition time could potentially be reduced further. However, the use of continuous gantry arm motion means that during acquisition of the projection images the tube and detector would be moving with respect to the breast. Such motion would cause blurring and potentially visible motion artifacts. The amount of blur associated with the motion of the tube and detector during an x-ray exposure can be quantified as follows.

When the gantry is stationary, a single point within the breast will project onto a single point on the detector over the x-ray exposure. Blurring occurs when the shadow of a single point from the breast projects onto more than one detector element. For a given angle $\Delta\theta$ traversed by the gantry during a single exposure, each point within the field of view (FOV) will experience varying amounts of blur depending upon its position with respect to the axis of rotation (AOR), x-ray detector, and x-ray source. Because the source produces a cone beam consisting of divergent x-rays, objects closer to the source and further from the detector have a larger magnification factor, which is the extent to which the size of the object is magnified in the image due to its position between the source and detector. The magnification factor is equal to the source to detector distance (SDD) divided by the source to object distance [96]. Points in the breast that have a larger magnification factor will project over more detector elements than points closer to the AOR. The maximum possible angular distance $\Delta\theta_{limit}$ that the gantry can be allowed to travel during an exposure can be calculated by putting a limit on the allowable blur. If blur is limited to the width of a single detector element, the resulting blur may not contribute appreciably to the overall system resolution in the direction corresponding to the motion. We therefore chose as an upper limit for acceptable motion blur the amount of source/detector rotation, $\Delta\theta_{limit}$, that would cause the image of the point in the breast furthest from the AOR to move one detector element width during the time that the beam was turned on.

For the calculation of $\Delta\theta_{limit}$, the detector's reference frame is used and the x-ray source is treated as a true point source. The advantage of the DMT system is that the x-ray source and detector always oppose each other as in 3rd generation CT systems. Unlike clinical DBT units, the breast is placed on a breast support 14 cm above the detector. Since the source and detector are not moving relative to each other, the breast appears to rotate in their reference frame, simplifying the calculation of $\Delta\theta_{limit}$.

Figure 2-4 is a schematic of the DMT DBT system for a 0° projection angle. The origin of this coordinate system is selected to be at the chest wall edge of the AOR. An image matrix coordinate system is also defined consisting of two axes u and v, which are parallel and perpendicular to the detector element columns and rows, respectively. The origin of the image plane is at the center of the chest wall edge of the detector. Here, u runs parallel to the x-axis and v runs parallel to the y-axis. Because all gantry motion is assumed to be about the y-axis, only blur along the u direction will be considered.

A point within the breast that starts off at some coordinate $[x_0, z_0]$ at the beginning of the exposure will project onto the detector at point $[u_0, v_0]$. The location on the detector that the point will project depends upon the source to imager distance (SID) h and the source-to-AOR distance (SAD) α:

$$u_0 = \frac{x_0 h}{\alpha - z_0} \tag{2-3}$$

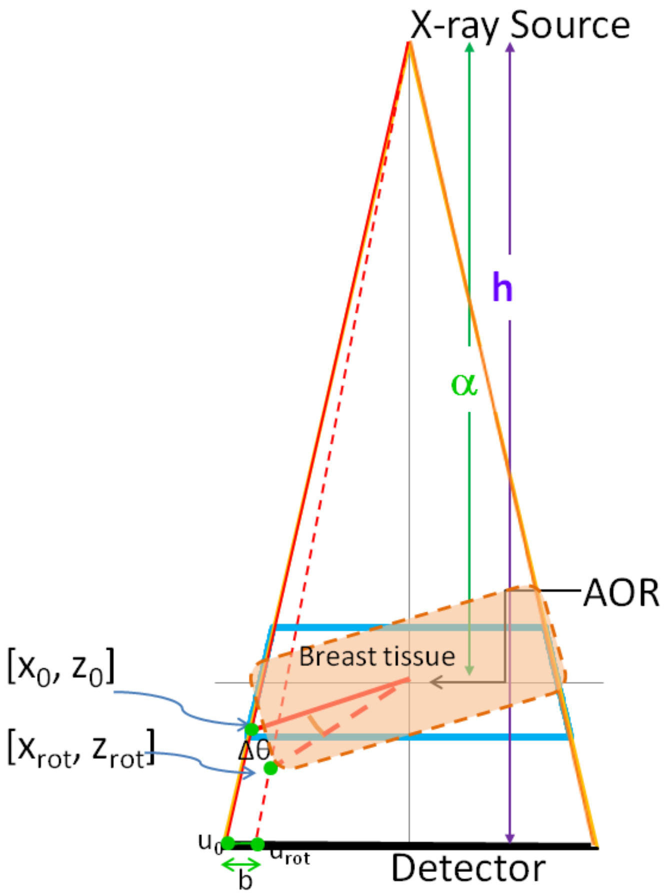

Figure 2-4: Diagram showing geometric parameters of DMT x-ray system where h and α are the source to detector distance (SDD) and source to AOR distance (SAD), respectively. A feature in the breast with initial coordinates of $[\mathbf{x_0}, \mathbf{z_0}]$ at the beginning of the exposure is shown within the x-ray field of view (FOV) illustrated by the triangular outline. The point is then rotated as the breast rotates within the source/detector reference frame during the exposure, finally resting at a new rotated set of coordinates $[\mathbf{x_{rot}}, \mathbf{z_{rot}}]$ at the end of the exposure. The rotated breast and projection are shown by dashed lines. The blur of the selected point is then quantified by the absolute difference between projected coordinates $\mathbf{u_0}$ and $\mathbf{u_{rot}}$.

After the gantry has traveled some angular distance $\Delta\theta$ by the end of the exposure, that same point will have new coordinates in the detector's reference frame $[x_{rot}, z_{rot}]$, found by using the rotation matrix:

$$\begin{bmatrix} x_{rot} \\ z_{rot} \end{bmatrix} = \begin{bmatrix} cos\Delta\theta & -sin\Delta\theta \\ sin\Delta\theta & cos\Delta\theta \end{bmatrix} \begin{bmatrix} x_0 \\ z_0 \end{bmatrix} \tag{2-4}$$

This rotated point will project onto the detector at a new set of coordinates $[u_{rot}, v_0]$, where u_{rot} can be found through plugging in x_{rot} and z_{rot} in for x_0 and z_0, respectively, in Equation (2-3). Blur b is the extent over which the chosen point is mapped onto the detector between the projected coordinates u_0 and u_{rot}:

$$b = |u_o - u_{rot}| \tag{2-5}$$

If Equations in for u_o and u_{rot} are plugged into Equation (2-5), the following expression is obtained for b:

$$b = h\left|\frac{x_0}{\alpha - z_0} - \frac{x_{rot}}{\alpha - z_{rot}}\right| \tag{2-6}$$

The variable we are trying to solve for is $\Delta\theta$, which is contained within the rotated coordinates x_{rot} and z_{rot}. Equation (2-6) can be rewritten as follows:

$$\frac{x_{rot}}{\alpha - z_{rot}} = \pm\frac{b}{h} + \frac{x_0}{\alpha - z_0} \tag{2-7}$$

Since everything on the right side of the equation is constant for a given known point within the x-ray FOV, they are all combined into a single constant K, which can then be plugged into Equation (2-8) to obtain Equation (2-9).

$$K = \pm\left[\frac{b}{h} - \frac{x_0}{\alpha - z_0}\right] \tag{2-8}$$

$$x_{rot} = K(\alpha - z_{rot}) \tag{2-9}$$

Then, using Equations (2-4), (2-8), and (2-9), the following expression in terms of $\Delta\theta$, x_0, and z_0 is obtained:

$$x_0 cos(\Delta\theta) - z_0 sin(\Delta\theta) = K(\alpha - (x_0 sin(\Delta\theta) + z_0 cos(\Delta\theta))) \tag{2-10}$$

Further substitutions can be made by using the trigonometric identities:

$$q = \sin(\Delta\theta) \tag{2-11}$$

$$\sqrt{1 - q^2} = cos(\Delta\theta) \tag{2-12}$$

Equation (2-13) is the result of plugging these terms back into Equation (2-10).

$$x_0\sqrt{1-q^2} - z_0 q = K(\alpha - (x_0 q + z_0\sqrt{1-q^2})) \tag{2-13}$$

Two new constants are defined with the following equations:

$$m = z_0 - x_0 K \tag{2-14}$$

$$n = x_0 + z_0 K \tag{2-15}$$

After combining terms further and incorporating Equations (2-14) and (2-15), a simplified quadratic expression is obtained in Equation (2-16).

$$q^2(m^2 + n^2) + q(2Km\alpha) + (K^2\alpha^2 - n^2) = 0 \tag{2-16}$$

The quadratic formula can be used to solve for q and set equal to sin $(\Delta\theta)$ from Equation (2-10). Then, taking the inverse sine of both sides of the resulting equation, the expression for $\Delta\theta$ is Equation (2-17).

$$\Delta\theta = sin^{-1}\left[\frac{-Km\alpha \pm \sqrt{(Km\alpha)^2 - (m^2+n^2)(K^2\alpha^2 - n^2)}}{(m^2+n^2)}\right] \tag{2-17}$$

Because K depends upon the initial coordinates $[x_0, z_0]$, it can be seen from the above equation that the angular rotation $\Delta\theta$ necessary to obtain a given value of b, will vary from point to point within the volume of the x-ray FOV. As $\Delta\theta$ is increased from 0º, the point in the FOV whose value of b becomes equal to the length of a detector element first is defined as the limiting point. The corresponding angular gantry rotation is defined as $\Delta\theta_{limit}$, and is the maximum angular distance the gantry will be allowed to move if no blur is to be seen anywhere in the image.

From equation (2-17), there are four possible solutions that result from solving for $\Delta\theta$ for each point, two for a positive value of b and two for -b, or blur in the opposite direction. Solutions can be eliminated by choosing the minimum out of all solutions for a given point and selecting only those solutions that correspond to the point's presence within the FOV at the beginning and end of the exposure (i.e. u_o and u_{rot} are both within the detector's image plane).

The number of points for which $\Delta\theta$ needs to be calculated can be reduced by considering just the portion of the FOV where there would be breast tissue. In addition, points furthest from the AOR will be translated more than those that are closer for a given angular rotation. Additional factors are the fraction of the translation vector that is projected onto the detector surface, and the degree of magnification of the translation onto the detector. The fractional projection of the translation vector is greatest for points starting near the detector midline (i.e. the translation vector is parallel to the detector surface) and the degree of magnification is greatest for points at the top (tube side) surface of the breast. Therefore, the limiting point will be somewhere along the blue outline shown in Figure 2-4 for a 0° projection view. The blue outline is comprised of four lines. Two of these lines are parallel to the x-axis. The bottom line corresponds to the breast support and has the following equation:

$$z = -l_b \tag{2-18}$$

where l_b is the separation between the breast support and the AOR. The top line corresponds to the height of the compression paddle for the largest compressed thickness T_{max} that can be accommodated by the DMT system and has equation:

$$z = l_t = T_{max} - l_b \tag{2-19}$$

The other two blue lines are the limits of the x-ray FOV which extend from the point source to the edges of the detector between the breast support and compression paddle.

Using the coordinates of the x-ray source and detector corners and the width of the detector w_{det}, the equations for these sloped lines are as follows:

$$z = \begin{cases} \frac{h}{\left(\frac{w_{\det}}{2}\right)} x + \alpha, & x < 0 \\ \frac{-h}{\left(\frac{w_{\det}}{2}\right)} x + \alpha, & x > 0 \end{cases} \tag{2-20}$$

where w$_{det}$ is the detector width. In terms of the polar coordinate φ, where $\varphi = 0$ is defined to begin along the positive x-axis and increase in the counterclockwise direction, the coordinate of a point $[x_0(\varphi), z_0(\varphi)]$ lying on the blue outline can be calculated by the following equations:

$$x = \begin{cases} \frac{\alpha}{(tan\varphi)-(\frac{-2h}{w_{\det}}))}, & -\eta < \varphi < \psi \\ \frac{l_t}{tan\varphi}, & \psi \leq \varphi \leq \pi - \psi \\ \frac{\alpha}{(tan\varphi)-(\frac{2h}{w_{\det}}))}, & \pi - \psi < \varphi < \pi + \eta \\ \frac{-l_b}{tan\varphi}, & \pi + \eta \leq \varphi \leq 2\pi - \eta \end{cases} \tag{2-21}$$

$$z = \begin{cases} \frac{-2h}{(w_{det})} x + \alpha, & -\eta < \varphi < \psi \\ l_t, & \psi \leq \varphi \leq \pi - \psi \\ \frac{2h}{(w_{det})} x + \alpha, & \pi - \psi < \varphi < \pi + \eta \\ -l_b, & \pi + \eta \leq \varphi \leq 2\pi - \eta \end{cases} \tag{2-22}$$

where $\psi = tan^{-1}(\frac{2hl_t}{-w_{det}(l_t-\alpha)})$ and (2-23)

$$\eta = tan^{-1}(\frac{-2hl_b}{w_{det}(-l_b-\alpha)}) \tag{2-24}$$

Angles ψ and η are determined from the locations of the edges of the FOV at the top and bottom surfaces of the breast, which are approximately at the same locations as the edges of the compression paddle and breast support for the largest possible compressed thickness that can be accommodated by the DMT compression system. Figure 2-5 shows angles ψ and η for the blue outline shown in Figure 2-5. The minimum in a plot of $\Delta\theta$ versus φ would identify the point on the border whose blur would reach the target value of b first as the gantry is rotated. For this $\Delta\theta_{limit}$ value, the resulting blur for all other points within the FOV is less than or equal to b.

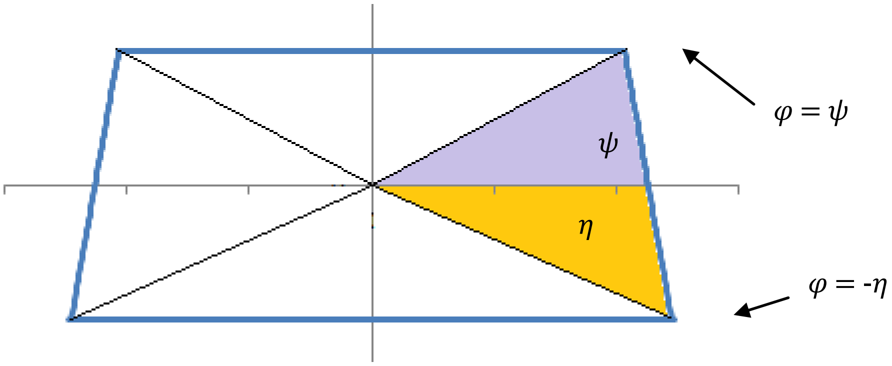

Figure 2-5: Schematic of angles ψ and η used to define the coordinates $x(\varphi)$ and $z(\varphi)$ of the region boundaries. The purple region shows the angle ψ between $\varphi = 0$ to $\varphi = \psi$, and the orange region shows the angle η between $\varphi = 0$ to $\varphi = -\eta$.

Parameter values for $h, \alpha, l_t, l_b,$ and w_{det} for the DMT system are given in Table 2-1. The detector element size of the x-ray detector used in DMT DBT is 75 microns.

Table 2-1: DMT Geometric Parameters

Constant	[mm]
h	826
α	643
l_t	55
l_b	55
b	0.075
w_{det}	290

Figure 2-6 shows a plot of $\Delta\theta$ versus φ when the constants from Table 2-1 are plugged into the above equations for the 0º projection angle. Arrows point to the minima in the plot in Figure 2-6 where $\Delta\theta_{limit} = 0.0475°$, which occur at φ values of 204º and 336º, corresponding to the edges of the FOV at the breast support surface. Therefore, to prevent blurring of features at these locations in the projection image, the DMT gantry must not travel by an angular distance larger than this value over any given exposure. This value for $\Delta\theta_{limit}$ is just slightly lower than that for those points that correspond to the compression paddle edges, at $\varphi =$ 28º and 152º degrees, which have the largest magnification, but are closer to the AOR than the edges of the support. The peaks in the plot of Figure 2-6 are $\Delta\theta$ for φ = 170º and 10º, which are for points that graze the FOV. Figure 2-7 shows the trajectory of the point [x_0(10º), z_0(10º)] that it appears to move in the source and detector's reference frame. The point starts off at the location where the green triangle is shown. In the source and detector's reference frame, the point can move along the blue line in the plot and still project onto the same detector element until the gantry moves a distance larger than 1.8º. As shown in Figure 2-7 the reason that this large angular displacement can still result in displacement of the point's image by less than a detector element width is that the point's direction of motion is nearly parallel to the direction of the incident x-rays at the right edge of the trapezoidal boundary of Figure 2-5.

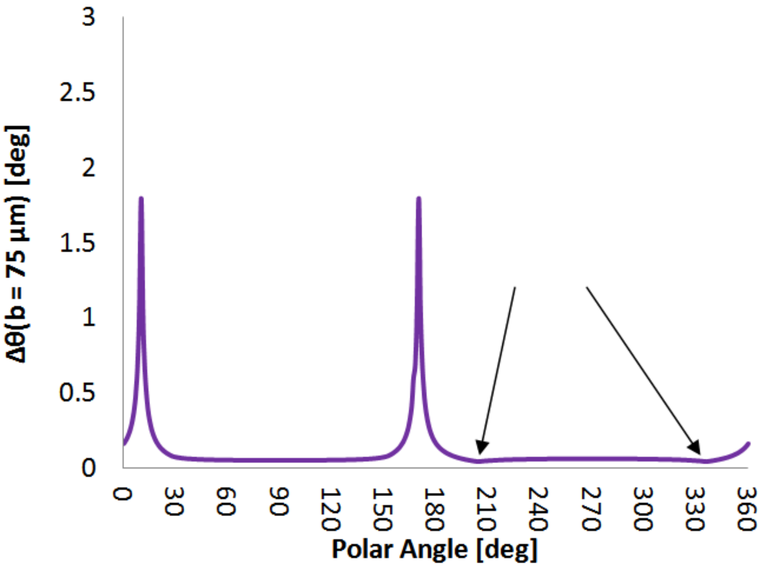

Figure 2-6: Plot of Δθ calculated from Equations (2-17), and (2-21) through (2-24) versus polar angle φ. Arrows point to the minima in the plot, which correspond to the edges of the breast support.

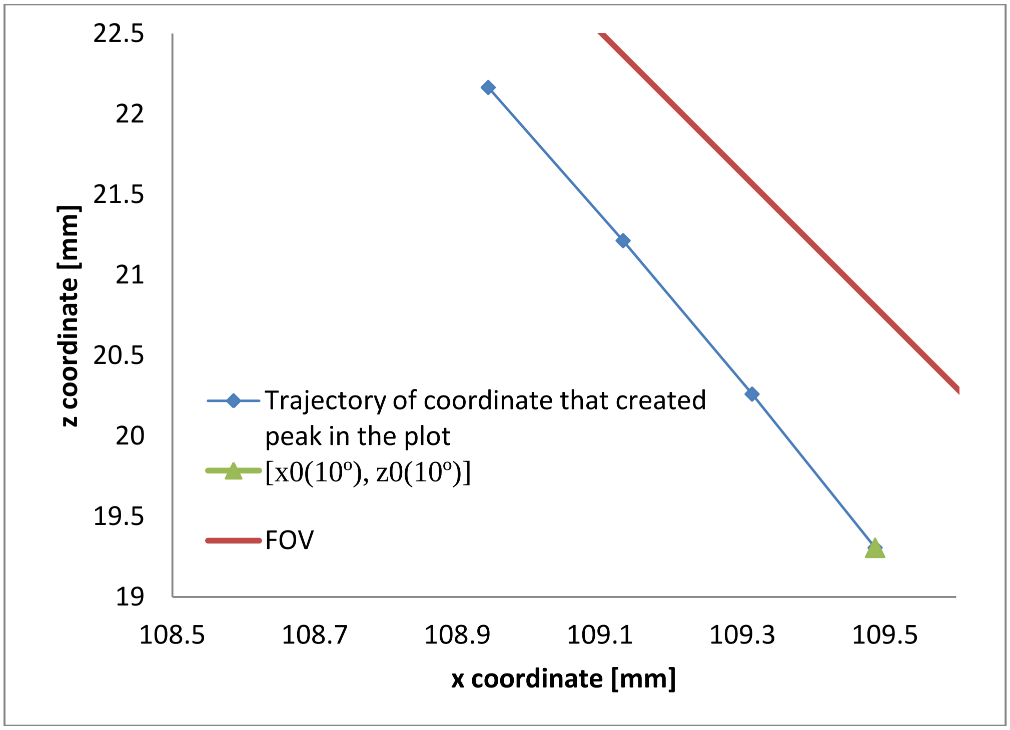

Figure 2-7: Plot of the trajectory of the coordinate [x_0 (10), z_0(10)] in the source and detector's reference frame that created the first peak in the plot of Figure 2-6. The trajectory shows the point grazing the FOV over its trajectory. Since the point travels nearly parallel to the direction of the incident x-rays the gantry would have to travel for a large $\Delta\theta$ (~1.8°) for its image to project over one detector element, as shown by the spike at φ = 10° in Figure 2-6.

The example shown above was for the 0º projection view. Limiting $\Delta\theta$ values for other projection views can be calculated by applying the rotation matrix on the initial coordinates $[x_0, z_0]$ of the outline for the 0º projection view to obtain new initial coordinates $[x_0, z_0]$ for a different acquisition angle where the angle used in the rotation matrix is equal to the desired projection angle. The same analysis was performed for a projection angle of -12º, which is widest angle currently used for DMT DBT. Negative angular rotation is in the clockwise direction as viewed along the positive y-axis in DMT. Figure 2-8 shows the outline of the compression system in the detector's reference frame when the gantry is at an angle of -12º.

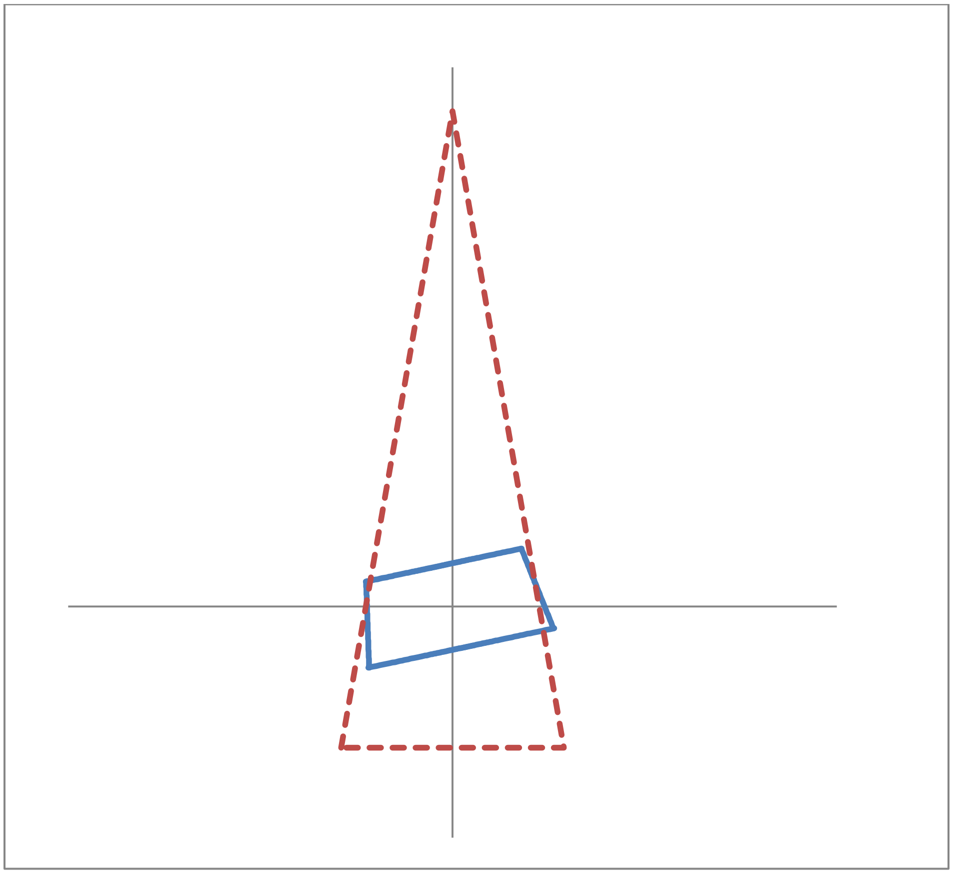

Figure 2-8: The solid line is the outline of the compression system in the detector's reference frame at a DMT gantry angle of -12º with respect to the direction of compression. The dashed line shows the outline of the FOV.

Similar to the plot shown in Figure 2-6, Figure 2-9 is a plot of $\Delta\theta$ versus φ for the -12° projection angle. The minimum in the plot in Figure 2-9 where $\Delta\theta_{limit,12°} = 0.0391°$ occurs at φ = 216°, which corresponds to the corner of the breast support that is closest to the detector, while the other breast support corner starts off outside of the FOV. The second minimum in the plot corresponds to the corner of the compression paddle at φ = 40° and has a value of $\Delta\theta = 0.0483°$. The peaks in the plot are located at φ = 16° and 178° and correspond to points that graze the sides of the FOV and thus have trajectories nearly parallel to the direction of x-ray incidence. Since peak values depend upon the point's radial distance away from the AOR, the peaks in this plot are lower than the peak values in Figure 2-6. Discontinuities in the plot correspond to points whose projections fall outside of the FOV (i.e. u_o and u_{rot} are both outside the detector's image plane) and so were excluded from the analysis.

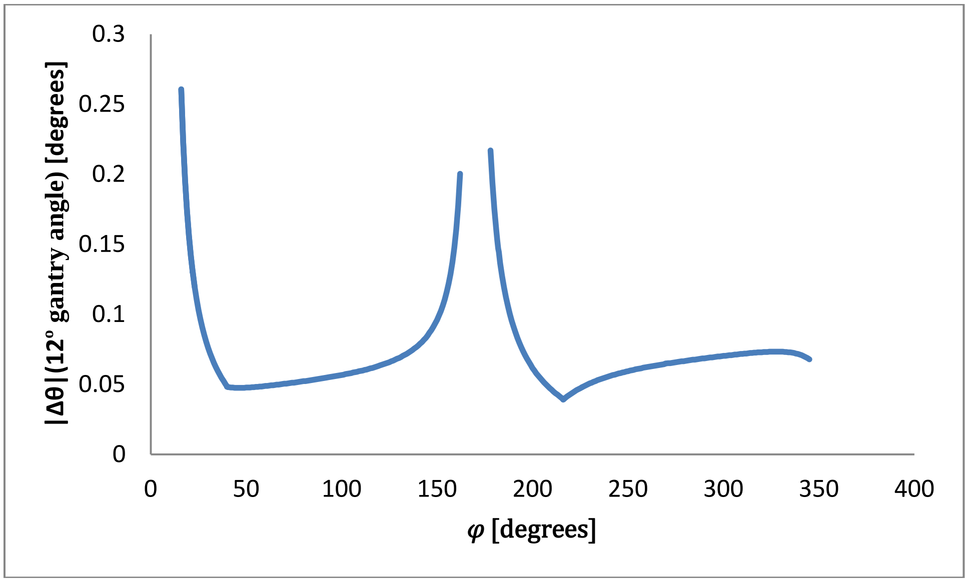

Figure 2-9: Plot of Δθ calculated from Equations (2-17), and (2-21) through (2-24) versus polar angle φ for a -12° projection view. The minimum in the plot is located at φ = 216°, which corresponds to the left edge of the breast support or the bottom left corner of the solid blue outline seen in Figure 2-8.

For this projection $\Delta\theta_{limit,12°}$ is lower than $\Delta\theta_{limit,0°}$ (limit for the 0° projection angle), suggesting that there would be more blurring seen at the edges of the breast support in this -12° image if the gantry goes at the speed limit found for the 0° projection angle. However, the second minimum in the plot of Figure 2-9 at φ = 40° suggests that most other points within the breast would not be blurred by the limit set by $\Delta\theta_{limit,0°} = 0.0475°$ as this is smaller than $\Delta\theta = 0.0483°$. Additionally, instead of initiating motion before the -12° projection angle, the gantry can acquire this image just before gantry motion is started to reduce blurring that could potentially be seen at this angle. Likewise, the last DMT DBT exposure at +12° can be acquired after the gantry has come to a complete stop.

2.2.5 Calculating Gantry Imaging Speed

With a limit on the maximum angular distance $\Delta\theta_{limit}$ that the gantry can move during an exposure, a motion profile can be developed for the gantry. Traversed angular distance over exposure time t_{exp} is equal to the integral of the gantry's angular velocity $\omega(t)$ over time:

$$\Delta\theta = \int_0^{t_{exp}} \omega(t)dt \qquad (2\text{-}25)$$

The angular speed $\omega(t)$ can be a non-constant value. However, if there is any constant, non-zero value of angular acceleration during imaging, $\Delta\theta$ will have a t^2-dependence with time, requiring very low values for acceleration if the acceleration were not followed by a compensating deceleration during the exposure. If $\omega(t)$ kept constant during the exposure the maximum allowable gantry speed during the exposure is given simply by

$$\omega_{limit} = \frac{\Delta\theta_{limit}}{t_{exp}} \tag{2-26}$$

If the gantry travels at this constant speed over the entire tomosynthesis scan, the total acquisition time T_{Scan} can be approximated by the following equation:

$$T_{Scan} = \frac{\Theta}{\omega_{limit}} = \frac{\Theta t_{exp}}{\Delta\theta_{limit}} \tag{2-27}$$

In the above equation Θ is the full angular range of 24° covered during the DMT DBT scan. As the exposure time increases, the total scan time also increases proportionally. Based on Equation (2-27), exposures must be kept short to minimize the total scan time. For example, if the exposure time is set to 320 ms, which is the typical value used in DMT SNS scans, an entire DBT scan would take 160 seconds for b = 75 microns, $\Delta\theta_{limit}$= 0.0475°, and ω_{limit} = 0.15°/s. This duration is longer than the original SNS scan. In order to reduce scan time, the exposure time would need to be minimized. However, there are consequences to shortening the exposure time.

For a given breast composition and compressed thickness, a certain radiation dose is necessary for maintaining acceptable image quality. A larger number of detected x-rays leads to a less noisy image, improving signal to noise ratio (SNR) [97]. Radiation dose to the breast is determined by the output of the x-ray tube. The fluence of photons at the detector surface is determined by the rate at which x-ray photons are emitted from the x-ray source and the exposure time, and is directly proportional to the mAs, which is the product of the exposure time in seconds and the tube current in mA [13]. If the exposure time is reduced, the tube current must be increased to maintain the same fluence level [81]. However all x-ray tubes have an upper limit on the achievable current (180 mA for the DMT system x-ray tube) because of the finite rate at which heat can be dissipated from the target, at which point exposure times must be increased to achieve higher fluence. This can be especially important for thicker breasts that attenuate more of the incident radiation than thinner breasts.

On average, in DMT clinical trials, for a breast with a compressed thickness of 8 cm the current-time product per projection view is approximately 40 mAs in order to achieve a target mean glandular dose approximately equal to the dose resulting from the subject's clinical mammogram. For a maximum tube current of 180 mA, the minimum allowable exposure time to obtain 40 mAs/view is 222 ms. The generator is capable of only specific values of exposure time around 222 ms, which are 160 ms, 200 ms, and 250 ms. For a 200 ms exposure time, if the gantry were kept at a constant speed of 0.0475 º /0.2 s = 0.2375º/s over the entire 24º angular range, the total scan time would be over 100 seconds. To avoid slower gantry speeds and limit blurring from patient motion, the shorter 160 ms exposure time was selected. The required imaging speed for this exposure time is 0.3º/s.

This scan time can be shortened further by increasing the speed of the gantry. Even though blurring artifacts may result in projection images, there is a possibility that these artifacts may not manifest noticeably in the reconstructed volume if the motion blur is small compared to the combined other mechanisms contributing to the spatial resolution in the reconstructed image. These other mechanisms include blurring created by the finite size of the focal spot [96], the blurring by the detector caused by all of the processes that convert the input signal to an output image, patient motion, and image binning [98]. Projections form the input to a reconstruction algorithm that generates a three-dimensional (3D) volumetric image of the breast. To limit the image matrix size and thus the computational burden in calculating the final reconstructed volume, projection images are typically binned. Projection binning is the process by which pixel values of adjacent pixels are combined together to create a single, larger pixel, thereby reducing the matrix size compared to the original image. For DMT DBT, the reconstruction algorithm is set to use 2x2 binning of the projection images. Since this binning effectively doubles the length of a single pixel from 75 microns to 150 microns, the constraint on the extent of image blur can be relaxed slightly to equal twice the detector element size, in turn, allowing for two times the gantry angular speed (0.6°/s rather than 0.3°/s) compared to the unbinned case. With double the speed, the scan time would then be approximately 40 seconds in length with uniform motion over 24°, which is less than half of the SNS scan time. On these shorter time scales, DMT hardware must be able to accommodate the higher rate of image acquisition.

2.3 Feasibility of Scan Time Reduction (STR)

DMT exposures taken by the SNS method are separated in time by several seconds. One method of STR is to decrease the inter-exposure gap time. Besides the limitations on gantry speed discussed in the previous section, the time scale of the final DBT scan is also dependent upon the readout time of the x-ray detector, the timing capability of the x-ray generator, which supplies the current and voltage to the x-ray tube, and the response time of the servo motor that rotates the gantry arm. All of these components must be synchronized to minimize unnecessary time delays during the scan. A program written in C# by the manufacturer of the x-ray detector controls all of these hardware components in the DMT scanner. This program was modified in Microsoft Visual Studio for testing all equipment and implementing STR.

2.3.1 X-ray Generator and Tube

A Sedecal generator controls the output of a Rad-70 Varian tube in the DMT system. Only specific values for the exposure time are accepted by the generator, of which the minimum is 1 ms and the maximum is 12500 ms, as specified by the manual of the communications protocol for the Sedecal generator. The maximum achievable tube current is 180 mA, and the maximum x-ray tube voltage is 49 kV. Parameters for setting tube voltage, tube current, and exposure time are specified in a command sent to the generator from the computer program. If all parameters are recognized, the generator sends an acknowledgement response back to the computer, which can take up to 80 ms. After this initial command, a separate command must be sent to the generator to trigger the exposure. Response times and true exposure times must be well characterized to synchronize the generator with the detector integration window. If the generator is triggered in such a way that x-rays are produced either before or after the detector's integration time window, there will be a loss of radiation detected, leading to an unnecessary dose to the patient.

In order to gauge how quickly the generator can respond to a trigger command sent by the acquisition program, a MagicMax radiation meter [99], which measures the fluence of x-rays incident on the meter as a function of time, was used to monitor the output of the x-ray tube. Dose rate data is given in units of Gy/s where 1 Gy is equal to 1 Joule of energy deposited in 1 kilogram of mass. Repeatability of tube output was measured by performing three exposures with a 160 ms exposure time at 29 kV tube voltage and a tube current of 75 mA.

Measuring the rise and fall times of the observed x-ray pulses is essential in understanding how quickly and consistently the generator can provide a uniform (constant flux) x-ray beam. Rise time was calculated by subtracting the time when the dose rate at the MagicMax detector reached approximately 10% of the target constant value from the time when it reached 90% of the target value. Fall time was calculated by subtracting the time when the dose rate reached 90% of the target value from the time when it reached 10% of the target value. The difference between the two time points is a measure of how long the tube can truly maintain uniform output.

Two sets of data were acquired. The first was acquired to determine how much variability there is in the response time of the generator to a trigger command. The second data set was obtained to measure uniformity (in time) of the tube output. All exposures were performed with a breast support and compression paddle in the x-ray beam, and the radiation detector was placed directly on top of the x-ray detector.

Figure 2-10 shows the pulse shape of these three trials. The average rise time, average fall time, and average pulse width are given in Table 2-2 along with the standard deviations of three trials. The percent error in the pulse width from the programmed exposure time of 160 ms was found to be 0.16% with a standard deviation of $1.7\text{x}10^{-4}$ seconds. Fluctuations in dose rate during the constant output region were found to be within 1.5% of the mean dose rate as determined by the standard deviation of the dose rate over the constant portion of the exposure.

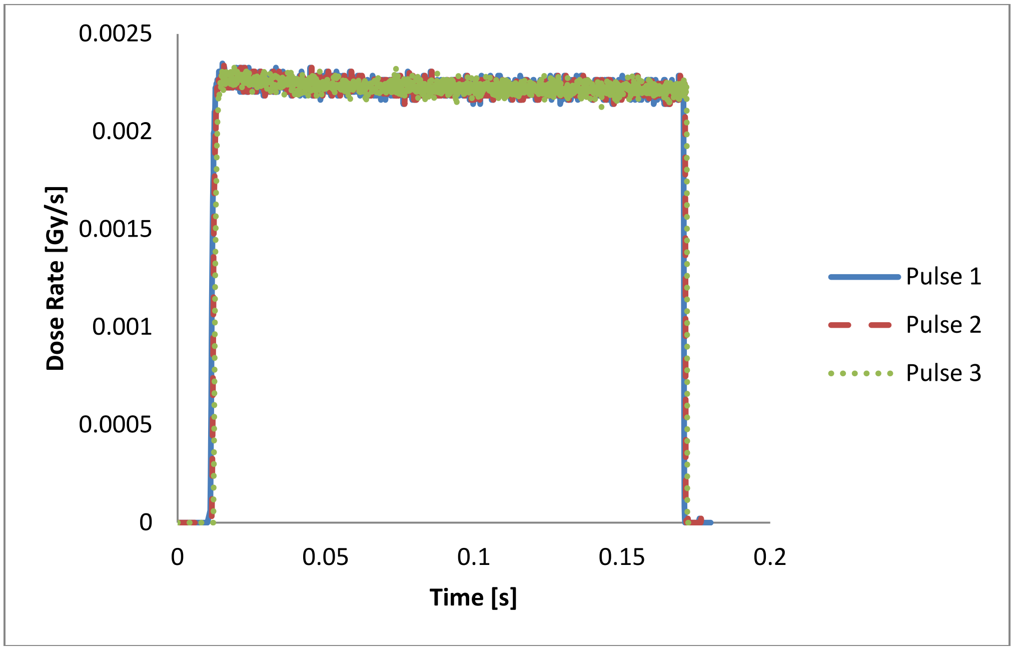

Figure 2-10: Pulse shapes of three 160 ms exposures to confirm repeatability of generator output

Table 2-2: X-ray pulse characterization

	Average [sec]	**Standard Deviation [sec]**
Measured Pulse Width	0.1584	1.73E-04
Rise Time	9.67E-04	5.77E-05
Fall Time	2.00E-04	1.00E-04

Consistency of the response time of the generator was measured by performing five consecutive exposures with fixed gap times between exposures. In addition, to see if there is any dependence of the generator response time upon the programmed gap time between triggers, multiple gap times ranging from 40 ms to 400 ms were programmed and tested. Figure 2-11 is a plot of the data measured by the radiation meter for a programmed gap time of 100 ms. True gap times were calculated by taking the difference between the times at which the dose rate dropped to 0 Gy/s at the end of each pulse and the point just before the dose rate rose from 0 Gy/s at the beginning of the following pulse.

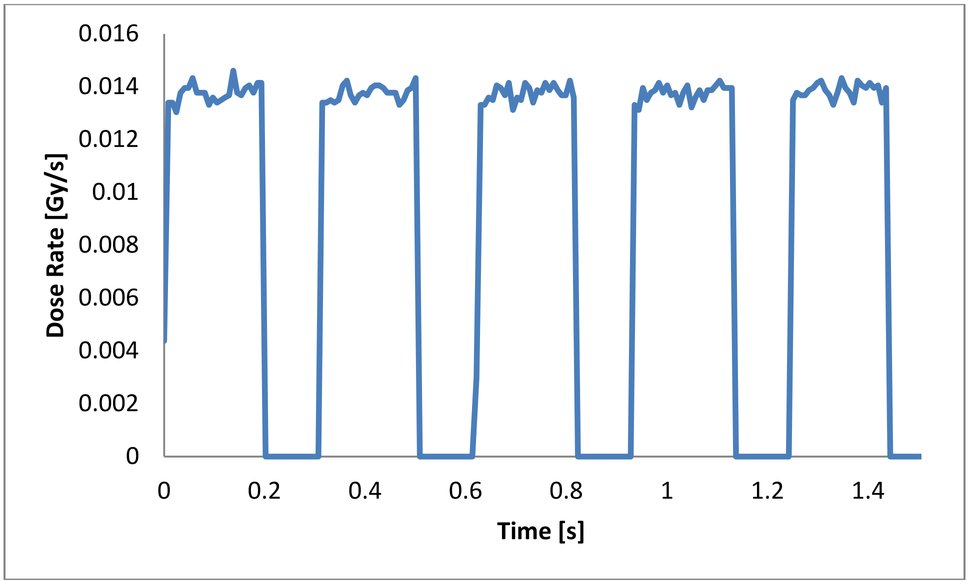

Figure 2-11: Pulse shape data provided by the MagicMax radiation meter showing dose rate over time.

Figure 2-12 is a plot of the average gap times versus the nominal programmed values between triggers. Error bars in the plot are the standard deviation of the four gaps between the five consecutive pulses that were executed for testing each value of gap time. A linear fit was applied to the plot of actual gap time τ_{actual} versus the programmed gap time $\tau_{programmed}$ with an equation of the form as follows:

$$\tau_{actual} = m\tau_{programmed} + b \tag{2-28}$$

Constants from the linear fit were m = 0.9922 and b = 6.3233 ms. This fit shows that there is some delay ~6 milliseconds from the generator before the x-rays are emitted from the x-ray tube, which does not appear to depend upon programmed gap time. However, the response time is small in comparison to the gap between images $\gtrsim$1 second, which is set by the time required for the gantry to travel between projections.

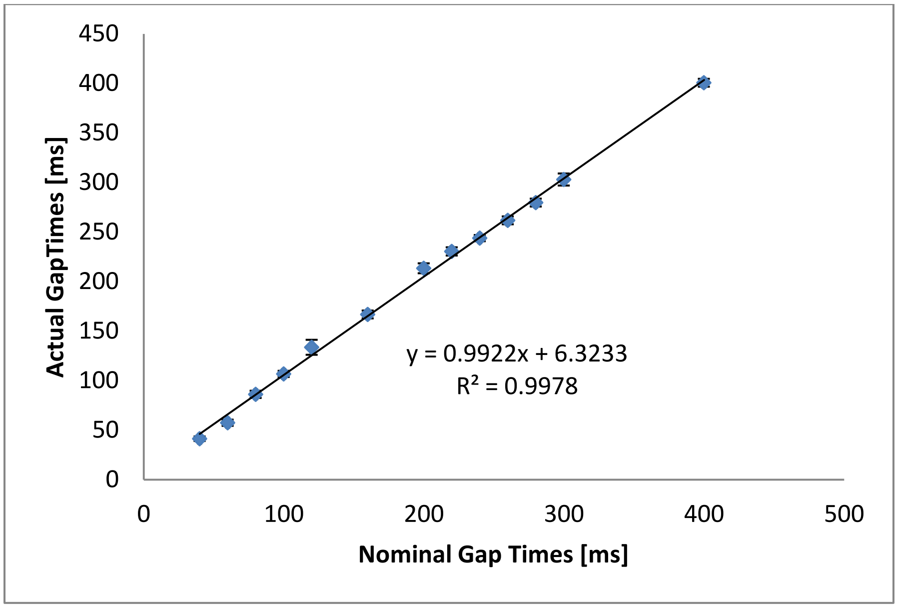

Figure 2-12: Plot of true gap times between consecutive exposures as measured by a radiation meter versus the nominal values programmed into the software that triggers the generator for initiating the exposure. Error bars in the plot are the standard deviation of four gaps between five exposures.

Generator output is consistent and uniform as demonstrated by the repeatability of the 160 ms x-ray pulses. Moreover, with sharp rise and fall times and short response times, the DMT generator and tube are capable of rapidly making exposures on the time scales required for STR. Short response times will make synchronization with the detector possible. However, the limit of 180 mA of the tube will limit the attainable fluence per projection view for a given exposure time.

2.3.2 X-ray Detector Exposure Modes

The 2923MAM used in DMT is a complementary metal-oxide-semiconductor (CMOS) flat panel x-ray detector manufactured by Dexela/Perkin-Elmer (London). It is an indirect detector that consists of a thallium-doped CsI scintillator that converts incident x-ray energy into visible light with a peak wavelength of 550 nm [100]. These lower energy photons are then converted into a current using photodiodes, the output from which is integrated by active pixel sensors (APS) [16]. Because of the use of CMOS APS, a second image can be quickly acquired after the charge acquired by each pixel from the first exposure is shifted and stored for readout later, allowing for high frame rates [101]. At full resolution (no data binning), the 2923MAM is cable of capturing 17 frames per second (fps). With a pixel size of 75 microns and an active area of 29 cm x 23 cm, the full resolution image has dimensions of 3888 x 3072 pixels^2.

The 2923MAM has four exposure modes for acquiring images. The first mode is called the expose-and-read (E&R) mode in which a single image is acquired when the detector is triggered, stored in a buffer, and then read out later. In the sequence exposure mode, the detector takes a programmed number of images successively with no inter-image gaps, and all with the same programmed exposure time. In the third acquisition mode, referred to as frame rate mode, a programmed number of exposures are acquired with a fixed exposure time and a user-defined, fixed gap time. The last mode is called the pre-programmed exposure mode in which several exposures can be programmed with varying exposure times and taken consecutively, again with a fixed gap time between images.

In the current acquisition scheme the projection views of DMT DBT scans are not equiangularly spaced within the 24° angular range traversed by the gantry. If the gantry travels at a constant speed over this range, the images would not be acquired at a constant rate. Since gap times between consecutive images would be equal to the time required for the gantry to traverse the distance between the two projection angles, gap times between images separated by larger angles would have longer gap times than images separated by smaller values. Because sequence mode, pre-programmed exposure mode, and frame rate mode all have a fixed gap time between exposures, these modes would not be ideal for

DMT DBT acquisitions that use the current non-uniform sampling approach. Also, even if views were uniformly spaced it could be more difficult to synchronize the detector integration with the generator and gantry arm motion. Therefore, the exposure mode that would be the most straightforward to implement with a non-uniform angular distribution of projection views is E&R mode.

When capturing images using E&R mode in SNS acquisitions, an additional 150 ms is added to the detector integration window. Once the image is acquired, the acquisition program waits for some time for the image to be transferred from a buffer to the computer before the gantry is moved for the next exposure. For STR, these additional steps would be required, but they would not add to the total scan time if these steps can be accomplished during motion between exposures. Therefore, the gantry motion must also be synchronized with both the detector and x-ray source.

2.3.3 Gantry Motor

The gantry motor used in the DMT scanner is a servo controlled rotary motor manufactured by Parker Hannifin Corporation. This servo motor is capable of performing trapezoidal motion profiles in which the load is accelerated at a constant rate A over a time interval t_1 to some constant angular speed ω_c between times t_1 and t_2 and then decelerated at a constant rate A_D between times t_2 and t_3. A programmed distance D would be traversed as a result of the motion. Values of A, ω_c, D, and A_D are all user-defined and adjustable. Figure 2-13 shows an example of this trapezoidal motion profile.

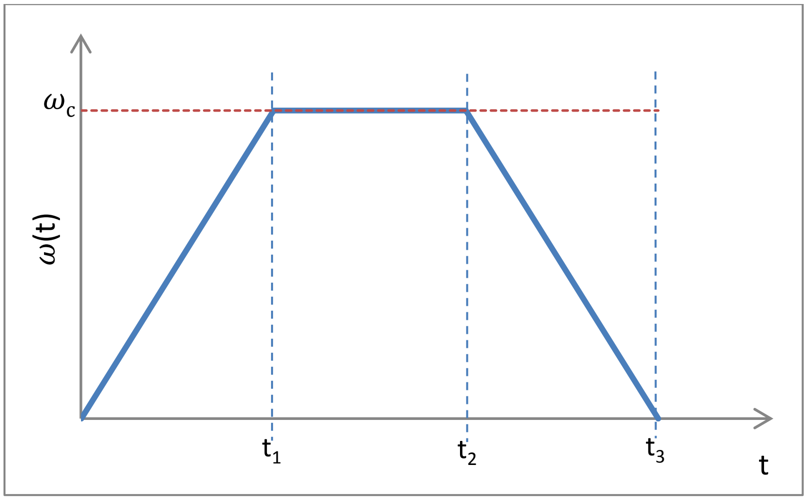

Figure 2-13: Example of a programmable motion profile of the DMT gantry. Angular speed is a piecewise linear function of time t.

To program motion, all values that are in units of degrees or radians must be converted to units of encoder counts. A Gemini servo motion controller is attached to a Parker motor that connects to a gear head with a 40:1 gear ratio G_R. The gear head is then connected by another gear attached to the gantry arm with a gear ratio G_A of 4:1. The servo encoder has a resolution DRES of 8000 pulses per motor revolution. The conversion from encoder pulses to gantry arm angular motion in degrees is given in Equation (2-29).

$$D = \theta_D \cdot DRES \cdot \frac{G_R \cdot G_A}{360} \tag{2-29}$$

The programmed distance D is then in units of encoder pulses, and the speed and acceleration are in units of motor revolutions/s and rev/s^2, respectively. Settings of A and A_D for DMT SNS acquisition are both 30°/s^2, and angular speed ω_c = 56°/s. Though it seems counterintuitive, the scan time can be reduced by lowering these parameters. Because lowering the deceleration would reduce jerky motion of the gantry arm when it comes to a stop just before imaging, a shorter pause just before the image is acquired is possible without adding perceptible blur to the image.

To gauge how accurately the gantry motor can execute slower commanded speeds, the encoder position of the motor was recorded while the gantry was moved over a 3º angle at the constant speed of 0.6º/s calculated in Section 2.2.5. Figure 2-14 is a plot of the gantry angular position over time as indicated by the servo motor encoder.

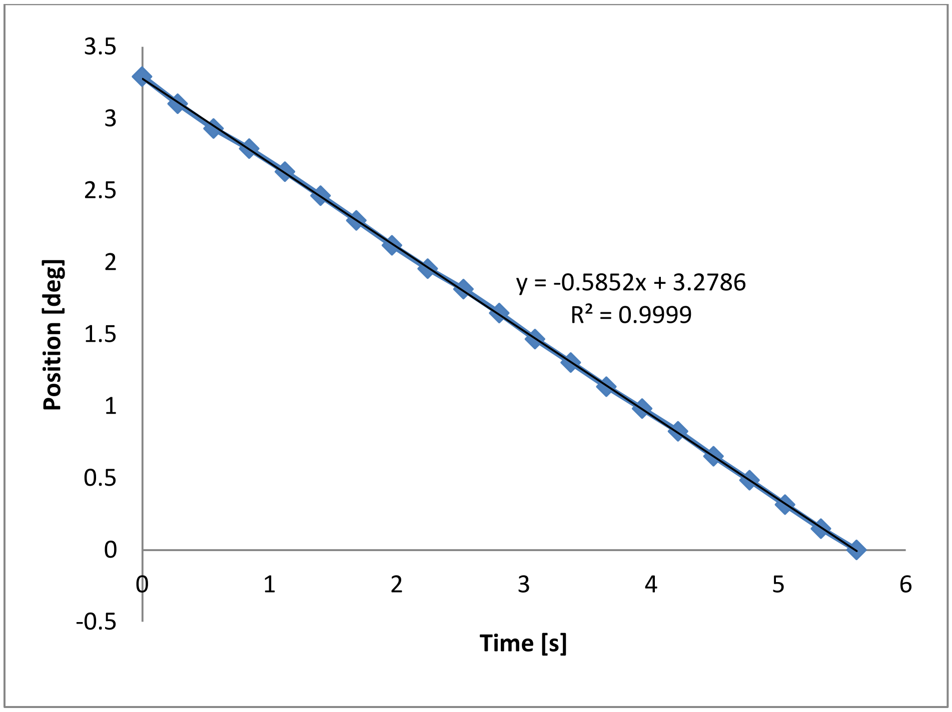

Figure 2-14: Plot of angular position of gantry arm over time for programmed constant angular speed of 0.6º/s. The negative value of the slope is due to the clockwise direction of motion as viewed from the patient's perspective.

A linear fit was applied to the plot to obtain the average angular velocity of the gantry arm with the following equation:

$$\theta = \omega_c t + \theta_0 \tag{2-30}$$

The R-squared value and nearly imperceptible fluctuations in the plot of Figure 2-14 show that the gantry is capable of this slower speed without large perturbations of the arm. The slope of the linear fit of ω_c = -0.5852°/s shows an error in actual speed of 2.5% from the programmed 0.6°/s. However, as long as the gantry does not greatly exceed the programmed speed, blur should theoretically be confined to 150 microns, or two pixels.

2.3.4 Accuracy of Measured Acquisition Angle

Integrity of the high spatial resolution of DBT demands a precise knowledge of the geometric parameters of the system [102]. One important set of geometric values are the values of the angles at which images are acquired for input to the reconstruction algorithm. Studies have shown that varying errors in projection angles can reduce lesion contrast by 20% [102]. For DMT SNS acquisitions, digital inclinometers provide angle measurements to the computer, which are saved to a text file for input to the reconstruction program. However, when the gantry is continuously moving, these inclinometers are incapable of providing angular values, displaying a value of 999 when in motion. Instead, the encoder of the servo motor can be used to provide angle information, the accuracy of which must be tested to gauge the impact on image resolution.

The spatial resolution of an imaging system can be characterized by how well the system can conserve modulations in an input signal and transfer that modulation to the resulting image [103]. The pre-sampling modulation transfer function (MTF) is commonly used for characterizing the resolution of digital detectors. The MTF is a spatial-frequency dependent function that quantifies the reduction in signal at a given spatial frequency as a result of all the processes that convert the input signal into an image [103]. If inaccuracies in encoder angle measurements reduce the spatial resolution of the reconstructed image, evidence of the degradation would be seen in a reduction in MTF at the spatial frequencies affected by the motion. Image MTFs are two-dimensional (2D) functions, which can be separated into two orthogonal components so that just the resolution along the direction of tube motion, which is assumed to be parallel to the columns (i.e. parallel to the 29 cm dimension of the detector) of the image matrix, is measured [104].

To confirm that angle measurements provided by the gantry motor encoder are accurate enough so that they do not negatively impact the reconstructed image, the MTF along the tube motion direction was measured from tomosynthesis images of a straight-edged piece of tungsten. The image set acquired by the SNS method was then reconstructed using two different sets of angles. The first set of angles was provided by inclinometer measurements. The second set of angles was measured by the encoder. The tungsten was placed on the edge of the breast support beneath the compression paddle. The slice in the reconstructed volume where the edge of the tungsten piece was the most in focus was selected for the presampling MTF, which was calculated using a program based upon the method described by Fujita et al [104]. It was written by former Williams lab students in the Interactive Data Language programming environment (IDL; Research Systems, Boulder, Colorado).

Figure 2-15 shows the MTF calculated from the two reconstructions. The dashed line shows the MTF of the reconstruction using inclinometer angle data. The Nyquist frequency of the reconstructed image after data binning is 3.33 mm^{-1}, which is half that of the full resolution image (6.67 mm^{-1}). The solid line shows the MTF of the reconstruction using encoder angle data.

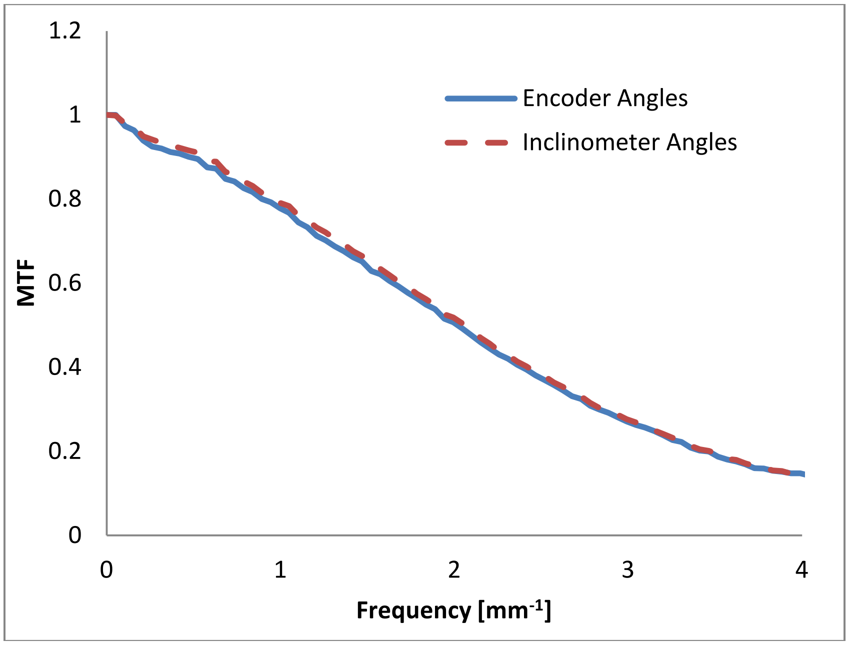

Figure 2-15: Pre-sampled modulation transfer function (MTF) obtained from a reconstructed slice of a tungsten edge.

MTF data shows that any error in encoder angle measurements do not result in any noticeable degradation of resolution as seen by the nearly overlapping curves in Figure 2-15. This plot shows that with a maximum of a ~3% reduction in MTF, the encoder angle can be used for accurately reconstructing data acquired by methods for STR.

2.4 Acceleration between Views

Feasibility of STR is not limited by the hardware of the DMT scanner. One of the major factors that does affect the total scan time is the angular range covered during the scan. Clinical systems cover angular ranges anywhere from 5° to 50° [65]. An angular span of 24° is covered during a DMT DBT scan, and a total of 13 images are taken at angles of $\pm 12°, \pm 8°, \pm 5°, \pm 3°, \pm 2°, \pm 1°,$ and $0°$ with respect to the direction of compression. If traveling at an angular speed of 0.6°/s over these angles, the total continuous motion scan would take 40 sec to complete. Even though this scan length is shorter than the current 90 sec SNS acquisition, scan time can be shortened further by accelerating the gantry between views separated by larger angles. For instance, traversing from $-12°$ to $-8°$ at a constant speed of 0.6º/s would take nearly 7 seconds. Since no images are acquired between these angles, the gantry can be moved at a much higher speed similar to the method proposed by Acciavatti et al [80]. Accelerating to higher speeds between these views would cut down gap times between images from ~7 seconds to ~1 second. The resulting gantry motion would then be a varying angular velocity profile. If gantry motion were stopped at some selected view, but not all, the resulting motion would be a hybrid motion profile (HMP) of both continuous motion imaging and the SNS method.

To limit ringing motion, one approach is to utilize constant angular velocity among views that are separated by only 1º since stopping the gantry for those views would introduce unnecessary jerky motion without much reduction in scan time. Additionally, for more widely spaced views the values of deceleration must be selected to be as small as possible so that gantry arm perturbations caused by backlash of the gears as the gantry arm is stopped can be minimized just before the exposures. Possible values of deceleration can be determined through the use of kinematic equations and limits on the total scan time.

When the gantry is accelerated and then stopped, the motion profile is a piecewise linear function consisting of three segments as in the example shown in Figure 2-13 of a symmetric trapezoidal motion profile. Angular acceleration of the gantry as a function of time has the following equation:

$$a(t) = \begin{cases} A, \ t_0 \leq t \ \leq t_1 \\ 0, \ t_1 < t \ < t_2 \\ A_D, \ t_2 \leq t \ \leq t_3 \end{cases} \tag{2-31}$$

The time intervals correspond to the values shown in Figure 2-13. The resulting angular speed as a function of time has the following equations:

$$\omega(t) = \begin{cases} At + \omega_0, \ t_0 \leq t \ \leq t_1 \\ \omega_c, \ t_1 < t \ < t_2 \\ A_D(t - t_2) + \omega_c, \ t_2 \leq t \ \leq t_3 \end{cases} \tag{2-32}$$

In the above equation, ω_c is the programmed constant angular speed of the gantry during the interval between periods in which the gantry is accelerated. To simplify calculations, the initial angular speed of the gantry ω_0 and its initial starting position θ_0 are set to 0°/s and 0°, respectively.

The total gap time $T_{gap,i,i+1}$ between projections i and $i + 1$ is equal to the sum of the time intervals required for execution of the three segments of the trapezoidal motion profile. Total scan time can be decreased by lowering the value of $T_{gap,i,i+1}$. Gap time cannot arbitrarily be reduced to some small value since there is a limit on the speed and acceleration the gantry motor can achieve. Each segment of the profile can be expressed as some fraction of $T_{gap,i,i+1}$ as follows:

$$f_a = \frac{t_1 - t_0}{T_{gap,i,i+1}} \tag{2-33}$$

$$f_c = \frac{t_2 - t_1}{T_{gap,i,i+1}} \tag{2-34}$$

$$f_D = \frac{t_3 - t_2}{T_{gap,i,i+1}} \tag{2-35}$$

In these equations, f_a, f_c, and f_D are the fractions of time of the total profile that the gantry motor accelerates, moves at constant speed, and decelerates, respectively.

The overall scan time can be reduced by accelerating gantry motion. However, because large acceleration and deceleration rates cause gantry arm oscillations, longer wait times would be required for gantry arm oscillations to damp out. As one way of identifying practical f_a, f_c, and f_D values, we start off with some initial set of acceleration (A) and deceleration values (A_D) that allow the total DMT DBT scan time to match that of commercial clinical SNS systems that use a similar angular range. These values are then increased to minimize the total scan time until gantry arm perturbations are observed. Values of A must also be kept low enough to limit sudden gantry arm motion that might make the patient flinch when in compression. In addition, if a larger fraction of time were allocated to allow for the gantry to slow down, smaller values of A_D can be chosen to reduce jerky motion just before the exposure.

If f_c approaches zero, a larger fraction of the profile can be designated for deceleration. The relation between f_a and f_D simplifies to Equation (2-36).

$$f_D = 1 - f_a \tag{2-36}$$

An equation for $T_{gap,i,i+1}$ can be determined by integrating Equation (2-32) over the time interval from t = 0 s to t=$T_{gap,i,i+1}$, which would be required to complete the motion between two consecutive projection angles separated by angle$\Delta\theta_{gap,i,i+1}$.

$$\Delta\theta_{gap,i,i+1} = \int_0^{T_{gap,i,i+1}} \omega(t)dt \tag{2-37}$$

Equation (2-38) is the result of integrating Equation (2-37) and substituting all time intervals for the fractional values of $T_{gap,i,i+1}$ from Equations (2-33) through (2-35).

$$\Delta\theta_{gap,i,i+1} = \frac{1}{2}A(f_a T_{gap,i,i+1})^2 - \frac{1}{2}A_D(f_d T_{gap,i,i+1})^2 \tag{2-38}$$

The angular speed $\omega_{c,i,i+1}$ that would be reached just before the deceleration portion of the profile can then be used to determine the value of A_D when given A, or vice versa as shown in Equation (2-39)

$$\omega_{c,i,i+1} = A\left(f_a T_{gap,i,i+1}\right) = -A_D\left(f_D T_{gap,i,i+1}\right) \tag{2-39}$$

$$A_D = -A\left(\frac{f_a}{f_D}\right) \tag{2-40}$$

Equation (2-41) is the equation for f_a in terms of the angular distance $\Delta\theta_{gap,i,i+1}$, the acceleration A, and the total translation time $T_{gap,i,i+1}$ when Equation (2-36) and (2-40) are plugged into Equation (2-38)

$$f_a = \frac{2\Delta\theta_{gap,i,i+1}}{A(T_{gap,i,i+1})^2} \tag{2-40}$$

By setting a limit on $T_{gap,i,i+1}$, $f_a$can be calculated from Equation (2-41). The total scan time is estimated from the sum of the gaps between the N = 13 projections and the exposure times t_{exp} as shown in Equation (2-42)

$$T_{Total} = \left(\sum_{i=0}^{3} T_{gap,i,i+1}\right) + Nt_{exp} + T_{3,9} + \left(\sum_{i=9}^{N-2} T_{gap,i,i+1}\right) \tag{2-42}$$

Acquisition time $T_{3,9}$ of the constant angular speed portion between projection angle θ_3 = 3° and projection angle θ_9= -3° can be approximated by the following equation:

$$T_{3,9} = \frac{(\theta_3 - \theta_9)}{2\omega_{limit}} \tag{2-43}$$

Angular speed ω_{limit} in Equation (2-43) is the maximum allowable gantry speed during imaging to limit blur to one detector pixel. If T_{Total} is set to 20 seconds similar to clinical SNS scan times of GE’s Senographe DS and Siemen’s Mammomat step-and-shoot systems [65, 105], the maximum allowable values of $T_{gap,i,i+1}$can be calculated. For

ω_{limit}= 0.3°/s and t_{exp} = 160 ms, maximum $T_{gap,i,i+1}$ = 1.30 seconds if all $T_{gap,i,i+1}$ in the summations of Equation (2-41) are kept equal.

Very high values of acceleration would cause jerky motion at the beginning of the motion profile, potentially increasing the likelihood of oscillations throughout the motion. To avoid initial gantry arm oscillations and sudden gantry motions that may cause the subject being imaged to move, A was selected to remain the same value of 30.0°/s^2 as in current DMT SNS acquisitions. If $T_{gap,i,i+1}$= 1.30 seconds and A remains the same value of 30.0°/s^2 as in SNS acquisitions, resulting values from Equations (2-40) and (2-41) are f_a = 0.158, f_D = 0.842, and A_D = 5.62°/s^2 for $\Delta\theta_{gap,i,i+1}$ = 4°. This fraction can then be used to set acceleration and deceleration values for the other angular increments of 3° and 2° from the following equations using $T_{gap,i,i+1}$ = 1.3 seconds:

$$A = \frac{2\Delta\theta_{gap,i,i+1}}{f_a(T_{gap,i,i+1})^2} \tag{2-44}$$

Table 2-3 contains the constants calculated from the above equations for programming the HMP for each angular interval used.

Table 2-3: Initial acceleration parameters

$\Delta\boldsymbol{\theta}$ [deg]	**A [deg/s^2]**	**A$_D$ [deg/s^2]**
1	0	0
2	15	2.81
3	22.5	4.22
4	30	5.62

Motion profiles were programmed using the values in Table 2-3 for the 4° angular distance. To reduce acquisition time further, the values of deceleration were then increased incrementally by 5°/s^2 and the gantry arm was observed during acquisition. When gantry oscillations were visible, the rate of deceleration was decreased by 1°/s^2 to the point where gantry arm oscillations just before the exposure were no longer obvious by visual inspection. Projection images of 1.5 mm diameter ball-bearings (BBs) were also monitored for any obvious signs of blurring. The resulting $T_{gap,i,i+1}$ was reduced to 0.94 s and f_a was raised to 0.3 by the increase in A_D. Table 2-4 contains the final values that were chosen for acceleration and deceleration for $T_{gap,i,i+1} = 0.94$ and $f_D = 0.7$. Appendix A contains the code that writes the program to the gantry motion controller's memory for executing the HMP.

Table 2-4: Final HMP acceleration parameters

$\Delta\boldsymbol{\theta}$ [deg]	**A [deg/s^2]**	**A_D [deg/s^2]**
1	0	0
2	15	6.5
3	25	11
4	30	13

With the decrease in gap time between images separated by more than 1°, total scan time can be reduced from two minutes to slightly less than 20 seconds with the described methods. For cases that require a higher exposure level per view than can be accomplished using a 160 ms exposure time, a faster version of the SNS method was programmed such that the gantry would decelerate at a slower rate to reduce the time between images that is required for allowing gantry arm oscillations to damp out. Consequences of continuous motion and lower achievable fluences due to shorter exposure times and tube current limits are discussed in the next chapter.

Chapter 3

Impact of STR on Image Quality

Specifications and testing of DMT hardware have shown that STR can be realized with a change in gantry motion profile and shorter exposure times. Theoretical calculations done in Chapter 2 provide a limit on the angular speed of the gantry arm during imaging to prevent blurring in the projection images. However, the shorter exposure times, necessitated by the continuous motion of the gantry arm, may result in noisier images if the readout noise from the x-ray detector electronics dominates over quantum noise at the potentially lower exposure levels. The overall effects of implementing shorter exposures and gantry motion during imaging will be determined by comparing images acquired for STR to those acquired by the SNS method. Assessment of lower exposures on read noise will be presented through the measurement of the detective quantum efficiency (DQE) of the x-ray detector.

3.1 Motion Blur in Images

3.1.1 Testing Constant Angular Speed during Imaging

Theoretical calculations were described in Chapter 2 of $\Delta\theta_{limit}$, the maximum allowable angle that the gantry can traverse within a single exposure for a single point in the object to map onto a single pixel in the image. In order to verify the results of the maximum allowable angular speed ω_{limit} during image acquisition, the modulation transfer function (MTF) is used again to gauge whether there will be any significant reduction in resolution resulting from gantry motion. Significant motion blur will result in a loss of spatial resolution in the projection image [106]. Broadening of features or a reduction in contrast resulting from motion blur would be discernible in a drop in MTF at the frequencies affected by the motion. Higher gantry speeds will cause larger drops in the MTF if all other acquisition parameters are kept fixed. The hypothesis of Chapter 2 is that motion blurring should not be noticeable in images acquired at ω_{limit}, the constant angular speed calculated by dividing $\Delta\theta_{limit}$ by the exposure time.

The same straight-edged piece of tungsten (W edge), described in Chapter 2, was employed for making the comparison between projection images acquired while the gantry was in motion and images acquired with a stationary gantry. For this analysis, the W edge was imaged at a 0^{o} projection angle after the gantry was put into motion at a constant angular speed. Gantry speeds tested were multiples of the limiting speed as follows: $\omega_{limit}, 2\omega_{limit}, 3\omega_{limit}$ and $4\omega_{limit}$ where $\omega_{limit} = 0.3°/s$ for the DMT system when the mapping of single point onto the detector was limited to a single 75 micron detector element. An SNS acquisition with the W edge in the same configuration was then taken at the same 0° angle. Exposure parameters of 26 kV tube voltage, 15 mA tube current, and 160 ms exposure time were constant for all acquisitions.

Figure 3-1 shows an example of a zoomed-in view of a projection image of the W edge acquired by the (a) SNS method and (b) during continuous gantry motion with a constant angular speed of $4\omega_{limit} = 1.2°/s$. Blurring can be seen in Figure 3-1(b), which lowers the resolution of the image as illustrated by the MTF in Figure 3-2. MTFs for images taken at each tested speed and with a stationary gantry are plotted for the direction of the image that is parallel to the direction of tube motion.

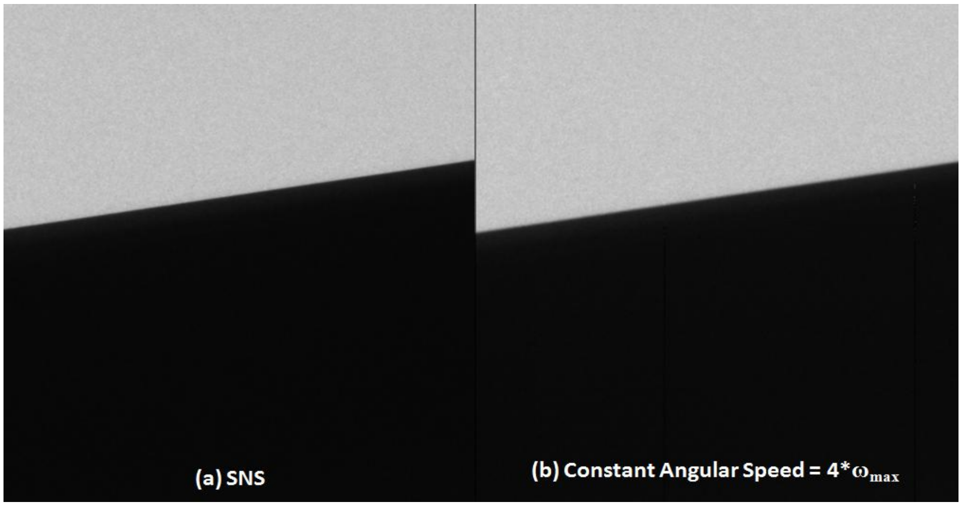

Figure 3-1: Zoomed-in view of the tungsten edge (W-edge) used for the MTF calculations to compare images taken when the gantry is (a) stationary and (b) moving at a constant angular speed where the gantry arm was moving at $4\omega_{limit} = 1.2°/s$. Direction of motion is in the vertical direction of the image. In the color scheme here darker pixels represent regions of higher attenuation.

As expected, the MTF curve of the stationary gantry case has the best performance over the frequency range from 0 mm^{-1} to the Nyquist frequency of 6.67 mm^{-1}. The Nyquist frequency here is half of the detector's sampling rate which is the inverse of the detector element size of 75 microns. The MTF curves for all of the tested speeds show a drop in MTF starting from a frequency of about 2 mm^{-1}, with the worst degradation seen for the fastest gantry speed tested.

Contrary to what was expected, the case where the gantry was moving at a speed of $2\omega_{limit}$ displayed better resolution than the lowest tested speed ω_{limit}. This behavior can be attributed to the fact that at this very low speed, the gantry arm exhibited more oscillatory motion, where the tube visibly rocked as it moved, which would have created some additional blurring in the image as seen by the MTF. Cogging torque ripple from servo motors could cause fluctuations in speeds or even discrete increments of motion at very low speeds [107]. In addition, there are five lead bricks attached to the DMT gantry arm that act as a counterweight for the x-ray tube and gamma camera. Two of the lead weights are not as rigidly attached to the gantry as the other hardware components. Discrete motion of the gantry arm could cause these lead bricks to oscillate if their inertia causes them to continue to move after the gantry has stopped, acting as a damped pendulum. This torque ripple could have caused the oscillatory motion of the tube that was witnessed at the slower tested speeds.

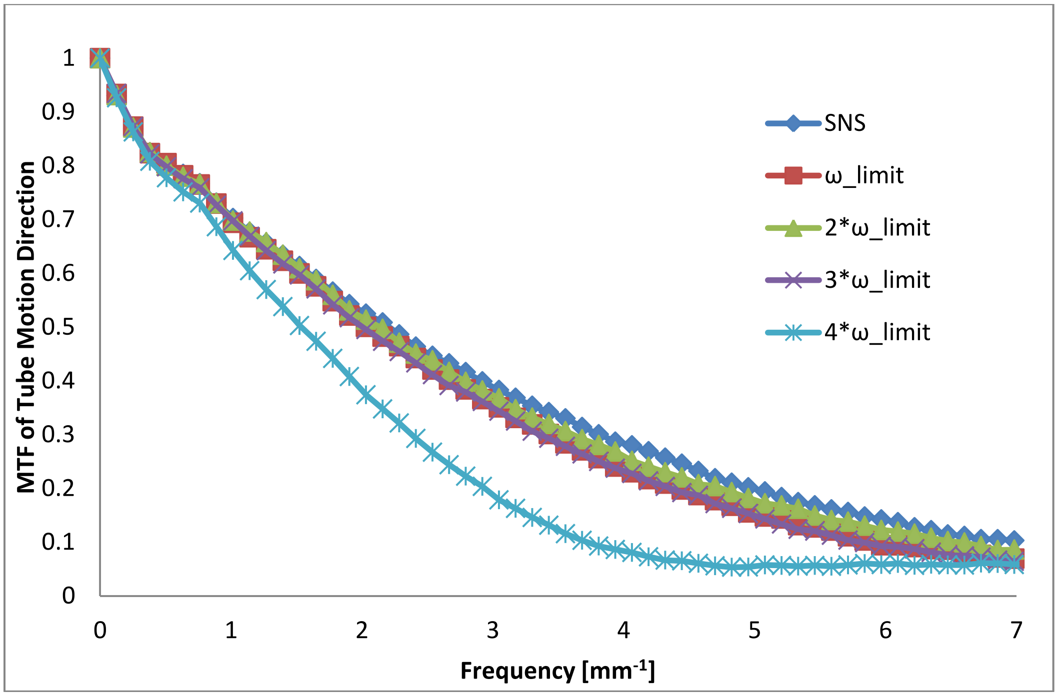

Figure 3-2: MTF curves plotted against spatial frequency for all tested speeds along with the stationary gantry case. Values of spatial frequency were multiplied by the magnification factor to account for the fact that the W edge was placed on top of the breast support rather than directly onto the detector.

The MTF improves at the speed of $2\omega_{limit}$ and drops down again at higher speeds. To reduce the size of the final reconstructed volume, images are typically binned. The reconstruction algorithm for DMT DBT is programmed to do 2x2 binning. Since this binning effectively doubles the length of a single pixel from 75 microns to 150 microns, the constraint on the extent of image blur can be relaxed slightly to double the detector element size, allowing for double the gantry speed as calculated from Equation (2-25). Degradation of spatial resolution from tube motion at $2\omega_{limit}$, compared to SNS, may not have as perceptible an effect when combined with data binning and other sources of image blurring as discussed in Chapter 2.

3.1.2 SNS versus Hybrid Motion Profile (HMP)

In one possible hybrid profile, the gantry travels at a constant angular speed during exposures separated by 1º but accelerates between views separated by 2º or more. Because the gantry motor creates ringing motion of the gantry arm with high rates of deceleration and very slow speeds, jerky motion must be limited by ensuring enough time is allowed for the gantry to slow down before the exposure is executed.

As discussed in Chapter 2, by designating the majority of the gap time between images separated by $> 2°$ for acceleration or deceleration, with little to no constant velocity time, the total gap time between the widely separated projections can be cut down to 1.3 seconds. This gap time is less than the time required for the gantry to travel at the constant speed of $2\omega_{limit} = 0.6°/s$ between projections separated by 1º, which is 1.67 seconds. Using the currently programmed acceleration of $30^{o}/s^{2}$, the input parameters for deceleration were calculated in Chapter 2. With a higher speed and acceleration between views, the total scan time using a hybrid motion profile (HMP) can be reduced to 20 seconds from the 90 second SNS acquisition time. Any loss of spatial resolution resulting from HMP can be detected by loss of resolution in the reconstructed image and potentially in errors in the estimated size and relative position of the objects being reconstructed.

For this analysis, a geometric calibration phantom (Geometrical Calibration Phantom, Hologic Inc., Bedford, MA) was used. This phantom has 44 BBs, metal spheres that attenuate most of the incident mammographic x-rays, embedded into two flat plastic surfaces that are 3 inches apart. The BBs are 1.5 mm in diameter and are separated by 1.5

inches between consecutive BBs configured into 4 rows and 5 columns. Figure 3-3 is a photograph of the geometric calibration phantom.

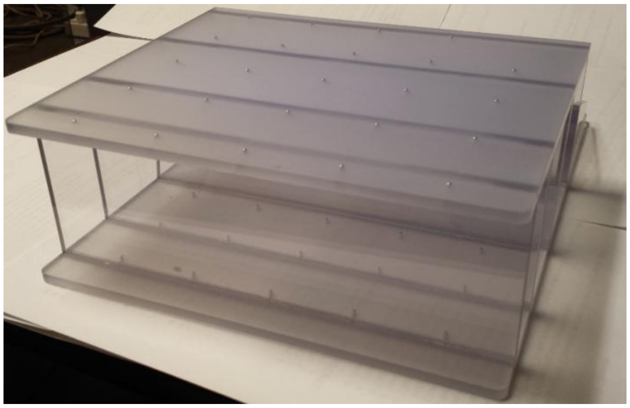

Figure 3-3: Geometric calibration phantom used for comparison of reconstructions of images acquired by the SNS method to those acquired by the HMP method.

The phantom was scanned at the angles discussed in Chapter 2 of ±12º, ±8º, ±5º, ±3º, ±2º, ±1º, and 0º by both the SNS method and then 5 trials of the HMP method. Figure 3-4 is a plot of the angular speed of the gantry versus gantry angle in the HMP acquisition. Exposure parameters of 26 kV tube voltage, 15 mA tube current, and 160 ms exposure time were constant for all acquisitions. There were no other objects in the beam except for the compression paddle, the breast support, and the phantom. The 3-D images were reconstructed from the projection images using the reconstruction algorithm provided by Dexela.

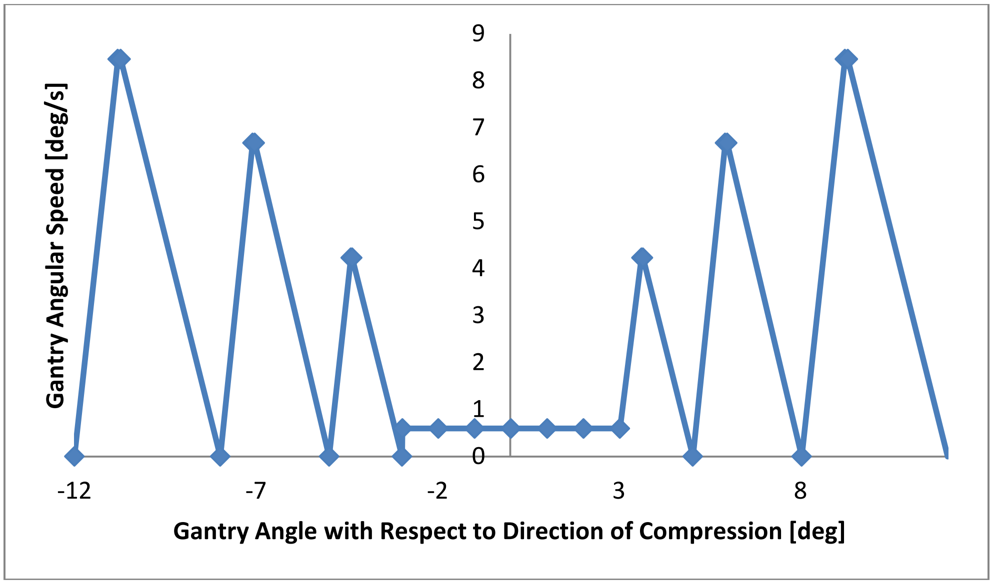

Figure 3-4: Plot of gantry angular speed versus gantry angle in the hybrid motion profile (HMP)

To find whether there were any differences in the relative position of the BB within the reconstructed volume between the acquisition methods, the locations of the BBs relative to each other were determined by finding the centroid location of each BB. The centroid $[u_{cm}, v_{cm}]$ was measured by getting the center of mass of the voxels within 30 x 30 voxel^2 regions of interest (ROIs) drawn around the BBs as shown in the following equations.

$$u_{cm} = \frac{\sum_{i=0}^{N} \sum_{j=0}^{M} V_{ij} i}{V_{Total}} \tag{3-1}$$

$$v_{cm} = \frac{\sum_{i=0}^{N} \sum_{j=0}^{M} V_{ij} j}{V_{Total}} \tag{3-2}$$

In the above equations, M and N are the number of voxels in each dimension of the ROI containing the BB, V_{Total} is the sum of all voxels within the ROI, and V_{ij} is the voxel value of the ith column and the jth row of the ROI.

To gauge whether there was any change in shape of the reconstructed BBs as a result of the HMP, widths (left-right dimension parallel to tube motion) and lengths (anterior-to-posterior dimension) of each BB were measured from profiles through the BBs. The widths and lengths were determined by finding the locations in the profile where the voxel value was ≥10% of the peak value in the profile and taking the difference between the highest and lowest indices of the voxel values that met this condition.

Figure 3-5(a) shows the slice in the reconstructed image from the SNS acquisition where one of the BBs is most in focus. Figure 3-5(b) is the corresponding slice from the reconstruction of the images acquired with the HMP. Because the voxel values in the reconstruction represent attenuation, higher intensity values (white) signify higher attenuation, as in the example of the BB. The acrylic background of the phantom does not attenuate as highly as the BBs, so voxel values outside of the BB are lower. The line profiles through the BBs along the red line in Figures 3-5(a) and (b) are plotted in (c).

Figure 3-6(a) is the centroid positions plotted for both acquisition methods for the BBs in the bottom plate of the phantom, and Figure 3-6(b) is plot of the BBs in the top plate. Error bars in the plot are the standard deviation of five trials of the HMP acquisition. However, since the error bars are smaller than the symbols used for plotting, not all error bars are visible.

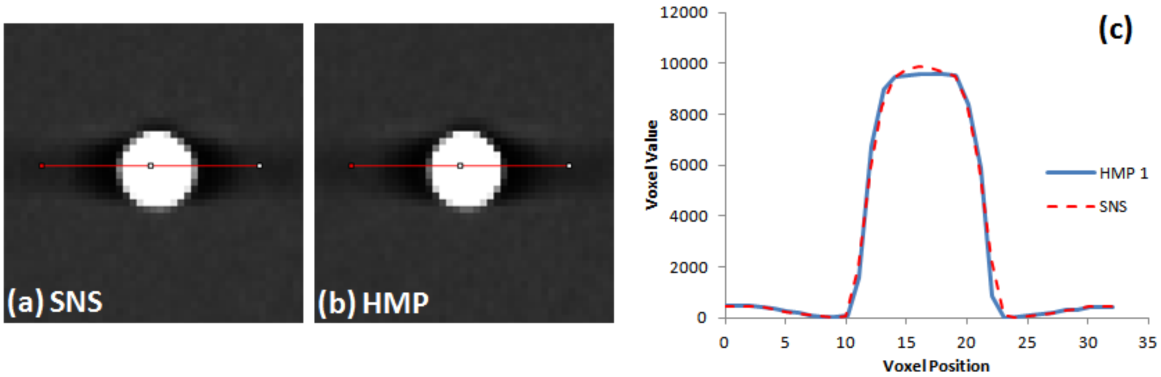

Figure 3-5: Reconstructed slices from images acquired by the (a) SNS method and with (b) the hybrid motion profile (HMP) of a BB. Because the voxel values in the reconstruction represent attenuation, higher grayscale values (brighter) signify higher attenuation as in the example of this BB. Line profiles through the BBs along the line shown in the reconstructed slices in are shown in (c).

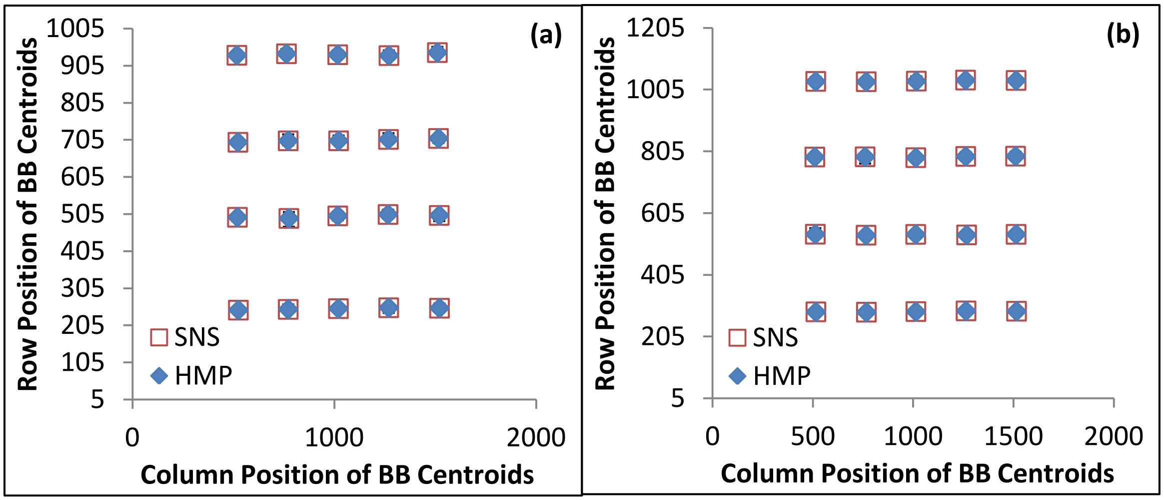

Figure 3-6: Centroid positions of BBs in (a) the bottom plate and (b) the top plate of the phantom.

Profiles through the BBs show that the HMP did not greatly degrade reconstruction image quality as the two curves overlap. There is a small amount of contrast lost as seen by a 2.6% reduction in peak value of the HMP profile as compared to the SNS profile. The BB widths were found to be comparable. The average width of the 40 BBs that were measured were found to be 1.47 mm with a standard deviation of 0.058 mm for SNS and 1.46 mm ± 0.049 mm for HMP, which are slightly smaller than the true 1.5 mm size of the BBs. A summary of the BB width and length results are provided in Table 3-1.

HMP acquisitions have slightly larger errors in the estimated sizes of the BBs, but these errors are well within the standard deviation of the lengths of the BBs in the SNS image. BB lengths are slightly larger than the expected value in both image sets. Note that motion blur due to continuous gantry motion would not affect BB length, but could affect the width. HMP BB widths are slightly smaller than those of the SNS images, but the errors relative to the known widths are also well within the standard deviation of the widths of the BBs in the SNS image.

Table 3-1: Average widths and lengths of BBs

Acquisition Method	BB Width	Standard Deviation	Percent Error	BB Length	Standard Deviation	Percent Error
SNS	1.474	0.0577	-1.75%	1.54	0.0678	2.75%
HMP	1.464	0.0486	-2.40%	1.55	0.0716	3.45%

In addition to negligible difference in the imaged lengths and widths of the BBs, the estimated locations of all features within the reconstructed volume were in good agreement between the SNS and HMP acquisition methods. With negligible changes in image quality relative to SNS, it is feasible to use the HMP during image acquisition for reducing total DMT DBT scan time. Line profile data shows that blurring artifacts are not perceptible in reconstructed images acquired with the HMP. However, the limit on tube output when using shorter exposure times could limit the fluence to the detector. To ensure that detectability is not affected by detector read noise at lower exposures, detector efficiency was characterized to find the range of exposures to the detector over which quantum-limited operation is possible.

3.2 Detective Quantum Efficiency (DQE) of the 2923MAM

The requirements associated with the acquisition of a series of rapid, low exposure projection images place greater demands on x-ray detectors used in tomosynthesis compared to those in planar FFDM. In particular, high quality, low dose tomosynthesis requires detectors with high x-ray absorption efficiency, high frame rates with low read noise, and low dark noise. Dark noise is the signal detected due to dark current in the detector's electronics in the absence of x-rays.

In an ideal imaging system where the signal follows Poisson statistics, the noise in the image will be approximately equal to the square root of the total number of detected photons [108]. However, a real detector will add its own read noise when converting incident photons into pixel values in the final digital image [108]. As the exposure times become shorter for STR, the total number of photons decreases for a fixed tube current [13]. At some exposure level, the read noise from the detector may not be negligible in comparison to the quantum noise, thereby degrading the quality of the image [108]. The CMOS detector used for DMT DBT is the 2923MAM manufactured by Dexela/Perkin-Elmer (London). Although it is possible to shorten the DMT DBT scan time by reducing the exposure time and acquiring images at a faster rate, it is essential to determine whether the overall image quality will suffer due to potentially lower tube output.

The spatial frequency dependent detective quantum efficiency (DQE(u)) is the most generally used indicator of how efficiently the detector can process the input x-ray signal. By using a standardized DQE measurement method, the performance of a detector can be determined for any given setup and compared to that of other systems [109]. For this reason, the widely accepted IEC-62220-1-2 Standard [110] was followed to test the Dexela 2923MAM CMOS x-ray detector.

The 2923MAM has a 75 micron detector element size in a 3888 x 3072 pixel matrix, for an overall sensitive area of approximately 29 cm x 23 cm. With no pixel binning the maximum frame rate is 17 frames per second (fps), rising to up to 78 fps for 4x4 binning. The 2923MAM includes a columnar CsI converter. All measurements described here were performed without pixel binning. There are also two possible operating modes for the Dexela detector: a high dynamic range (HDR or high full well capacity) mode and a high-sensitivity mode (HS or low full well capacity) setting. A comparison was made between the DQE for HDR operation and HS operation over a range of entrance exposures that were less than or comparable to a single projection view in a typical tomosynthesis acquisition.

3.2.1 Calculating DQE

DQE is a function of spatial frequency, defined as the ratio of the image signal to noise ratio (SNR) squared to the SNR of the input signal squared as shown in Equation (3-3).

$$DQE(u) = \frac{{SNR_{out}}^2(u)}{{SNR_{in}}^2(u)} \tag{3-3}$$

For signals that obey Poisson statistics, ${SNR_{in}}^2(u)$ is equal to the number of x-ray quanta, which is proportional to the input fluence. The output $SNR_{out}(u)$ is determined by all of the cascading processes involved with converting the input signal to a digitized image, which includes a conversion from x-ray light to visible light, then a conversion from visible light to an electric signal, and finally to a digital value [16]. The noise power spectrum (NPS) is a function of spatial frequency that characterizes the pixel-to-pixel fluctuations caused by quantum noise as well as the series of steps performed for creating the image from the incident signal [111]. The square root of the image NPS would estimate the noise in the image at a given frequency, which would serve as the denominator of $SNR_{out}(u)$. The image signal, or numerator of $SNR_{out}(u)$ can be calculated by the convolution of the input photon count ${SNR_{in}}^2$ and detector gain g with the modulation transfer function (MTF) T, which simplifies to a product of all three in frequency space. An expression can then be obtained for $SNR_{out}(u)$ as shown in Equation (3-4).

$$SNR_{out}(u) = \frac{g\ {SNR_{in}}^2(u)\ T(u)}{\sqrt{NPS_{out}(u)}} \tag{3-4}$$

If Equation (3-4) is plugged into Equation (3-3), the resulting expression for $DQE(u)$ is given in Equation (3-5).

$$DQE(u) = \frac{g^2 {SNR_{in}}^2(u) T^2(u)}{NPS_{out}(u)} \tag{3-5}$$

The IEC Protocol 62220-1-2 was followed in calculating the DQE for the Dexela 2923MAM CMOS detector, though minor modifications were made as described in the following sections. As given in the IEC protocol, the equation for the frequency-dependent $DQE(u)$ becomes the following [110]:

$$DQE(u) = T^2(u)(\frac{NPS_{in}(u)}{NPS_{out}(u)}) \tag{3-6}$$

Equation (3-7) shows how the two-dimensional (2D) image NPS $NPS_{out}(u_n, v_k)$ is calculated according to the protocol [110].

$$NPS_{out}(u_n, v_k) = \frac{\Delta x \Delta y}{M \cdot 256 \cdot 256} \sum_{m=1}^{M} \left| \sum_{i=1}^{256} \sum_{j=1}^{256} \left(I(x_i, y_j) - S(x_i, y_j) \right) \exp\left(-2\pi i \left(u_n x_i + v_k y_j \right) \right) \right|^2 \quad (3-7)$$

Summation is done over the rows and columns of the image matrix over M number of 256 x 256 pixel regions of interest (ROI) of the full projection image. The image is acquired with no attenuating material in the beam. The posterior-to-anterior direction (23 cm dimension of the detector) is parallel to the rows in the image and is designated as x in position space and u in frequency space. The direction parallel to the image columns in the 29 cm dimension of the detector will be denoted as y in position space or v in frequency space. The gain term g from Equation (3-5) becomes a part of $NPS_{out}(u_n, v_k)$ through the use of a conversion function that relates input fluence to pixel value. For the 2923MAM, this relation is linear [16]. The linearized image data is $I(x_i, y_j)$ in Equation (3-7) and has units of fluence per unit area. $S(x_i, y_j)$ is an optional 2D second-order polynomial fit subtracted from the ROI to remove any trends that might influence the overall $NPS_{out}(u)$. Cuts through the 2D $NPS_{out}(u_n, v_k)$ are made either parallel or pendicular to the image matrix for the final one-dimensional (1D) $NPS_{out}(u)$ in Equation (3-6). $NPS_{in}(u)$ is the noise power spectrum at the input of the detector and is defined in Equation (3-8).

$$NPS_{in} = K_a SNR_{in}^2 \quad (3\text{-}8)$$

Air kerma K_a is defined as the kinetic energy released in mass of air as a result of ionizing radiation [112], which, in the protocol, is to have units of $(mm^2 \mu Gy)^{-1}$. The squared signal-to-noise ratio SNR_{in}^2 is of the input signal per unit air kerma, which is a constant provided in Table 2 of IEC-62210-1-2 for a given target/filter combination. The product of air kerma with SNR_{in}^2, as defined by the IEC protocol, has units of photons per unit area, ensuring that the resultant $DQE(u)$ is unitless.

3.2.2 Geometry and Radiation Quality

A diagram of the tube and detector setup is shown in Figure 3-7. The distance between the focal spot and the closest point on the detector surface is 81 cm. The x-ray tube contains a tungsten target, exit window filtration of 0.76 mm of beryllium, and an external filter of 0.050 mm of rhodium. Additional external filtration of 1.4 mm of Al was added to match the half value layer (HVL) of 0.75 mm of aluminum (Al) specified in the IEC Protocol for W/Rh target/filter systems operated at 28 kVp. HVL is the thickness of Al required to cut down the beam intensity by half of its intensity without the Al. Agreement of HVL with the protocol validates the use of SNR_{in}^2 as provided by the IEC since the DMT spectrum would, in theory, then match that of the standard protocol beam with the given target/filter combination. As per protocol requirements, all images and measurements were taken at a tube voltage of 28 kVp. From this setup, we were able to use 5975 $(mm^2\mu Gy)^{-1}$ as the SNR_{in}^2 value for a tungsten target with a 50 µm rhodium filter at 28 kVp.

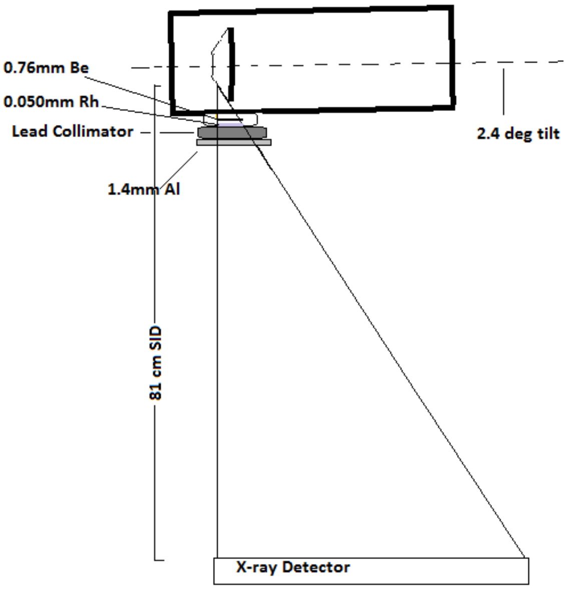

Figure 3-7: Setup of the x-ray tube and detector showing the sources of beam filtration and the geometric parameters. The tube has a tilt of 2.4° with respect to the surface of the detector. The source to detector distance (SID) is 81 cm. Filtration of the beam for the measurements described here includes 0.76 mm of beryllium, 50 microns of rhodium, and 1.4 mm of aluminum. In clinical practice the Al filtration is not present.

3.2.3 Detector Response and Determination of Conversion Function

The conversion function is the relationship between the large area detector output (i.e. average pixel value) in a corrected image and the input x-ray fluence. Prior to the determination of the average pixel value in all of the images used, corrections were made to the raw images (replacement of bad pixels, dark image subtraction, and flat-fielding) as permitted by the standard. Flat-fielding is the process by which variances in detector gain from pixel to pixel are compensated so that the final image has a uniform pixel intensity distribution when a uniform object is placed in the beam [113]. The conversion function was then used to convert pixel values into units of fluence. For many digital x-ray detectors, this relationship is linear to a high degree in which case the conversion function reduces to a proportionality constant and a pixel value offset.

The detector response was measured for both HDR and HS modes by recording the average pixel value over a range of input kerma values in the uncorrected images. A Radcal Accu-Pro ion chamber was used for determining the air kerma, and inverse square law corrections were made to calculate the exposure at the detector surface. Figure 3-8 is a plot of the mean pixel value, within a region of interest (ROI) drawn at the focal spot projection in uncorrected images, versus exposure. The portion of each curve in Figure 3-8 that is linear has been fit with a linear equation and projected forward to show the detector's deviation from a linear response at higher input fluences.

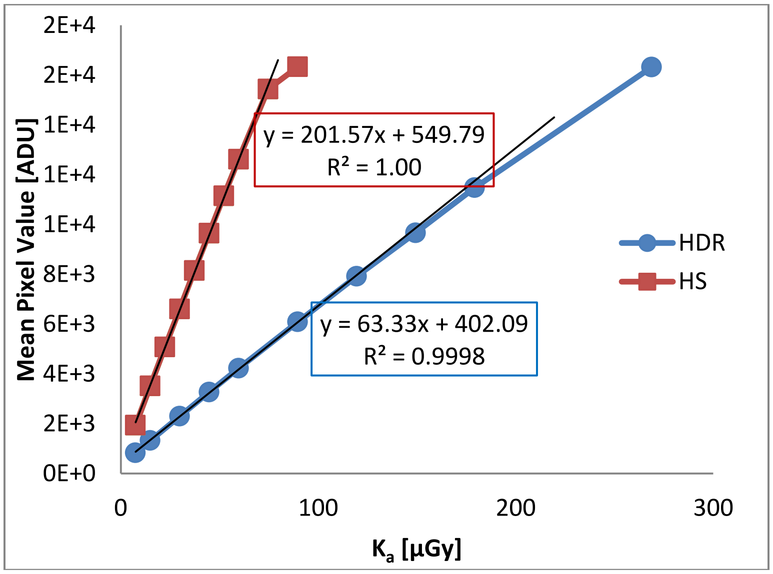

Figure 3-8: Mean pixel value versus air kerma. Pixel values come from uncorrected images taken with nothing in the x-ray beam except for the internal and external filters. Least squares fits are shown to the portion of each curve exhibiting linear behavior.

The highest tested air kerma levels chosen for each mode are just below the point at which the detector stops behaving linearly with increasing fluence. The air kerma levels tested here are 1.69 µGy, 3.57 µGy, 7.34 µGy, 15.1 µGy, 30.0 µGy, and 60.1 µGy for HS mode. The same levels were tested in HDR mode with two additional levels at 89.9 µGy and 119 µGy.

The conversion function for both modes is shown in Figure 3-9. In HDR mode, the conversion function slope is 0.008388 ADU·mm^2/photon and in HS mode it is 0.02750 ADU·mm^2/photon. The zero fluence values shown in Figures 3-8 and 3-9 are due primarily to DC offset values digitally added to each pixel value during the dark subtraction and uniformity correction procedures.

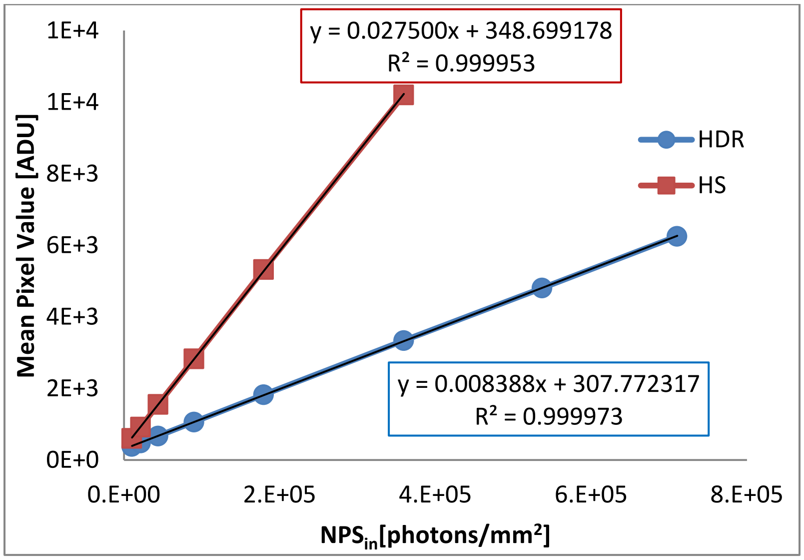

Figure 3-9: Conversion function in both HDR mode and HS mode. A linear fit was applied to each curve and the fit equation and R-squared values are shown next to each curve.

3.2.4 MTF

The MTF was measured using a straight-edged piece of tungsten rather than the aluminum test device suggested by the IEC Standard. The presampling MTF was calculated using a program based upon the method described by Fujita et al [104]. It was written by our lab in the Interactive Data Language programming environment (IDL; Research Systems, Boulder, Colorado). Figure 3-10 shows the calculated presampled MTF plotted for both image dimensions in both modes.

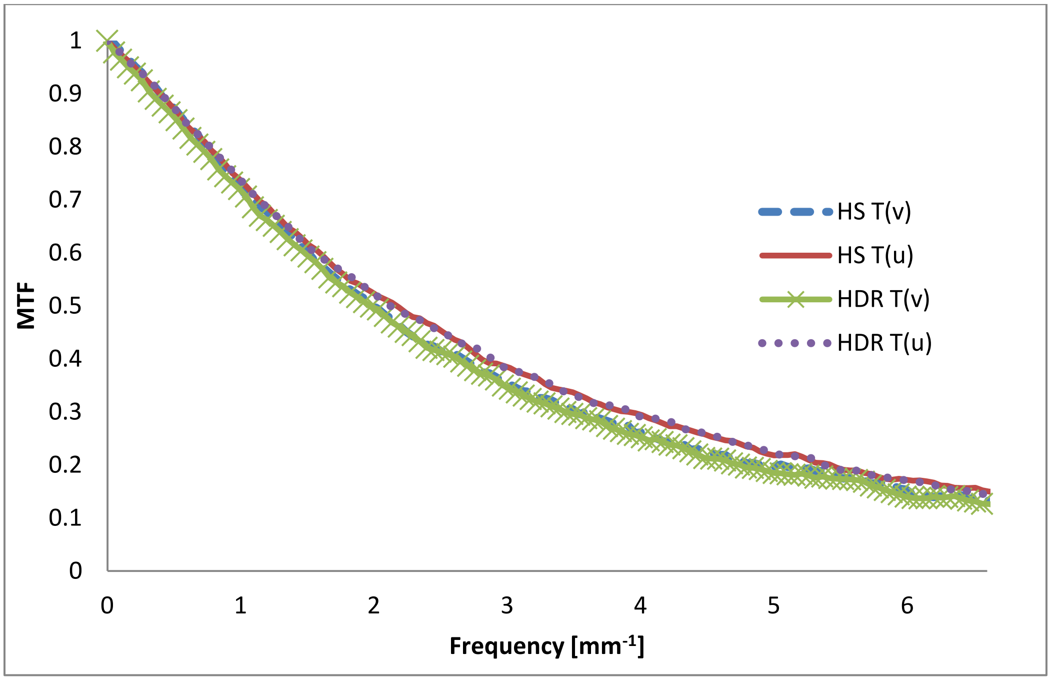

Figure 3-10: Modulation transfer function along the image rows (T(u)) and columns (T(v)) for HS mode and HDR mode.

3.2.5 NPS$_{out}$

The IEC protocol was followed in determining NPS$_{out}$ for each exposure. An ROI chosen within the image for the NPS calculation had dimensions of 17.85cm x 27.48cm corresponding to an area of 8720320 pixels^2. The final 2D NPS$_{out}$ was found by averaging over noise power spectra from 459 overlapping 256 x 256 pixel sub-regions within the ROI. The 1-D NPS$_{out}$(u) was obtained by averaging over 7 rows above and 7 rows below the v = 0 mm^{-1} frequency axis. The same was done for NPS$_{out}$(v) about the u = 0 mm^{-1} frequency axis. Additionally, a 2D second-order polynomial fit was subtracted from each ROI to improve the estimation of low frequency noise in NPS$_{out}$.

Figures 3-11 and 3-12 are the plots of NPS$_{out}$(u) and NPS$_{out}$(v), respectively, for both HS mode and HDR mode for exposure levels of 1.69 µGy, 7.34 µGy, 30.0 µGy, and 60.1 µGy. As an additional quantification of image noise, a log-log plot of the standard deviation σ in the NPS_{out} images versus K_a is shown in Figure 3-13 for both HS mode and HDR mode. In all cases it was verified that the integral of the 2-D NPS between ±Nyquist frequencies was equal to σ^2. As a measure of quantum limited behavior a power fit was applied to both curves. The fit equation and the R-squared value are shown next to each curve. In quantum limited operation the fit exponent is 0.5.

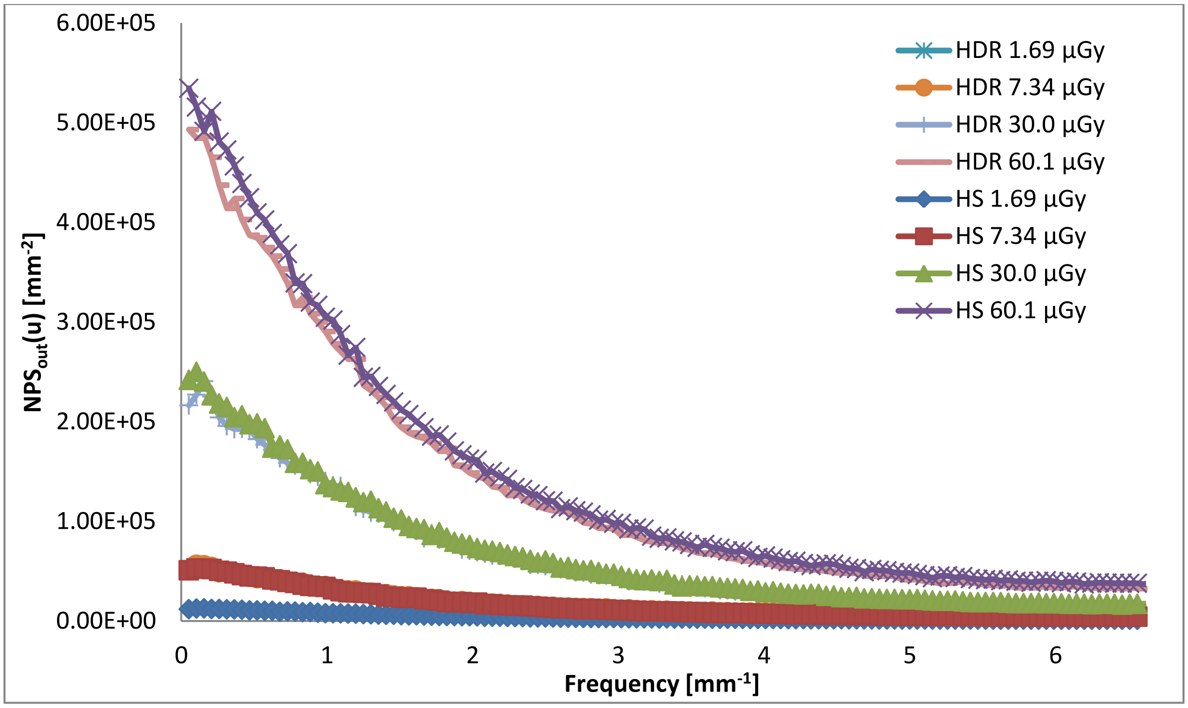

Figure 3-11: Plot of NPSout(u) in units of fluence for air kerma levels of 1.69 µGy, 7.34 µGy, 30.0 µGy, and 60.1 µGy in both HS mode and HDR mode.

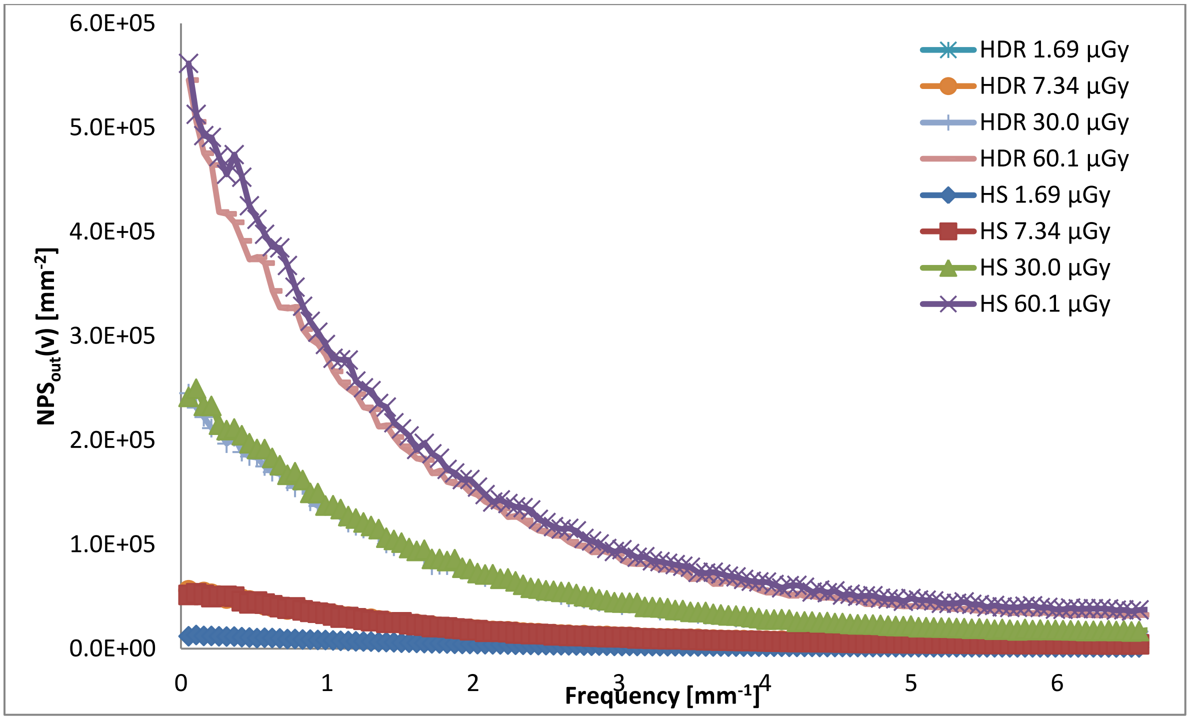

Figure 3-12: Plot of NPSout(v) in units of fluence for air kerma levels of 1.69 µGy, 7.34 µGy, 30.0 µGy, and 60.1 µGy in both HS mode and HDR mode.

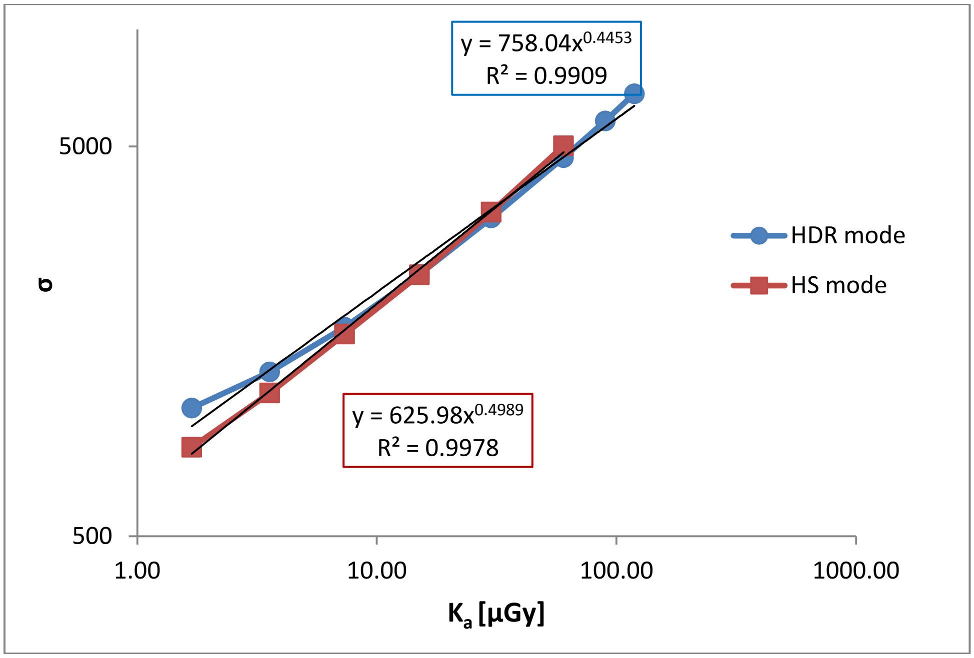

Figure 3-13: Log-log plot of standard deviation of the linearized NPSout images σ versus air kerma for both HS mode and HDR mode. A power fit was applied to both curves. The fit parameters and the R-squared values are displayed next to each curve.

3.2.6 DQE Curves

Figures 3-14 and 3-15 are plots of DQE(u) and DQE(v), respectively, for HDR mode. Figures 3-16 and 3-17 are plots of DQE(u) and DQE(v), respectively, for HS mode. A subset of all exposures tested is shown in each figure. Data are plotted within a frequency range of 0 mm^{-1} to the Nyquist frequency of 6.67 mm^{-1}. The 0 mm^{-1} frequency points were omitted since it does not correspond to an achievable physical quantity.

For K_a values between ~7 µGy and 60 µGy the DQE is similar in either HDR mode or HS mode, with a value of ~0.7 at low frequency and ~0.15 – 0.20 at the Nyquist frequency f_N = 6.7 mm^{-1}. As would be expected, the change in DQE at either very low or very high input fluence differs between the two modes of operation. In HDR mode, the DQE remains virtually constant for operation with K_a values between ~7 µGy and 119 µGy but decreases for K_a levels below ~7 µGy. In HS mode, the DQE is approximately constant over the full range of entrance air kerma tested between 1.7 µGy and 60 µGy but, as seen in Figure 3-8, kerma values above ~75 µGy produce hard saturation.

Comparison of DQE(u) and DQE(v) show that for either HDR mode or HS mode operation, a slight difference exists between the shapes of the DQE in the x- and y-directions, with DQE(v) having a more linear drop off with increasing spatial frequency compared to DQE(u). The results show a slightly better detector performance in the posterior-to-anterior direction than in the orthogonal dimension. Higher efficiency in the y-direction will be necessary, especially when tube motion blur degrades the resolution further in this orthogonal dimension.

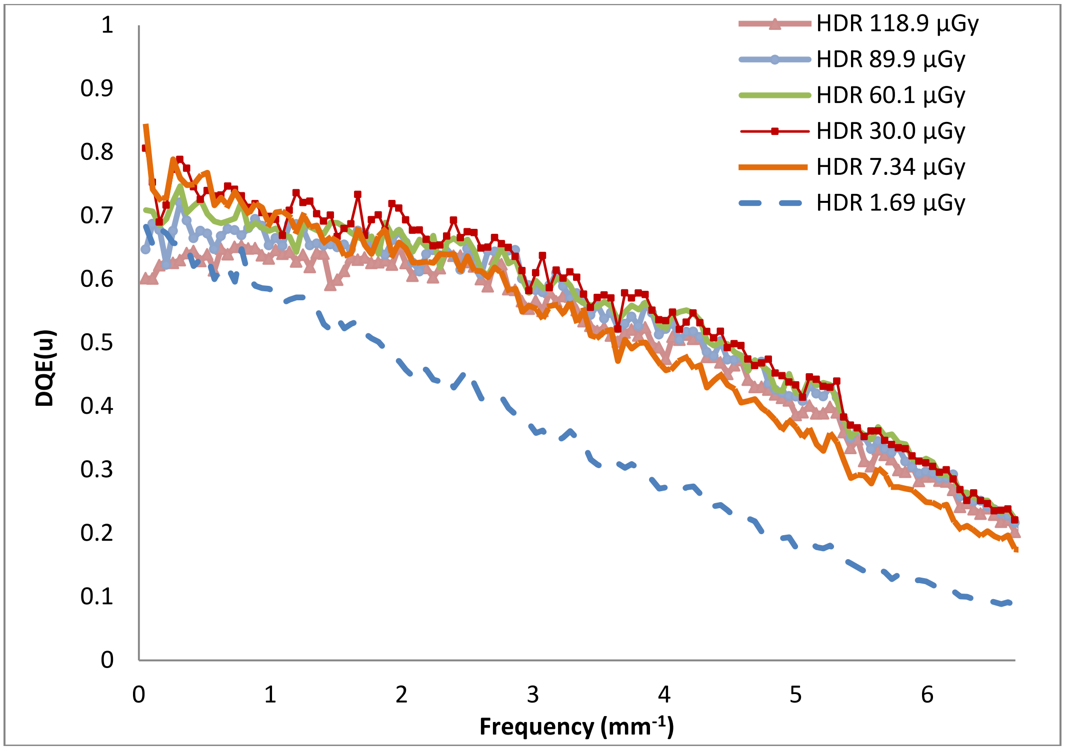

Figure 3-14: DQE along detector rows at the tested entrance dose levels of 1.69 µGy, 7.34 µGy, 30.0 µGy, 60.1 µGy, 89.9 µGy and 118.9 µGy in HDR mode.

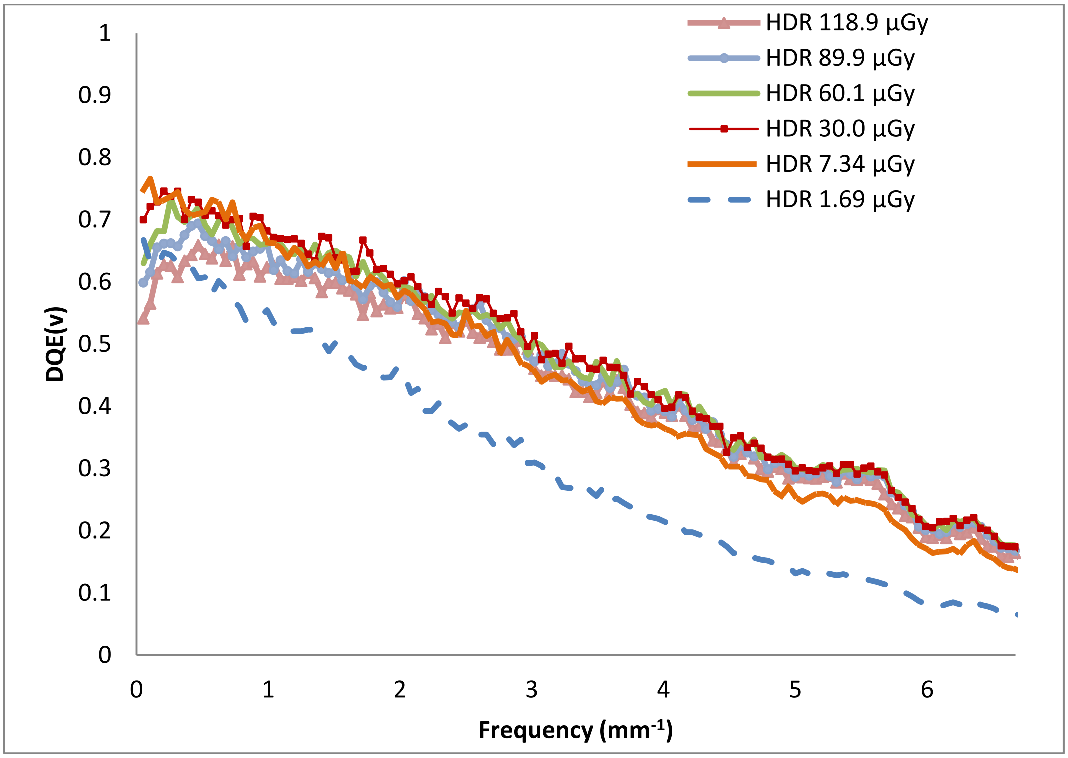

Figure 3-15: DQE along detector columns at the tested entrance dose levels of 1.69 µGy, 7.34 µGy, 30.0 µGy, 60.1 µGy, 89.9 µGy and 118.9 µGy in HDR mode.

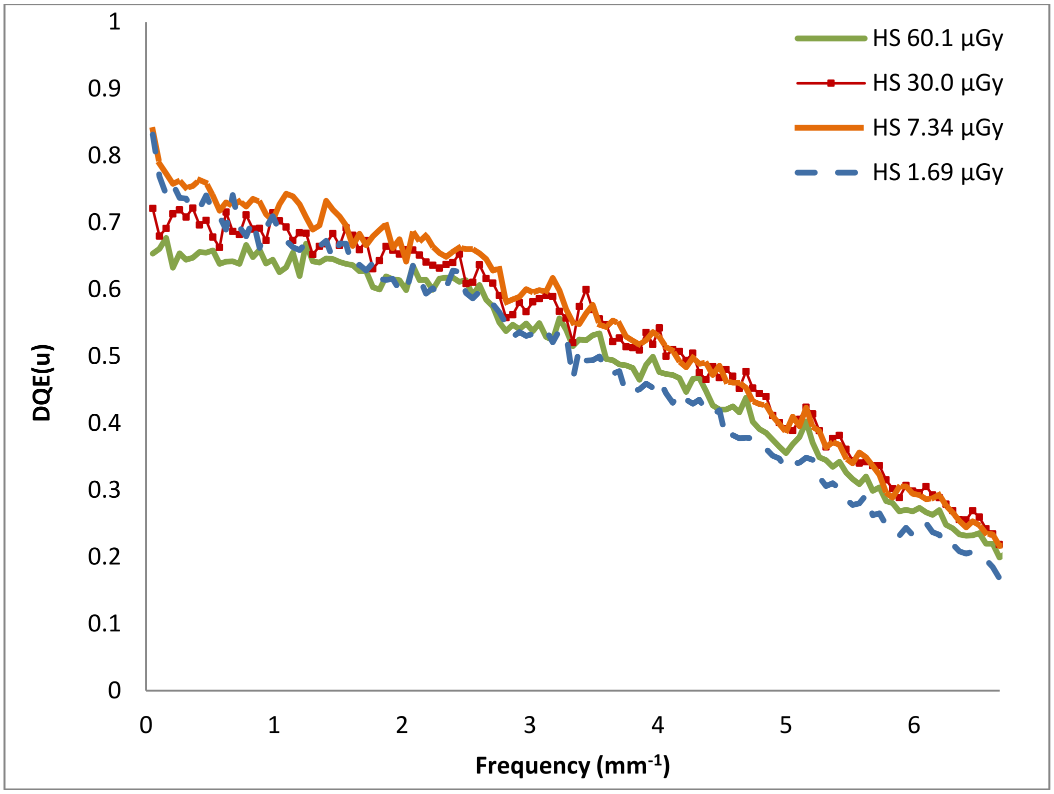

Figure 3-16: DQE along detector rows at the tested entrance dose levels of 1.69 µGy, 7.34 µGy, 30.0 µGy, and 60.1 µGy in HS mode.

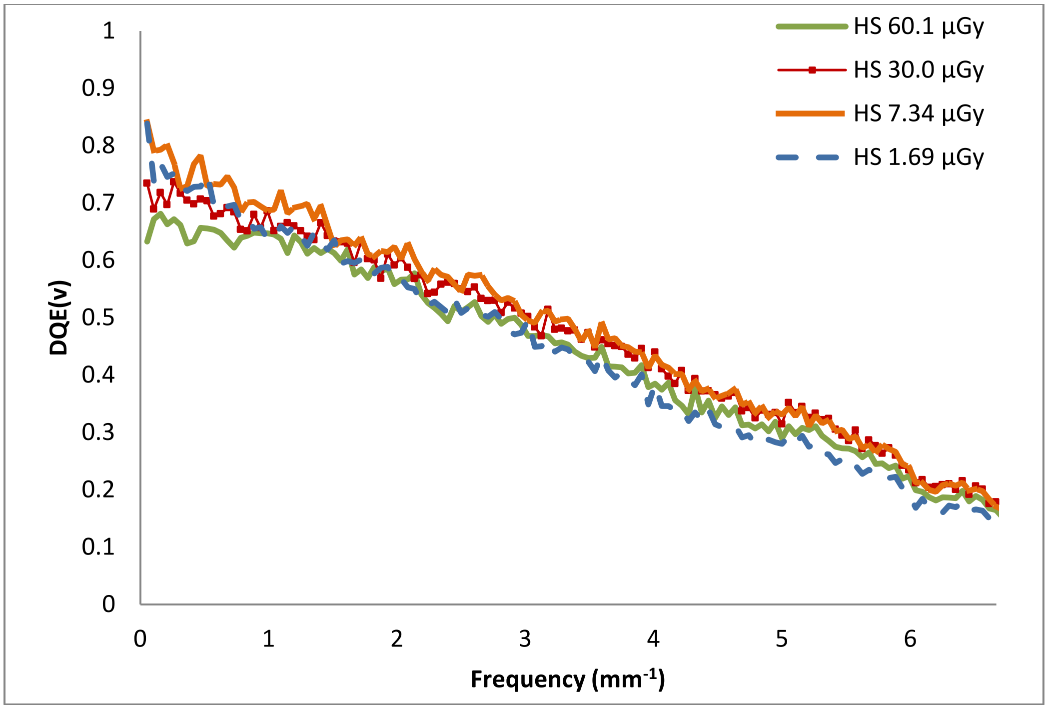

Figure 3-17: DQE along detector columns at the tested entrance dose levels of 1.69 µGy, 7.34 µGy, 30.0 µGy, and 60.1 µGy in HS mode. This direction is parallel to tube motion.

The exponential relationship between the RMS image noise and the input kerma with exponent of ~0.5 (Figure 3-13) shows that the image variance increases approximately linearly with increasing input fluence as would be expected for quantum limited operation. However, in addition to the deviation from quantum limited operation at low exposure in HDR mode operation, there is a slight deviation at high exposure in either mode, most prominently in HDR mode.

HS mode will be valuable when considering generator limitations associated with the shorter exposure times of HMP acquisitions, especially for thick breasts. For example, for mostly fatty breast with compressed thickness of ~8.5 cm as were observed in human studies of DMT, the exposure techniques used for each projection of the DMT DBT acquisition were 28 kV tube voltage, 56 mA tube current, and 320 ms exposure time. In those cases the mean pixel value in a projection view of the breast below the focal spot was ~2100 ADUs when using HS mode. Using the linear fit in Figure 3-8, this pixel value corresponds to a detector entrance air kerma of approximately 7.9 µGy. Even if this exposure were cut down by half when cutting the exposure time down to 160 ms for HMP acquisitions, the read noise of the 2923MAM in HS mode would remain negligible in comparison to the Poisson noise present at either exposure level (Figures 3-16 and 3-17). Figures 3-14 and 3-15 suggest that while quantum limited operation at 7.9 µGy is possible using HDR mode, it may not be for slightly lower detector entrance kerma levels.

The two operating modes of the 2923MAM together provide high DQE over a large exposure range. The combined abilities of very low dose operation and rapid readout make STR feasible without image degradation from system noise. However, this analysis does not account for information loss from scattered radiation. The next chapters discuss x-ray scatter and the method proposed for rejecting scattered radiation from DMT DBT.

Chapter 4

Scatter in DMT Projections

When ionizing radiation is used for breast imaging, a large fraction of the radiation will inevitably interact with the breast. The three possible interactions between mammographic x-rays and breast tissue are photoelectric absorption, Rayleigh scattering, and Compton scattering [114]. Though absorption is essential to image contrast, the other two processes tend to reduce the contrast of features, diminishing the effectiveness of the x-ray imaging modality at differentiating between various internal structures of the breast. All x-ray imaging modalities are susceptible to scattered radiation, and scatter increases with more scattering material. Compton scattering is the main process by which mammographic x-rays are scattered due to the 15 to 30 keV energy range typical of mammograms and tomosynthesis images.

Medical x-ray imaging provides structural information by exploiting the differing x-ray attenuation properties of various tissue types with the goal of differentiating between abnormal and healthy tissue. In breast cancer imaging, when the attenuation of tumors is similar to that of surrounding tissue, these cancers can be missed. Scattered radiation in projection x-ray imaging decreases lesion contrast and increases image noise. In tomographic x-ray imaging, such as CT, it produces cupping and streak artifacts and causes errors in the measurement of the spatially varying x-ray attenuation coefficients (i.e. errors in the voxel values). Scatter increases strongly with increasing object thickness [70].

In digital breast tomosynthesis (DBT) imaging, the x-ray tube is moved relative to the breast in order to obtain a series of low-dose projection images over a limited angular range from which a 3D image of the breast can be reconstructed. DBT, in conjunction with FFDM, has been shown to reduce recall rates and improve positive predictive value (PPV) and cancer detection rate in a screening population, especially for women with radiodense breasts [28, 29]. As in CT, DBT images consist of voxels whose values are ideally linearly related to the linear attenuation coefficient μ of the tissue within the voxel. However, the limited angular range of DBT does not provide a complete tomographic data set. Therefore, the estimate of μ for a given voxel is affected by artifacts arising from structures in nearby slices. Scatter in DBT introduces additional errors in the form of cupping artifacts and attenuation quantitation errors, similar to those in CT [69, 67, 68, 66]. Using Monte Carlo simulations Wu et al. found that for a 5 cm thick breast image, contrast for a 1.4 cm mass is reduced by 30%, the voxel value is reduced by 28%, and the signal difference to noise ratio (SDNR) is reduced by 60% [115].

This chapter presents a quantification of scatter in DMT projection images and a potential method for its rejection from DMT DBT.

4.1 Methods of Scatter Rejection

Software for correcting scatter from DBT images is a favored method currently under investigation due to its implications of reducing radiation dose [116, 117, 118, 119, 120]. However, because scatter distribution changes with cone beam geometry, breast shape, and thickness, this method would not be straightforward to implement for all breasts and scanners [120, 121, 122]. Increasing the air gap between the exit surface and the entrance surface of the detector has also been discussed as an effective method of scatter reduction [123]. The larger gap allows for the scattered rays that are diverging away from the primary ray direction to scatter out of the detector's field of view, thereby, reducing the SPR.

To remedy the "foggy" appearance of images that resulted from scattered rays, Gustav Bucky invented the anti-scatter grid to be placed between the detector and the object being imaged to reduce the amount of scattered radiation that reaches the detector [124]. In modern mammography, anti-scatter grids have been shown to improve contrast by anywhere from ~15% to over 70%, depending upon the thickness and composition of the breast, when placed between the breast and the x-ray detector [9, 10, 11]. Figure 4-1 is a schematic of how anti-scatter grids are typically implemented. Many anti-scatter grids used in mammography are 1-dimensional (1D), or linear, comprised of narrow strips, aligned in the posterior-anterior direction. Lamellae are made from high atomic number materials that remove secondary photons whose trajectories have appreciable components perpendicular to the direction of the strips [2].

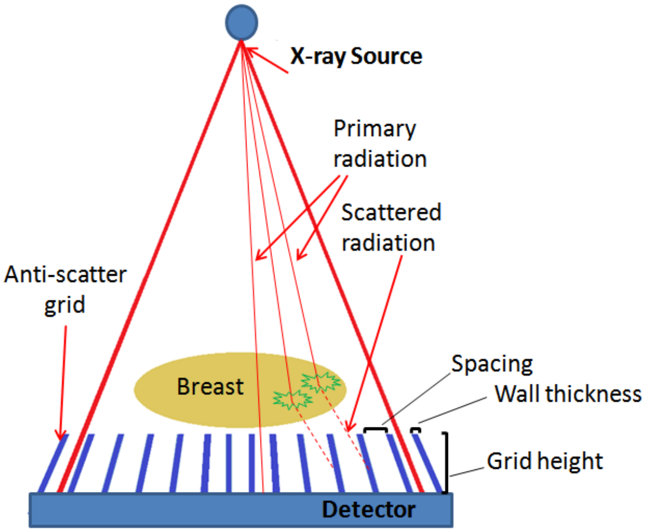

Figure 4-1: Schematic of how anti-scatter grids are employed in FFDM. Walls of the grid block a large portion of scattered rays that are generated within the breast while primary rays are transmitted through the grid spaces. The height of the walls, the material used for building the grid, and thickness and spacing of the walls determine grid performance.

To minimize cutoff of primary rays originating from cone beams, most 1D grids are focused, wherein strip orientations are increasingly non-normal to the detector surface with increasing distance from the grid midline. Gaps between the strips are oriented such that their axes all intersect at a single line in space. Lower atomic number material, such as aluminum or carbon fiber, are at times used to separate and align grid walls, which attenuate more of the primary rays than grids consisting of air interspaces [125]. A linear grid can be characterized by a grid ratio, which is the ratio of the height of the grid to the thickness of the interspace material, and its strip density, provided as a frequency expressed in line pairs per cm or line pairs per inch (lp/cm or lp/in). The grid pitch, which is the sum of the widths of a single wall and a single space, is then the inverse of this grid frequency. The degree of scatter rejection will depend upon the attenuating material, the grid ratio, and the grid pitch. Larger grid ratios generally provide better scatter rejection [126, 127]. Grid ratios typically used in mammography are of the order of 5:1, and grid frequencies are typically ~30 lp/cm [128].

Scattered photons traveling parallel to the strips are still transmitted, so only partial elimination of scatter is possible using a 1D grid. Focused 2D anti-scatter grids increase scatter rejection by using an array of holes rather than strips to block scatter [129, 130]. Most cellular grids have square holes, and only the central hole at the chest wall edge has walls that are perpendicular to the surface of the grid. All other holes in both the anterior direction and the left and right directions away from the central hole have increasingly angled walls to match the paths of primary rays originating from the x-ray source. When extended, the axes of these holes intersect at a single point in space, referred to as the grid focal point (GFP). The GFP is located a fixed distance measured perpendicularly from the midpoint of the grid's posterior edge, called the grid focal distance. When a 2D grid is centered on the detector, the GFP is located in the same point in space as the x-ray focal spot (XFS).

While both 1D and 2D anti-scatter grids are available for FFDM, these grids cannot readily be used in most clinical tomosynthesis systems. During DBT scans, the x-ray detector typically is stationary or rotated through a small angle and thus does not maintain a fixed alignment with respect to the moving x-ray source. Therefore, either a conventional 1D grid or a 2D grid would produce unacceptably large attenuation of primary (unscattered) radiation for most DBT tube positions.

In contrast, focused 2D anti-scatter grids can be used in cone-beam computed tomography breast imaging (CTBI) systems, which are also plagued by scatter. Rather than single row CT, CTBI systems make use of multiple detector rows for wider fields of view (FOV), further increasing the importance of scatter rejection with wider cone beam angles [131, 132, 68]. In CTBI, lamellae of a 2D grid would attenuate a negligible number of primary rays since the detector and source rotate together about a single axis that runs through the pendant breast [133]. Two-dimensional anti-scatter grids have been shown to drastically reduce scatter from CTBI images, leading to marked improvement in image quality [134].

Much like CTBI, the DMT x-ray tube and detector rotate around a common axis. This C-arm geometry keeps the orientation of the detector and tube fixed and makes DBT equivalent to limited angle CT using a 3rd generation CT gantry. This geometry raises the possibility of using a 2D (cellular) focused anti-scatter grid, as has recently been employed in cone-beam or many-row CT scanners.

4.2 Scatter to Primary Ratios (SPR)

The amount of scattered radiation relative to primary, or scatter to primary ratio (SPR), in projection images can be quantified through multiple methods. Cooper et al. have proposed estimates made through edge spread functions (ESF) [135]. Modulation transfer functions (MTF) [136] and Monte Carlo simulations [137, 138, 139, 140] have also been proposed as a means of characterizing the scatter presence in projection images. These approaches have their own merits, but they also come with disadvantages, including difficulty in achieving the correct experimental setup [135] and large errors in experimental results seen in data acquired by applying scatter rejection methods [136].

A technique that is widely used for measuring SPR is the beam stop method [70, 141, 142, 143, 126], which is the method of choice here. Figure 4-2 is a schematic of the experimental setup of the beam stop method. In these tests, a lead blocker, thick enough to attenuate all of the primary rays that are incident on its surface, is placed over scattering material and is imaged using a given set of x-ray parameters. Then, the blocker is removed and the scattering material alone is imaged at the same exposure parameters.

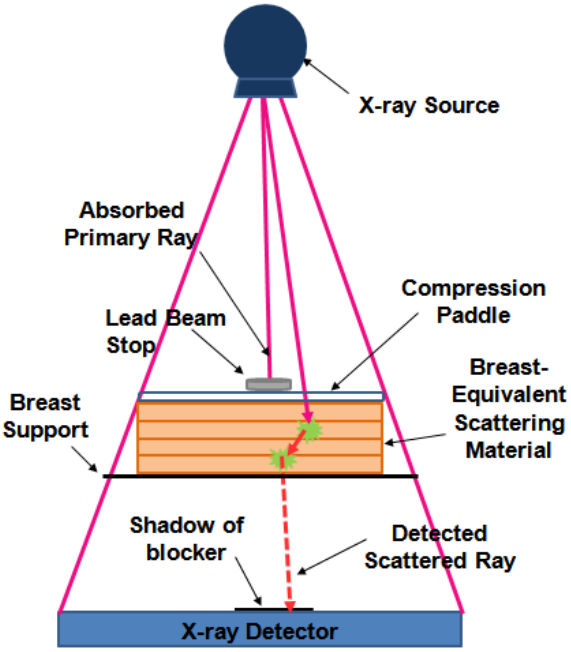

Figure 4-2: Schematic of the setup of beam stop experiments used for quantifying SPR in DMT 0º projection images.

For digital systems, pixel values within the image are proportional to the total energy of the incident detected x-rays. If there are any photons detected behind the blocker, they are attributed to scattered radiation, and the resulting x-ray image would have non-zero pixel values where the shadow of the blocker is seen. Likewise, the pixel values in the same corresponding position of the blocker-free image result from detection of both scattered and primary rays. By comparing the pixel values in these two images, the relative intensity of scattered radiation in comparison to that of primary radiation can be calculated. The background and experimental setup outlined here follows the method described by Fetterly and Schueler [126].

A single blocker alone is not sufficient in accurately measuring the true relative amount of scatter for a given point on the detector. More scattered rays are detected around the periphery of the blocker, the intensity of which drops off towards the center of the blocker. For a given amount of scattering material, as the blocker size gets smaller, more scatter will be detected behind the center of the blocker. Therefore, the true amount of scatter at a given point would be detected behind a blocker that is infinitesimally small, or with zero width.

The method by which this true value is obtained is by imaging several varying sizes of blockers. The number of scattered rays S is measured from the mean pixel value in a region of interest (ROI) that is drawn around the center of the blocker image and has a size that is half that of the whole blocker to avoid any extra scatter counts from the blocker's periphery [126]. The number of scattered rays S plus primary rays P, or (S+P), is then obtained from the mean pixel value within the same ROI of the blocker-free image. The ratio of scatter relative to primary for a given blocker SPR_B can be estimated by the following equation:

$$SPR_B = \frac{S}{(S+P)-S} \tag{4-1}$$

These values are then plotted for each blocker against the size of the blocker. Finally, the true amount of relative scatter is obtained by extrapolating the value of relative scatter for a blocker of zero width from a plot of SPR_B versus blocker size. Since the number of scattered rays increases with increasing thickness of scattering material, the same experiment is carried out for each desired compressed thickness.

These calculations use the assumption that the same number of primary x-rays and scattered rays are generated for every exposure of a given set of techniques. However, there will be some variation in tube output from one exposure to the next. To account for this variation, an ROI is drawn in the background of the image away from the blocker following a similar procedure described by Fetterly and Schueler [144]. If all exposures were truly identical, the mean value within this background ROI would be the same for all images for a fixed set of exposure parameters. Since this value is slightly different for each exposure, a correction factor k_b is calculated from the background outside of the blocker as follows:

$$k_b = B_b / B_{nb} \tag{4-2}$$

B_b is the mean value of the background in the blocker image and B_{nb} is the mean pixel value of the background in the no-blocker image. Blocker image mean values were then multiplied by these correction factors to calculate SPR_B values using Equation (4-3)

$$SPR_B = \frac{k_b S_b}{(S_{nb}+P_{nb}) - k_b S_b} \tag{4-3}$$

S_b is the mean pixel value behind the blocker in the blocker image, $(S_{nb} + P_{nb})$ is the mean pixel value in the same corresponding position of the no-blocker image.

Two different kinds of phantoms were used for these measurements. Projection images were acquired of lead blockers placed over uniform phantoms consisting of CIRS blocks with dimensions of 10 cm x 12.5 cm [145], which were built from a set of blocks varying in thicknesses from 5 mm to 2 cm. There were three sets of these blocks that simulated breast glandular/adipose compositions of 30/70, 50/50, and 70/30. For each composition, three phantoms were built from two 5 mm thick skin-simulating blocks, included at the entrance and exit surfaces, and different combinations of block thicknesses of the desired composition to obtain total phantom thicknesses of 4 cm, 5.5 cm and 7 cm. The various configurations allowed for the generation of a total of 9 different phantoms.

To get an estimate of SPR for a 50/50 composition breast that would cover more of the detector's 23 cm x 29 cm field of view (FOV), the same experiments were performed with blocks of polymethyl methacrylate (PMMA) with dimensions of 16 cm x 24 cm x 1 cm thick, which simulate a 50/50 breast glandular/adipose composition. There was no skin-simulating material included for the PMMA phantoms. Data from these images were then compared to projection images using the same set of CIRS and PMMA block thicknesses, but without any lead blockers, to obtain the final SPRs.

For these experiments, five circular blockers were used with sizes of 6.2, 9.6, 14.4, 22.4, and 25.6 mm. The blockers were placed on top of the compression paddle, which came into contact with the top surface of each phantom. Since SPRs will vary over the FOV and with breast shape [137], the blockers were placed at a position within the FOV that was centered on the scattering material to get an average SPR, representative of the tested compressed thickness.

Each blocker was imaged separately for a total of five blocker images and one image of the scattering material alone. Exposure techniques given in Table 4-1 were fixed for all images of a given thickness. The tube current was set to be within the quantum-limited range of the x-ray detector for 500 ms exposures

Table 4-1: Exposure Techniques

Thickness	Tube Voltage [kV]	Tube Current [mA]
4	24	115
6	26	115
8	31	75

4.2.1 Without Scatter Rejection

Figure 4-3 is a plot of the pixel value ratios SPR_B obtained for each blocker. Data is plotted using diamonds, squares, and triangles for the 4, 6, and 8 cm phantoms, respectively.

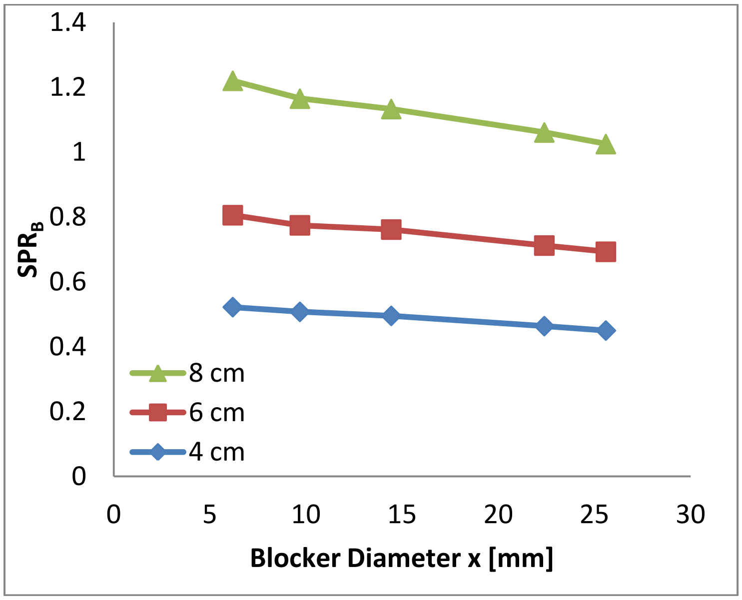

Figure 4-3: Scatter-to-primary ratio (SPR) versus lead blocker diameter found from comparison of mean pixel values in 0° projection views of scattering material with blockers to projections acquired with only the scattering material.

The correct function for fitting these curves has been debated, as the final SPR values obtained from these extrapolations is sensitive to the choice of function used for fitting [137]. A third-order polynomial was fit to this data with the form shown in Equation (4-4) because it provided the highest R^2 values from all the fits tested.

$$SPR_{B,Poly}(x, t_c) = ax^3 + bx^2 + cx + d \quad (4\text{-}4)$$

$SPR_{B,Poly}$ is a polynomial function of the blocker diameter x applied to the SPR_B data for each tested compressed thickness t_c. Final point SPR values were calculated by setting x in Equation (4-4) to 0 mm for each tested thickness.

Figure 4-4 shows scatter-to-primary ratios (SPRs) in the 0º projection view plotted versus phantom thickness for the 10 cm x 12.5 cm CIRS phantom blocks and the larger PMMA phantoms.

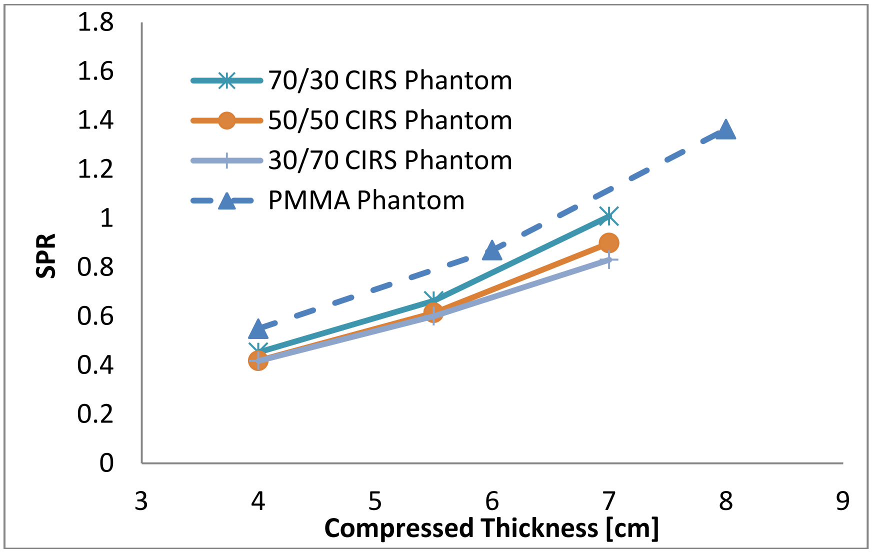

Figure 4-4: SPRs for uniform CIRS phantom blocks simulating 30/70, 50/50, and 70/30 breast compositions and for the PMMA phantom (dashed line). The PMMA phantom covered more of the full field of view (FOV) and simulated a 50/50 breast composition.

Solid lines are used to plot SPRs for 30/70, 50/50, and 70/30 breast compositions of the smaller CIRS phantoms. The dashed line with the triangles is a plot of the SPRs for the PMMA phantom.

SPR values illustrate the presence of a large amount of scatter, with scatter dominating over primary for the largest tested compressed thickness. This magnitude of scatter impacts image quality and necessitates some form of scatter rejection for improvement in detectability of cancerous structures that may otherwise become imperceptible.

4.2.2 SPR Data with Grid Prototypes

Three 2D focused cellular grid prototypes were available for testing in the DMT system. All three had the same grid pitch, or width of a wall plus a space, and focal length. The only varying characteristics among the three were material and grid height. The first grid was made from tungsten-polymer (W-poly) and had a grid height of 3.6 mm. The other two grid prototypes were made from copper and had heights of 2.1 mm and 3.85 mm and will be referred to as Cu-1 and Cu-2, respectively. All three had a wall spacing of 1 mm, 0.1 mm septum, and 80 cm focal distance.

For characterizing the performance of each grid prototype, beam-stop experiments, as described previously, were repeated with the grid prototypes in the beam just above the detector surface. All phantoms and blocker configurations and x-ray techniques were replicated for these grid-in experiments. The active area, or area that consists of spaces, of the grid prototypes is 17 cm x 26 cm. Since this area is smaller than the 23 cm x 29 cm imaging area of the x-ray detector, only the portion of the detector covered by the grid was used for this analysis.

Figure 4-5 shows SPR data for the PMMA phantom without any form of scatter rejection (dashed line) and with the anti-scatter grid prototypes. Figure 4-6 is a plot of the SPR data obtained with the CIRS phantoms of varying compositions. Dashed lines are used to plot data where there was no form of scatter rejection and solid lines plot data obtained with the inclusion of the Cu-2 grid.

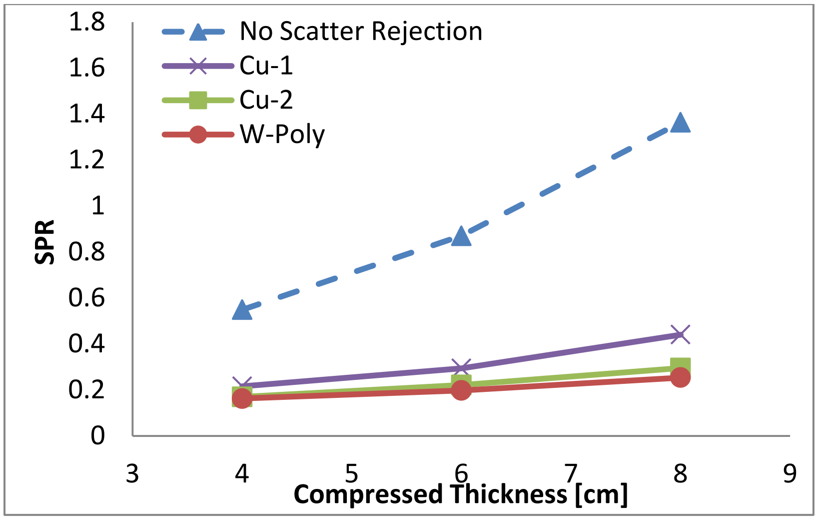

Figure 4-5: SPRs are plotted for varying thicknesses of PMMA in (b). The dotted line shows the SPR when there is no form of scatter rejection. The solid lines plot the SPR with the W-poly (circle symbols) and Cu (triangle symbols) grids located just above the detector surface.

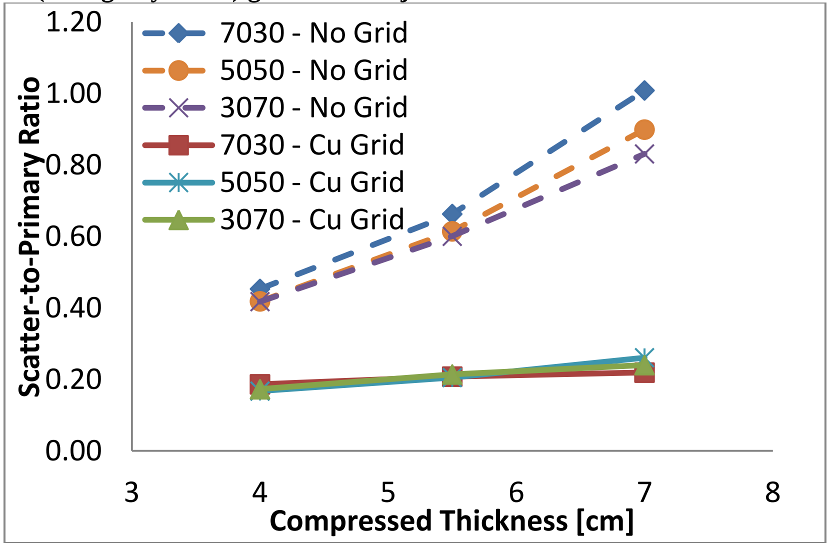

Figure 4-6: SPR Ratios shows SPRs for uniform CIRS phantom blocks simulating 30/70, 50/50, and 70/30 breast compositions. Grid-out SPRs are represented by dashed lines and Cu grid-in SPRs are plotted as solid lines

SPRs increase with compressed thickness and with glandularity when there is no form of scatter rejection. SPR was reduced by more than a factor of 3 with use of the Cu-1 grid and by more than a factor of 4 with use of the Cu-2 and W-poly grids. In addition, SPR is nearly constant over all tested thicknesses and compositions when the Cu-2 prototype was used. The anti-scatter grid that had the best performance in scatter rejection was the W-poly grid whose inclusion cut down SPR by a factor of more than 5 times that of the grid-out case for the 8 cm PMMA phantom. The grid with the second highest performance was the Cu-2 grid.

There is a large amount of scatter in DMT images that will degrade image quality, especially at the large compressed thicknesses typical of DMT clinical trials. At an average compressed thickness of 7.7 cm, some form of scatter rejection is necessary to improve DMT DBT image quality. Based upon the results of beam stop experiments, the grid prototypes significantly reduce scatter. However, these prototypes cannot be used in clinical trials as they are much smaller than the 23 cm x 29 cm active area of the x-ray detector and have large borders that would cut out a sizable portion of the breast image at the chest wall edge. A full-sized grid is required with optimized parameters to simultaneously reduce scatter transmission and maximize transmission of primary rays.

4.3 Selecting Optimal Grid Parameters

Based upon SPR data, a W-poly grid would be the first choice for grid fabrication. However, W-poly grids that have dimensions large enough for the FOVs of modern FFDM and DBT systems are not currently available. Although the W-poly prototype provided the most scatter rejection for the same primary transmission, the performance of the Cu-2 prototype was similar, making copper a favorable alternative. The specifications of the full-sized grid that determine performance are grid height, septal thickness, and grid hole spacing. There are an infinite number of possible combinations of these values. By characterizing scatter and primary transmission properties of the two available copper grid prototypes, optimal specifications for the full-sized grid were determined for achieving target performance.

4.3.1 Characterizing Scatter Transmission of Grid Prototypes

Anti-scatter grids do not reject all scattered radiation. There is always a probability of a scattered ray penetrating through the wall of the grid and traveling to the detector. In addition, since scattered rays do not have any preferential direction, they will also go through the holes of the grid. Therefore, the total scatter detected S_T will be the sum of the scatter that gets through the walls S_{walls} and through the holes S_{holes}:

$$S_T = S_{holes} + S_{walls} \tag{4-5}$$

Properties that determine the transmission of these scattered rays through the grid are septal thickness, hole size, and grid height. A common factor used for estimating performance is the grid ratio, which is the ratio of the grid height L to the grid spacing d. Larger grid ratios provide better scatter rejection [146, 144].

Total transmission of scattered rays through a grid can be measured from scatter to primary ratios. The scatter to primary ratio α when no grid is present is the ratio of the number of scattered photons S to the number of primary photons P:

$$\alpha = \frac{S}{P} = \frac{T_S I_0}{T_p I_0} \tag{4-6}$$

T_S is the fraction of primary photons that turned into scattered rays, T_p is the fraction of primary rays that do not interact with the scattering material before being detected, and I_0 is the initial detected beam intensity before attenuation by any scattering material. Similarly, when the grid is placed in the beam, the scatter to primary ratio α_g has the following equation:

$$\alpha_g = \frac{S_g}{P_g} = \frac{T_{s,g}I_0}{T_{p,g}I_0} \tag{4-7}$$

where S_g is the number of scattered photons that were not rejected by the grid, P_g is the number of unattenuated primary photons, $T_{s,g}$ is the detected fraction of scattered rays, and $T_{p,g}$ is the fraction of primary rays that are detected from the initial beam intensity I_0. The ratio of these SPR values is as follows:

$$\frac{\alpha_g}{\alpha} = \left[\frac{T_{s,g}I_0}{T_{p,g}I_0}\right]\left[\frac{T_pI_0}{T_sI_0}\right] \tag{4-8}$$

The relative fraction of scattered rays f_s that are transmitted through the grid is equal to the ratio of $T_{s,g}$ to T_s. Rearranging Equation (4-9), f_s can be calculated using Equation (4-9):

$$f_s = \frac{T_{s,g}}{T_s} = \frac{\alpha_g T_{p,g}}{\alpha T_p} \tag{4-9}$$

The fraction $T_{p,g}$ / T_p is the transmission of incident primary rays through the grid, which depends on the fraction of the grid that does not attenuate any x-rays, or the open area fraction (OAF) of the grid. Equation (4-10) shows the OAF calculation for a grid with square holes.

$$OAF = \frac{d^2}{(d+t)^2} \approx \frac{T_{p,g}}{T_p} \tag{4-10}$$

From these equations, the total transmission of scattered rays through the grid prototypes was estimated using Equation (4-11).

$$f_s = \frac{\alpha_g}{\alpha}(OAF) \tag{4-11}$$

The results of the scatter transmission values for each grid are shown in Table 4-2, which were calculated from the SPR data plotted in Figure 4-5.

Table 4-2: Scatter Transmission

Grid Prototype	Scatter Transmission
Cu-1	26.3%
Cu-2	19.5%
W-poly	17.7%

4.3.1.1 Septal Penetration

Penetration through the walls of the grid will account for some fraction of the total transmitted scatter. Its contribution can be limited by selecting grid parameters that would allow only a small percentage of rays through based upon the photon energy and the geometric and attenuation properties of the grid. The walls of a focused grid become increasingly angled away from the center of the chest wall edge of the grid. As a result, each hole will have a slightly different geometry, depending upon its location in the grid. However, the walls of the grid will be nearly parallel to the photon path of the primary rays that pass through the spacing between these walls. To simplify the geometry, all calculations can be done on two central holes, which have nearly parallel walls to one another, and generalized to all of the other holes of the grid. For this simplified analysis, septal penetration calculations were performed similar to those of gamma camera collimators [147], which are grids with all lamellae parallel to one another.

Figure 4-7 is a diagram of a single scattered ray that travels from the top, right-most side of a grid hole, through a single wall, and then exits through the bottom, left-most side of an adjacent hole.

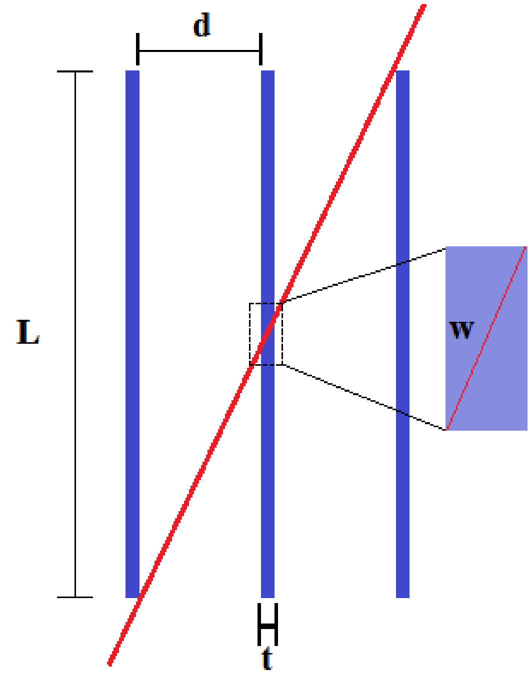

Figure 4-7: Schematic of the shortest path w a photon can make through a single wall of the grid. L is defined as the height of the grid, d is the spacing, t is the septal thickness.

If only looking at rays that are incident upon the walls of the grid, this scattered ray would be traveling through the least amount of grid material w in this trajectory. According to the Beer-Lambert law, the probability of the ray penetrating through the wall decreases exponentially with increasing wall thickness for a given grid material and photon energy as seen in Equation (4-12).

$$P_T = e^{-\mu_{grid} w} \tag{4-12}$$

P_T is the probability of the scattered photon transmitting through thickness w of the material of the grid with attenuation coefficient μ_{grid}. Here, w is calculated from similar triangles using grid height L, spacing d, and wall thickness t:

$$\frac{w}{t} = \frac{\sqrt{L^2+(2\mathrm{d}+\mathrm{t})^2}}{(2\mathrm{d}+\mathrm{t})} \tag{4-13}$$

The probability of transmission for the shortest path through the grid wall was calculated for each prototype for a photon with energy of 19 keV, which is the typical beam energy of the DMT system for the range of tube voltages used. The attenuation coefficient of copper and tungsten at this energy was interpolated from x-ray mass attenuation coefficients provided by NIST [148]. Table 4-3 summarizes the results of the septal penetration calculations.

Table 4-3: Attenuation Coefficients and Theoretical Septal Transmission

Grid Prototype	Height [mm]	w [mm]	μ(19 keV) [cm^{-1}]	Theoretical Septal Penetration
Cu-1	2.1	0.141	302.1	1.4%
Cu-2	3.85	0.209	302.1	0.18%
W-poly	3.6	0.198	694.2	0.00010%

Based upon this theory, scattered rays with a maximum energy of 19 keV would have essentially 0% transmission through the walls of the W-poly grid prototype. The results also show that better scatter rejection is possible with a higher grid ratio as seen in the decrease in penetration for the taller Cu-2 grid in comparison to the thinner Cu-1 grid.

4.3.1.2 Scatter Transmission through Grid Spaces

Since scattered rays do not have any preferential direction, it is very likely for scatter to go through the holes of the grid without being attenuated by the walls. Scattered rays originating from a wide range of directions can go through a grid hole if it scatters from a region that is open to the hole. This region can be defined by a cone angle φ, which is derived from the spacing and the height in equation (4-14).

$$\varphi = 2\tan^{-1}\left(\frac{d}{L}\right) \tag{4-14}$$

For larger cone angles, more scatter will pass through the grid holes. As the cone angle decreases, more scatter is blocked out for a fixed wall thickness. The inverse of the grid ratio goes into the cone angle equation, illustrating how larger grid ratios would improve scatter rejection.

Source to detector and breast to detector geometry affect how much scatter will go through the grid holes. If the fraction of detected scatter that makes it through the grid holes can be determined for the DMT system, a relationship between cone angle φ and grid ratio can be derived from the copper prototypes. A target cone angle can be determined from this relationship for the final full-sized grid from the maximum allowed scatter transmission through the holes. The total amount of detected scatter as a fraction of all scatter generated by the breast $f_{s,T}$ is the sum of the scatter fraction that gets through the holes $f_{s,holes}$ and through the walls $f_{s,walls}$:

$$f_{s,T} = f_{s,holes} + f_{s,walls} \tag{4-15}$$

The fraction of scattered rays that get through the grid spaces $f_{s,holes}$ can be estimated by subtracting the septal penetration values $f_{s,walls}$ in Table 4-3 from the scatter transmission values $f_{s,T}$ in Table 4-2. Table 4-4 shows the results for $f_{s,holes}$.

Table 4-4: Cone Angle and Scatter Transmission Fractions

Grid Prototype	Cone Angle [deg]	Total Scatter Transmission ($f_{s,T}$)	Septal Penetration ($f_{s,walls}$)	Hole Transmission ($f_{s,holes}$)
Cu-1	50.93	26.3%	1.4%	24.9%
Cu-2	29.12	19.5%	0.18%	19.3%
W-poly	31.05	17.7%	0.00001%	17.7%

A plot of $f_{s,holes}$ versus cone angle is shown in Figure 4-8 for just the 2 copper grids since the final full-sized grid will be made from copper. Moreover, since the W-poly prototype had many imperfections including extra material between spaces, the estimate of scatter transmission through the holes would be lower than for a grid without these artifacts.

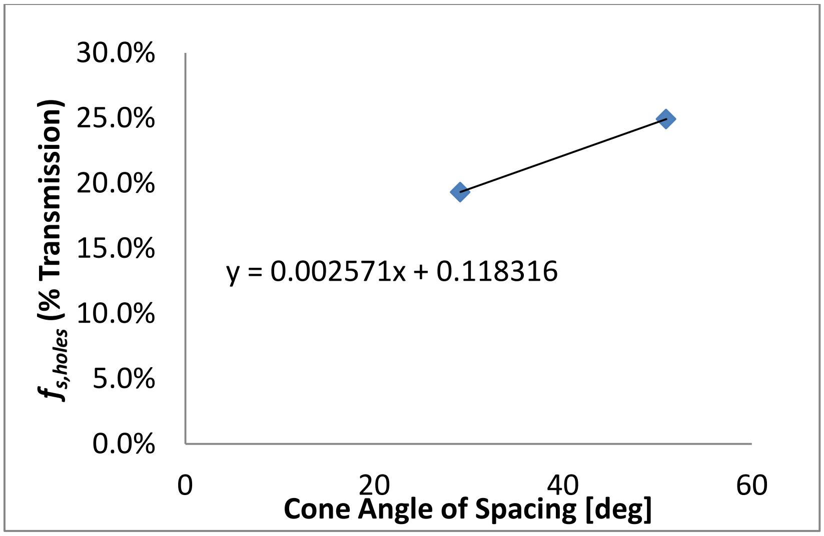

Figure 4-8: Transmission of scatter through the holes of the grid as a function of the cone angle formed by the spacing and height of grid holes.

A linear fit was applied to obtain a simple relationship between cone angle φ and scatter transmission through the grid spaces $f_{s,holes}$ as shown in Equation (4-16):

$$f_{s,holes} = a\varphi + b \tag{4-16}$$

Constants a and b from this linear fit have values of a = 0.002571 deg^{-1} and b = 0.118316. The y-intercept of the linear fit b would be expected to be nearly 0 for a 0º cone angle. This deviation from the expected can partially be attributed to an underestimation of septal penetration, which would raise the offset above zero. In addition, scatter that is created inside the detector housing [136, 127] would create errors in the estimation of the total scatter transmission through the grid, which would also increase the offset. Despite these errors, a grid with a grid ratio that is close to that of the Cu-2 grid should provide similar scatter rejection.

4.3.2 Selected Grid Parameters for DMT

The three main parameters of spacing, height, and septal thickness for the final full-sized grid were calculated by setting limits on scatter and primary transmission. A larger OAF of 85% was chosen to increase primary transmission. To maintain a high enough grid ratio for this larger OAF, a limit of L = 3 mm was placed on the height of the grid. Spacing d of the final grid was calculated using Equation (4-17) with L = 3 mm and a limit of $f_{s,holes}$ = 18.4%, which was the average of values of the Cu-2 grid and W-poly grids.

$$d = L \tan\left(\frac{f_{s,holes} - b}{2a}\right) \tag{4-17}$$

Next, the septal thickness t of the grid was calculated by solving for t from Equation (4-10) and using the calculated spacing d from the result of Equation (4-17). The final selected parameters and the total theoretical scatter transmission $f_{s,T}$ are given in Table 4-5.

Table 4-5: Parameters Selected for Full-Sized Grid

OAF	Height (L) [mm]	Spacing [mm]	Septal Thickness [mm]	Total Scatter Transmission ($f_{s,T}$)
85%	3	0.68	0.058	14%

Beam stop experiments and scatter characterization illustrate the potential improvement in DMT x-ray projection image quality with the inclusion of an anti-scatter grid. Further analysis is required to determine how the necessary radiation dose and final image quality would be affected by the presence of this grid.

Chapter 5

Anti-Scatter Grid Reciprocation

In addition to removing a portion of the scattered photons exiting the breast, anti-scatter grids also remove primary (non-scattered) photons. The missing primary photons result in an image of the high-attenuation components of the grid, superimposed on that of the breast. Stationary, ultra-high strip density linear grids with thinner walls and densities of 70 to 100 lp/cm were found to reduce the impact of grid wall shadows and improve visibility of microcalcifications for denser breasts [149]. However, these grids oftentimes led to an increase in radiation dose due to interspace material and increased wall density, along with decreased sensitivity to calcifications, which are important indicators of malignancy [150].

To minimize the image of the grid walls, grids are reciprocated (translated) in the left-right direction during the x-ray exposure. Hollis E. Potter found that every position on the detector must experience the same attenuation by the grid over the duration of the exposure, which can be accomplished by translating the grid at a uniform speed by some multiple of grid repeat distances [151]. The repeat distance r_d is thus defined as the distance measured in the direction of translation over which the pattern of the grid walls repeats [128]. For linear grids, the repeat distance is simply the grid pitch, or the sum of a wall and a space. Potter explained that the most effective method of blurring grid lines was to move the grid by at least 10 to 20 repeat distances for linear grids [151]. Therefore, the correct grid motion profile can blur the grid shadows enough to make them imperceptible in the image. Equation (5-1) shows the calculation for a constant grid reciprocation speed v_g for a given exposure time t_{exp} and a multiple N of grid pitches, assuming a constant x-ray fluence over t_{exp} for any given point on the imager.

$$v_g = \frac{N r_d}{t_{exp}} \tag{5-1}$$

Similar to linear grids, cellular grids also form artifacts in the image when kept stationary during exposure. Stationary, high frequency cellular grids have been proposed by Kim and Lee for digital systems where the grid wall artifacts can be removed through homomorphic filtering [152]. They explain that if a grid’s frequency, or the inverse of its pitch, is small in comparison to the sampling frequency of the detector, the grid will not remove any information from the object being imaged. Kim and Lee present an example of an imaging system with sampling frequency of 72 lp/cm whose optimal grid frequency would be 43 lp/cm. While this is an effective method for eliminating the possibility of artifacts, higher resolution systems with sampling frequencies of ~13 lp/cm would require much higher frequency cellular grids than may be readily available.

5.1 Reciprocating Focused 2D Grids

Blurring by reciprocation is relatively straightforward for 1D grids where grid motion is perpendicular to the direction of the strips, enabling the posterior edge of the grid to extend beyond the posterior edge of the field of view of the detector throughout the exposure. In contrast, the 2D nature of the holes (usually square in shape) of cellular grids make removal of the grid image via reciprocation more challenging. Cellular grids must also be moved by a specific distance in order to uniformly reduce the fluence to every point on the detector. However, if the grid walls were oriented to be parallel to the translation direction, dark bands would form in the image where only the shadows of the parallel walls fall on the detector as illustrated in Figure 5-1.

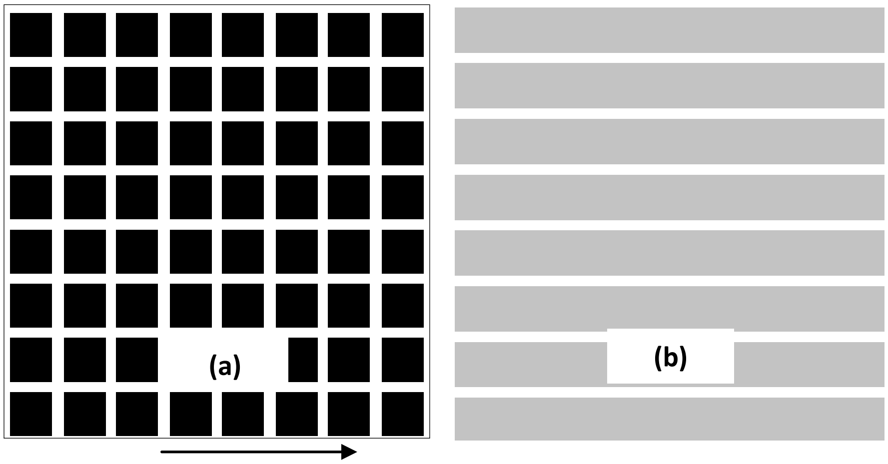

Figure 5-1: Schematic of how reciprocating a 2D grid whose lines are parallel to the direction of motion would form streaking artifacts. (a) is an attenuation map of the 2D grid and (b) is the resulting image where detector pixels beneath the horizontal walls are covered over the entire exposure. In this color scheme, darker pixels represent areas of lower attenuation.

For this reason, the square hole matrix of 2D grids is typically rotated by an angle φ so that left-right translation is not parallel to the direction of any walls. There must also be a repeating pattern in the grid for all points on the detector to witness the same attenuation by the grid. Unlike linear grids where the repeat distance is equal to the grid pitch, cellular grids have repeat distances that are not as straightforward. The lamellae of square grids are periodically spaced in two orthogonal directions. In order for a repeat pattern to be created, Pellegrino et al. explain that an integer number of pitches must be translated in both grid dimensions [153]. A repeat distance can then be calculated as shown in Equation (5-2) from integers n and m that correspond to numbers of grid pitches p in the two orthogonal directions of the grid matrix.

$$r_d = p\sqrt{m^2 + n^2} \tag{5-2}$$

An example of a rotated grid with m = 4 and n = 5 is shown in Figure 5-2, which has a pattern of walls and spaces that repeats every $r_{d.}$

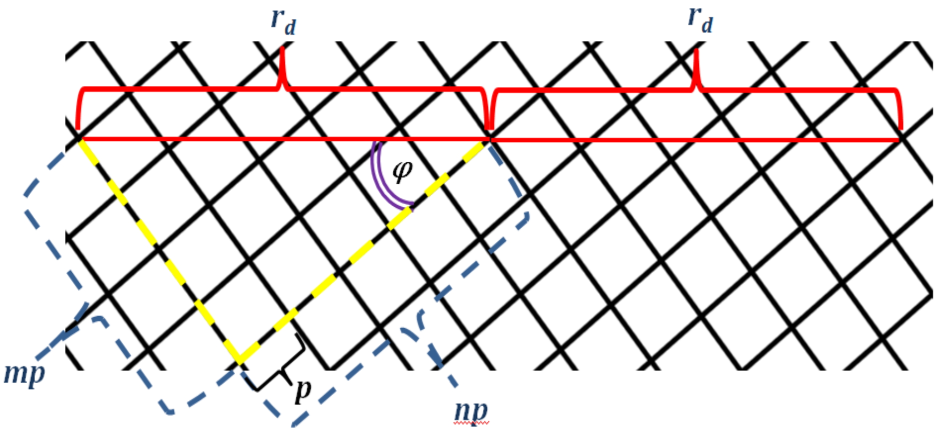

Figure 5-2: Schematic of a cellular grid with rotation angle φ illustrating the distance in the direction of translation over which the grid pattern repeats. The repeat distance is a function of integers m and n and the grid pitch p, which determines the rotation angle of the grid φ.

A right triangle is formed from the repeat distance and the walls with lengths mp and np as shown. Integers n and m can then be used to define a grid rotation angle φ as shown in Equation (5-3).

$$\varphi = \tan^{-1}\left(\frac{m}{n}\right) \tag{5-3}$$

For the case of $m = n$, a 45º grid rotation angle is formed, and the repeat distance is then simply $\sqrt{2}p$. Similar to Hollis Potter's findings, Pellegrino et al. also explain that the more grid lines that are traversed, the less precise the motion of the grid would have to be, leading to less artifacts in the image [153]. Therefore, for the case of $\varphi = 45°$, the grid must be translated by multiple repeat distances. However, Pellegrino et al. also explain that a 45º angle of rotation would lead to bright streaks in the image where the attenuation by the aligned intersections of the grid would be lower than that of the walls adjacent to these intersections because the amount of material at the intersections that covers the detector is nearly half of that covered by the sum of the adjacent walls [153].

Figure 5-3 illustrates this formation of bright streaks caused by the grid using an image of a portion of a grid where $m = n$. Figure 5-3(a) is an attenuation map of the grid where non-zero pixel values indicate attenuating material and zero pixel value indicates air interspaces.

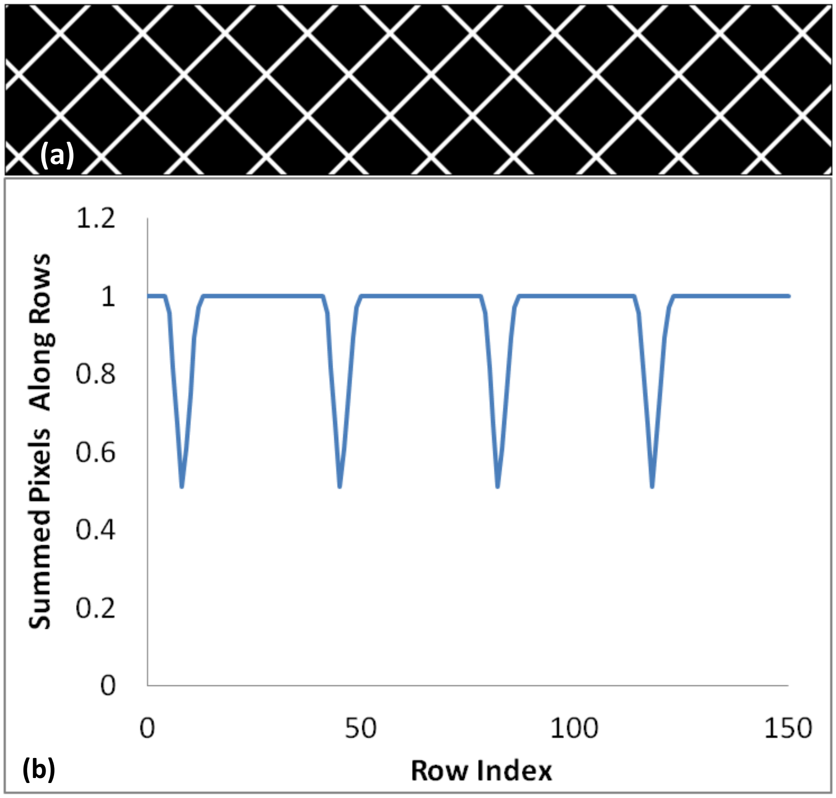

Figure 5-3: Example of the attenuation by a grid with a rotation angle of $\varphi = 45°$ (a) attenuation map of the grid walls where non-zero pixel values show presence of attenuating material and zero pixel values show air interspaces. (b) is a plot of the sum of pixel values along the rows of the image in (a) versus the row index, which indicate attenuation experienced by a given detector pixel. Sums were taken over a length of ten repeat distances where $r_d = \sqrt{2}p$.

Ten repeat distances are included in the image. Results of summing the pixels through this grid image along the rows of the image matrix simulate the total attenuation that would be experienced by a given detector element beneath the grid shown in Figure 5-3(a) moving at a uniform speed. The total normalized attenuation by the grid can then be plotted versus the index of the row to simulate the attenuation seen by a column of detector elements as is shown in Figure 5-3(b). Dips in the plot of Figure 5-3(b) show where the detector would see more primary rays due to the lower attenuation of the intersections described by Pellegrino et al. [153].

Cha-Mei Tang describes a way of remedying these brighter bands by placing additional material at the intersections to increase the attenuation at these locations [154], which would remove the valleys seen in the plot of Figure 5-3(b). Another method of reducing these fluctuations, as presented by Pellegrino et al., is to use a rotation angle that is slightly offset from 45º such that less of the intersections are aligned along the direction of translation [153]. Values of n and m suggested by Pellegrino et al. ranged from $m = 9$, $n = 1$ to $m = 9$, $n = 8$, which would result in values of $r_d$ranging from approximately $9p$ to $12p$. Because the number of grid lines that covers each detector element would be sufficiently large at these values of n and m, these grids would only need to be translated by a single repeat distance [153].

Figure 5-4(a) is an example of a grid with $m = 9$, $n = 8$, or $\varphi = 48.4°$. Figure 5-4(b) is a plot of the estimated attenuation that a column of detector elements would experience as a function of the row index similar to Figure 5-3(b). This choice of n and m notably reduces the non-uniformity in fluence to the detector along a column of pixels, indicating a lower probability of seeing bright band artifacts in the final image. The additional material as described by Tang [154], which would create “bowties” at the intersections of these grids, would reduce the remaining non-uniformities further. The grid prototypes described in the previous chapter have n = 12 and m = 13 and bowties at their intersections.

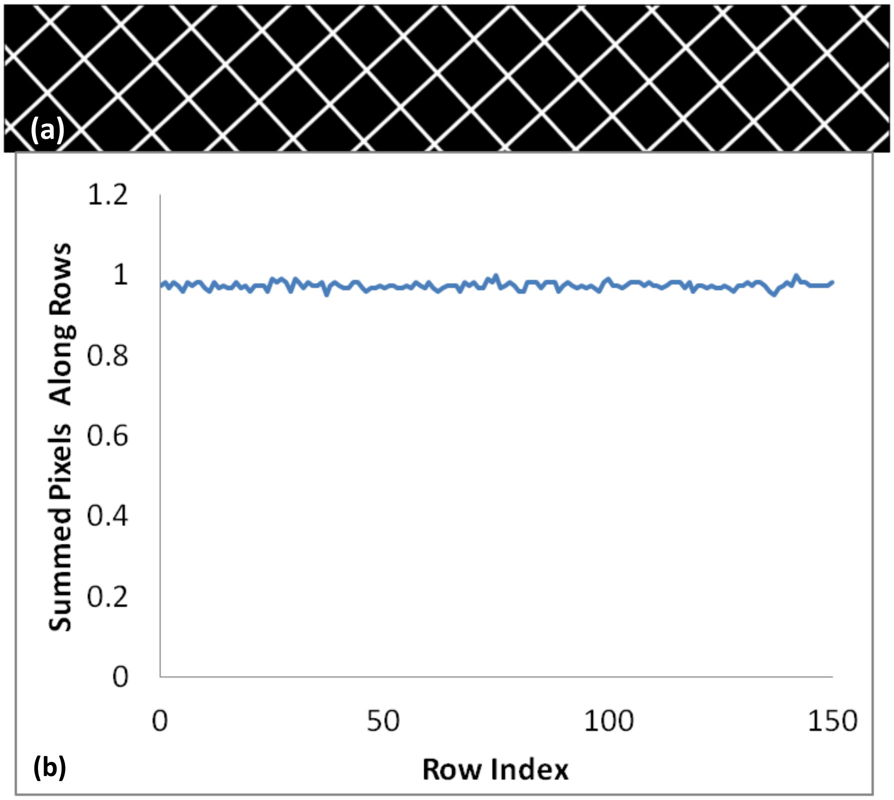

Figure 5-4: Example of the attenuation of a grid with a rotation angle of $\varphi = 48.4°$ (a) mapping of the attenuation by the grid walls where non-zero pixel values show attenuating material and zero pixel values show air interspaces. (b) plot of the sum of pixel values along the rows of the image in (a) versus the row index over a length of one repeat distance where $r_d = 12p$.

5.2 Shift-and-Twist (ST) Motion Scheme

In digital x-ray imaging systems, the utilization of a grid not only reduces the amount of scattered radiation reaching the detector, but also the amount of primary radiation. Attenuation of primary photons makes images look grainier, leading to lower detectability of suspicious structures. X-ray exposure to the breast is typically increased in order to compensate for the lost signal at the detector, thereby increasing breast radiation dose [9]. Thus the change in detectability due to the introduction of a grid depends on the relative reduction in signal (primary) and noise (scatter) photons.

To maximize primary transmission through a focused 2D grid, the distance between the x-ray focal spot (XFS) and grid focal point (GFP), as described in Chapter 4, should be minimized over the entire x-ray exposure, which is not the case for conventional planar grid reciprocation. For alignment of the XFS and GFP throughout grid motion, the grid trajectory would ideally be such that the grid's midpoint at its posterior edge traveled along an arc of a circle whose center is located at the XFS and whose radius is equal to the grid focal distance. In this trajectory, each point along the grid's edge would trace out a circle. The largest circle would be traced out by the corners of the grid, the radius of which is equal to the distance between the corner and the GFP.

In a coordinate system where the XFS is located at the origin at a focal distance h above the grid, the curve traced out by a corner of the grid along the chest wall edge of the grid can be defined as in Equation (5-4).

$$z = -\sqrt{(h^2 + {w_{grid}}^2) - x^2} \tag{5-4}$$

The x-coordinate corresponds to the direction that is parallel to the chest wall edge and is the location of the corner of the grid as it moves during the exposure. The z-coordinate represents the dimension that is perpendicular to the detector surface, and w_{grid} is half the width of the grid. Grid corner motion is constrained to travel within the interval of $\left[w_{grid} - \frac{r_d}{2}, w_{grid} + \frac{r_d}{2}\right]$ where r_d is the repeat distance of the grid. Since grid motion repeat distances of the order of centimeters are small in comparison to the large focal spot-to-detector distances typical of x-ray breast imaging (60 to 80 cm), the ideal arc trajectory traced by the corners of the grid can be well approximated by a straight line trajectory tangent to these arcs which would have the following slope values:

$$m = \begin{cases} \frac{-w_{grid}}{h}, & x < 0 \\ \frac{w_{grid}}{h}, & x > 0 \end{cases} \tag{5-5}$$

To achieve this, one edge of the grid can be driven along a flat surface oriented at an angle θ with respect to the detector surface, while the opposite non-driven edge of the grid is constrained to track along a second flat surface oriented at an angle $\pi - \theta$ where θ is defined in Equation (5-6).

$$\theta = \tan^{-1}(\frac{w_{grid}}{h}) \tag{5-6}$$

Figure 5-5 illustrates graphically an example of the trajectory of the right-most corner of a focused grid as viewed from the patient's perspective for three different motion schemes. The origin of the coordinate system in the plot represents the location just above the midline of the detector where the midline of the grid surface would be located when the GFP and XFS are both in the same point in space. In the presented example, the anti-scatter grid has a width of 32 cm, a focal distance of 80 cm, and a 2.5 cm repeat distance. The dotted plot shows the ideal arc trajectory traced by the grid's right corner when XFS and GFP are always kept aligned during reciprocation. This arc has a radius equal to the distance between the GFP and the grid's right-most corner. The solid line with diamonds shows a line that is tangent to the point along the arc where the grid midline overlaps the detector midline. The angle of inclination θ of the line for the given example is 11.3°. This angle will vary depending upon the grid focal distance and the selected transverse point at which the grid is driven. For the small 2.5 cm repeat distance, the tangent line approximates well the ideal arc trajectory as seen by more overlap between these two curves than for the translation-only case.

Since the described motion is along straight lines, it is possible for a linear positioning stage that is mounted in the same orientation at the angle θ to drive the motion of the focused grid. However, it is necessary for the proposed design to have an extra degree of freedom that allows the GFP to be oriented towards the XFS as the grid is driven by the linear stage. The system would allow the grid to twist towards the focal spot as it is shifted along the inclined surfaces. This scheme will be referred to as a shift-and-twist (ST) motion.

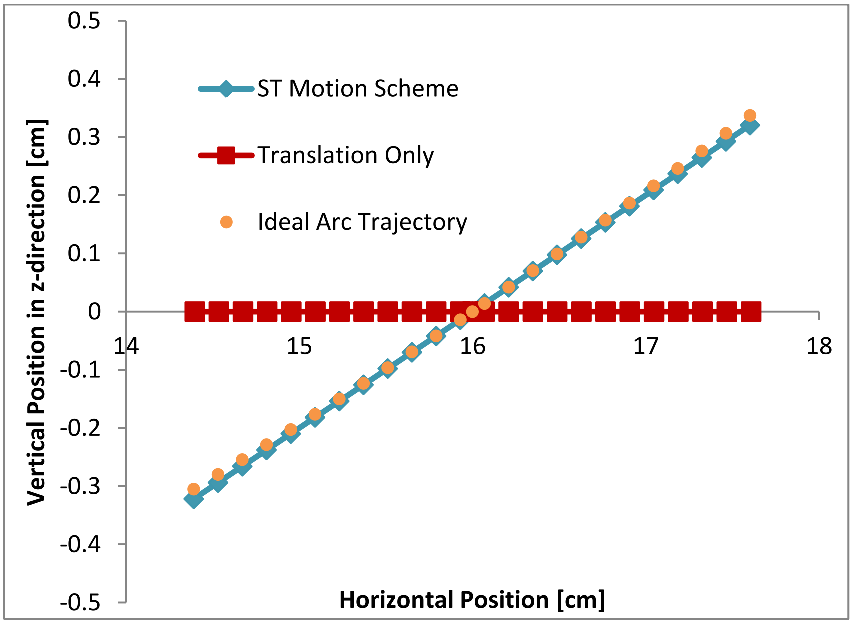

Figure 5-5: Trajectory of right-most corner of grid as viewed from patient's perspective for three different motion schemes. The dotted plot shows the ideal trajectory of the grid such that the x-ray focal spot (XFS) and grid focal spot (GFP) are always aligned. The solid line with diamonds shows a line tangent to the arc traced out by the right corner of the grid in the ideal trajectory at the point where the grid surface has a zero degree orientation with respect to the x-ray detector surface. The trajectory with translation only is shown with square symbols along a solid line.

5.3 Reciprocating Grid Prototype

To test the efficiency of the ST motion scheme, an embodiment of the ST design has been built, installed, and tested on the DMT scanner. The drawings for the design are provided in Appendix B. Primary transmission through a 2D focused copper anti-scatter grid prototype (the Cu-2 grid described in Chapter 4) reciprocated by the ST motion scheme was compared to the case where maximum primary transmission is achieved through the grid prototype as in the case when the grid is stationary and the XFS and GFP are aligned over the entire exposure.

5.3.1 Image Acquisition

All images were taken with the detector in high-sensitivity (HS) mode [126]. The focused 2D anti-scatter grid prototype used for these experiments was stack-laminated by Mikro Systems, Inc from copper. The grid holes are square. Hole size, septal thickness, and grid height are 1 mm, 0.1 mm, and 3.85 mm, respectively. The prototype grid has an active area of 17 cm x 26 cm and a focal distance of 80 cm. The grid rotation angle is 47^{o} and has a repeat distance r_d of 19.8 mm. A voice coil motor, manufactured by H2W Technologies, Inc., was used for grid reciprocation. The exposure time t_{exp} was 500 ms for all acquired images. The positioning stage was programmed to provide an approximately constant speed over the duration of the exposure, which was calculated from Equation (5-1). All image analysis was done using ImageJ.

Code written in C# by the x-ray detector manufacturer was modified to incorporate the HMP and grid reciprocation system into DMT DBT acquisitions. Grid motion was initiated just before the generator was triggered and just after the detector integration window was opened so that the grid could accelerate up to the correct speed just before the exposure. Appendix C contains the code for making grid-in acquisitions with the HMP described in Chapter 2.

5.3.2 Alignment of XFS and GFP

Figure 5-6 illustrates the distance between the XFS and the GFP as a function of the transverse distance that the midline of the grid is moved away from its aligned orientation during an x-ray exposure for the three motion schemes presented in Figure 5-5. The distance between XFS and GFP for the ideal case is shown with circles, the ST motion design is shown with diamonds, and that of the conventional, translational-only scheme is shown with squares. In this plot, the center at 0 cm along the x-axis corresponds to the one point during the grid's motion where the grid midline and detector midline overlap. This plot illustrates better alignment of XFS and GFP in the ST motion scheme where the grid edge is driven along the flat surface inclined at angle θ rather than in the translation-only configuration. In theory, this better alignment should allow for greater primary transmission through the grid during reciprocation over the translation-only design.

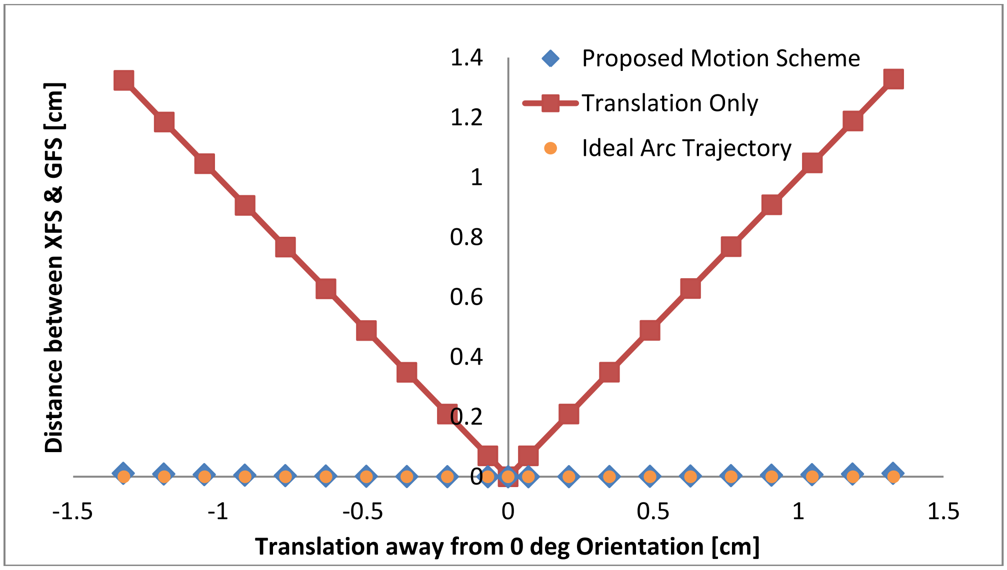

Figure 5-6: Distance between XFS and GFP during an x-ray exposure as a function of the distance the grid is moved away from the orientation where grid midline and detector midline overlap. The distance between XFS and GFP for the proposed ST design is shown with diamonds, and that of the translational-only scheme is shown with squares. The ideal trajectory is shown with circles. For maximum transmission of primary x-rays the distance between XFS and GFP should ideally be 0 over the entire x-ray exposure.

5.3.3 Primary Transmission of Copper Grid Prototype

The primary transmission of the reciprocating grid was measured by comparing images acquired with the grid in the beam to images acquired using the same techniques but without the grid prototype in the beam. To measure the maximum achievable efficiency of the grid prototype, the primary transmission through the stationary grid was also calculated. The stationary grid was oriented such that the XFS and GFP were both aligned for maximum primary transmission throughout the exposure, simulating the ideal arc trajectory case. There was no compression paddle or breast support present for these images. To ensure a linear detector response to input fluence in HS mode and avoid detector pixel saturation, tube paramaters of 28 kV and 2.5 mAs were used. Five consecutive images were acquired at a projection angle of 0° for both grid-in and grid-out acquisitions. Images were corrected for dark current but were not flat-field corrected.

Two rectangular regions of interest (ROIs) were drawn over the images. The first ROI consisted of a 300 x 300 pixel^2 area beneath the focal spot projection of the x-ray source on to the detector. The second ROI included a 2100 x 2900 pixel^2 area of the image that was covered by just the moving active area of the grid. To calculate primary transmission T_P through the grid, the mean pixel values within these two regions of the grid-in images were divided by the mean pixel values within the same regions in the grid-out images. To account for any changes in tube output from one exposure to the next, a factor α was calculated as described by Fetterly and Schueler [126] and as shown in Equations (5-7) and (5-8)

$$T_P = \alpha \overline{R_{grid-in}} \Big/ \overline{R_{grid-out}} \tag{5-7}$$

$$\alpha = \left(\overline{R_{Bkg,grid-out}} / \overline{R_{Bkg,grid-in}}\right) \tag{5-8}$$

Since the grid is smaller than the active area of the x-ray detector, there is a region of the detector that is not covered by the grid or its border. This background region where the grid-in ROI $R_{Bkg,grid-in}$ is drawn should have about the same mean value $\overline{R_{Bkg,grid-in}}$ as the mean value $\overline{R_{Bkg,grid-out}}$ in the background of the grid-out image $R_{Bkg,grid-out}$. These equations were used to calculate the primary transmission for both ROIs.

Figure 5-7 shows the images acquired for calculation of T_P. Figure 5-7(a) is an example of a grid-out projection image. The stationary grid-in image is shown in Figure 5-7(b), and the reciprocated grid-in image is shown in Figure 5-7(c). Each panel in Figure 5-7 has three boxes to illustrate where ROIs were drawn for determining primary transmission. The box with solid lines connected by squares shows the ROI used for calculating the primary transmission beneath the XFS projection, and the dashed line shows the ROI drawn for calculating T_P for most of the grid active area. A background ROI for calculating α in Equation (5-8), which accounts for any variation in tube output, is shown by the solid box on the left side of each image.

Table 5-1 contains the results of the calculations of the primary transmission under the focal spot projection and over the grid active area calculated using Equations (5-7) and (5-8). R_{FS} is the ROI under the focal spot projection onto the detector, and R_{Full} is the ROI that covers the majority of the active area of the moving grid.

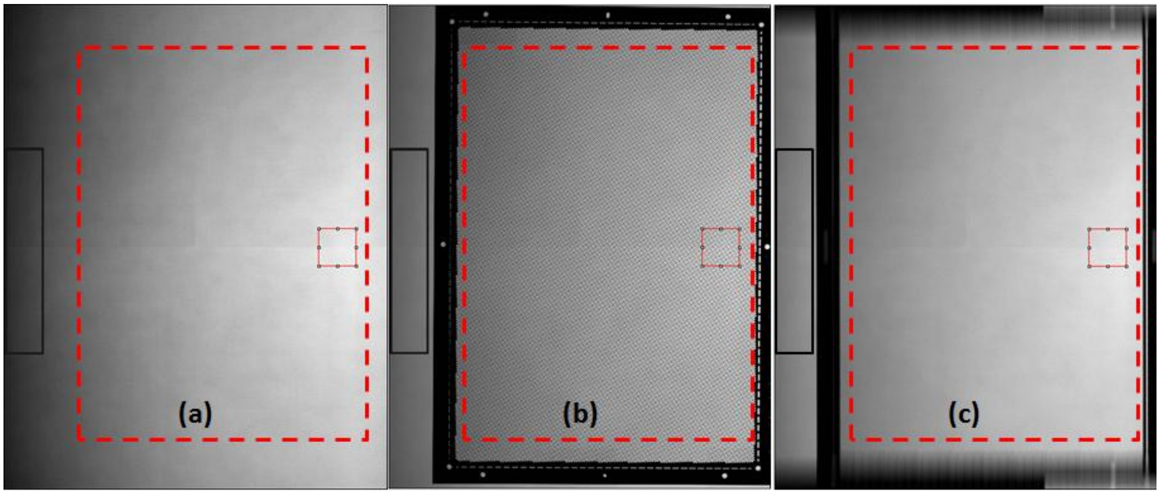

Figure 5-7: Zero-degree projection images acquired with (a) nothing in the x-ray beam, (b) with the stationary grid prototype aligned with the XFS for maximum primary transmission, and (c) with the grid prototype moving with the described ST motion scheme. ROIs were drawn for determining primary transmission below the focal spot (solid lines connected by squares) and over the full active area of the moving grid (dashed line) as well as the background ROI (solid box) for calculating α in Equation (5-8).

Table 5-1: Primary Transmission

	T_P of R_{FS}	T_P of R_{Full}
Stationary Grid	74.5%	74.2%
Moving Grid (ST Motion)	73.5%	72.2%

Transmission values in Table 5-1 show that there is an overall 2% reduction in transmission when reciprocated by the ST motion scheme as compared to the maximum transmission case. With the grid parameters of the full-sized grid described in Chapter 4, higher primary transmission may be possible given a smaller grid height of 3 mm and a larger open area fraction (OAF) of ~85% as opposed to the ~83% of the grid prototype. Despite promising results illustrating the feasibility of the ST motion scheme, grid line artifacts appeared in the projection images. Analysis of the lines and methods of their removal are discussed in the next sections.

5.4 Residual Grid Line Artifacts (GLAs)

Large variations in fluence rate by a non-uniform x-ray beam would cause a non-uniform distribution of the attenuation experienced by all pixels of the detector, thereby increasing the likelihood of grid line artifacts (GLAs). However, data from the MagicMax meter in Chapter 2 show that the DMT x-ray beam is fairly uniform over the entire exposure. With less than 1.5% fluctuation in the fluence rate of the DMT tube, there is less of a chance that GLAs will result from large variations in tube output.

The other factor that affects GLA presence is grid motion. To limit the presence of potential GLAs, the speed at which the grid was reciprocated was optimized using image analysis. The magnitude of the presence of GLAs in a given image can be measured from its 2D image power spectrum (PS) [111] [155, 156]. The presence of grid lines in a region of interest (ROI) of a projection image *I* can be seen as peaks in its 2D PS calculated as shown in Equation (5-9) from the 2D fast-Fourier transform (FFT).

$$PS = 10 \cdot log_{10}(|FFT(ROI)|^2) \tag{5-9}$$

Because of the grid’s distinct pattern and pitch, peaks in the PS resulting from grid artifacts can be found at integer multiples of the spatial frequency corresponding to the grid pitch.

Image analysis was done using ImageJ. PS are calculated and displayed in ImageJ by 2D 8-bit images [157] where the pixel intensities within the image are proportional to the amplitudes of points in the spectra at frequencies specified by the location of the pixel in the image matrix. Dimensions of the PS were determined by the size of the ROI chosen. The frequency axes of the PS matrix cover a range from +Nyquist to –Nyquist frequency with the center of the image being the origin [157]. Since all detector elements of the 2923MAM are square, the Nyquist frequencies for both axes of the 2D PS are equal. Therefore, the spatial frequency of a given point in a square PS image can be calculated by dividing the point's distance from the origin by half the width or height of the PS image and then multiplying by the Nyquist frequency.

Despite adjustment of grid speed to minimize the appearance of grid lines, GLAs were not completely removed from the image PS. Because grid motion in the presented design scheme is not confined to a single plane, all detector elements will not witness the same coverage by the septa and spacing of the grid. X-rays travel through a varying fraction of the walls as the grid surface twists towards the XFS. As a result, GLAs manifest in the projection images even after speed optimization.

5.4.1 Characterizing Grid Line Artifacts in Projection Images

For analysis of grid-line artifacts, studies were performed using two phantoms. The first phantom was a 2.5 cm uniform block of acrylic covering the full field of view (FOV) of the detector. The second phantom consisted of four 1 cm slabs of the CIRS Model 020 BR3D (will be referred to as BR3D) [158] to create a 4 cm phantom simulating a breast composed of approximately 50% glandular and 50% adipose tissue. Features simulating calcifications (speck groups), masses, and fibers were embedded within one of the four slabs. This second phantom was selected to assess how noticeable GLAs would be given a real human breast that typically has many overlaying complicated structures and patterns. Two projection images were acquired of each phantom at 0^o with respect to the direction of compression. The first was acquired without any form of scatter rejection. The second image was acquired with the copper prototype grid in the beam reciprocated by the ST motion. All images were acquired with the phantoms placed on the breast support and compressed by the compression paddle. Phantom position and exposure techniques were kept fixed for both grid-in and grid-out acquisitions for a given phantom. Dark current subtraction and flat-field correction (FFC) were performed on all images. The grid was not present during the acquisition of the FFC images (FFCIs).

Figure 5-8(a) shows a 512 x 512 pixel^2 ROI of a projection image of the 2.5 cm uniform acrylic phantom without any scatter rejection. Figure 5-8(b) shows the same phantom imaged with the reciprocating grid. Obvious GLAs can be seen in the grid-in image of Figure 5-8(b), which present as peaks in the PS shown in Figure 5-9.

Because of the grid rotation angle and pitch, peaks in the PS that result from grid artifacts can be found at specific locations within the PS. Since the grid prototype has a rotation angle of 47^o and has square holes, the grid peaks in the PS that correspond to the grid line artifacts are approximately at the same angle with respect to one of the frequency axes. In Figure 5-9(b) the distance from the center to the first grid peak along the 47^o angle away from the horizontal axis is 35 pixels, which is at a frequency of approximately 0.9 mm^{-1}, consistent with the 1.1 mm pitch of the grid prototype (0.91 mm^{-1} frequency). Peaks at higher frequencies away from the center were confirmed to be higher harmonics of this frequency. The peaks that are close to the x-axis can be attributed to the bowtie intersections of the grid prototype.

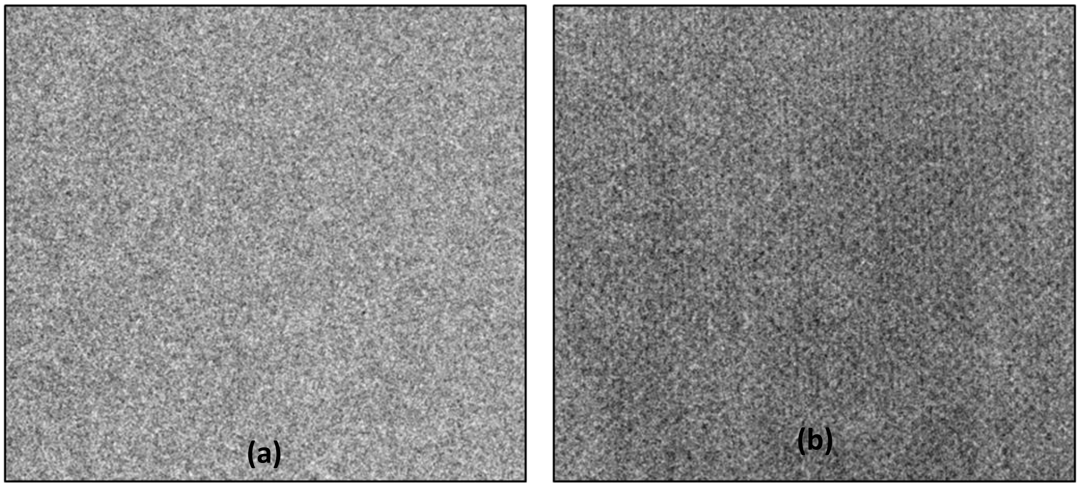

Figure 5-8: Close-up of 0º projection view of acrylic phantom (a) without the grid and (b) with the reciprocating grid. The grid was reciprocated in a direction that goes from the bottom to the top of the image.

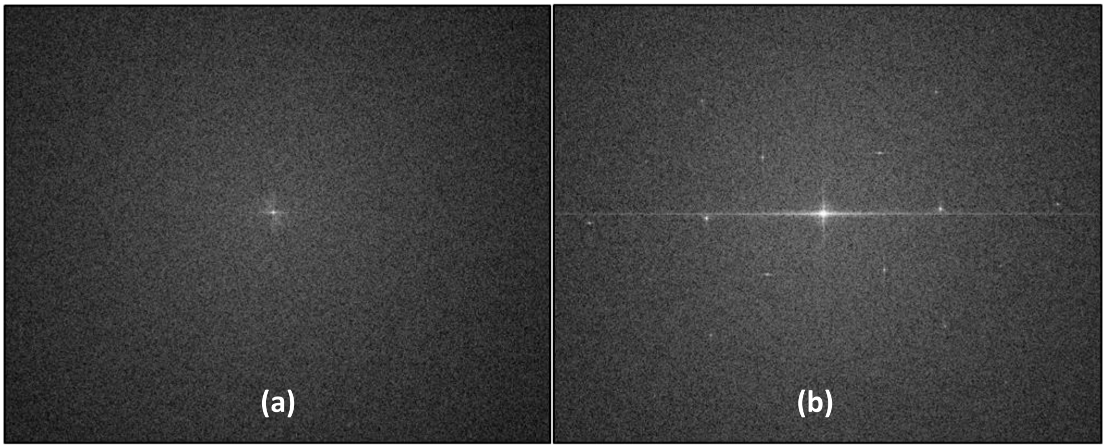

Figure 5-9: Close-up view of power spectra (PS) of the images shown in Figure 5-8 for the (a) grid-out and (b) grid-in projection. PS images have the same 512 x 512 pixel dimensions as the ROIs of Figure 5-8

Figure 5-10 shows the breast-simulating phantom (a) without and (b) with the reciprocating grid. The red square in the figure shows the ROI drawn for calculating the PS of a 512 x 512 pixel^2 region. Close-up views of these ROIs are shown in Figure 5-11, and Figures 5-12(a) and (b) are the PS of the grid-out and grid-in ROIs, respectively.

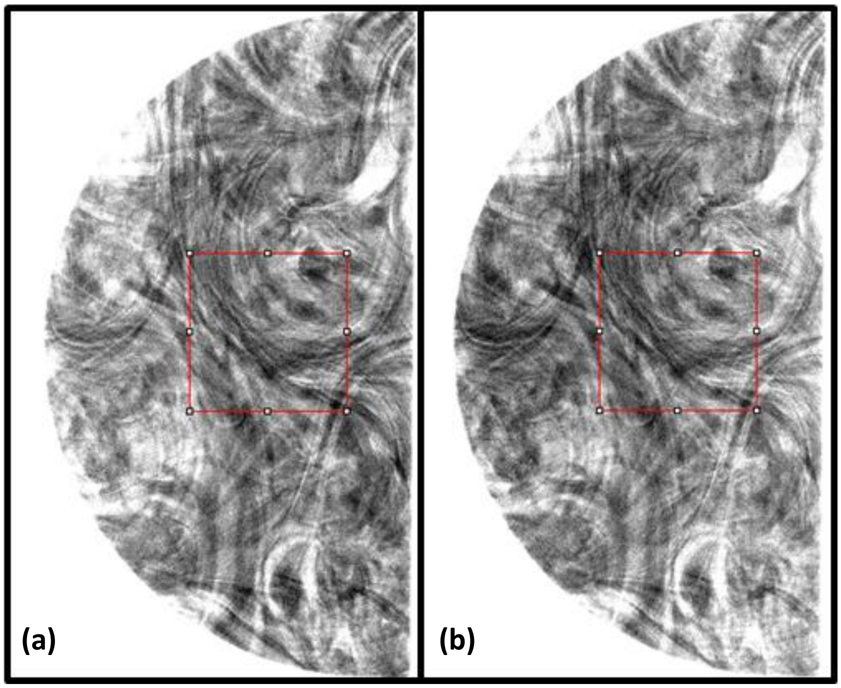

Figure 5-10: Projection view of BR3D phantom (a) without the grid and (b) with the reciprocating grid in ST motion. A red square shows where the ROI was drawn for calculating the PS. In projection images, the color scheme is inverted so that higher attenuation is displayed as darker gray.

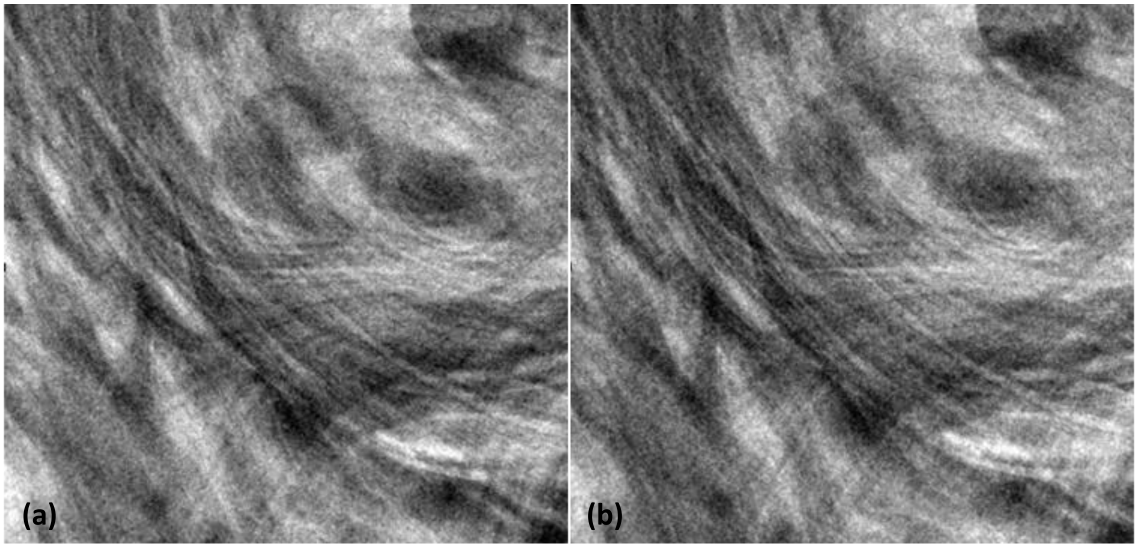

Figure 5-11: Close-up view of BR3D phantom (a) without the grid and (b) with the reciprocating grid. Both sets of projection images were corrected with the same grid-out FFCI.

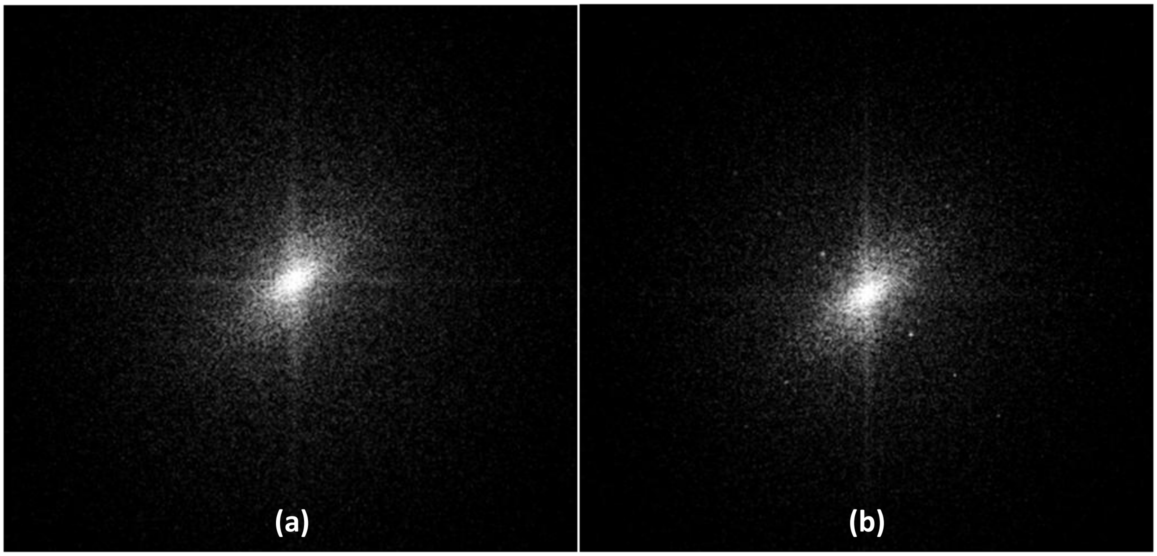

Figure 5-12: PS of the images shown in Figure 5-11 for the (a) grid-out and (b) grid-in projection. PS images have the same 512 x 512 pixel dimensions as the ROIs of Figure 5-11. Peaks in the grid-in PS caused by GLAs can be seen at a 47º angle with respect to the horizontal axis.

The higher frequency GLAs are not as conspicuous in the BR3D phantom as they are in the uniform acrylic phantom. This can be seen by the relative amplitudes of the grid peaks in the PS of the two grid-in phantom images. Not only is there more scattering material, there is also more structure within the BR3D, which makes the higher-harmonic GLAs less noticeable.

This grid pattern is not uniform over the entire projection. To show how the walls of the grid look slightly different depending upon the location of the detector over which they project, Figure 5-13 shows the PS of the full images of Figure 5-10. There are many more peaks seen in the PS of both grid-in and grid-out images. The peaks in the grid-out image are caused by the detector housing itself which contains a honeycomb pattern as shown in Figure 5-14. When the detector is saturated at high exposures, as in the case where there is no attenuation of incident rays outside of the BR3D phantom, this pattern appears as a result of the flat field correction (FFC). The ROI size and location for the

BR3D were chosen so that the grid peaks could be more easily detected in the PS since all of the structures within the phantom and the detector pattern outside of the phantom make it difficult to pick out the grid peaks. Also, because grid motion is not confined to a single plane, different portions of the detector see different fractions of the grid pitches, creating minor streaks through the points in the PS of Figure 5-13(b).

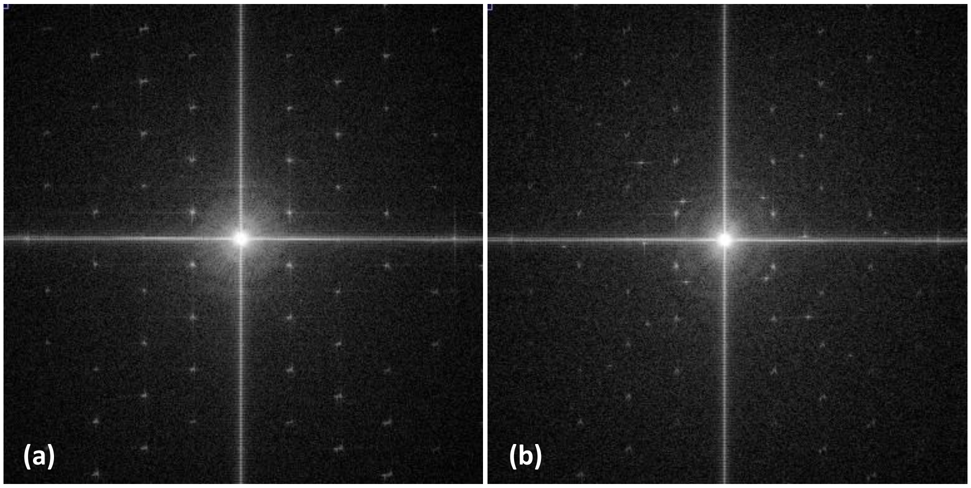

Figure 5-13: Close-up view of the PS of the (a) grid-out and (b) grid-in projection images in Figure 5-10. Peaks in the grid-in PS caused by GLAs can be seen at a 47° angle with respect to the horizontal axis. The remaining peaks seen in both grid-in and grid-out images are attributed to artifacts created by flat-field correction when the detector is saturated.

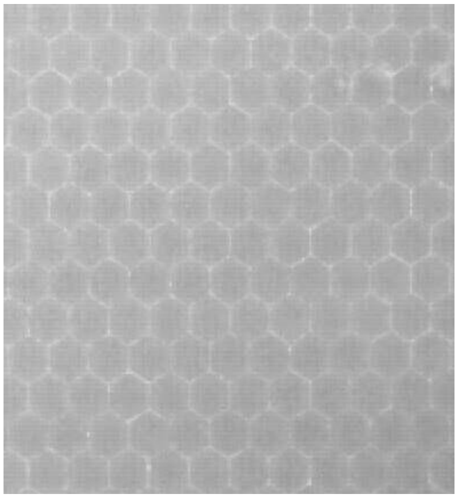

Figure 5-14: Close-up view of the saturated portion of the image just outside of the BR3D phantom showing a honeycomb pattern, which is a part of the detector's housing.

5.4.2 Flat-Field Correction of GLAs

As illustrated by Figure 5-14, there are fixed patterns within the raw projection images acquired by the x-ray detector which must be processed before image reconstruction. DMT DBT images are first dark-subtracted and then flat-field corrected. Dark subtraction involves removing the pixel value offset created by the dark current inside the detector in the absence of x-rays. FFC processes out patterns that are fixed from one projection to the next that would otherwise create artifacts in the final image [113]. For a DMT DBT FFCI, seven images are acquired of the uniform 2.5 cm acrylic phantom. The median pixel values from these seven images for a given detector element are used to create a single FFCI I_{FFCI}. Equation (5-10) shows how the final processed projection image I_{final} is obtained after the dark-subtracted raw image $I_{ds,raw}$ is corrected by the FFCI.

$$I_{final} = \frac{I_{ds,raw}}{I_{FFCI}} \cdot \overline{I_{FFCI}} \tag{5-10}$$

The fixed patterns are divided out of the raw image and then the result is multiplied by the mean value of the FFCI $\overline{I_{FFCI}}$ to correctly calibrate the gain of each pixel. One such example of a fixed pattern is the honeycomb pattern created by the carbon fiber housing of the x-ray detector. This method can also be applied for correction of the GLAs from the projection images if they are consistent form image to image.

Appraisal of the effectiveness of FFC in correcting GLAs was done by using the same phantoms and correcting the acquired images by the described method. Two sets of FFCIs were acquired, one set with the grid in and a second set without the grid. For both grid-in and grid-out, the FFCIs were created by combining seven consecutive exposures of the 2.5 cm acrylic block placed directly on the 1.2 mm thick carbon fiber breast support whose surface was approximately 11 cm below the bottom surface of the polycarbonate compression paddle. All images were acquired at a 0º projection angle. Three image sets were generated each for the uniform phantom and the BR3D phantom from the grid-in and grid-out phantom projections and the two FFCIs. The first set consisted of grid-out data corrected with the grid-out FFCI. The second data set was of the grid-in projections corrected with the grid-out FFCI to intentionally create the worst potential GLAs. Lastly, grid-in data was corrected with grid-in FFCIs.

Image PS were obtained from projection views of the acrylic and breast phantoms. Effectiveness of the flat-field correction method was tested by comparing 1D profiles that were drawn through the 2D PS along the line in frequency space upon which the GLA peaks lay. The line was determined from the spectrum of the data set in which the peaks were easily identifiable because they were derived from grid-in projections corrected by grid-out FFCI.

Figure 5-15 contains the 0º projection view of the uniform acrylic phantom. Figure 5-15(a) is the grid-out image corrected by the grid-out FFCI, (b) is the grid-in image corrected by the grid-out FFCI, and 5-15(c) is the same grid-in projection corrected by the 0º grid-in FFCI. Figure 5-16(a) shows the PS of the grid-out image, and Figures 5-16 (b) and (c) are the PS for Figures 5-15 (b) and 5-15 (c), respectively. Figure 5-17 contains profiles through the 2D PS images along the line where peaks were found that were a result of GLAs seen in the projection image in Figure 5-15(b).

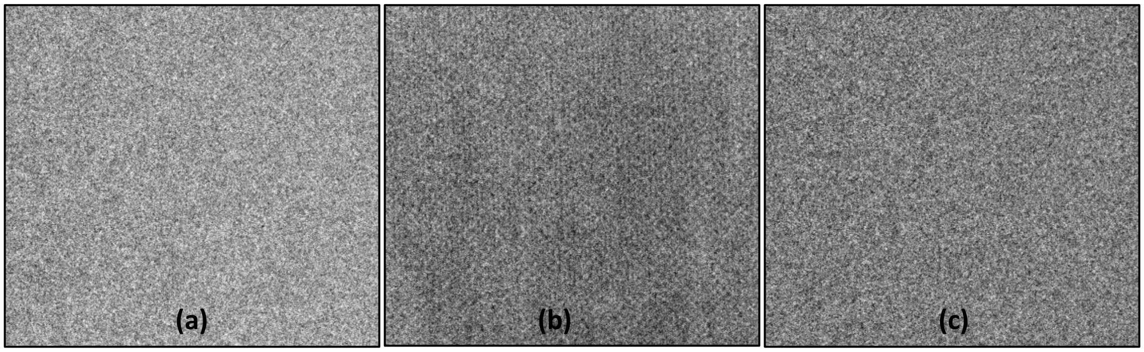

Figure 5-15: Zero degree projection image of uniform acrylic phantom. (a) Grid-out projection corrected by grid-out FFCI. (b) Grid-in projection image corrected by grid-out FFCI (c) Grid-in projection corrected by grid-in FFCI.

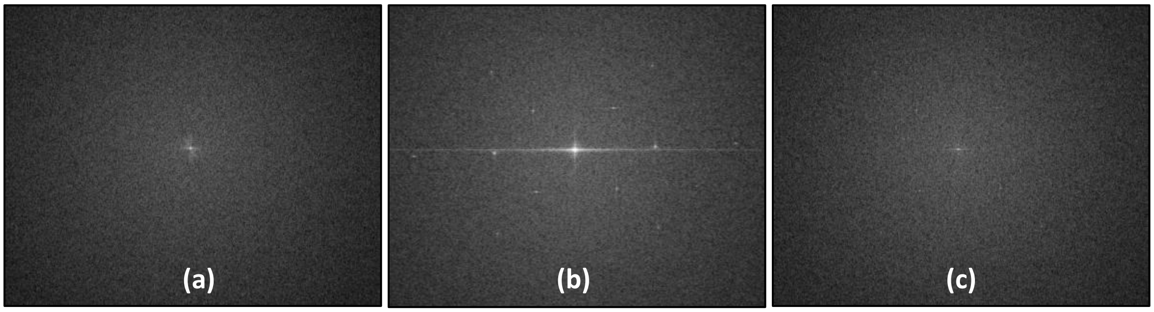

Figure 5-16: 2D PS of the 0° projections shown in Figure 5-15 (a) grid-out projection corrected with grid-out FFCI, (b) grid-in projection image corrected with grid-out FFCI (c) grid-in projection corrected with grid-in FFCI.

Figure 5-17(a) is the same 2D PS in Figure 5-16(b), which shows where the profile was drawn. Figure 5-17(b) is the profile plot of the grid-out PS. Figures 5-17(c) and (d) are profile plots of the grid-in 0° projection image corrected by the grid-out FFCI and grid-in FFCI, respectively.

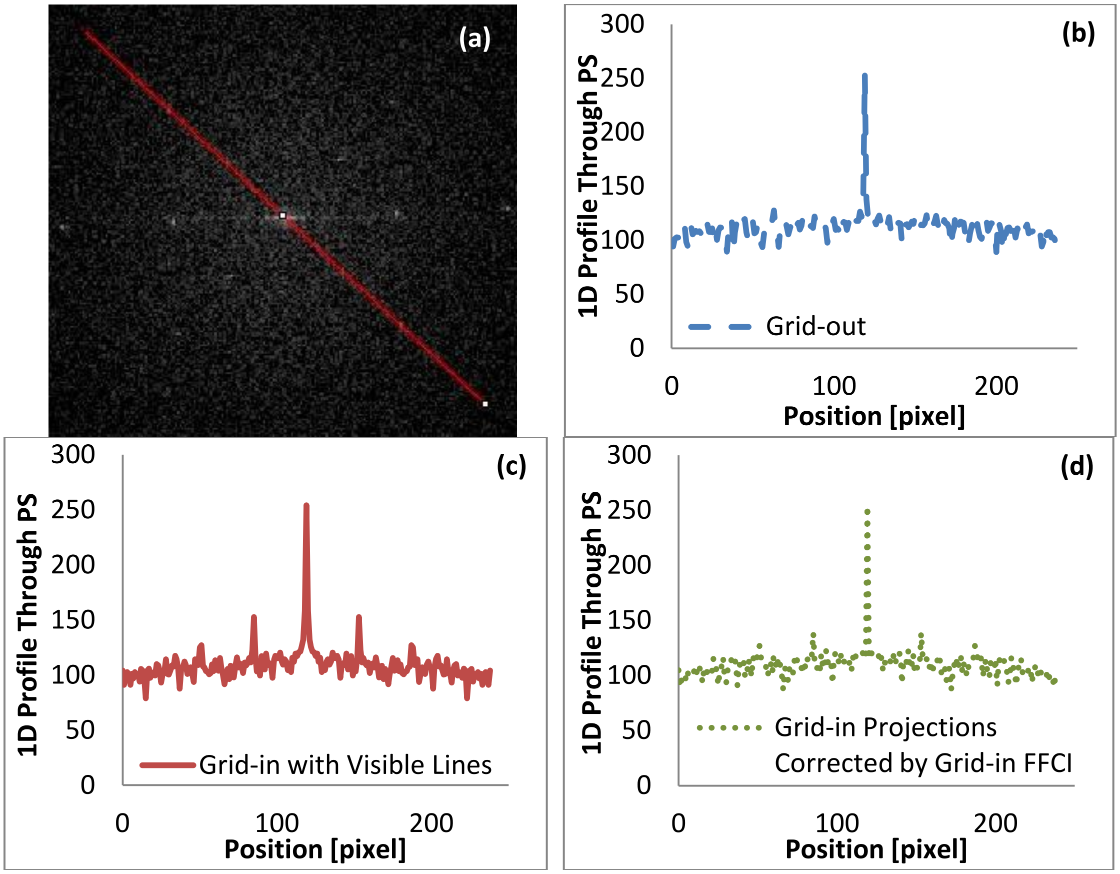

Figure 5-17: (a) shows the PS of the grid-in 0º projection image shown in Figure 5-15(b) over which a line is drawn along the grid peaks to show where a profile was drawn for (b) the grid-out PS image in Figure 5-16(a), (c) the grid-in image in Figure 5-16(b) with visible grid lines, and (d) the grid-in image in Figure 5-16(c) corrected with the grid-in FFCI.

The same analysis was done on the BR3D phantom. Figure 5-18 contains the 0º projection view of this phantom (a) without the grid-out, (b) with the grid in and corrected with the grid-out FFCI, and (c) with the grid in and corrected with the 0º grid-in FFCI. Figure 5-19 contains the PS of the ROIs of Figure 5-18. Figure 5-20 contains the profile plots along the line that runs through the grid peaks shown in Figure 5-20(a), which is the PS of the grid-in BR3D image corrected with the grid-out FFCI.

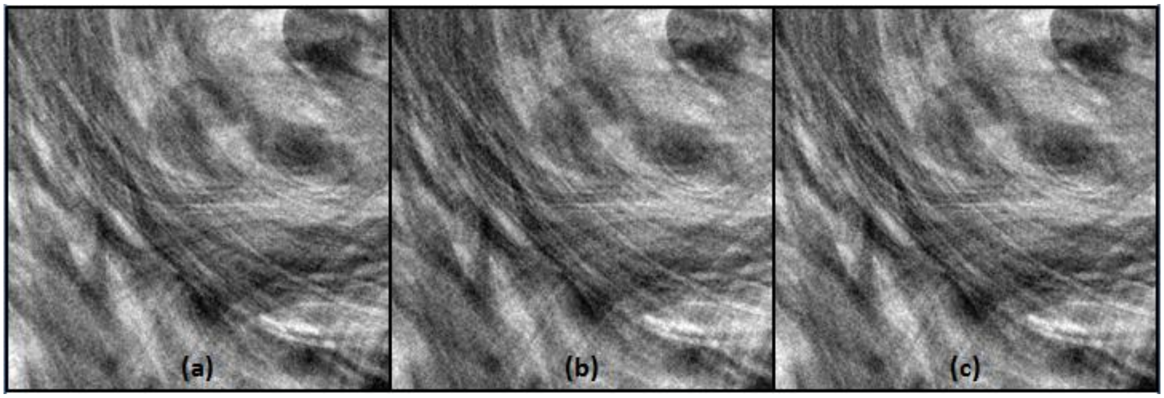

Figure 5-18: ROIs of the BR3D phantom (a) Grid-out projection corrected by grid-out FFCI. (b) Grid-in projection image corrected by grid-out FFCI (c) Grid-in projection corrected by grid-in FFCI.

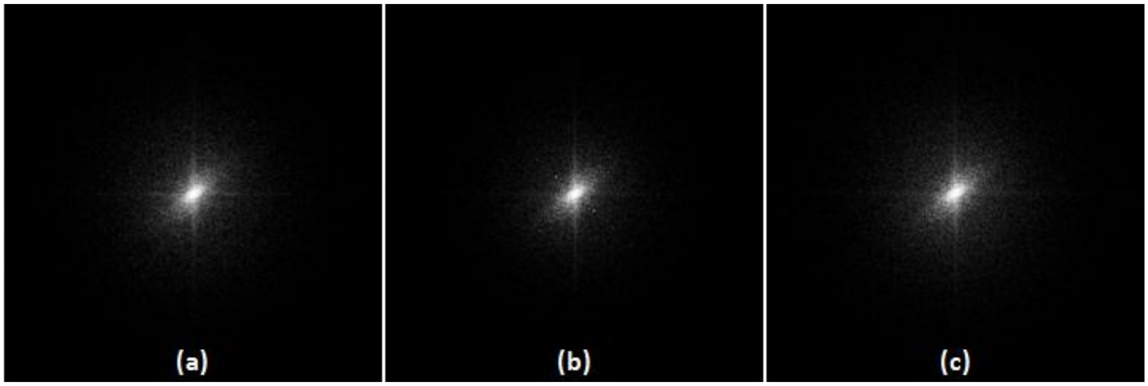

Figure 5-19: 2D PS images of the 0º (a) grid-out projection corrected by grid-out FFCI, (b) grid-in projection image corrected by grid-out FFCI (c) grid-in projection corrected by grid-in FFCI.

Flat-field correction of the grid-in images with the grid-in FFCI effectively reduced the grid artifact peaks associated with the grid's fundamental frequency. The zeroeth order GLA peak in the grid-in image corrected by the grid-out FFCI had an amplitude that was approximately 60% of the 0mm^{-1} frequency peak, which was lowered by nearly 6% for the acrylic phantom and by nearly 8% for the BR3D through FFC, bringing the amplitude of these peaks closer to those of surrounding features. There were some subtle GLA peaks seen in grid-in images of the acrylic phantom corrected with the grid-in FFCI. However, with more attenuation as in the case of the BR3D phantom, GLA peaks were imperceptible with grid-in flat-field correction. This method of GLA correction effectively made GLA peaks less obvious when the projection angle was the same as the angle used for acquisition of the FFCI. For successfully avoiding the propagation of GLAs to the reconstructed volume, this method must work for all projection angles.

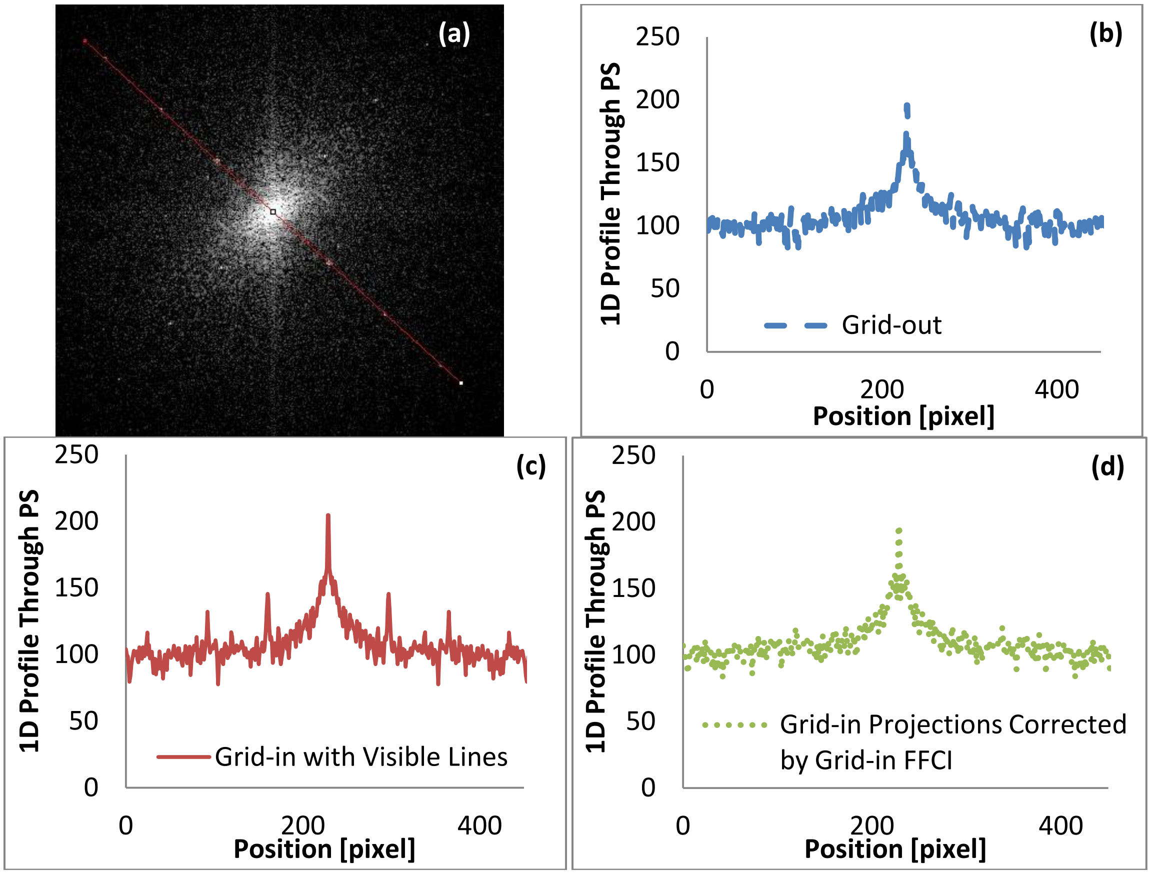

Figure 5-20: (a) shows the PS of the grid-in 0° projection image shown in Figure 5-18(b) over which a line is drawn along the grid peaks to show where a profile was drawn for (b) the grid-out PS image in Figure 5-19(a), (c) the grid-in images in Figure 5-19(b), and (d) the grid-in image in Figure 5-19(c).

5.4.3 GLAs in Reconstructed Images

Motion of the grid is reproducible such that a grid-in projection image acquired at the same gantry angle as the grid-in FFCI can be adequately corrected for GLAs. However, for tomosynthesis acquisitions, images will be acquired at multiple angles. In addition, the reconstruction algorithm combines all projections to create a single 3D volume. Subtle GLA contributions from all projections could potentially amplify the presence of

GLAs in the reconstruction. Therefore, the reconstructed images were analyzed for any residual GLAs as well.

Image reconstruction was performed on the tomosynthesis images presented here using iterative reconstruction software provided by the manufacturer of the x-ray detector. The resulting images have reconstructed slice thicknesses of 1 mm and in-plane voxel dimensions of 150 microns. Presence of GLAs in the reconstruction images of the uniform acrylic phantom and BR3D phantom was quantified through the 2D image PS of individual reconstruction slices after image reconstruction. A method of GLA removal from the reconstruction volume through filtering in frequency space is described. All image analysis and filtering was done using ImageJ and Matlab.

5.4.3.1 Generation of FFCIs for Tomosynthesis Acquisitions

The effectiveness of the grid-in FFC method was tested for tomosynthesis acquisitions using all of the same exposure techniques, phantoms, and experimental setup as described in Section 5.4.1. The exposure techniques were set to obtain an average glandular dose (AGD) of approximately 1.15 mGy. This total dose was divided equally among thirteen 500 ms exposures using the SNS method. DBT acquisitions of these phantoms were performed using the same projection angles described in Chapters 2 and 3 of ±12º, ±8º, ±5º, ±3º, ±2º, ±1º, and 0º relative to the direction of compression.

Typically, for DMT DBT acquisitions, a single grid-out FFCI obtained at a 0º projection angle is sufficient for processing all subsequent grid-out images regardless of projection angle. Because the source and detector do not move relative to each other, the patterns that are corrected out are the same in all projections, making it feasible to use a single 0º FFCI. Likewise, for this method to be applicable to the grid-in images, the

GLAs must be fixed for all projection angles. To test whether a separate projection image was needed for all angles, the 0º was used to correct all thirteen images of the tomosynthesis acquisition.

It was discovered that the rotation of the DMT gantry during DBT scanning results in changing gravitational force on the grid, producing slight variations in grid motion from projection to projection. Figure 5-21(a) shows a ROI of a grid-in projection image acquired at 12º with respect to the direction of compression, which was then corrected using a grid-in FFCI acquired at 0º. Figure 5-21(b) is the PS of the ROI in (a). Though they are not as obvious as in Figure 5-15(b), GLAs are visible in the 12º projection in Figure 5-21(a).

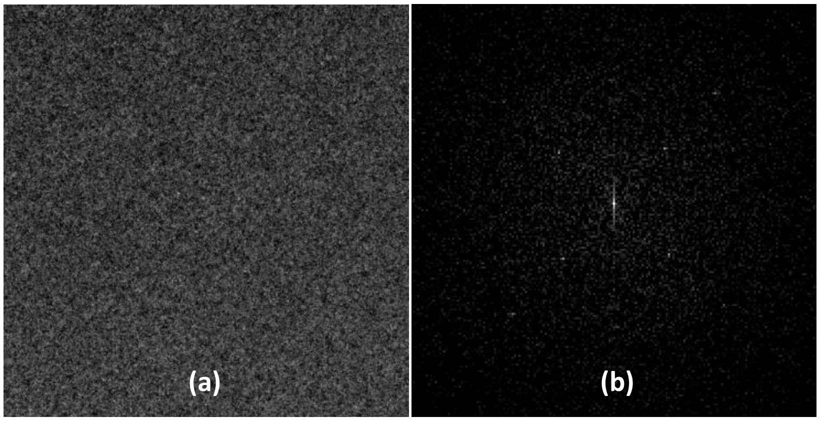

Figure 5-21: (a) 12º grid-in projection image of uniform acrylic phantom corrected with a grid-in FFCI acquired at 0º. (b) Close-up view of grid peaks in PS of ROI shown in (a). The display settings of the PS were adjusted so that the grid peaks would be visible.

Instead of a single FFCI acquired at 0º, multiple grid-in FFCIs can be acquired at several gantry arm angles for flat-fielding of the grid-in projections, depending upon the compression angle. For example, Figure 5-22(a) shows the same 12º projection that is corrected with a grid-in FFCI acquired at the same angle. GLA peaks are not easily identifiable within the image PS of Figure 5-22(b).

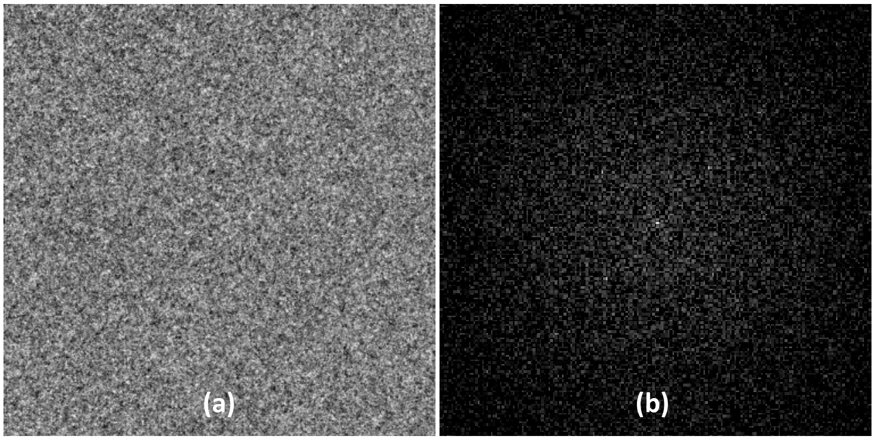

Figure 5-22: (a) 12º grid-in projection image of uniform acrylic phantom corrected with a grid-in FFCI also acquired at 12º. (b) Close-up view of the PS of the ROI shown in (a). The same window display setting used in Figure 5-21(b) was used for Figure 5-22(b).

It was found that a separate FFCI was not required for each individual angle. Depending upon the angle of compression, FFCIs only needed to be acquired for a smaller subset of the projection angles of the DBT acquisition. It was found that for an MLO compression, a single FFCI acquired at 0º with respect to the direction of compression was sufficient for correcting all thirteen projections acquired for either an RMLO or LMLO scan. On the other hand, for a CC compression, multiple FFCIs were necessary due to the directional change in the force applied by the positioning stage for moving the grid. Because the grid motor drives the grid motion from the right side to the left of the detector for all projections, the grid is reciprocated for the exposure and then placed back at its starting position to prepare it for the subsequent exposure. This is done to keep motion more consistent for all exposures.

For an MLO compression, the grid motor is either always pushing the grid with gravity or against gravity for the 24º angular range covered during the scan. As a result, the GLAs for these scans are relatively consistent from projection to projection such that a single grid-in FFCI is sufficient for correcting all 13 projections of the MLO scan.

On the other hand, for a CC compression, a component of the force applied on the grid is in the same direction as the gravitational force for some of the projection angles and opposes the gravitational force for the rest of the angles. Therefore, projections separated by large angles require separate FFCIs. However, it was found that since variations in motion between -3° to +3° were small, it was possible to use the 0° FFCI to correct the projections taken within this angular range at ±3°, ±2°, ±1°, and 0°.

For analysis of GLAs in reconstruction images, CC views were simulated for the phantoms tested. Grid-in FFCIs were obtained at each of the following angles: ±12°, ±8°, ±5°, and 0°. These seven grid-in FFCIs were used for correction of projections acquired at the same angles, with the 0° FFCI used for correcting the DBT images acquired at ±3°, ±2°, ±1°, and 0°.

Three image sets were again generated for each phantom. The first image set was processed by correcting the grid-out projections with the grid-out FFCI. To illustrate artifact formation in grid-in images when the grid is not present in the FFCI, the second image set was obtained by correcting the grid-in projections with the grid-out FFCI. The third image set was created by correcting the grid-in images by the grid-in FFCIs.

5.4.3.2 GLA Presence in Reconstructed Images

When used in DBT acquisitions, grid line artifacts from the projection images created artifacts in the reconstructed volume when the projections were not corrected with grid-in FFCIs. Some subtle residual GLAs also appeared in the images reconstructed from grid-in images corrected with the grid-in FFCIs. However, because the reconstruction algorithm also removes some degree of overlap [159] of the grid shadows from each plane of the reconstructed breast, grid line artifacts are not apparent over all slices. Figure

5-23 contains grid-in reconstruction slices of the uniform acrylic phantom where the projection images were corrected using the grid-out FFCI. The grid lines are obvious in the slice shown in Figure 5-23(a), which corresponds to a slice near the top of the phantom, but lines are not obvious in Figure 5-23(b) the slice corresponding to three millimeters into the phantom above the breast support.

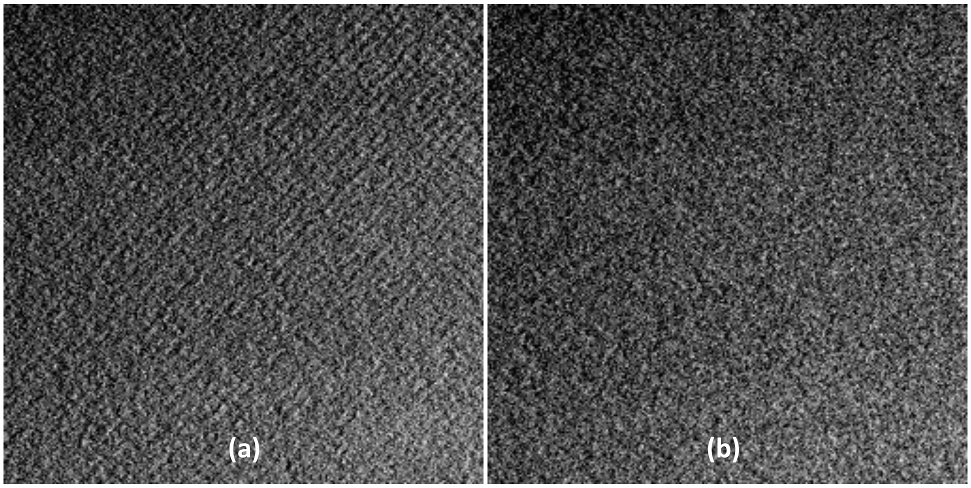

Figure 5-23: Reconstructed slices of the grid-in acrylic phantom projections corrected with the grid-out FFCI. (a) Slice 18 (18 mm above breast support) of the phantom where GLAs are obvious. (b) Slice 3 (3 mm above breast support) where GLAs are not as conspicuous.

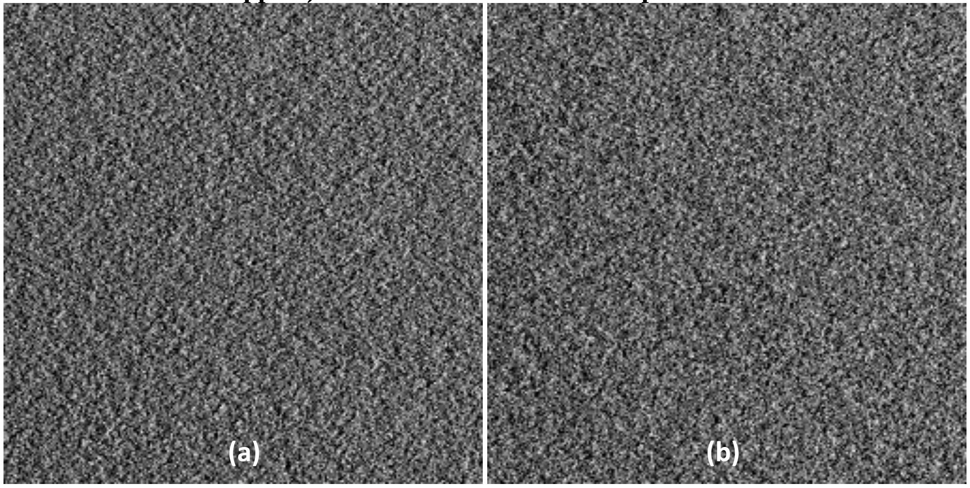

Figure 5-24: Reconstructed slices of the grid-in acrylic phantom projections corrected with the grid-in FFCIs. (a) Slice 18 (18 mm above breast support) and (b) slice 3 of the phantom are shown.

Figure 5-24 contains the same grid-in reconstructions slices of the same phantom from projection data that was corrected with grid-in FFCIs. The resulting GLAs are less conspicuous in slice 18 of Figure 5-24(a) than in Figure 5-23(a) as seen by the PS in Figure 5-25 for grid-in data corrected with (a) the grid-out FFCI and (b) the grid-in FFCI.

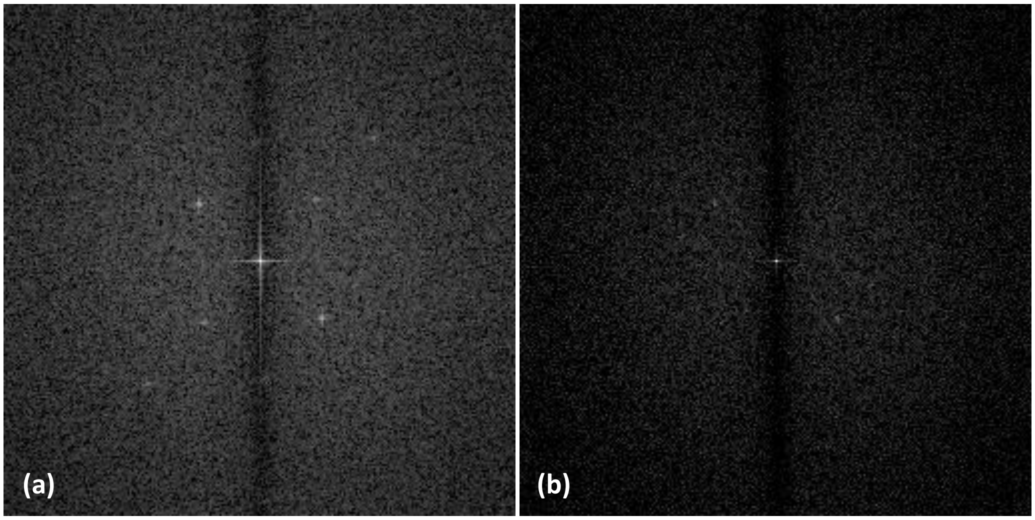

Figure 5-25: PS of the ROIs drawn within slice 18 shown in (a) Figure 5-23(a) of the image corrected with the grid-out FFCI and (b) Figure 5-24(a) of the image corrected with the grid-in FFCI. Display settings on each image were adjusted for better GLA peak visibility.

5.5 Image Filtering

5.5.1 Filtering Algorithm

Flat-fielding the projection images using the procedure described above ensured that the reconstructed images have minimal GLAs. However, in cases where the residual grid artifacts are unacceptably visible after flat-field correction, additional artifact removal is necessary.

Because of their predictable locations, the amplitude of the grid peaks in the 2D PS can be reduced through custom filtering that is specific to each slice. First, a 512 x 512 voxel ROI $R_{0,k}$ containing grid line artifacts was selected for a given slice k of the reconstructed volume. Next, the 2D fast-Fourier transform (FFT) of $R_{0,k}$ was computed. The $PS_{0,k}$ was calculated as shown in Equation (5-11) for slice k.

$$PS_{0,k} = 10 * log_{10}(\left|FFT(R_{0,k})\right|^{2}) \qquad (5\text{-}11)$$

This PS was then modified by targeting the peaks from $PS_{0,k}$ that were attributed to grid line artifacts. An algorithm was written in Matlab for finding grid peaks along the line on which they were known to lie. Pixels in $PS_{0,k}$ were identified as resulting from grid artifacts when the pixels had values above a threshold of 60% of the 0^{-1} mm frequency peak. This threshold level was chosen because it was the average of the ratio of the brightest grid peak to the 0^{-1} mm frequency peak. A modified PS, referred to as $PS_{mod,k}$, was created by setting the pixels that had values above the threshold to unity. $PS_{mod,k}$ was then divided by $PS_{0,k}$ as shown in Equation (5-12) to create a customized filter $F_{,k}$ for the k^{th} slice of the reconstruction volume.

$$F_k(i,j) = \frac{PS_{mod,k}(i,j)}{PS_{0,k}(i,j)} \qquad (5\text{-}12)$$

In the above equation, i and j are the indices of the rows and columns, respectively, of each of the 2D PS image matrices. The filter has a value of 1 in all frequency bins except those that contained grid artifact peaks in the original PS, where its value is the inverse of the peak values.

Once the filter image was created, it was convolved with the whole area of the k^{th}slice. In this step, the FFT of the original slice is multiplied by a resized version of F_k whose dimensions match that of the FFT of the original slice. Resizing was done in Matlab by using the imresize function, which uses bicubic interpolation for increasing the size of the PS to match the size of the original image slice [160]. The inverse Fourier transform (iFFT) is taken of this product to create the filtered slice $I_{Filtered,k}$ as shown in Equation (5-13).

$$I_{Filtered,k} = iFFT(FFT(I_{0,k}) \cdot F_k) \tag{5-13}$$

Multiplication in Equation 11 is done element by element rather than by matrix multiplication. Finally, the voxel values for the given slice k were scaled to convert the floating point values of the filtered image to 16-bit unsigned integers to match the mean value and data type of the original image as seen in Equation (5-14).

$$I_{Final,k} = I_{Filtered,k}\left(\overline{R_{0,k}}/\overline{R_{F,k}}\right) \tag{5-14}$$

The final filtered image slice $I_{Final,k}$ is a product of the filtered image slice $I_{F,k}$ and a constant factor equal to the ratio of $\overline{R_{0,k}}$, the mean voxel value within $R_{0,k}$, and $\overline{R_{F,k}}$, the mean voxel value within the same corresponding ROI location in the filtered image $R_{F,k}$. The algorithm for executing image filtering is provided in Appendix D.

This algorithm was executed on both projection data and reconstructed images to evaluate its efficacy in removing GLAs while still maintaining the integrity of the original data. The projections and reconstructions of the acrylic and BR3D phantoms presented previously were filtered with this algorithm. To determine whether there was any loss of information as a result of the filtering, profiles were drawn through the 2D PS of the filtered image and compared to that of the un-filtered grid-in PS. In addition, the number of visible features in the BR3D phantom was counted in both the grid-out and filtered grid-in reconstructions to see if there was any reduction in the number of detectable features as a result of the filtering.

5.5.2 Filtered Projection Images

Figure 5-26 shows close-up views of a ROI that was drawn in the 0º projection view of the acrylic phantom. Figure 5-26(a) is the grid-in 0º projection view where the projection data was corrected using the grid-out FFCI. Figure 5-26(b) is the same image shown in (a) after it was filtered.

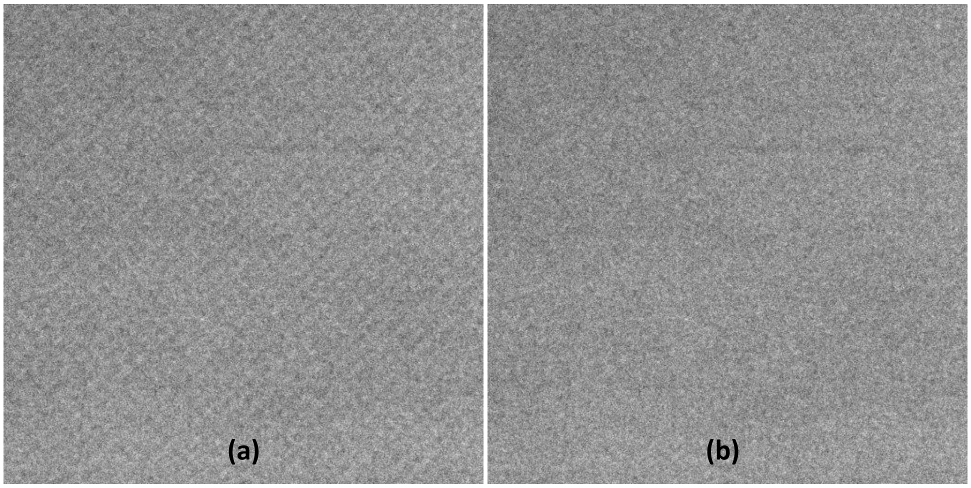

Figure 5-26: Grid-in 0º projection view of acrylic phantom corrected using the grid-out FFCI (a) before and (b) after image filtering.

This image was used since grid lines were intentionally left in the projection images to exaggerate visibility of grid lines. This projection view was also chosen as a representative image since all other projections had similar results. The PS data and filter that were used to reduce GLAs from Figure 5-26(a) is shown in Figure 5-27. A modified PS was created from Figure 5-27(a) (PS of Figure 5-26(a)) by setting GLA peak pixel values in the PS to unity as seen in Figure 5-27(b). Figure 5-27(c) is the resulting filter image, which was created by dividing PS_{mod} (Figure 5-27(b)) by PS_0 (Figure 5-27(a)) using Equation (5-10). Figure 5-28(a) is the PS of the original image with obvious GLAs and Figure 5-28(b) is the PS of the filtered image.

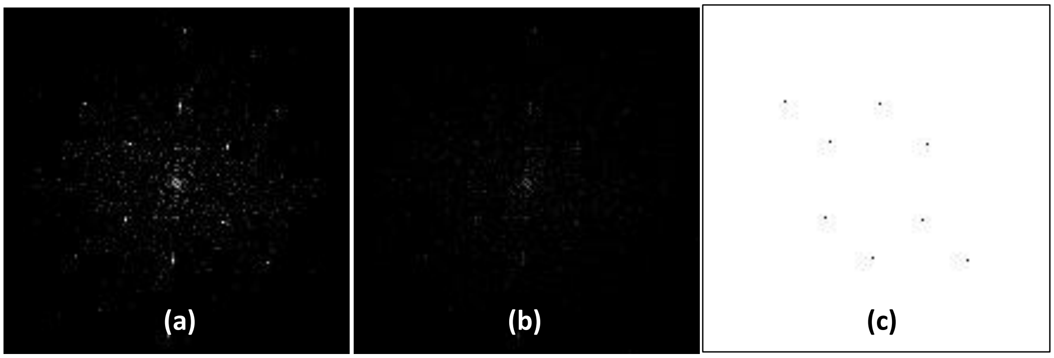

Figure 5-27: (a) PS_0 of the of the grid-in image in Figure 5-26(a). (b) Modified PS_{mod} where grid peaks have been set to unity. (c) Custom filter that was produced by dividing (b) by (a). The dark spots in (c) correspond to the peak locations and have fractional pixel values while the surrounding pixels are equal to unity.

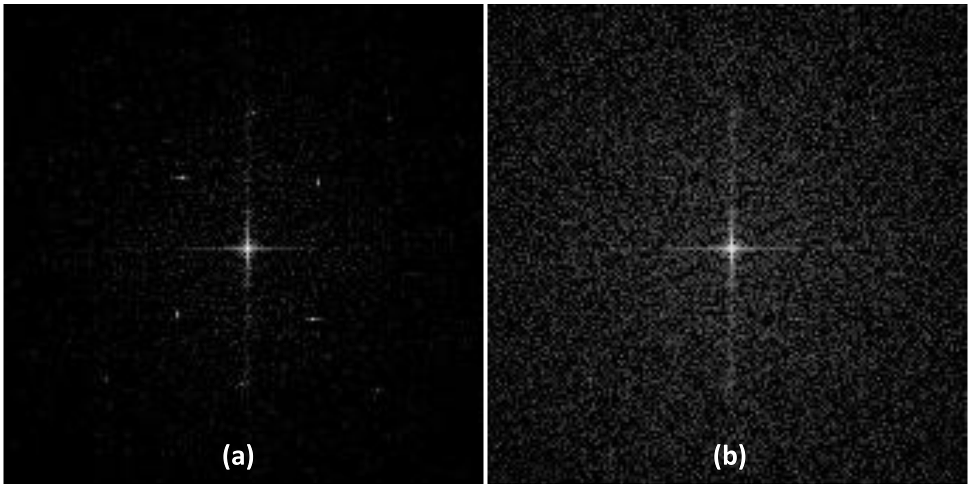

Figure 5-28: Close-up of PS of grid-in acrylic phantom projection view shown in Figure 5-26 (a) before and (b) after filtering.

Figures 5-29(a) is the 0° grid-in projection view of the BR3D phantom corrected with the grid-out FFCI, and Figure 5-29(b) is the filtered slice. Figure 5-30 contains the PS and filter used for correcting GLAs from the BR3D phantom projection. Figures 5-31(a) and (b) are the PS of the smaller ROIs shown in red boxes in Figure 5-29 of the original image and the filtered image, respectively. The smaller ROI was chosen to be on the location where additional line artifacts generated by the filtering algorithm can be seen in the upper right corner of the slice in Figure 5-29(b).

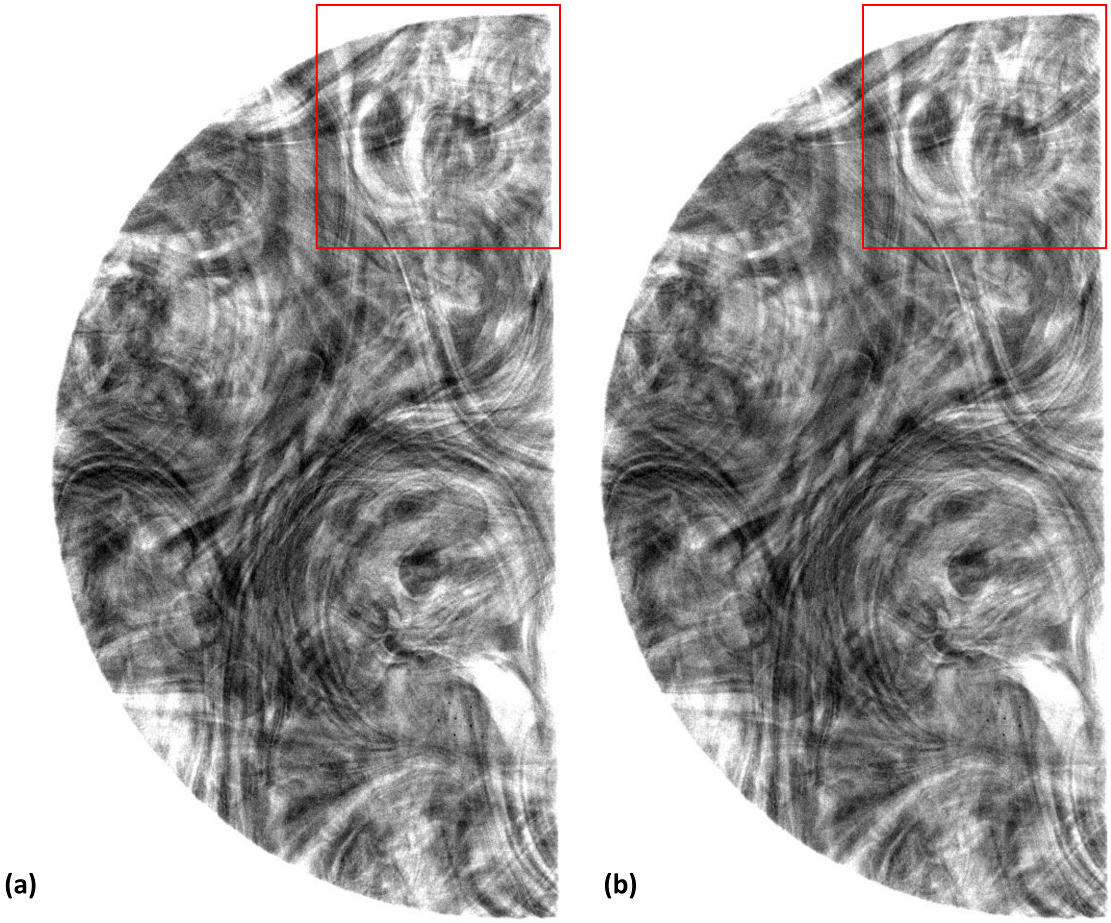

Figure 5-29: Grid-in projection view of BR3D phantom corrected using the grid-out FFCI (a) before and (b) after image filtering. The red box shows the ROI that was chosen for displaying the PS in Figure 5-31.

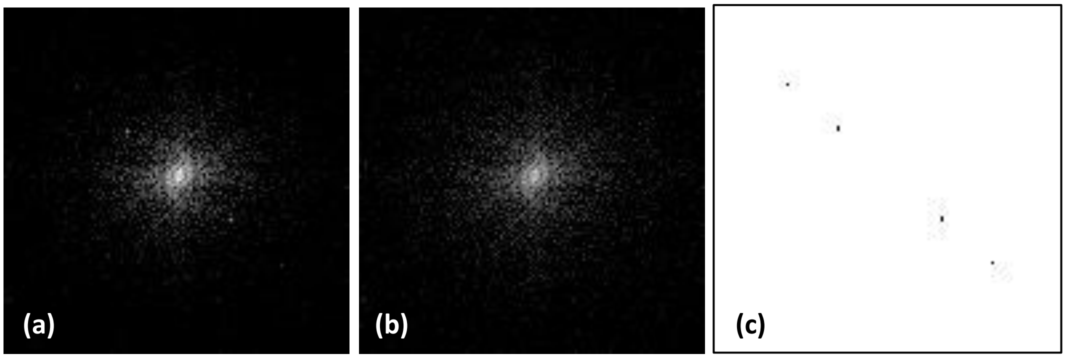

Figure 5-30: (a) PS_0 of the of the grid-in image in Figure 5-29(a). (b) Modified spectrum PS_{mod} where grid peaks have been set to unity. (c) Custom filter that was produced by dividing (b) by (a). The dark spots in (c) correspond to the peak locations and have fractional pixel values while the surrounding pixels are equal to one.

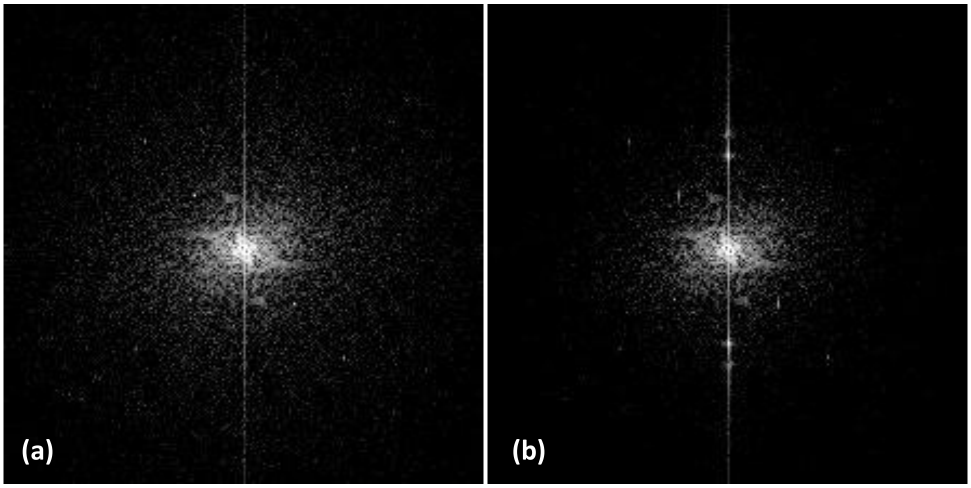

Figure 5-31: PS of grid-in BR3D phantom projection view shown in Figure 5-29 (a) before and (b) after filtering

The filtering method worked effectively for the acrylic phantom. However, filtering of the BR3D projections created more artifacts in the filtered projections. One major difference between the acrylic and BR3D phantoms is the non-uniformity in attenuation of the BR3D phantom. There are large differences in the detected intensity over the FOV of the BR3D phantom. Because of these variations, the grid artifacts are not the same over the entire FOV as they are in the case of the acrylic phantom images. Therefore, a single ROI that is a subset of the image cannot be used to correct the entire projection image.

Figure 5-32(a) is a smaller ROI that was cropped from the grid-in projection image corrected with the grid-out FFCI shown in Figure 5-29(a). This cropped portion contains GLAs that are fairly uniform over the entire area of the cropped image. Figure 5-32(b) is the same cropped image after filtering. Figure 5-33 contains the PS of an ROI drawn in the center of Figure 5-32 of (a) the original image with obvious GLAs and (b) the filtered image. The GLA peaks were reduced from the cropped projection image and are imperceptible in the PS in Figure 5-33(b).

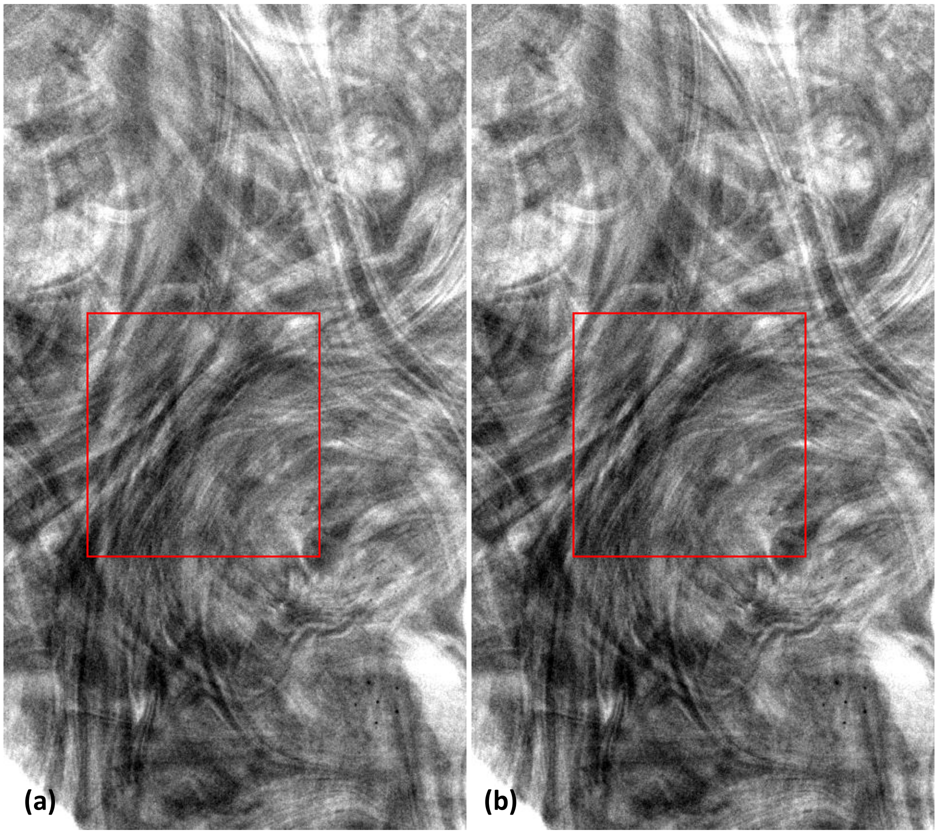

Figure 5-32: Cropped region of the grid-in BR3D projection view corrected using the grid-out FFCI (a) before and (b) after image filtering. These images are cropped from the original image to show how additional GLAs are not created by the filtering algorithm when GLAs are uniform over the whole area of the original image. The red box shows where an ROI was drawn for the PS in Figure 5-33.

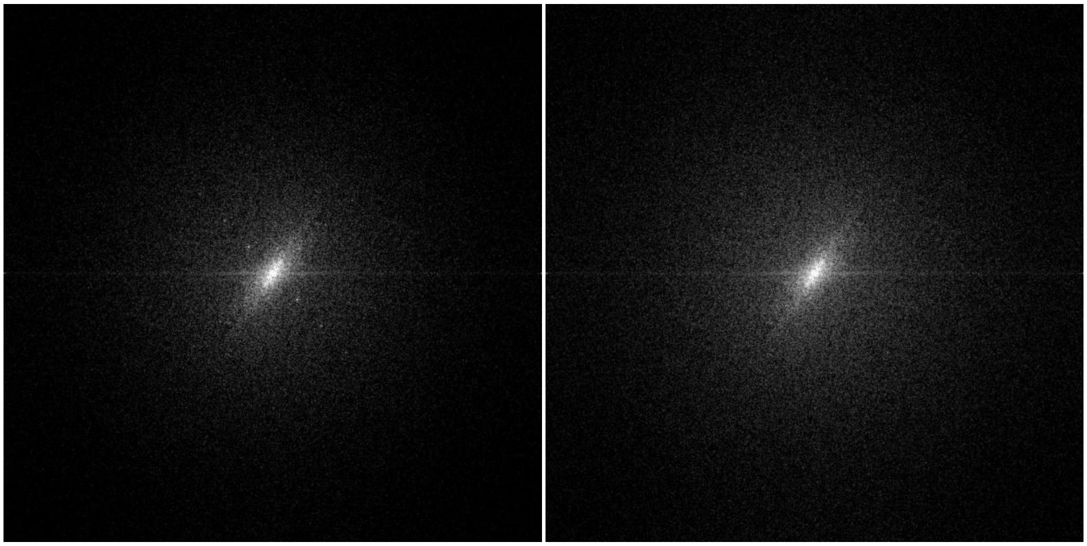

Figure 5-33: PS of ROIs drawn in the center of the grid-in BR3D phantom projection views shown in Figure 5-32 (a) before and (b) after filtering showing how grid peaks were effectively removed through filtering.

Despite additional artifacts created in the BR3D phantom, the filtering algorithm can potentially be modified to filter regions separately. Alternatively, the current filtering method may be more useful when applied to reconstructions. Because the reconstruction algorithm combines data from all projections, GLAs may be distributed more evenly over a given slice allowing for a single, smaller ROI to be used for filtering the entire slice.

5.5.3 Filtered Reconstruction Slices

Figure 5-34 shows close-up views of the ROI that was drawn in the top-most slice of the BR3D reconstruction images. This slice corresponds to the location of the axis of rotation (AOR) of the x-ray source and detector system. Figure 5-34(a) is a reconstruction slice of the grid-out image. Figure 5-34(b) shows the slice of the grid-in reconstruction where the projection data was corrected using the grid-out FFCI. Figure 5-34(c) is a slice of the grid-in reconstruction where the projection data was corrected using the grid-in FFCIs. This slice was selected because it had the most obvious grid line artifacts as seen in Figure 5-34(b).

Figures 5-35(a) – (c) are the 2D PS images of Figures 5-34(a) – (c), respectively.

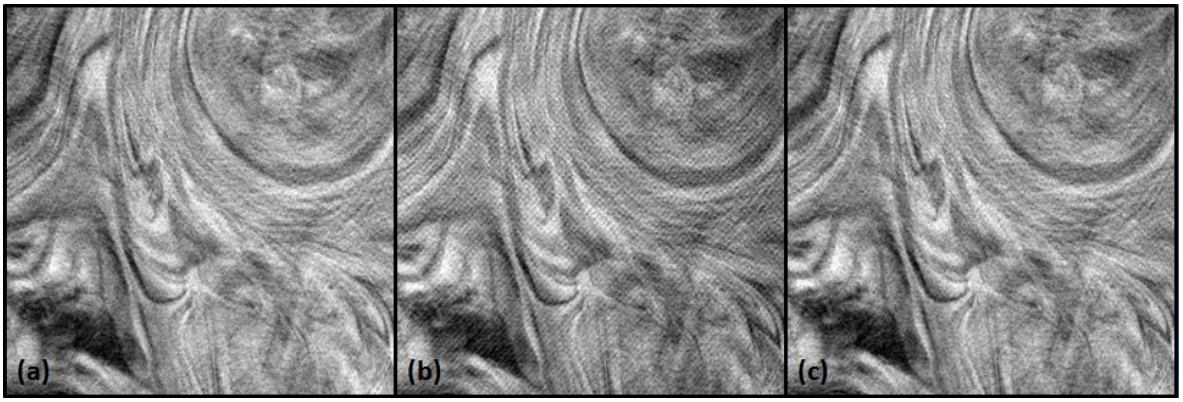

Figure 5-34: Close-up of slice 40 (slice corresponding to the location of the source and detector axis of rotation (AOR)) in the reconstruction images where the worst artifacts are seen in the grid-in images. (a) Reconstruction slice from grid-out projection data. (b) Reconstruction slice from grid-in projection data corrected by grid-out FFCI (c) Reconstruction slice from grid-in projections corrected by grid-in FFCIs. Grid lines are most obvious in (b)

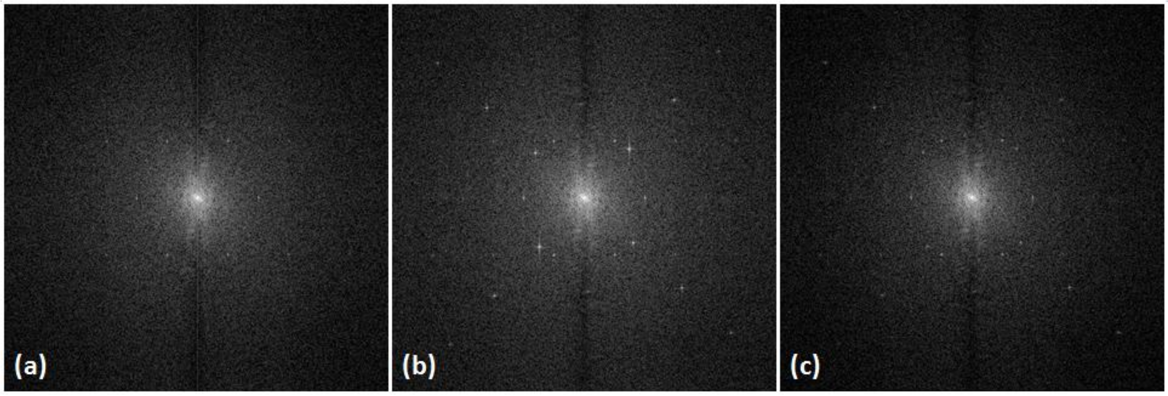

Figure 5-35: 2D PS images of the image slices shown in Figure 5-32. (a) Reconstruction slice from grid-out projection data corrected by grid-out FFCI. (b) Reconstruction slice from grid-in projection data corrected by grid-out FFCI. (c) Reconstruction slice from grid-in projections corrected by grid-in FFCIs.

The peaks in the PS that are associated with the grid line artifacts are located along a line that is at approximately a 47° angle with respect to the x-axis of the 2D PS. This angle is consistent with the rotation angle of the cells of the grid prototype. To filter out the lines from slice 40 of the grid-in data corrected with the grid-out FFCI, a modified PS was created from Figure 5-35(a) by setting GLA peak pixel values in the PS to unity as seen in Figure 5-36(b). Figure 5-36(c) is the resulting filter image. Figure 5-37(a) is the original slice seen in Figure 5-34(b), and Figure 5-37(b) is the filtered image.

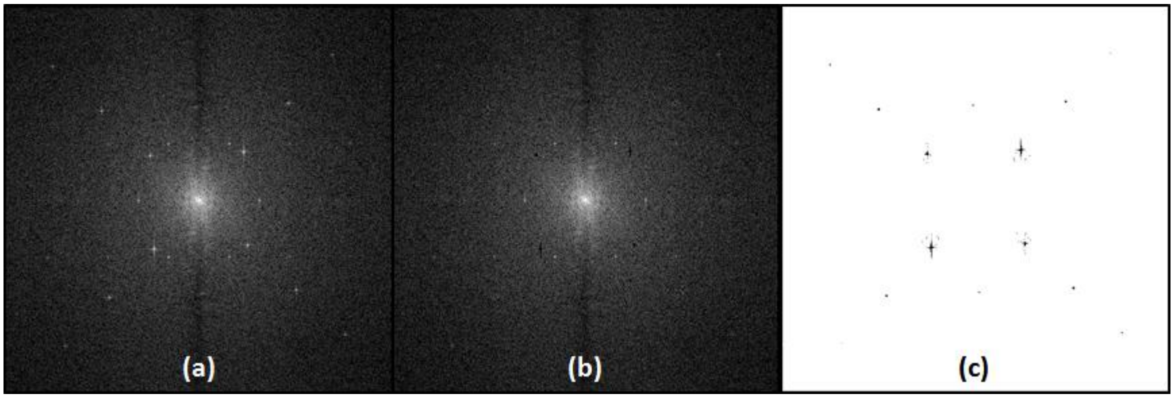

Figure 5-36: (a) PS_0 of the of the grid-in image in Figure 5-34(b). (b) Modified $PS_{mod,40}$ where grid peaks have been set to unity. (c) Custom filter that was produced by dividing (b) by (a). The dark spots in (c) correspond to the GLA peak locations and have fractional pixel values while the surrounding pixels are equal to 1.

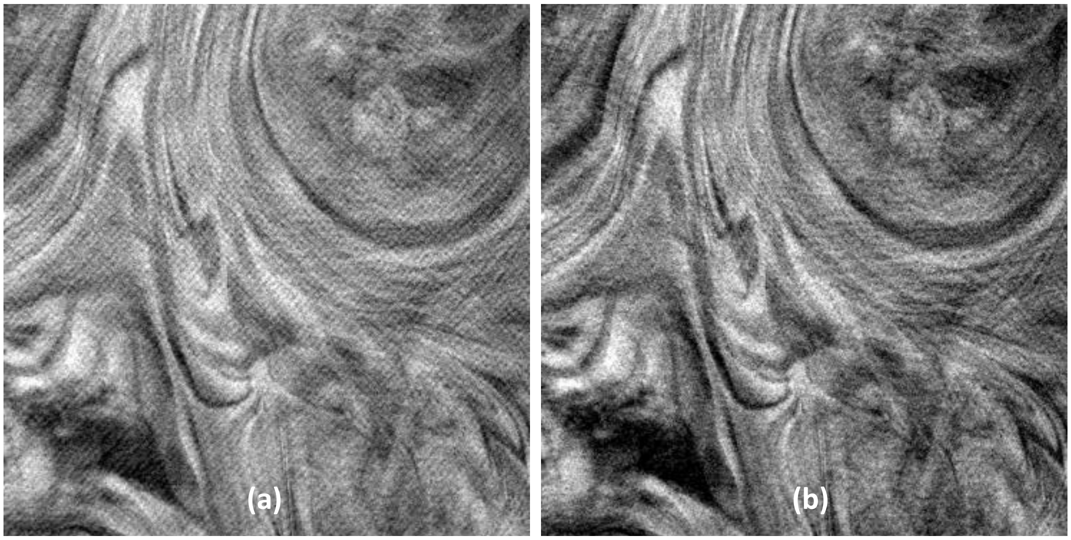

Figure 5-37: (a) Close-up view of grid-in image seen in Figure 5-34(b), which has been filtered using Figure 5-36(c), the result of which is shown in (b).

Unlike with the BR3D projection images, additional lines were not generated by the filtering algorithm in the reconstructed slices. To ensure that information was not lost, voxel value profiles were extracted along the red lines shown in Figure 5-38(a) of the grid-in image with GLAs and Figure 5-38(b) of the filtered image. These profiles are plotted in Figure 5-38(c), and their difference is plotted in Figure 5-38(d). The effectiveness of the filtering method can be seen by the fact that the difference of the two profiles in (d) contains primarily modulation with a wavelength of approximately 8 voxels or 1.2 mm, which translates to spatial frequencies corresponding approximately to the grid’s fundamental frequency.

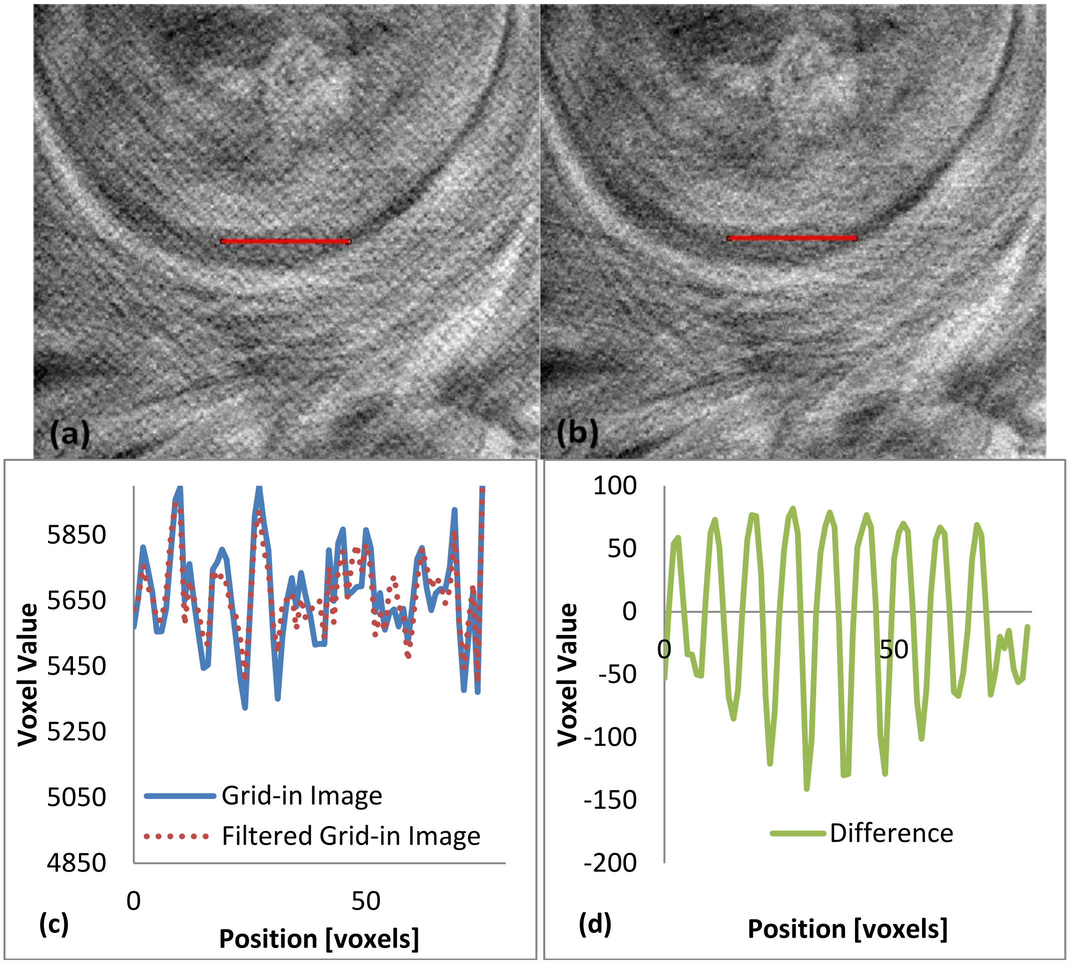

Figure 5-38: Close-up of reconstruction slice from grid-in projection data corrected by grid-out FFCI (a) before and (b) after filtering by the described method. (c) Profiles along the lines shown in (a) and (b) are plotted in (c), and their difference is plotted in (d).

Line profiles through the 2D PS of the filtered image also show that there are no gaps in the PS that would indicate missing information. Figure 5-39(a) is the PS of Figure 5-37(a) showing where a line profile was drawn through the grid peaks. The same line was drawn in the grid-out PS image, and this profile is plotted in Figure 5-39(b). The profile through the PS of the grid-in reconstruction with obvious GLAs is plotted in Figure 5-39(c), and the profile through the PS of the filtered image is plotted in Figure 5-

39(d). The filtering process reduced the amplitude of the fundamental frequency by over 23%.

Speck groups, masses, and fibers of varying sizes are embedded within the BR3D phantom. Further evidence that there was no major loss in information is the fact that the same features are detectable in both the grid-out and filtered grid-in reconstructions. Figure 5-40 contains the reconstructed slice with all features for the (a) grid-out and (b) filtered grid-in images. The grid-in image has slightly better visibility of the mass margins seen in the circles on the right side of the image slices.

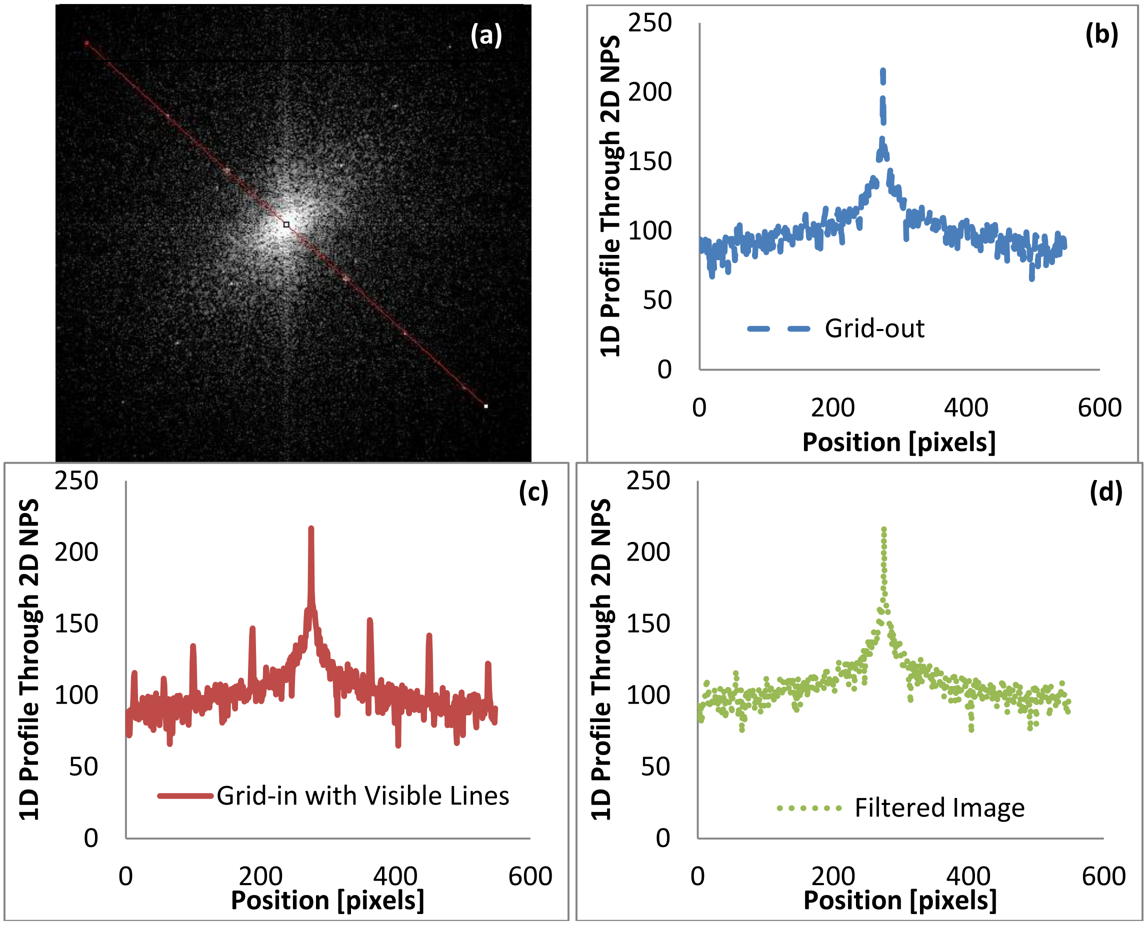

Figure 5-39: (a) PS of the unfiltered image showing where a line was drawn for creating the profile plots of (b) the grid-out PS of slice 40, (c) the grid-in image shown in Figure 5-37(a), and (d) the grid-in filtered image in Figure 5-37(b).

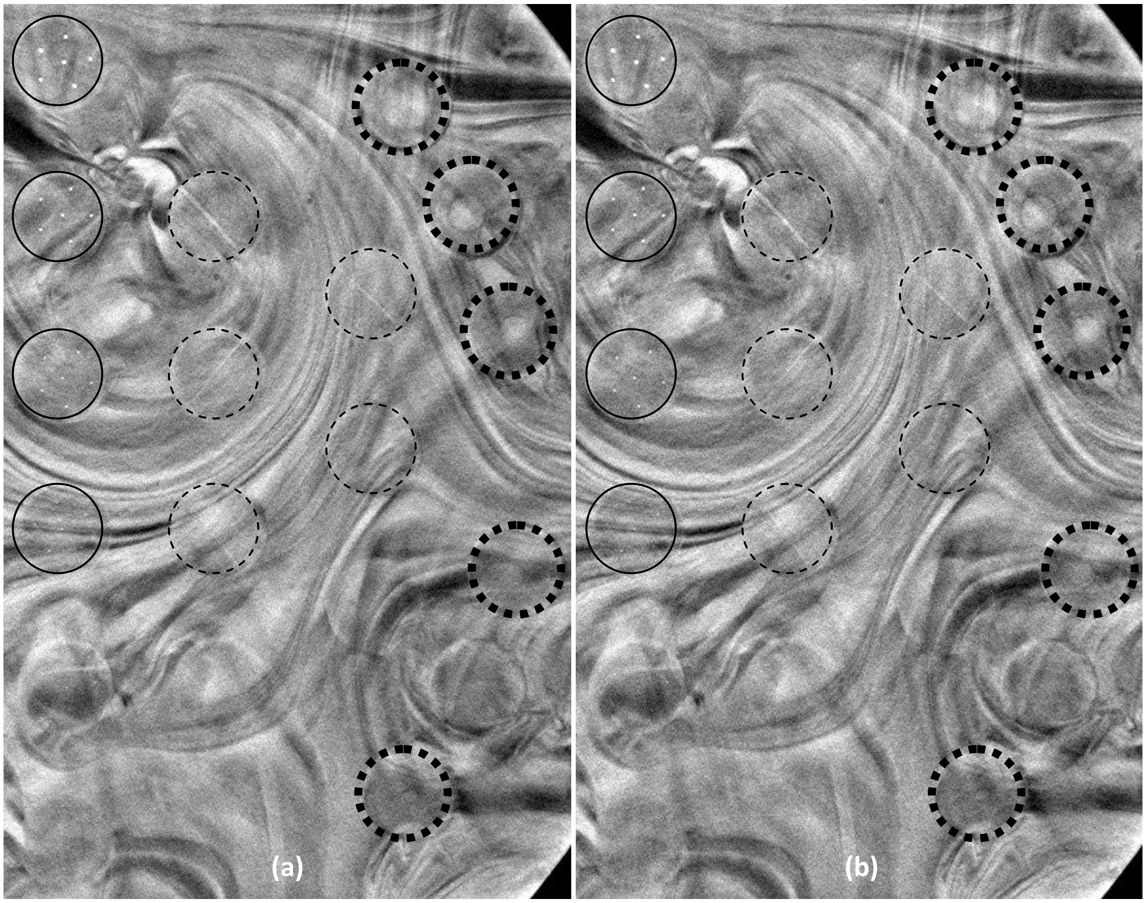

Figure 5-40: Reconstruction slice of features embedded in BR3D phantom (a) without the grid and (b) after filtration of reconstruction image that was produced from grid-in data corrected with the grid-out FFCI. Speck groups, fibers, and masses that are easily visible in the grid-out image are circled by solid, dashed, and dotted lines, respectively, with the corresponding findings in the filtered grid-in image.

5.6 Discussion of ST Motion and Image Filtering

The presented ST motion scheme reduces primary transmission through the grid by 1% beneath the focal spot as compared to the same grid kept stationary and placed for maximum primary transmission. There is an overall 2% reduction in transmission over the full active area of the moving grid in comparison to the stationary grid case.

Though primary transmission is reduced by a relatively small amount when reciprocated by the described motion, grid line artifacts are created in the projection images. PS images show presence of grid line artifacts at frequencies along a diagonal line with an angle matching that of the grid rotation angle. The first method of grid line removal that uses flat-field correction effectively reduces the presence of grid lines, which can be seen by the reduction in amplitude of the grid line peaks from the projection images. However, some grid line artifacts did appear in the reconstructed images of these grid-in flat-field corrected projections. These artifacts may have resulted from small differences in motion between the grid-in FFCIs and the grid-in projection images. Residual GLAs may also have resulted from the combination of all projections by the reconstruction algorithm, which could have amplified very subtle GLAs.

While the grid lines are not removed completely by flat-field correction due to the limited data set, they are also not obvious over the full reconstruction volume. Because the reconstruction algorithm removes some degree of overlap [159] of the grid shadows from each plane of the reconstructed breast, GLAs are not apparent over all features and slices. Other methods for reducing grid line visibility can be employed, such as tube output adjustment as described by Gauntt and Barnes [161]. Much like the flat-field correction method presented here, the tube output would need to match closely and reproducibly with grid motion for artifact removal to be consistent. Because of the possibility of inconsistency from one acquisition to the next, image filtering was considered. Marayuma and Yamamoto proposed a median filtering method for smoothing grid lines from x-rays films [162]. While this reduces image artifacts, it has the potential for removing data as with other filtering processes.

The correction software described in this chapter uses the image itself to correct for GLAs. The process requires a ROI that is smaller than the full image in order to be able to find and remove the grid artifact peaks from the PS. If the whole image were used to create a filter, the grid artifact peaks would not be easily detectable when embedded in the data that corresponds to both the object and its background, making the threshold technique for targeting GLA peaks difficult to implement. When the square ROI is ~256 or 512 pixels (or voxels) in size, peaks are more easily identifiable. This smaller ROI is used for filter generation, which is applied to the entire area of the original image slice or projection.

It was found that while image filtering was effective on the projections of the acrylic phantom that covered the full detector FOV, additional grid line artifacts were generated by the software correction technique when it was applied to the projection images of the breast phantom. The amplitudes of the GLAs over the entire FOV vary slightly as illustrated by Figure 5-13. These variances in fluence through the grid over the entire area of the breast phantom projections cause the PS in one ROI of the image to differ from the PS of a different area of the same image. Because the filtering process uses a smaller representative ROI to filter out the full image, the software will over-correct the GLA peaks in regions that may otherwise not have as strong artifacts as the representative ROI, resulting in more GLAs. One possible way of implementing software correction of the projection image would be to target smaller sections and filter each area separately to ensure that peaks are not added and essential data is not removed. However, this would only be in extreme cases where the grid artifacts cannot be suppressed through flat-field correction.

Correction of grid artifacts in the reconstructed image was possible using the described software method. The grid lines in the projection images increase the estimated attenuation of the breast in a periodic pattern in the reconstructed slices. Because the reconstruction algorithm combines GLAs from all projections, it creates a uniform pattern of lines over the entire area of any given slice. For this reason, it was feasible for a filter created from a single ROI in a given slice to be applied to the whole slice without the production of additional lines.

Grid peaks in the PS were found at frequencies typical of breast structures in the projection image. The reconstruction algorithm used for this study bins the data to effectively decrease the sampling frequency. Here 2x2 binning was used, which doubled the voxel size from 75 microns to 150 microns and lowered the sampling frequency, allowing for the possibility of less information loss from filtering. Essential information was not found to be removed as a result of the described filtering process. Profiles through the 2D PS images of the filtered reconstruction slices show that there were no gaps or obviously missing data when compared to the grid-out PS. In addition, since the discovered peaks had to be above a certain threshold, not all were attenuated by the filtering algorithm. Profiles through the images in Figure 5-38 show that a periodic pattern was removed by the filtering process without a noticeable change in the remaining structures. More importantly, all features that were visible in the grid-out reconstruction of the BR3D phantom were still visible in both grid-in flat-field corrected and grid-out flat-field corrected images that were filtered as can be seen in Figure 5-40.

The described nonplanar ST motion scheme was found to allow nearly the same primary transmission as for the focused, stationary grid case, with a 2% reduction in intensity over the full active area of the grid. Grid ST motion can provide efficient removal of scatter, potentially limiting the increase in radiation dose to the patient that may be necessary for maintaining the signal to the x-ray imager during grid-in acquisitions. Paulis et al have found that 1D grid-in DBT acquisitions of thicker breasts require lower dose than grid-in FFDM for a given breast [163]. With a more efficient scatter removal method made possible with this design and better scatter rejection provided by a 2D grid [129], this dose can potentially be lowered further while simultaneously improving image quality. Assessment of scatter-rejected images is discussed in the next chapter.

Chapter 6

Assessment of Scatter Rejected Images

In this chapter, image quality comparison is made between DMT images acquired without any form of scatter rejection and those acquired with the incorporation of the anti-scatter grid design described in Chapter 5 and the HMP acquisition strategy described in Chapters 2 and 3. For this assessment, optimal imaging parameters were first determined for grid-in acquisitions. Finally, results are presented of a study done to gauge the change in image quality when using an anti-scatter grid in the DBT portion of a DMT scan under conditions of fixed radiation dose to the phantom.

6.1 Beam Optimization

Medical x-ray imaging provides structural information by relying on the differing x-ray attenuation properties of various tissue types with the goal of differentiating between abnormal and healthy tissue. Attenuation properties of these tissues depend not only on the material in question, but also upon the energy spectrum of the irradiating beam. While higher energy x-rays penetrate through more material, they also limit the amount of contrast between different types of tissues. On the other hand, if lower tube voltages are applied, a larger number of x-rays would be required for more photons to be detected due to a greater likelihood of photoelectric absorption by the breast at lower mammographic x-ray energies.

Scattered radiation in projection x-ray imaging decreases lesion contrast and increases image noise by adding incoherent scattered photons carrying no spatial information to the coherent primary (image-forming) photons in the image. Breast composition, thickness, and scatter presence are all factors in considering the most advantageous tube voltage, or beam energy for a given imaging system. With the inclusion of an anti-scatter grid, the optimal beam energy may differ from that when there is no available method of scatter rejection. The most favorable tube voltage for a variety of phantom compositions and thicknesses when the grid is present in the DMT scanner was identified by testing a range of tube voltages and tracking changes in the signal-difference-to-noise ratio and radiation dose using the method described by Williams et al. [164].

6.1.1 Figure of Merit (FOM)

The signal difference to noise (SDNR) is a measure of the detectability of an object (the signal) amidst a noisy background. Detector characterization curves for the 2923MAM in HS mode show that since the detector does not add a large amount of read noise compared to the x-ray noise, even at relatively low exposure levels, the detector operates in the quantum-limited regime during acquisition of DBT projection images. Therefore, the change in SDNR with an increasing number of photons at a given energy is expected to follow Poisson behavior and rise as the square root of the fluence. Despite image quality improvement at higher exposure levels, the radiation dose to the patient also increases with higher tube output, increasing in direct proportion to the fluence. The AGD is the average radiation dose to the fibroglandular portion of the breast, or the amount of energy absorbed per mass of glandular tissue.A figure of merit (FOM), which incorporates both SDNR and the AGD, can be used to determine the optimal beam energy for a given compressed thickness and breast composition, taking into account both image quality and radiation dose. The FOM chosen for this analysis following the method of Williams et al. [164] is defined in Equation (6-1):

$$FOM = \frac{SDNR^2}{AGD} \tag{6-1}$$

Since the $SDNR^2$ is proportional to the photon fluence, and as is the AGD, the above FOM is insensitive to the particular choice of x-ray fluence for operation in the quantum-limited regime.

Analysis was done on 0^o projection views with the inclusion of an anti-scatter grid prototype in the beam using dose levels that are typical of single tomosynthesis projections rather than those of full-field digital mammography (FFDM) scans as described by Williams et al [164]. Results from these tests also demonstrate when use of the grid may be detrimental to image quality.

6.1.2 Average Glandular Dose (AGD)

Radiation dose to the breast is defined as the amount of energy absorbed per mass of glandular tissue since this tissue is at higher risk of contracting radiation-induced cancer than any other tissue in the breast [165]. The probability of photoelectric absorption depends upon the energy of the incident x-ray beams, which are typically not monoenergetic in mammography. The output beam of an x-ray tube contains a spectrum of photon energies and is filtered to remove the lower energy components that unnecessarily add to the radiation dose without contributing to the image. While AGD can be more easily estimated for monoenergetic rays, AGD for mammographic beams can be estimated by using an effective beam energy [166]. Beam characterization can be done through measurements of half value layer (HVL) [166]. HVL is a measure of the thickness of a specific material, customarily aluminum, required to decrease beam intensity to half of its initial, unattenuated value I_0 as shown in Equation (6-2) [166]:

$$\frac{I}{I_0} = e^{-\mu_{Eff} \cdot HVL} = 0.5 \tag{6-2}$$

In the above equation, μ_{Eff} is the effective linear attenuation coefficient of aluminum and I is the intensity of radiation that gets through the thickness HVL of aluminum. Monte Carlo simulations of monoenergetic beams were performed by Boone through which lookup tables were generated of normalized AGDs for a given breast compressed thickness, target/filter combination, HVL, and breast composition [167]. HVL values and ion chamber measurements of exposure per mAs of all tested tube voltages with the DMT system, which has a tungsten target and rhodium filter, are given in Table I of Appendix E. Estimates of normalized AGD for a given tested composition and thickness were then based upon measured HVL and interpolation of the values found from the lookup tables of AGD provided by Boone [167].

6.1.3 Measurement of Signal Difference to Noise Ratio (SDNR)

The reciprocating W-polymer prototype grid with an 80 cm focal distance, 0.1 mm wall thickness, 1 mm spacing, and a 3.65 mm height was used in these experiments. All images were acquired using the HS mode of the 2923MAM x-ray detector. To reduce any effects of read noise, x-ray techniques were set such that the exposure level to the detector was well below the saturation point of the detector and within the quantum-limited exposure range, which would be typical of a single 0º projection in a DMT DBT scan consisting of 13 total projection images. The target pixel value within the phantom was between 3000 to 4000 ADUs. All projections were corrected with grid-in flat-field correction images.

Two 0º projection view images with identical exposure parameters were acquired consecutively of each phantom built from the CIRS research set model 012A blocks (CIRS, Inc., Norfolk, VA) simulating three different breast compositions of 30% adipose/70% glandular (30/70), 50% adipose/50% glandular (50/50), and 70% adipose/30% glandular (70/30). For simulation of skin, two 5 mm thick 100% adipose blocks were placed on the entrance and exit surfaces of all phantoms to obtain total compressed thicknesses ranging from 4 cm to 9 cm in increments of 1 cm. The tube current was set such that the mean pixel value in a uniform region of the phantom was similar for all tested tube voltages. To find the optimal tube voltage for DMT scans, multiple 500 ms exposures were acquired at tube voltages ranging from 24 kV to 36 kV in 1 kV increments between 24 kV to 29kV and then in 2 kV from 29 kV to 36 kV. These increments were chosen because there was not much difference seen in HVL at the higher tube voltages.

Two step wedges are embedded in the phantom to simulate varying thicknesses of masses and calcifications (calcs). Simulated thicknesses of the mass steps ranged from 2 to 10 mm and those of the calc steps ranged from 0.05 to 0.3 mm. Figure 6-1(a) shows an example of a projection image of the 5 cm phantom with 50/50 composition. SDNR was calculated as shown in Equation (6-3) for both the thickest calc labeled as 1 and the thickest mass step to the right of the box labeled as 3 in Figure 6-1(a).

$$SDNR = \frac{(\overline{R_2} - \overline{R_1}) - (\overline{R_4} - \overline{R_3})}{\sigma} \qquad (6\text{-}3)$$

$\overline{R_1}$, $\overline{R_2}$, $\overline{R_3}$, and $\overline{R_4}$ are the mean pixel values of ROIs numbered in Figure 6-1(a) as 1, 2, 3, and 4, respectively. Image pairs were acquired for the calculation of σ, which is the standard deviation of pixels within the difference image of the image pairs whose location is shown by the larger rectangular ROI drawn above the steps in the difference image in Figure 6-1(b). The noise was obtained from difference images rather than single images in order to minimize the effect of fluence non-uniformity from sources such as the x-ray tube heel effect, as well as from any non-uniformities within the phantoms.

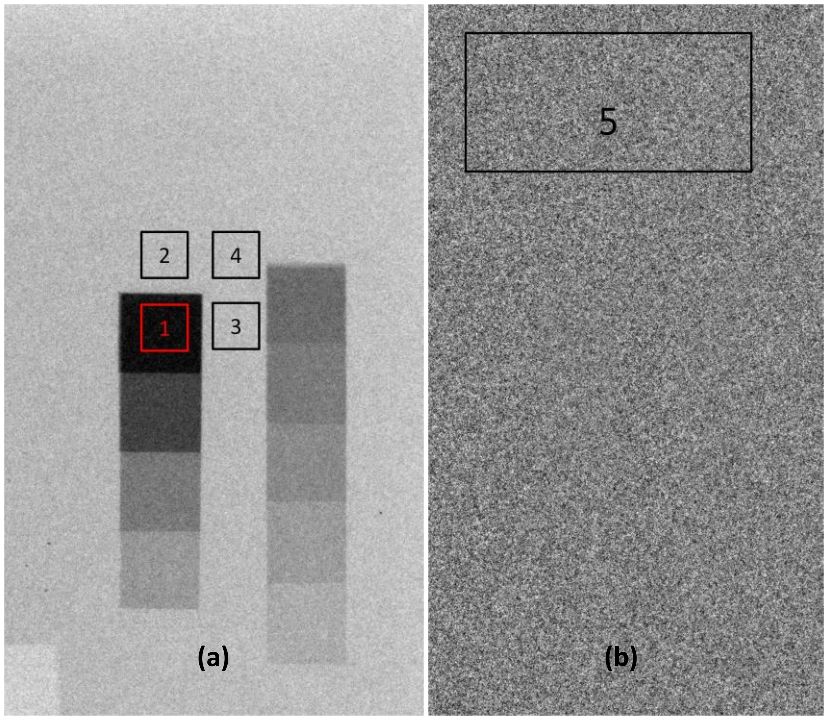

Figure 6-1: (a) is a grid-in projection image of the 5 cm 50/50 phantom used for obtaining SDNR data, which is calculated using Equations (6-3) and (6-4) from mean pixel values found within ROIs R_1, R_2, R_3, and R_4. (b) is the difference image of the same phantom, which was created by subtracting two consecutive projection images acquired using the same exposure techniques. The box numbered as 5 shows the location in the difference image where the ROI was drawn for obtaining the estimate of the noise σ.

Equation (6-4) shows the equation used for calculating σ.

$$\sigma = \frac{1}{\sqrt{2}}\sqrt{\frac{1}{(N-1)}\sum_{i=1}^{N}(R_{5,i} - \overline{R_5})^2} \tag{6-4}$$

$\overline{R_5}$ is the average value of all pixels $R_{5.i}$ within the large background ROI numbered 5 in Figure 6-1(b) consisting of N = 162482 pixels.

6.1.4 FOM of Grid-in Acquisitions

Figures 6-2(a), (b), and (c) are plots of the SDNRs of the thickest calc step, AGDs, and resulting FOMs, respectively, plotted versus tube voltage for the 5 cm phantoms. The FOMs were calculated from the measured SDNRs and calculated AGDs using Equation

(6-1). The maximum value of each FOM curve corresponds to the optimum tube voltage for maximizing SDNR for a minimum dose.

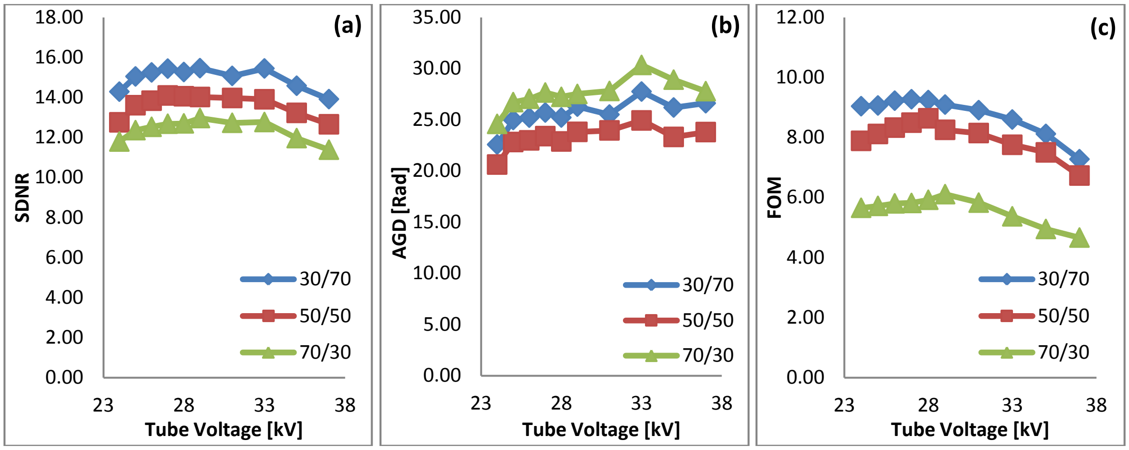

Figure 6-2: Plots of (a) SDNR, (b) AGD, and (c) FOM as functions of tube voltage for the 5 cm phantoms. Data for the 30/70, 50/50, and 70/30 composition phantom are plotted with diamonds, squares, and triangles, respectively, in all graphs.

Tables II and III in Appendix E contain optimal tube voltage values for each phantom thickness and composition tested, obtained with the grid in. In Table II signal difference was based on both the thickest calc step and in Table III on the thickest mass step. Table IV in Appendix E contains optimized values for grid-out acquisitions for just the thickest calc step because this was the only step that was visible in all grid-out projections. Optimal beam energies are slightly higher for the grid-out acquisitions than for the grid-in acquisitions, especially at the largest compressed thickness tested.

The FOMs calculated from this grid-in data were then compared to FOMs found when no grid was included by taking the grid-in/grid-out FOM ratio. Figure 6-3 contains plots of the FOM ratios found for all phantoms and tested compositions.

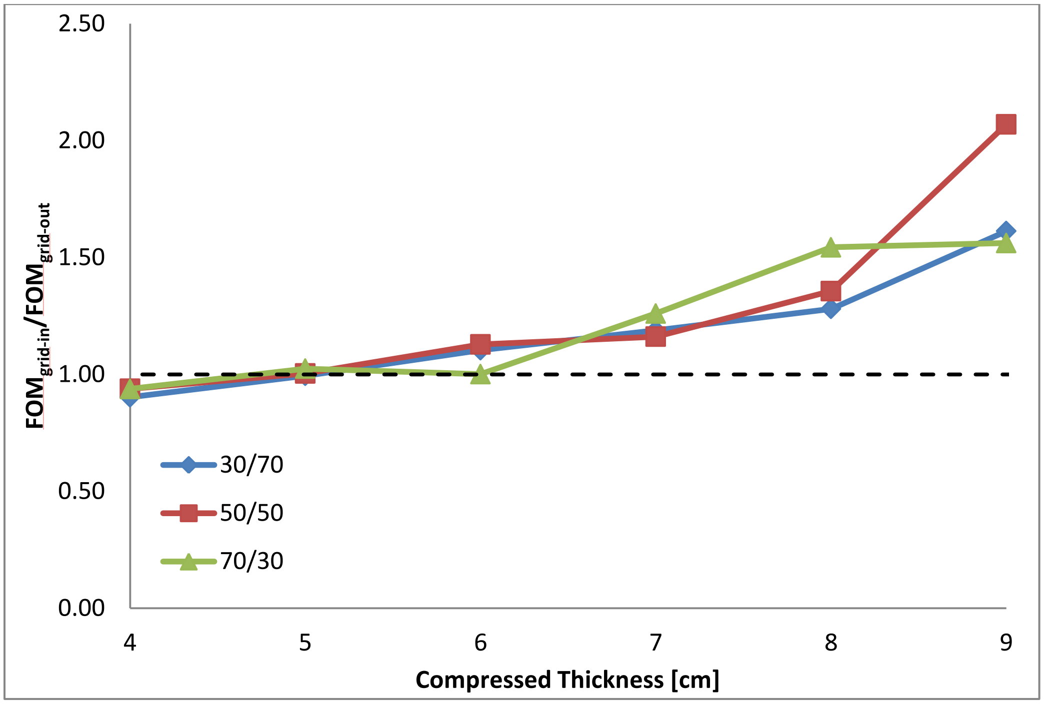

Figure 6-3: FOM ratios of the grid-in to grid-out data for all tested compressed thicknesses and compositions using the thickest calc step.

In addition to a significant reduction in scattered radiation, the grid also removes some of the primary rays from the image. As a result, the SDNR could possibly be lowered below that of grid-out acquisitions for smaller compressed thicknesses, where the amount of scatter is relatively low and the benefits of scatter removal may be outweighed by the negative effect of primary removal. . Figure 6-3 shows that the FOM is maintained for the 5 cm and 6 cm phantoms and is improved for compressed thicknesses above 6 cm for all compositions.

Scatter distribution varies and increases with increasing beam incident angle relative to the direction of breast compression [120]. Accordingly, since this analysis was performed using only 0^{o} projection views, inclusion of the grid may be more advantageous for views at larger angles. For a more thorough investigation of tomosynthesis images, a comparison was made between grid-in and grid-out reconstructed images.

6.2 Effect of Anti-scatter Grid on DMT DBT Images

6.2.1 Methods & Material

Phantom experiments were performed to assess the improvement in image quality when using a reciprocating anti-scatter grid in the DBT portion of a DMT scan. All x-ray images were taken using HS mode. The focused 2D anti-scatter grid prototype used for these experiments was the tungsten-polymer (W-poly) grid. The grid was reciprocated using the method described in the previous chapter for all grid-in acquisitions.

The Computerized Imaging Reference Systems, Inc. (CIRS) phantom Model 011A [168] was chosen for comparing grid-in DBT image quality to grid-out DBT image quality. This model simulates a breast of 50% glandular/50% adipose (50/50 composition) surrounded by a 5 mm thick layer of fat-simulating material. A step wedge is embedded in this phantom with 1 cm blocks, simulating tissue compositions of 0% glandular/100% adipose (0/100), 30% glandular/70% adipose (30/70), 50% glandular/50% adipose (50/50), 70% glandular/30% adipose (70/30), and 100% glandular/0% adipose (100/0). Also included in the phantom are fibers, speck groups, and masses of various sizes. A range of phantom thicknesses were tested by placing additional 1 cm thick slabs of PMMA onto the 4.5 cm CIRS phantom. For a given phantom thickness, all imaging parameters and phantom positions were kept fixed for both grid-in and grid-out images, the only difference in the two acquisitions being the presence or absence of a grid prototype.

6.2.1.1 Data sets with and without Hybrid Motion Profile (HMP)

SDNR and contrast can be affected both by the acquisition strategy employed (e.g. SNS or HMP) and by the absence or presence of the anti-scatter grid. Simulation studies performed by Shaheen et al. without any anti-scatter grid have shown that peak contrast of microcalcifications decreased by 8-9% and lesion SDNR decreased by 1-2% with tube motion when compared to an SNS acquisition of the same phantom [169]. Likewise, for a DMT DBT scan, contrast may be decreased due to a possible loss in spatial resolution from gantry motion during imaging when using a hybrid motion profile (HMP).

As shown in Figure 6-3 the presence of an anti-scatter grid improves image quality as measured by the $(SDNR)^2/AGD$ figure of merit for breast thickness greater than ~5 cm. In the following sections we further explore the impact of the anti-scatter grid on image quality. First, comparisons are made within the context of SNS acquisition, where changes in image quality are due only to the presence or absence of the grid. Second, comparisons of image quality are made between SNS acquisitions without the grid and continuous motion acquisition (HMP) acquisitions made with the grid. In those comparisons changes in image quality can result from both the grid and the use of continuous motion.

Two phantom experiments were performed with the CIRS phantom, one for testing scatter rejection alone, and the second was performed to test scatter rejection in combination with HMP gantry movement. For the first set of experiments (labeled as the ‘SNS-grid vs. SNS-no grid’ data set) to analyze the effects of scatter rejection alone, all grid-in and grid-out images were taken with the SNS method. The second data set (‘HMP-grid vs. SNS-no grid’ data set) was used to compare images acquired with the SNS method without the grid to images acquired using the HMP with the grid. For both data sets tube kVp, mA, and exposure time were the same for the two scan types being compared. (See Table 6-2 below for a list of all parameters for both data sets).

6.2.1.2 Exposure Parameters

Dosimetric studies performed by Feng and Sechopoulos have shown that DBT acquisitions require anywhere from 8% to 83% higher dose than FFDM, depending upon breast compressed thickness and composition [170]. More recent studies done by Paulis et al. show that the dose of DBT acquisitions with the use of a 1D anti-scatter grid is comparable to the FFDM dose for thinner breasts and slightly lower than FFDM for thicker breasts [163]. Based upon these results, the exposure parameters used for this experiment were adjusted so that the resulting AGDs were similar to those from the clinical screening mammograms of 9 DMT study subjects whose breast compositions were approximately 50% glandular and 50% adipose. These subjects were chosen because the scanners used to obtain their FFDM scans also used a tungsten target/rhodium filter combination. Figure 6-4 shows the AGDs of the screening mammograms plotted versus the compressed thickness. This data was collected from the header files of the 16 DICOM images included in the data set.

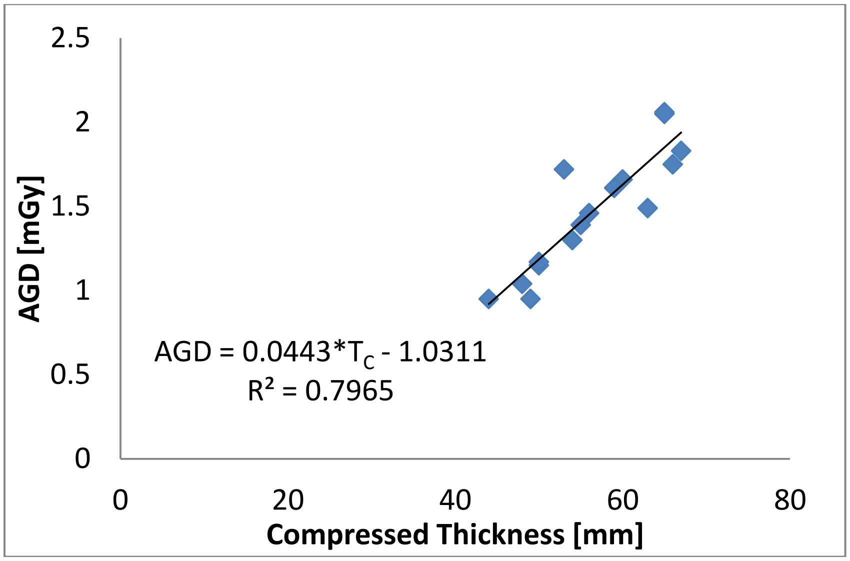

Figure 6-4: A plot of FFDM average glandular doses (AGDs) versus compressed thickness for breasts of approximately 50/50 tissue composition imaged by clinical systems with tungsten targets and rhodium filters.

A linear fit to this data was applied, and the resulting relation provided an approximate AGD for a given value of compressed thickness T_C as shown in Equation (6-5).

$$AGD = a \cdot T_C - b \tag{6-5}$$

The coefficients a and b from the linear fit of Figure 6-4 have values of a = 0.044 mGy/mm and b = 1.03 mGy. The exposure techniques were set to obtain approximately the same AGDs that were calculated from the linear fit. These total doses were divided equally among thirteen 500 ms exposures for the SNS-grid vs. SNS-no grid data set and among thirteen 160 ms exposures for the HMP-grid vs. SNS-no grid data set. The projection angles were ±12º, ±8º, ±5º, ±3º, ±2º, ±1º, and 0º relative to the direction of compression for all DBT scans. The tube voltage was determined from the $(SDNR)^2$/AGD optimization method described in Section 6.1. Using Boone conversion tables [167], tube current and exposure time parameters were selected to attain the target AGD.

Table 6-1 shows, for 4.5 cm, 6.5 cm, and 8.5 cm compressed thickness and 50/50 composition phantoms of the SNS-grid vs. SNS-no grid data set, the AGD values obtained from the curve fit of Figure 6-4, the kVp setting resulting from the $(SDNR)^2/AGD$ maximization procedure, and the entrance surface air kerma. Also provided in the table are the HVLs and effective beam energies for each tube voltage setting.

Table 6-1: Exposure parameters for CIRS Model 011A phantom for the SNS-grid vs. SNS-no grid data set

Compressed Thickness (cm)	Tube Voltage (kVp)	Half Value Layer (mm)	Average Glandular Dose (mGy)	Entrance Surface Air Kerma (mGy)	Effective Beam Energy (keV)
4.5	28	0.60	1.05	3.2	18.6
6.5	29	0.61	1.85	7.37	18.7
8.5	31	0.62	2.95	14.5	18.8

Tube parameters for the HMP-grid vs. SNS-no grid data set were adjusted such that the same FFDM-equivalent doses described for the SNS-grid vs. SNS-No grid data set were achieved, except for the 8.5 cm phantom. One drawback of the HMP method used here was that because the exposure time was limited to 160 ms to avoid motion blur during the moving views the maximum achievable tube current-exposure time product (mAs) for the 8.5 cm phantom was lower than the mAs used in the SNS-grid vs. SNS-No grid data set. As a result, a lower AGD of 2.35 mGy, rather than 2.95 mGy had to be used for the 8.5 cm phantom in the HMP-grid vs. SNS-no grid data set. Table 6-2 contains the techniques for all acquisitions that were performed and presented here.

Table 6-2: Exposure techniques used for all acquisitions performed

	Compressed Thickness (cm)	Tube Voltage (kVp)	Tube Current (mA)	Exposure Time (ms)	HMP or SNS	Scatter Rejection
SNS-grid vs. SNS-no grid	4.5	28	20	500	SNS	No grid
		28	20	500	SNS	Grid
	6.5	29	43	500	SNS	No grid
		29	43	500	SNS	Grid
	8.5	31	72	500	SNS	No grid
		31	72	500	SNS	Grid
HMP-grid vs. SNS-no grid	4.5	28	63	160	SNS	No grid
		28	63	160	HMP	Grid
	6.5	29	134	160	SNS	No grid
		29	134	160	HMP	Grid
	8.5	31	180	160	SNS	No grid
		31	180	160	HMP	Grid

Image reconstruction was performed using iterative reconstruction software provided by the manufacturer of the x-ray detector. The resulting images have reconstructed slice thicknesses of 1 mm and in-plane voxel dimensions of 150 microns. All analysis of image quality was done using ImageJ.

6.2.2 Accuracy of Estimated Linear Attenuation Coefficients

In order to assess the accuracy of the image-based estimates of the linear attenuation coefficients μ of materials within the phantoms, voxel values within the reconstructed images were converted to estimates of μ and compared to theoretical μ values. Theoretical values μ_T of the blocks embedded in the phantom at selected energies were provided by CIRS. To calculate the approximate theoretical μ_T values for the polyenergetic spectra used for these phantom experiments, effective monoenergetic beam energies were calculated from HVL measurements for each kVp setting used. The measured HVLs and effective energies are listed in Table 6-1. The effective beam energies were used to interpolate the μ versus energy data from CIRS to obtain theoretical μ_T values for each of the block compositions, which are listed in Table 6-3.

Table 6-3: Linear attenuation coefficients μ_T (cm^{-1})

Tube Voltage (kV)	0/100	30/70	50/50	70/30	100/0
28	0.67	0.77	0.84	0.80	0.91
29	0.66	0.76	0.83	0.79	0.90
31	0.65	0.75	0.81	0.78	0.88

In order to obtain DBT images of the various tissue-simulating materials under low scatter conditions, DBT images were acquired of 5 mm thick blocks simulating compositions of 0/100, 30/70, 50/50, 70/30, and 100/0 compositions. These were part of the same CIRS phantom set used for the SPR and beam optimization experiments. No compression paddle was present during these acquisitions to further reduce the presence of scatter. DBT images were obtained for each composition at tube voltages of 28 kVp, 29 kVp, and 31 kVp, both with and without the W-poly grid.

A linear relationship between the voxel value of the 5 mm blocks $V_{S,5mm}$ and the theoretical linear attenuation coefficient μ_T is defined as follows:

$$V_{S,5mm} = m \cdot \mu_T + k \tag{6-6}$$

Thus linear fits to plots of $V_{S,5mm}$ versus μ_T permit the coefficients k and m to be found for a given kVp setting. These coefficients can then be used to calculate the image-based linear attenuation coefficients μ_S of the five blocks embedded in the CIRS 011A breast phantom from their respective mean voxel values V_S using Equation (6-7):

$$\mu_S = \frac{V_S - k}{m} \tag{6-7}$$

6.2.3 Image Quality Comparison

To assess the impact of the grid on DBT images of objects whose attenuation is slightly higher than that of the surrounding tissue, as is the case for breast masses, the signal difference (SD), SDNR, and contrast in the reconstructed image slices were calculated for the blocks with glandularities higher than the 50/50 background. This was done for both the SNS-only and HMP-grid vs. SNS-no grid data sets. All measurements of SD, SDNR and contrast were made from a single slice in the reconstructed image that corresponded to the approximate center of the 1 cm blocks. Background and signal block mean voxel values were determined by Equations (6-8) and (6-9), respectively.

$$V_{Bkg} = \frac{1}{N}\sum_{i=0}^{N} v_{Bkg,i} \tag{6-8}$$

$$V_S = \frac{1}{N}\sum_{i=0}^{N} v_{S,i} \tag{6-9}$$

In the above equations, $v_{Bkg,i}$ are the voxel values within a 60 x 60 voxel ROI drawn over the 50/50 block consisting of N = 3600 voxels, and $v_{S,i}$ are the voxel values within ROIs of the same size centered on the 70/30 and 100/0 signal blocks. The 50/50 block was used for drawing the background ROI to measure the average background voxel value and the background noise since the background region of the phantom is composed of the same material. The mean voxel values of Equations (6-8) and (6-9) were used to calculate SD, SDNR, and contrast C as defined in Equations (6-10) through (6-12):

$$SD = V_S - V_{Bkg} \tag{6-10}$$

$$SDNR = \frac{SD}{\sigma_{Bkg}} \tag{6-11}$$

$$C = \frac{SD}{V_{Bkg}} \tag{6-12}$$

Noise σ_B was estimated by Equation (6-13) using the standard deviation of the voxel values $v_{Bkg,i}$ within the background ROI.

$$\sigma_B = \sqrt{\frac{1}{(N-1)}\sum_{i=1}^{N}(v_{Bkg,i} - V_{Bkg})^2} \tag{6-13}$$

The SD, SDNR, and contrast were measured in both grid-in and grid-out images, and the grid-in/grid-out ratios were calculated for each. Data from five trials of the grid-in acquisitions were averaged together for the final values.

Because the CIRS phantom has a uniform background throughout most of its volume, the reconstructed image slices should ideally have a uniform background voxel value within a given slice. However, scattered radiation does not have a uniform distribution over the projection images, with the scatter-to-primary ratio increasing around the periphery of the breast, due to scatter originating in the compression paddle that is scattered under the shadow of the breast [120]. To assess the variation in voxel value resulting from the spatially varying scatter, intensity profiles along the posterior-anterior direction were drawn through the 50/50 block in slices centered on the block in each phantom image. Twenty profiles were averaged together to create a single, smoother profile. Profiles were also drawn within the same slice along a direction perpendicular to the posterior-to-anterior direction. The profiles were sufficiently long to include the fat-simulating outer layer of the phantom.

6.2.4 Quality Control (QC) Check of HMP Images

In clinical DBT systems, quality control (QC) must be performed to ensure that image quality is maintained for patient imaging. Phantom QC tests are recommended to be done weekly on Hologic's Selenia Dimensions DBT scanner [171]. For these tests, an

American College of Radiology (ACR) accredited mammography phantom is imaged using a fixed set of x-ray techniques. This phantom simulates a 4.2 cm compressed breast of 50/50 composition, similar to the 4.5 cm CIRS phantom. The reconstructed image of the ACR phantom is examined to check visibility of the speck groups, fibers, and masses of varying sizes that are embedded in the phantom. For digital (FFDM or DBT) systems passing criteria are stipulated by the manufacturer of the mammographic unit. According to Hologic's criteria, in order for the unit to pass the QC test, 4 fibers, 3 whole speck groups, and 3 masses must be clearly visible [171].

As an added test for assessing whether image quality of the HMP-grid vs. SNS-no grid data set would be acceptable clinically, the sizes of the smallest features that were visible in the grid-in 4.5 cm CIRS phantom from the HMP-grid vs. SNS-no grid data set were compared to the smallest size of features within the ACR phantom above which all larger features would need to be visible for a DBT unit to be considered as passing. Figure 6-5 is a schematic of the ACR phantom with a dashed box around a fiber, a solid box around a speck group and a dotted line around a mass. For a scanner to pass QC, all features that have sizes that are greater than or equal to these boxed features should be visible in the DBT image.

To analyze the effects on image quality of tube motion independent of the effects of scatter rejection, the ACR phantom was imaged using the HMP and the SNS methods with no grid present for either one. Identical exposure techniques were used for the two scans with 28 kV tube voltage, 98 mA tube current, and 160 ms exposure times. The SD, SDNR, and contrast of a 4 mm thick acrylic disk that is located on the top surface of the ACR phantom was calculated along with the HMP/SNS ratio of each value.

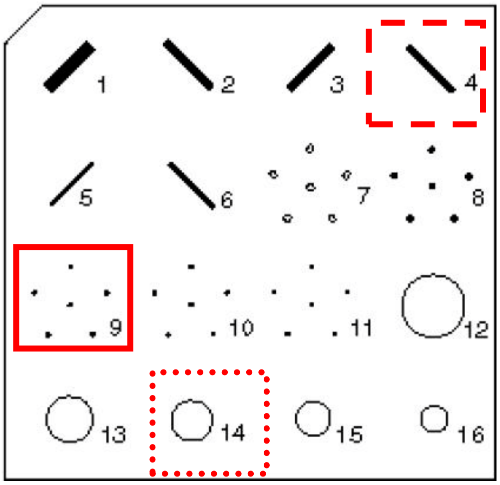

Figure 6-5: Schematic of ACR phantom. All features that are greater than or equal to in size to the boxed features should be easily identifiable for a clinical DBT unit to pass QC. Image courtesy of Gammex, Inc. [172]**.**

Figure 6-6 is a schematic of the CIRS phantom with boxes around the analogous features.

Table 6-4 contains the sizes of these features in the ACR and CIRS phantoms.

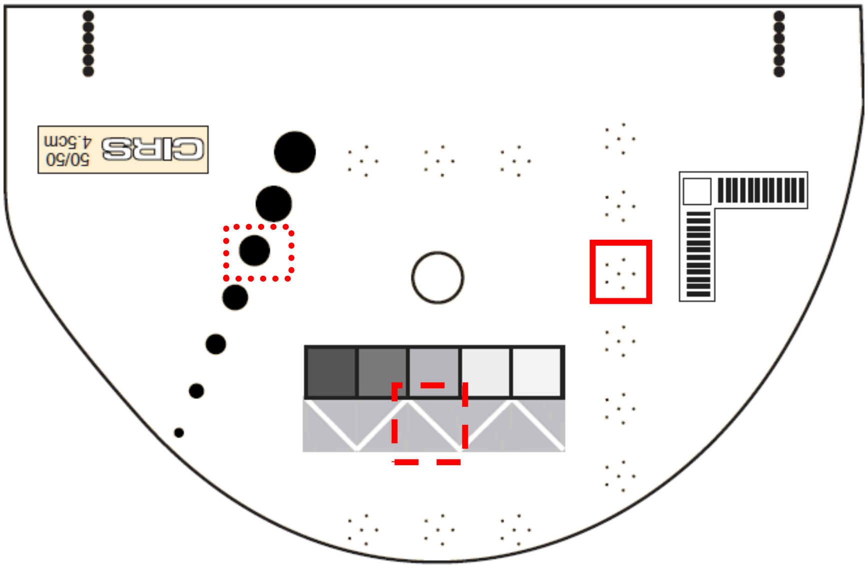

Figure 6-6 Schematic of CIRS phantom. Image is courtesy of CIRS, Inc. [168] and has not been drawn to scale. The fiber, speck group and mass similar in size to those of the ACR phantom in Figure 6-5 are boxed with a dashed, solid, and dotted square, respectively. Sizes of the speck groups below the boxed group in the actual phantom decrease with increasing distance away from the chest wall edge of the phantom. Fibers going from left to right and the masses going from the top to the bottom of the image also decrease in size within the actual phantom.

Table 6-4: Phantom feature size in mm

Feature	ACR	CIRS
fiber	0.75	0.71
speck group	0.32	0.275
mass (diameter)	5	4.76

6.2.5 Experimental Results of SNS-grid vs. SNS-no grid data set

6.2.5.1 *Voxel Value Conversion*

Figure 6-7 shows the mean voxel values $V_{S,5mm}$ of the 5 mm blocks simulating 0/100, 30/70, and 50/50, 70/30, and 100/0 compositions, plotted versus their theoretical linear attenuation coefficients μ_T. Figures 6-7 (a), (b), and (c) are for tube voltages of 28, 29, and 31 kVp, respectively. In each graph, the $V_{S,5mm}$ values measured both with and without the W-poly grid are plotted. Grid-in data has slightly higher voxel values, which can be attributed to removal of scattered x-rays.

These plots were then used to generate estimates of the linear attenuation coefficients of the 1 cm blocks embedded in the CIRS 011A breast phantom using Equations (6-6) and (6-7). A linear fit was applied to each plot of Figure 6-7 to determine, for each kVp setting, the constants *k* and *m* in Equation (6-6). Fitted values of constants *k* and *m* are given in Table 6-5 for each kVp, as measured either with or without the anti-scatter grid. The grid-in and grid-out coefficient values differ slightly because a small but non-negligible amount of scatter was generated by the 5 mm thick phantom blocks.

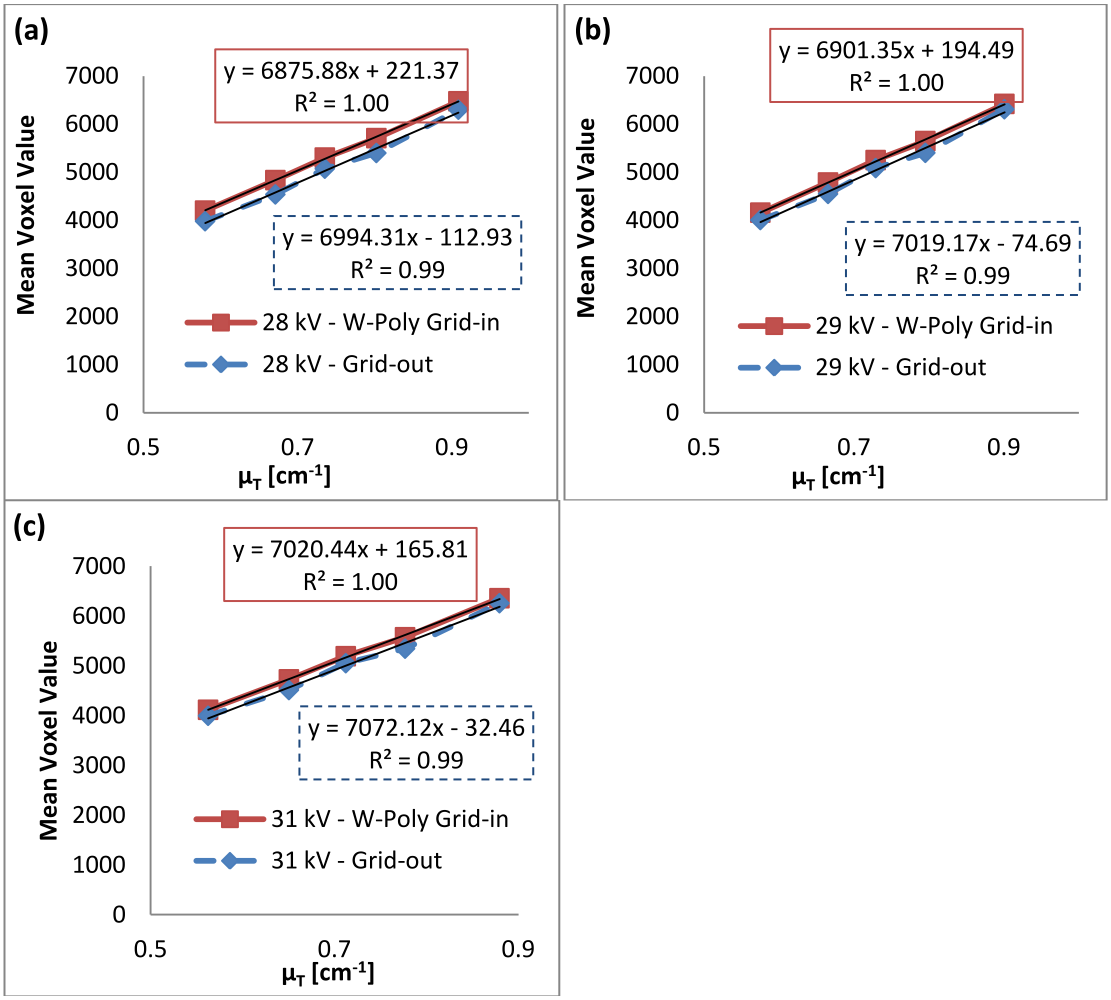

Figure 6-7: Plots of mean voxel value versus theoretical attenuation coefficients μ_T of material with 0/100, 30/70, 50/50, 70/30, and 100/0 compositions acquired at tube voltages of (a) 28 kV, (b) 29 kV, and (c) 31 kV.

Table 6-5: Linear fit parameters for calculating image-based attenuation coefficients

	Grid-in		Grid-out	
Tube Voltage (kV)	*m* (Voxel Value/cm^{-1})	*k* (Voxel Value)	*m* (Voxel Value/cm^{-1})	*k* (Voxel Value)
28	6875.9	221.4	6994.3	-112.9
29	6901.3	194.5	7019.2	-74.7
31	7020.4	165.8	7072.1	-32.5

Figures 6-8 (a), (b), and (c) are plots of the voxel based μ_S values for the 1 cm blocks embedded in the CIRS 011A phantom derived using the constants in Table 6-5 and Equation (6-7) along with the theoretical linear attenuation coefficients. Plots are shown for 4.5 cm, 6.5 cm, and 8.5 cm phantom thickness, respectively, for both grid-in and grid-out conditions.

For the thicker (6.5 cm and 8.5 cm) phantoms the removal of scatter by the grid elevates the μ_S values for all block compositions. However, comparison to the theoretically expected values shows that the μ_S values of blocks with glandularities lower than that of the surrounding 50/50 composition material of the 011A phantom are higher than expected, whereas those of lower glandularity blocks are lower than expected. This phenomenon is a result of artifactual smearing of background attenuation information into the block slices during DBT reconstruction. The artifacts are a result of the limited acquisition angular range (24º) used here.

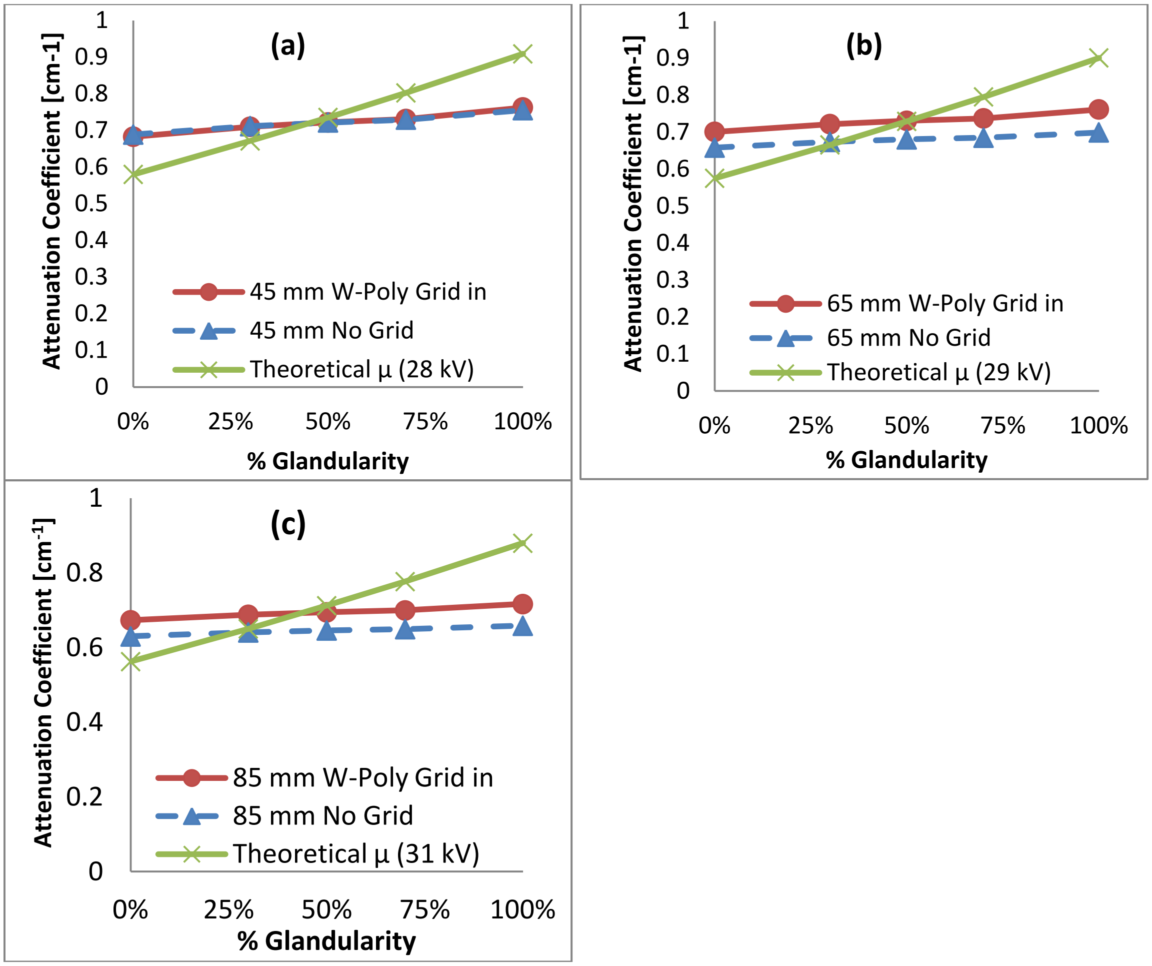

Figure 6-8: Linear attenuation coefficients μ_S of embedded 1 cm blocks derived from image voxel values and the linear fit parameters of Table 6-5. Plots show the calculated values of μS versus glandularity for the grid-in images (circles with solid line), the grid-out images (dashed line with triangles), and the theoretical values μ_T (x symbols connected with solid lines) for the (a) 4.5 cm, (b) 6.5 cm, and (c) 8.5 cm phantoms.

Figure 6-9 shows the resulting percent errors relative to the theoretical values, in the image-based linear attenuation coefficients for the 4.5 cm, 6.5 cm, and 8.5 cm phantoms, respectively.

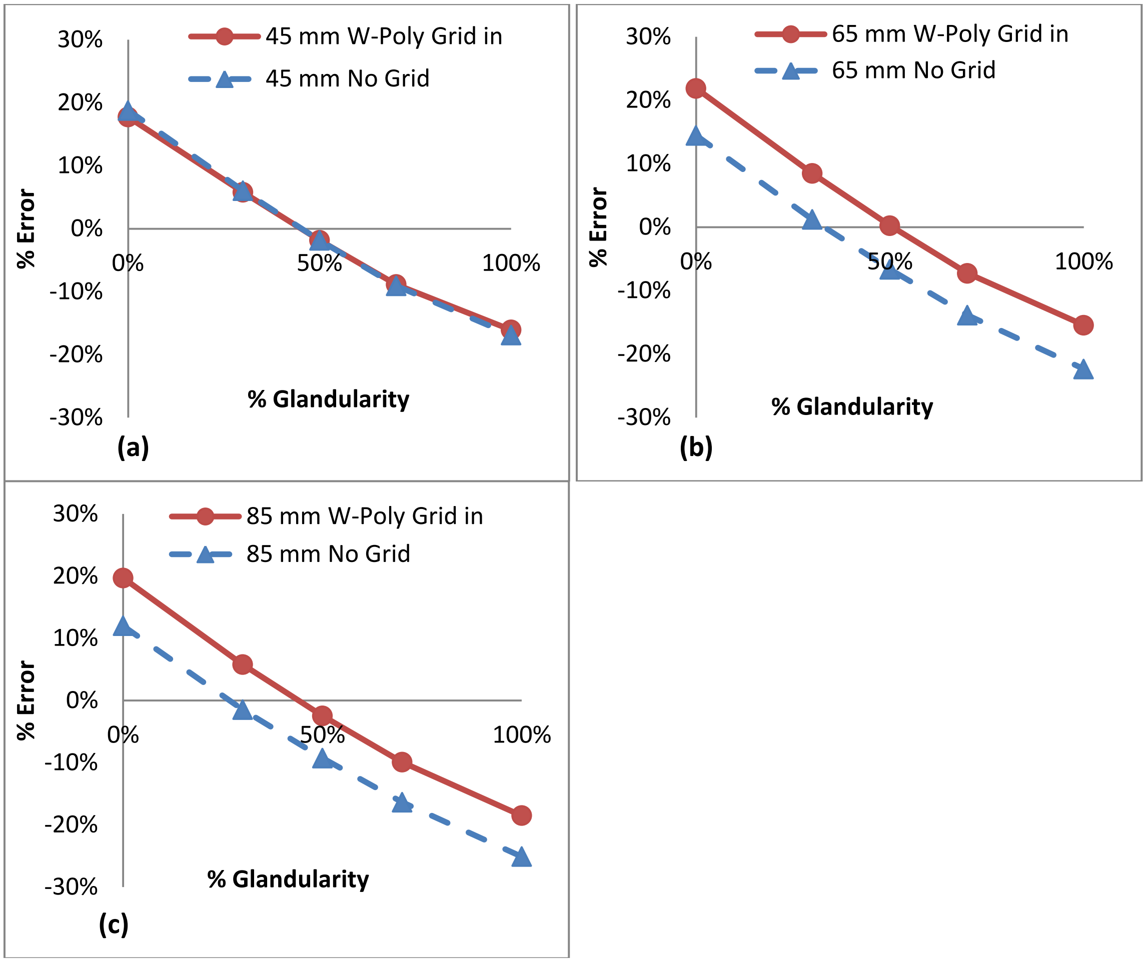

Figure 6-9: Percent error in image-based estimates of attenuation coefficients μ_S as compared to theoretical values μ_T plotted versus glandularity for the (a) 4.5 cm, (b) 6.5 cm, and (c) 8.5 cm phantoms. Grid-in results (solid lines and circles) and grid-out results (dashed lines and triangles) are shown.

6.2.5.2 Reconstructed Slices

Figure 6-10 shows the reconstructed slices from the SNS-grid vs. SNS-no grid data set from which SD, SDNR, and contrast data were measured. Images in Figure 6-10 where a grid was not present during acquisition are shown in the left column for the (a) 4.5 cm, (c) 6.5 cm, and (e) 8.5 cm thick phantoms. The corresponding slices from SNS DBT acquisitions of the same phantoms taken with the W-poly grid in the beam in Figure 6-10 are shown in the right column in (b) 4.5 cm, (d) 6.5 cm, and (f) 8.5 cm. The greater uniformity in background voxel value with the grid present is especially evident for the 6.5 cm and 8.5 cm phantoms. Fibers located below the 1 cm blocks and masses in the 8.5 cm phantom are more visible in the grid-in image than without the grid.

Figure 6-11 shows regions of slices in which some of the speck groups and spherical masses embedded in the phantom are most in focus. Grid-out slices are shown in Figure 6-11(a), (c), and (e) for the 4.5 cm, 6.5 cm, and 8.5 cm phantoms, respectively, and grid-in slices are shown in (b) 4.5 cm, (d) 6.5 cm, and (f) 8.5 cm. The window and level settings for each of the images in Figure 6-11 were set to maximize the visibility of the speck groups. In the adjustment of image display, the 1 cm blocks of varying glandularity and the smaller masses at the bottom of the grid-out images become less visible with increasing compressed thickness.

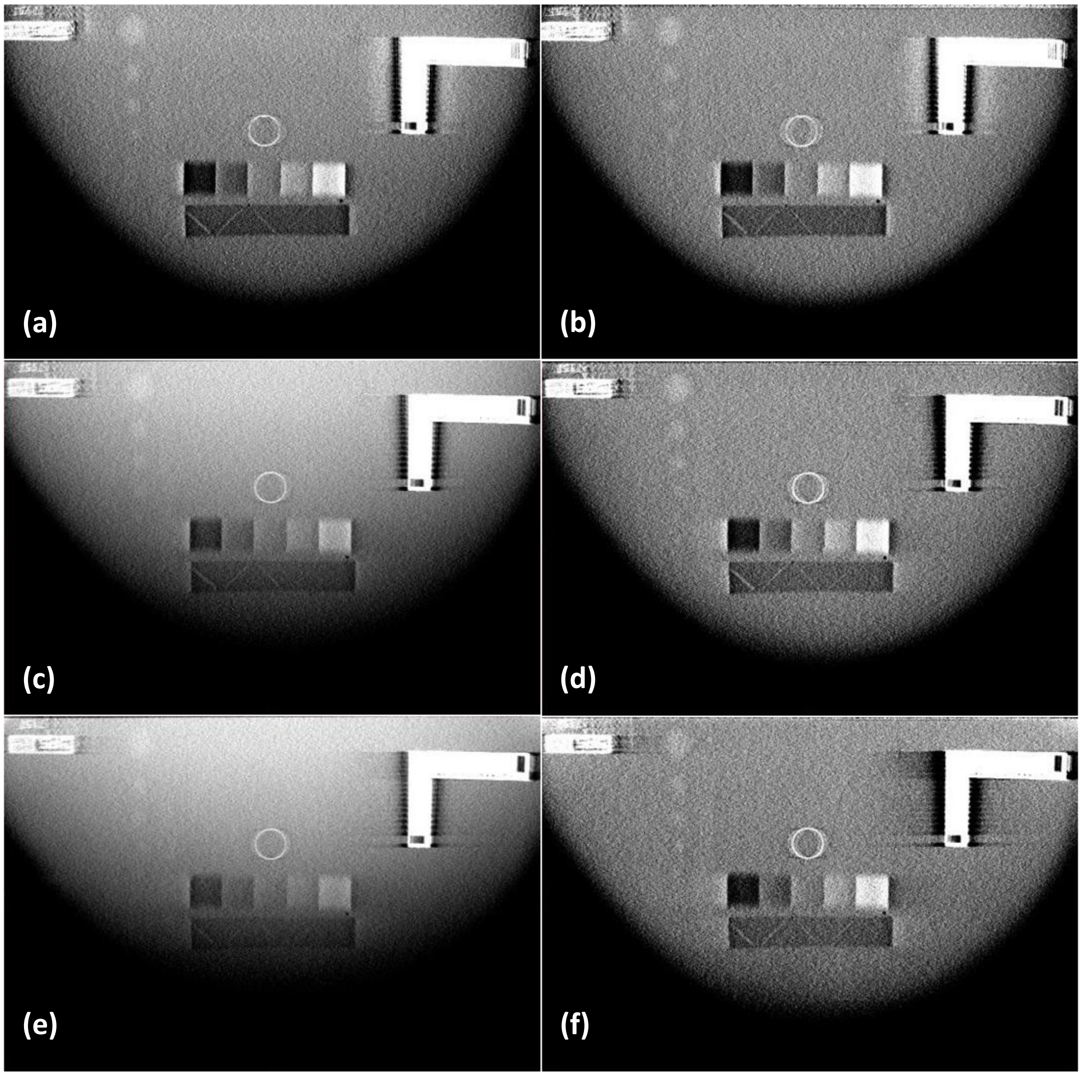

Figure 6-10: Reconstructed slices from the SNS-only data set of the phantoms built from the CIRS model 011A phantom and additional scattering material. Slices from acquisitions without the grid prototype are shown in (a), (c), and (e) for the 4.5, 6.5, and 8.5 cm phantoms, respectively. The corresponding slices from the acquisitions with the W-poly grid are shown in (b), (d), and (f) for the 4.5, 6.5, and 8.5 cm phantoms, respectively. The posterior edge of the detector is at the top of each image.

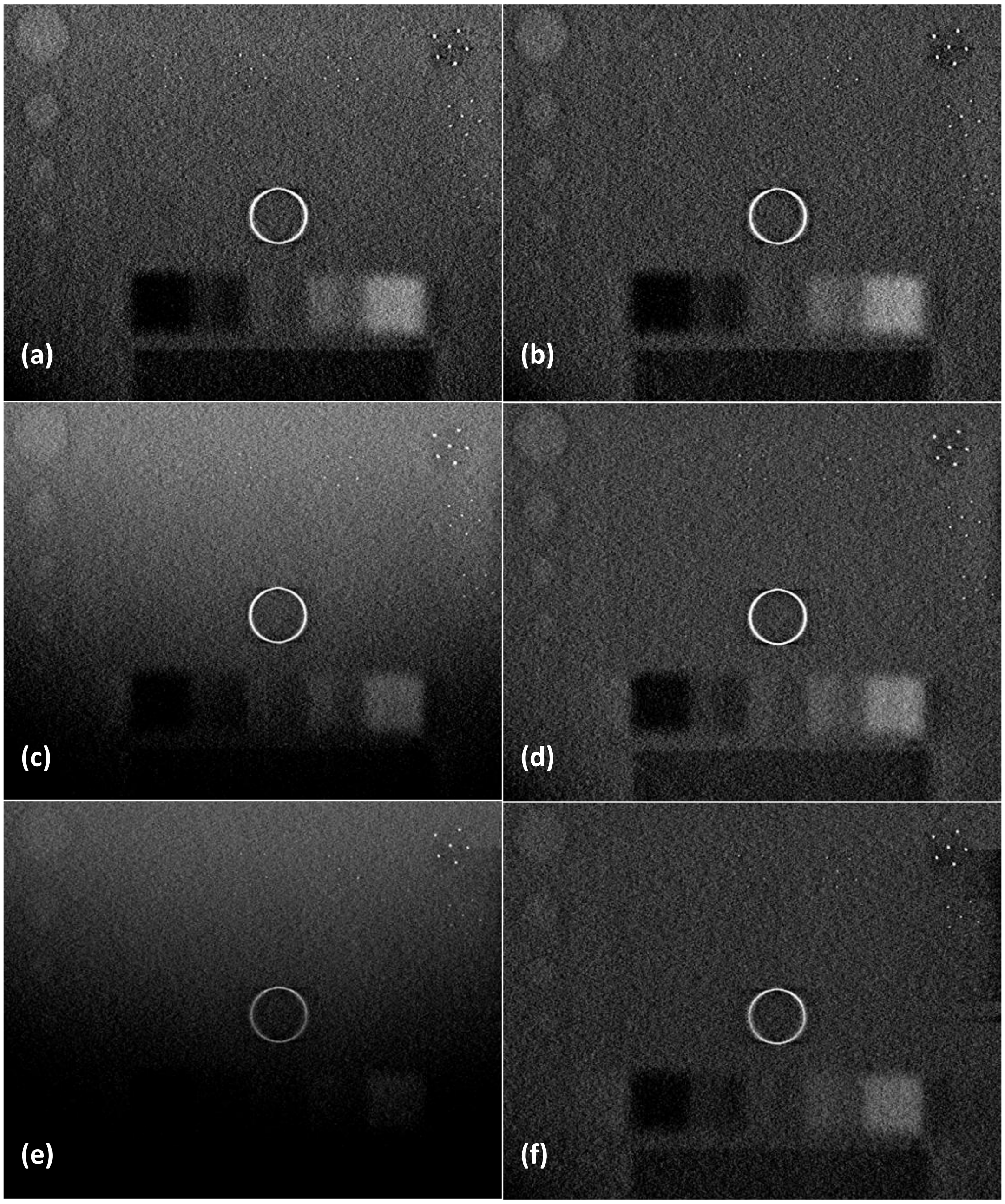

Figure 6-11: Reconstructed slices from the SNS-only data set showing a zoomed view of some of the speck groups and spherical masses embedded in the phantom. Grid-out slices are shown in (a), (c), and (e) for the 4.5 cm, 6.5 cm, and 8.5 cm phantoms, respectively. The corresponding W-poly grid-in slices are shown in (b), (d), and (f) for the 4.5 cm, 6.5 cm, and 8.5 cm phantoms, respectively. The posterior edge of each image is at the top.

6.2.5.3 Line Profiles Through Uniform Background

Figure 6-12(a) is a region of a reconstructed slice of the 4.5 cm grid-out image (SNS-grid vs. SNS-no grid data set) with a red region indicating adjacent columns of voxels that were averaged to create a line profile through the 50/50 block. The anterior side of the phantom is at the bottom of the image. The plots in Figures 6-12(b), (c), and (d) are the averaged profiles through grid-out and grid-in images of the 4.5 cm, 6.5 cm, and 8.5 cm phantoms, respectively. The zero voxel position is at the posterior end of the red region in Figure 6-12(a) and the 100 position is at the anterior end.

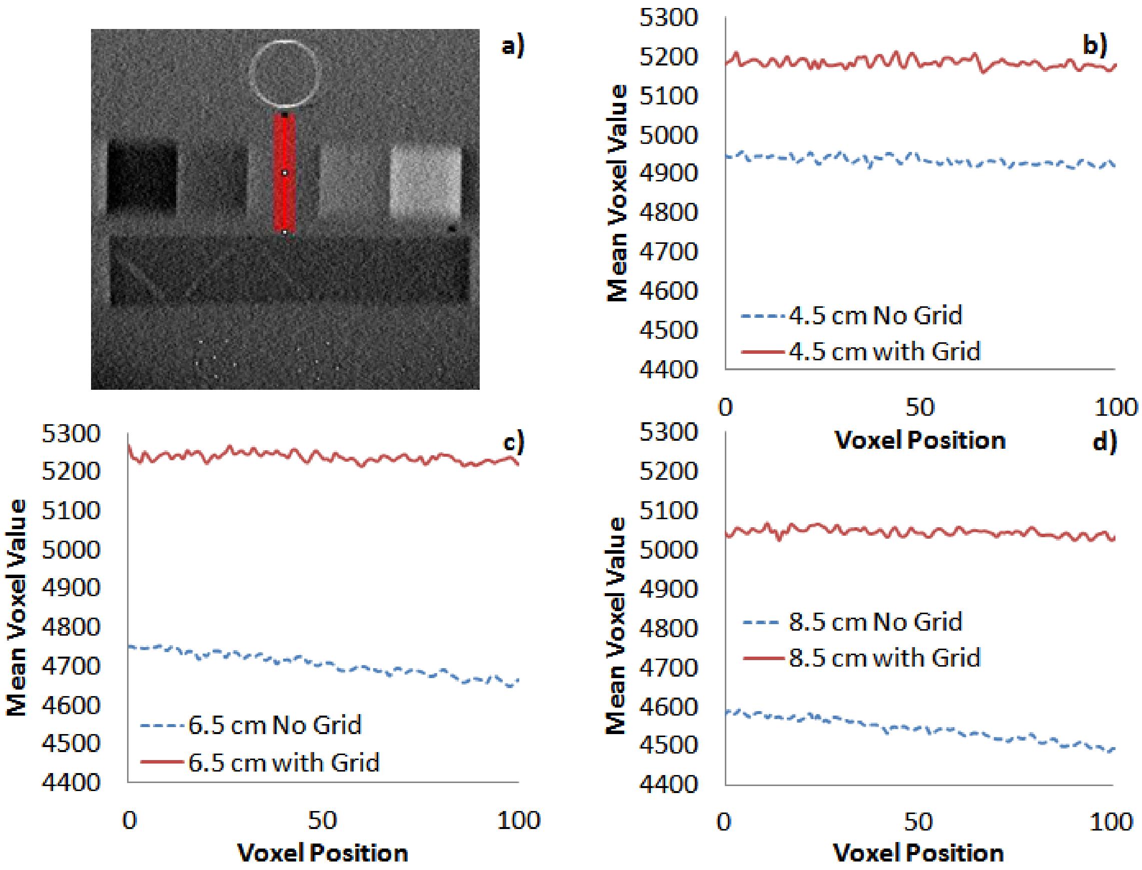

Figure 6-12: Panel (a) is a reconstructed slice of the 4.5 cm phantom showing a region (red) used to create an average profile through the 50/50 block. The anterior side of the phantom is at the bottom of the image. (b), (c), and (d) show the profiles for the 4.5 cm, 6.5 cm, and 8.5 cm phantoms, respectively. Grid-out data are illustrated by the dashed line and grid-in data are shown by the solid line. Voxel position 0 is the posterior-most end of each profile.

Similarly, Figure 6-13(a) shows the same slice as in Figure 6-12(a), but containing a red region used to create an averaged profile in the left-to-right direction parallel to the posterior edge of the detector. Figures 6-13(b), (c), and (d) are the averaged profiles through the 4.5 cm, 6.5 cm, and 8.5 cm phantoms, respectively. The fat layer of the phantom begins at approximately voxel position 20 and transitions to the uniform 50/50 phantom background near voxel position 70 where a shoulder in the profile can be seen. In each case, the grid-in profile has a larger average voxel value.

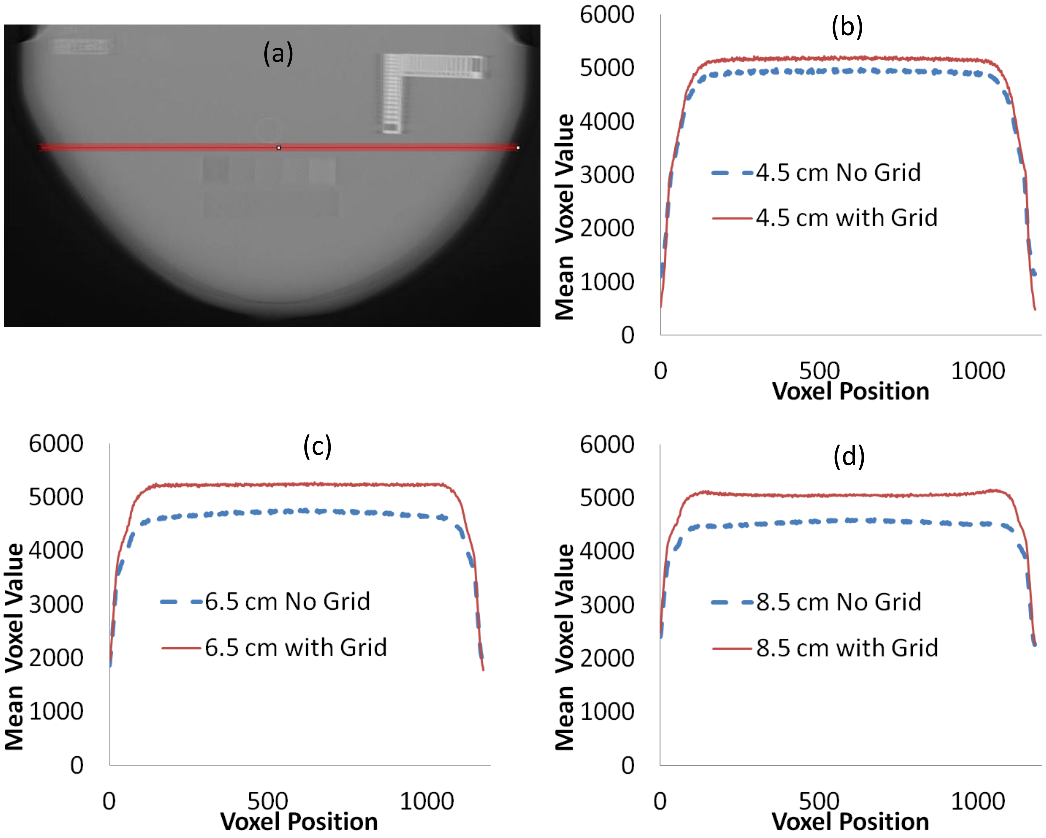

Figure 6-13: Panel (a) is a reconstructed slice of the 4.5 cm phantom from the SNS-only data set showing the red region in which columns were averaged to create a profile through the uniform background in the direction parallel to the posterior edge of the detector. The window/level settings have been chosen to permit visualization of the 0/100 composition skin layer at the phantom periphery. (b), (c), and (d) show the profiles for the 4.5 cm, 6.5 cm, and 8.5 cm plots, respectively. The left side of the image corresponds to the 0 position on the profile plots.

6.2.5.4 SDNR and Contrast Ratios

Figure 6-14 contains plots of the SD, SDNR, and contrast ratios for all phantoms tested in the SNS-grid vs. SNS-no grid data set. Figure 6-14(a) is an example image showing where the ROIs were drawn over the signal blocks and the background block.

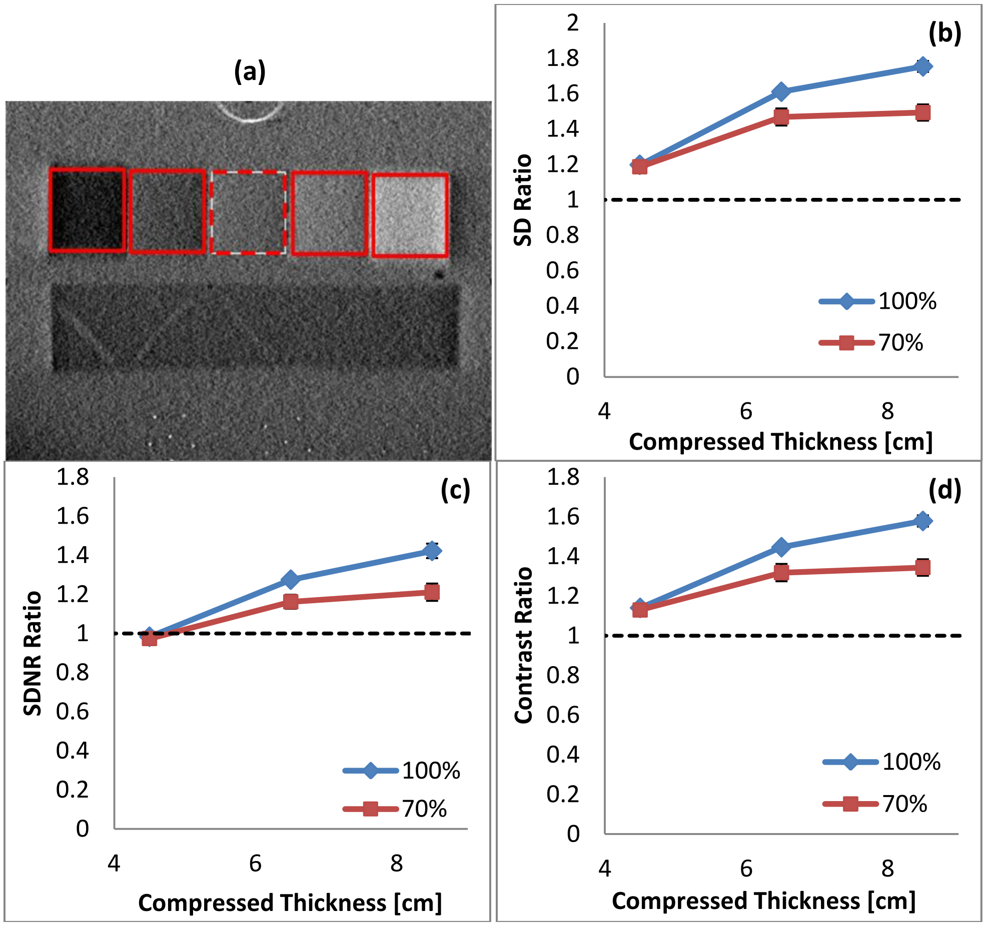

Figure 6-14: (a) shows the locations of the ROIs drawn for measurements of signal difference, SDNR, and contrast. The dashed square in (a) shows the central ROI used for determining the mean background (i.e. 50/50) voxel value and background noise, and the solid ROIs, from left to right, show the 0/100, 30/70, 70/30 and 100/0 ROIs, respectively. (b) is a plot of the ratio of signal difference of the grid-in image to that of the grid-out image versus compressed thickness for the 70/30 and 100/0 block compositions in each phantom. (c) and (d) are the SDNR ratios and contrast ratios, respectively, plotted versus compressed thickness. Diamonds and squares signify the ratios for the 100/0 and 70/30 blocks, respectively. Error bars on the plots are the standard deviation of five trials of the grid-in acquisitions.

The dashed square shows the ROI drawn within the 50/50 block. The 4th ROI from the left in the image is for the 70/30 block and the rightmost ROI is drawn over the 100/0 block. Since the phantoms were not altered or moved between grid-in and grid-out acquisitions, the ROI positions and sizes are identical for a given tested thickness. Additionally, ROIs were drawn large enough to cover most of the block so that any reconstruction artifacts would be averaged out when taking the mean voxel value.

To illustrate the change in the image noise resulting from use of the grid, Figure 6-15 is a plot of the standard deviation σ_B of the voxel values within the 50/50 blocks plotted versus compressed thickness for all phantoms tested. Values of σ_B for the grid-in acquisitions are plotted as circles connected by a solid line and those for the grid-out acquisitions by triangles connected by a dashed line.

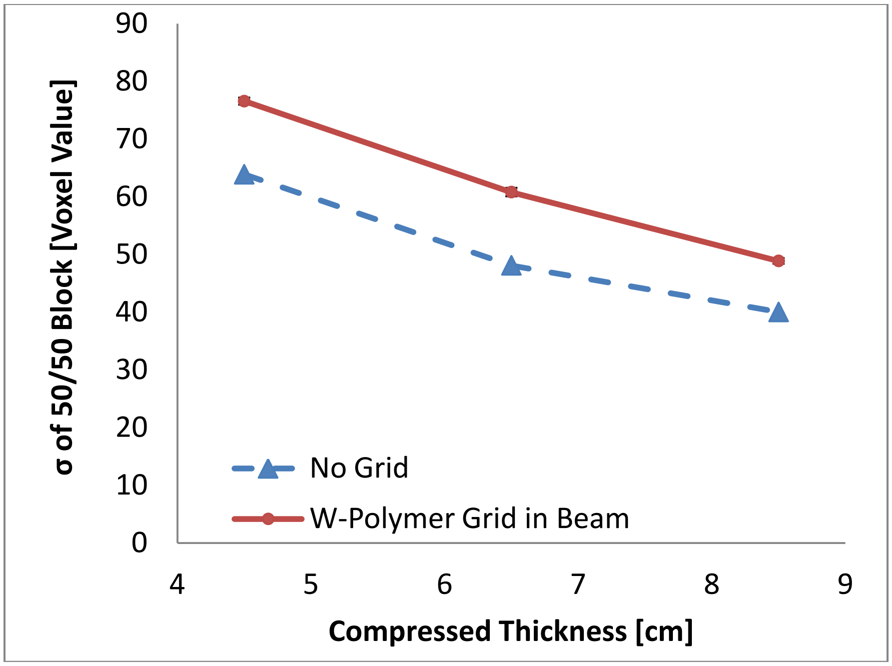

Figure 6-15: Plot of the standard deviation σ_B of the voxels within the background ROI for each tested phantom thickness of the SNS-grid vs. SNS-no grid data set. Grid-out noise is represented by triangles connected by a dashed line, and grid-in noise is plotted using circles connected by a solid line. Error bars from the standard deviation of five trials of the grid-in acquisitions are included, but are smaller than the plotted circular symbols.

The plot shows that the RMS noise in the grid-in image slices is 20%, 26%, and 22% higher than that in the grid-out images for phantom thicknesses of 4.5 cm, 6.5 cm, and 8.5 cm, respectively.

6.2.6 Experimental Results of STR with Scatter Rejection

Because there was not much difference in voxel value between the SNS-only and HMP-grid vs. SNS-no grid data sets, voxel value conversion to μ values of HMP data produced similar results to those seen in Figure 6-8. Profiles through the background of the HMP images were also similar in shape and voxel value to those of the SNS-grid vs. SNS-no grid data set. There were small differences in SD between the SNS-grid data and the HMP-grid data, which resulted in notable differences in the grid-in/grid-out SD, SDNR, and contrast ratios between the two data sets.

6.2.6.1 Reconstructed Slices of CIRS Phantoms

Figure 6-16 contains the slices from the HMP-grid vs. SNS-no grid data set from which SD, SDNR, and contrast were calculated. Figures 6-16(a), (c), and (e) are the grid-out SNS (160 ms exposures) images and Figures 6-16(b), (c), and (d) are the corresponding grid-in HMP images of the 4.5 cm, 6.5 cm, and 8.5 cm phantoms, respectively. While the grid improves the foggy appearance of the 6.5 cm and 8.5 cm phantoms, the lower dose that was applied to the 8.5 cm phantom caused some loss in the visibility of the fibers as compared to the same phantom imaged at a higher exposure level in the SNS-grid vs. SNS-no grid data set in Figure 6-10(f).

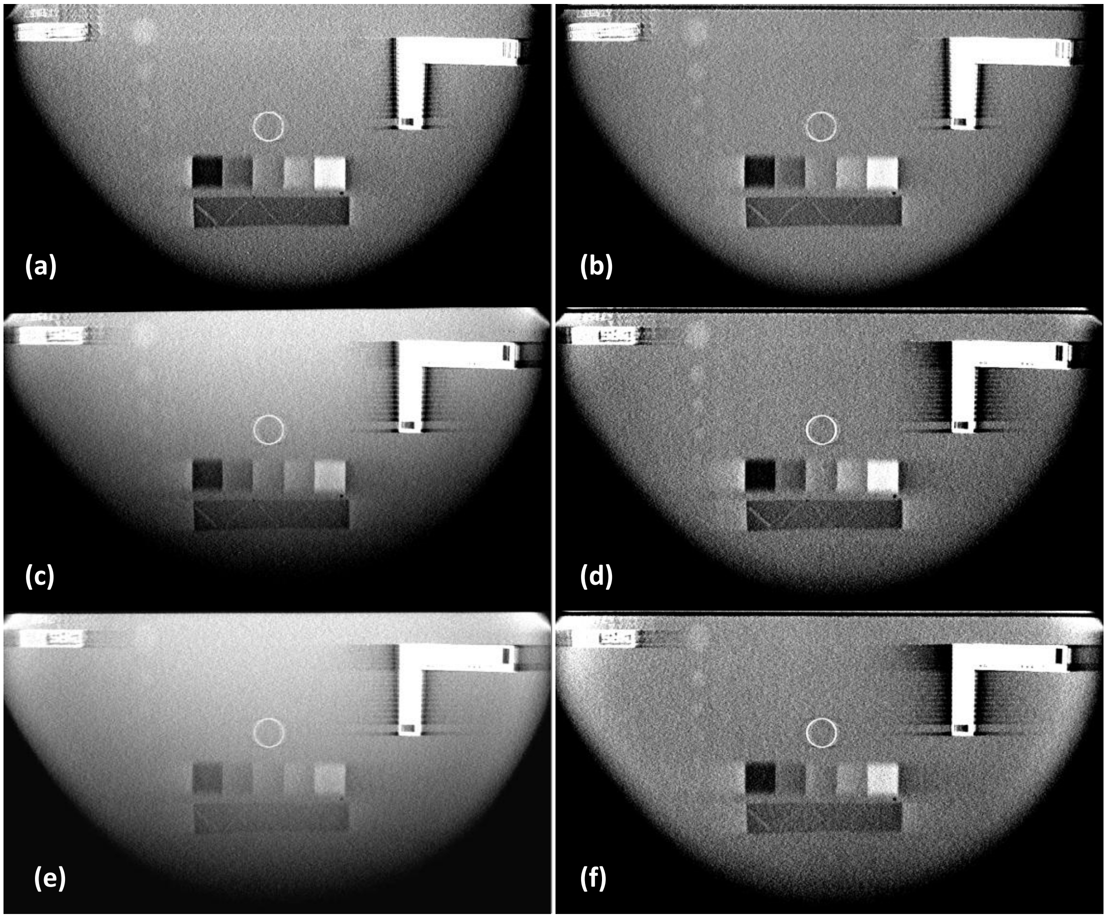

Figure 6-16: Reconstructed slices from the HMP-grid vs. SNS-no grid data set of the phantoms built from the CIRS model 011A phantom and additional scattering material. Slices from 160 ms SNS acquisitions without the grid prototype are shown in (a), (c), and (e) for the 4.5, 6.5, and 8.5 cm phantoms, respectively. The corresponding slices from the HMP acquisitions with the W-poly grid are shown in (b), (d), and (f) for the 4.5, 6.5, and 8.5 cm phantoms, respectively. The posterior edge of the detector is at the top of each image. Tube motion is in the left-to-right direction.

Figure 6-17 contains the SD, SDNR, and contrast ratio plots for all phantoms tested in both the SNS-only and HMP-grid vs. SNS-no grid data sets.

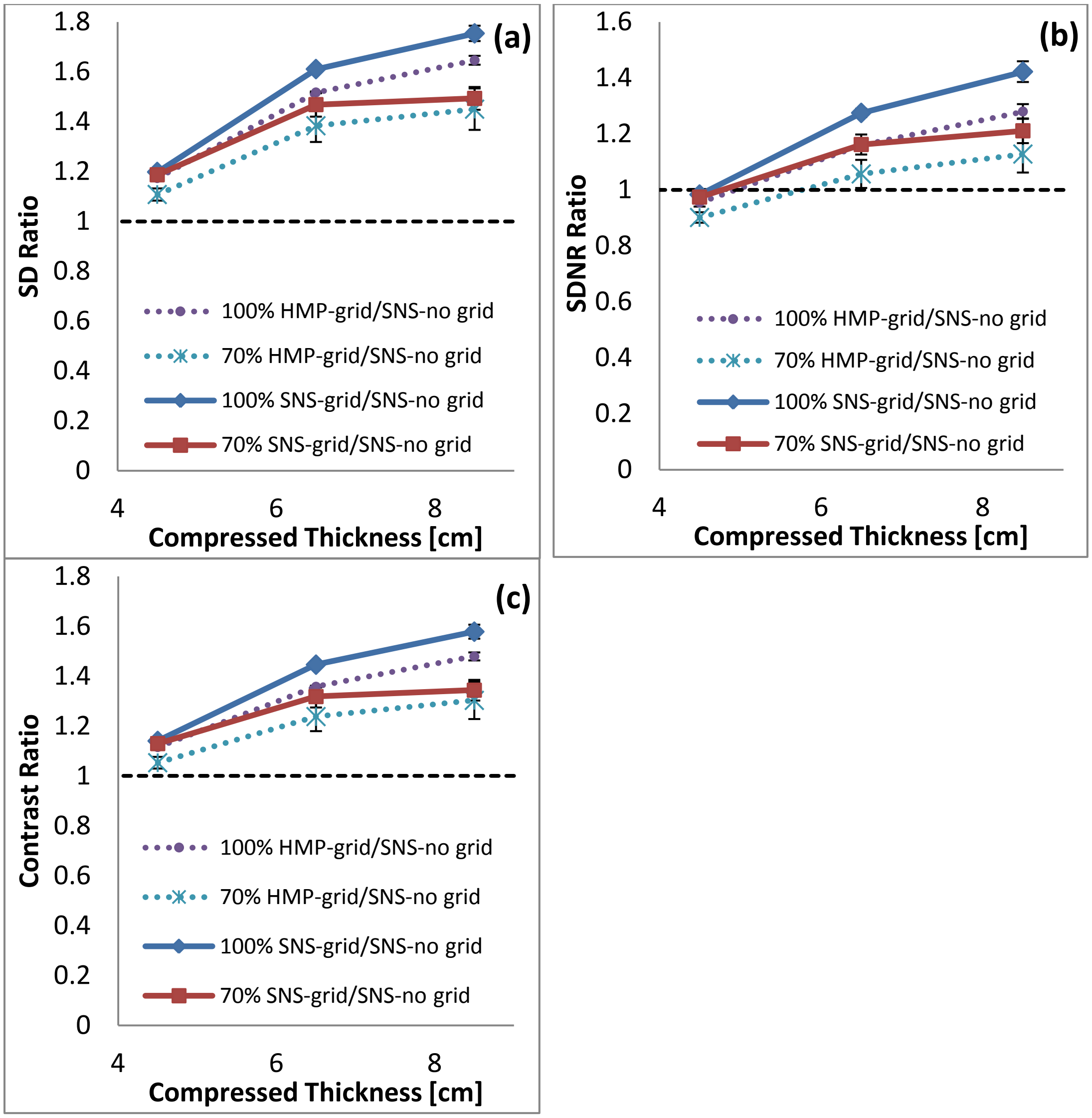

Figure 6-17: (a) is a plot of the ratio of SD of the grid-in image to that of the grid-out image versus compressed thickness for the 70/30 and 100/0 block compositions in each phantom from both SNS-only and HMP-grid vs. SNS-no grid data sets. (b) and (c) are the SDNR ratios and contrast ratios, respectively, plotted versus compressed thickness. Diamonds and squares signify the ratios for the 100/0 and 70/30 blocks, respectively in the SNS-grid vs. SNS-no grid data set. Circles and asterisks connected by dotted lines represent the 100/0 and 70/30 blocks, respectively, in the HMP-grid vs. SNS-no grid data set. Error bars on the plots are the standard deviation of five trials of the grid-in acquisitions.

ROIs for the HMP measurements were drawn in the same locations as for the SNS-only images as shown in Figure 6-14(a). Dotted lines were used for plotting data from the HMP-grid vs. SNS-no grid data set and solid lines were used for data from the SNS-grid vs. SNS-no grid data set.

Figure 6-18 shows σ_B measured from the 50/50 step plotted versus phantom thickness for both the SNS-only data set (reproduced from the curves plotted in Figure 6-15) and the HMP-grid vs. SNS-no grid data set.

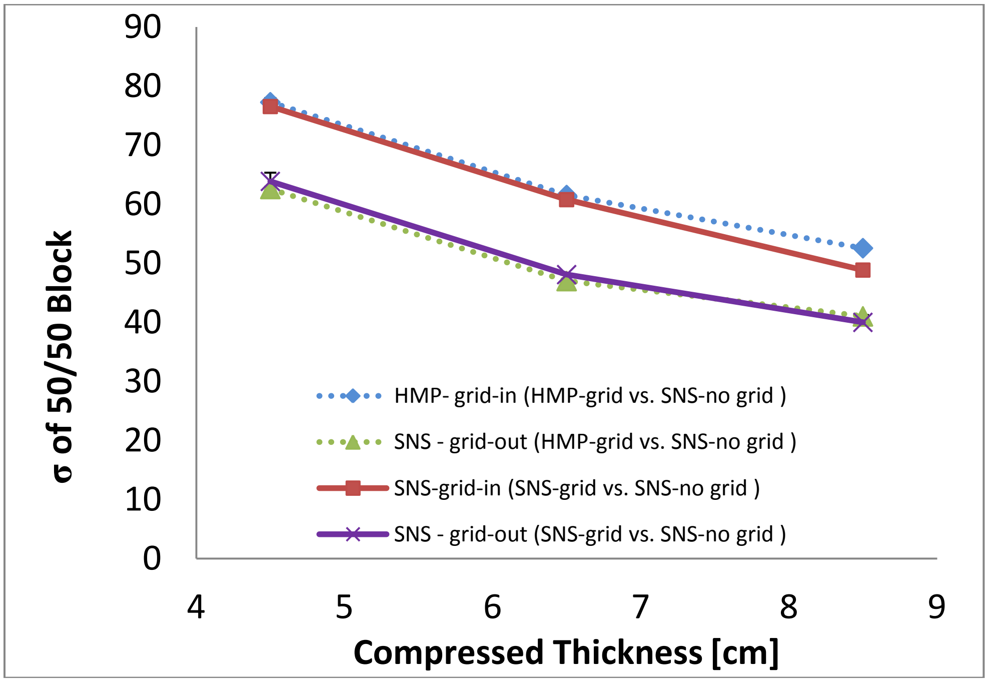

Figure 6-18: Plot of the standard deviation σ_B of the voxels within the background ROI for each tested phantom thickness of both the SNS-grid vs. SNS-no grid and HMP-grid vs. SNS-no grid data sets. For the SNS-grid vs. SNS-no grid data set, grid-out noise is represented by x's connected by a solid line, and grid-in noise is plotted using squares connected by a solid line. For the and HMP-grid vs. SNS-no grid set, grid-out noise is represented by triangles connected by a dotted line, and grid-in noise is plotted using diamonds connected by a dotted line. Error bars from the standard deviation of five trials of the grid-in acquisitions and two trials of the grid-out acquisitions are included, but are smaller than the plotted symbols.

Note that the acquisition parameters for the SNS grid-out from both data sets (purple solid line and green dotted line) were nominally identical except at 8.5 cm thickness, where the mAs per view is lower (28.8 mAs) in the HMP-grid vs. SNS-no grid data set compared to that in the SNS-grid vs. SNS-no grid data set (36 mAs). However Figure 6-18 shows that the noise in the SNS grid-out scans of both data sets was virtually identical at all phantom thicknesses. The reason that the noise was not higher for the 8.5 cm phantom scan in which the mAs per view was lower is unclear. The noise in the

HMP-grid scan (dotted blue line) of the HMP-grid vs. SNS-no grid data set was nearly identical to that of the SNS-grid scan (solid red line) of the SNS-grid vs. SNS-no grid data set except at 8.5 cm phantom thickness, where the increase was slightly higher for the HMP acquisition because of the lower mAs used.

HMP acquisition with the grid in resulted in lower contrast and SDNR ratios compared to SNS acquisition with the grid in. Figure 6-19 is a plot of SD for all blocks within the phantoms for both data sets for (a) 4.5 cm, (b) 6.5 cm, and (c) 8.5 cm phantoms. Figure 6-20 is a plot of the SDNR values for all blocks within the phantoms for both data sets for (a) 4.5 cm, (b) 6.5 cm, and (c) 8.5 cm phantoms.

Despite a difference in SD of ~10% between the grid-in HMP acquisition and grid-in SNS acquisition for the 4.5 cm and 6.5 cm phantoms, the SD for the grid-in data in the HMP-grid vs. SNS-no grid data set is still higher than that of all grid-out data for both 70/30 and 100/0 blocks. The SD for the 8.5 cm phantom is lower in the HMP-grid vs. SNS-no grid data set because of the lower dose used.

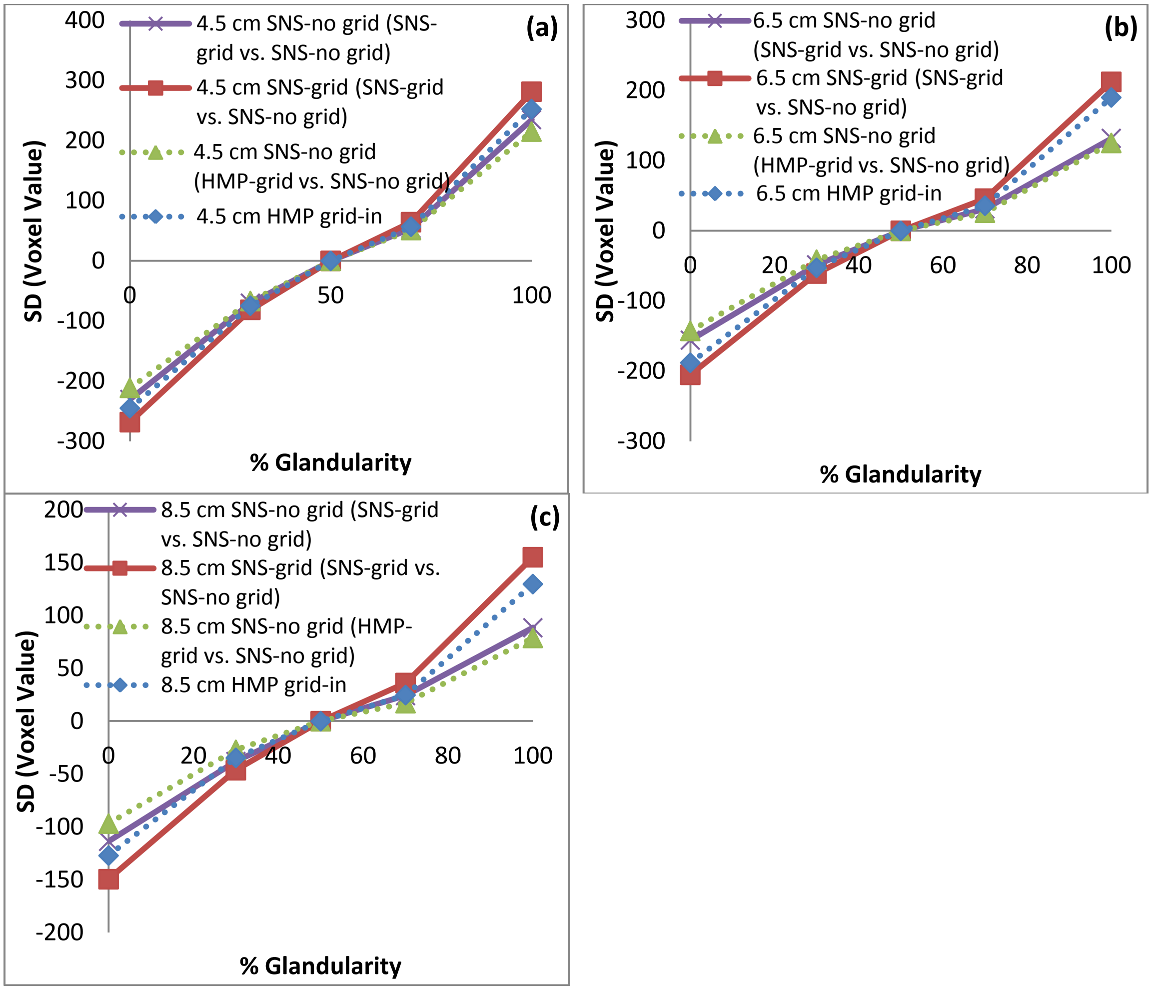

Figure 6-19: Plot of the SDs for all blocks of each tested phantom thickness of both the SNS-grid vs. SNS-no grid and HMP-grid vs. SNS-no grid data sets. Grid-out SDs are represented by x's for the SNS-grid vs. SNS-no grid data set (500 ms) and by triangles connected with dotted lines for the 160 ms SNS acquisitions. Grid-in SDs are plotted using squares for the SNS-grid vs. SNS-no grid data set and diamonds connected with dotted lines for the HMP-grid vs. SNS-no grid data set.

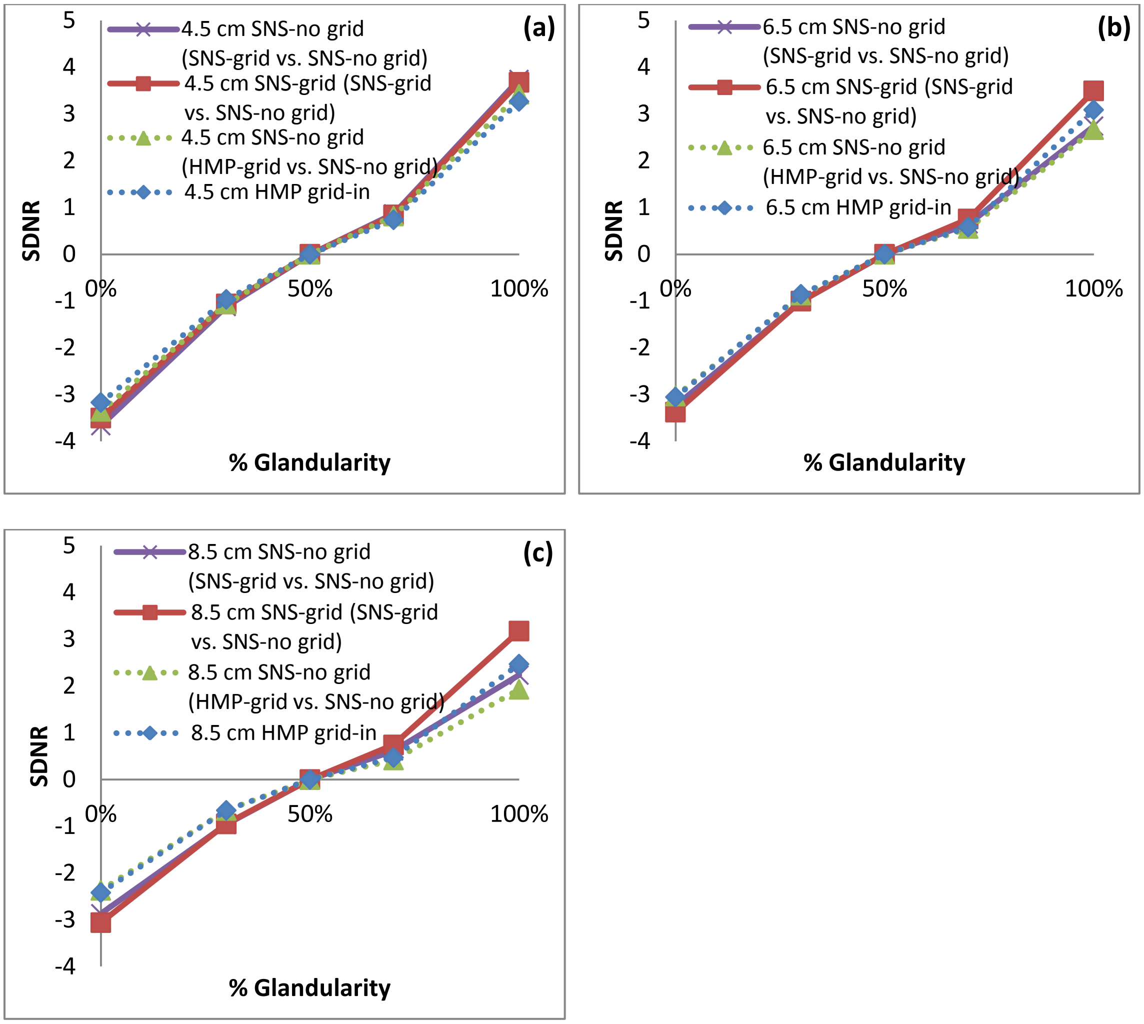

Figure 6-20: Plot of the SDNRs for all blocks of each tested phantom thickness of both the SNS-grid vs. SNS-no grid and HMP-grid vs. SNS-no grid data sets. Grid-out SDNRs are represented by x's for the SNS-grid vs. SNS-no grid data set (500 ms exposures) and by triangles connected with dotted lines for the 160 ms SNS-no grid acquisitions of the HMP-grid vs. SNS-no grid data set. Grid-in SDs are plotted using squares for the SNS-grid vs. SNS-no grid data set and diamonds connected with dotted lines for the HMP-grid vs. SNS-no grid data set.

6.2.6.2 Results of QC Check of HMP Images

To assess whether the small loss in SDNR for the 0% and 100% glandularity blocks using HMP-grid compared to SNS- no grid (HMP-grid vs. SNS-no grid data set) for the 4.5 cm phantom (see Figure 6-20(a)) resulted in unacceptable image quality, the smallest visible features in the grid-in image of the 4.5 cm phantom were compared to what would be considered as passing in clinical DBT QC tests of the ACR phantom. The speck groups are made from aluminum oxide (Al_2O_3), having a higher attenuation than the 100% glandular block [172]. The fibers and mass groups have attenuation coefficients that have not been specified by the manufacturers of the ACR phantom. However, the masses in the CIRS phantom are composed of material simulating 75% glandular and 25% adipose tissue. Figure 6-21 shows focal slices of the smallest visible features in the grid-in HMP image of the 4.5 cm phantom.

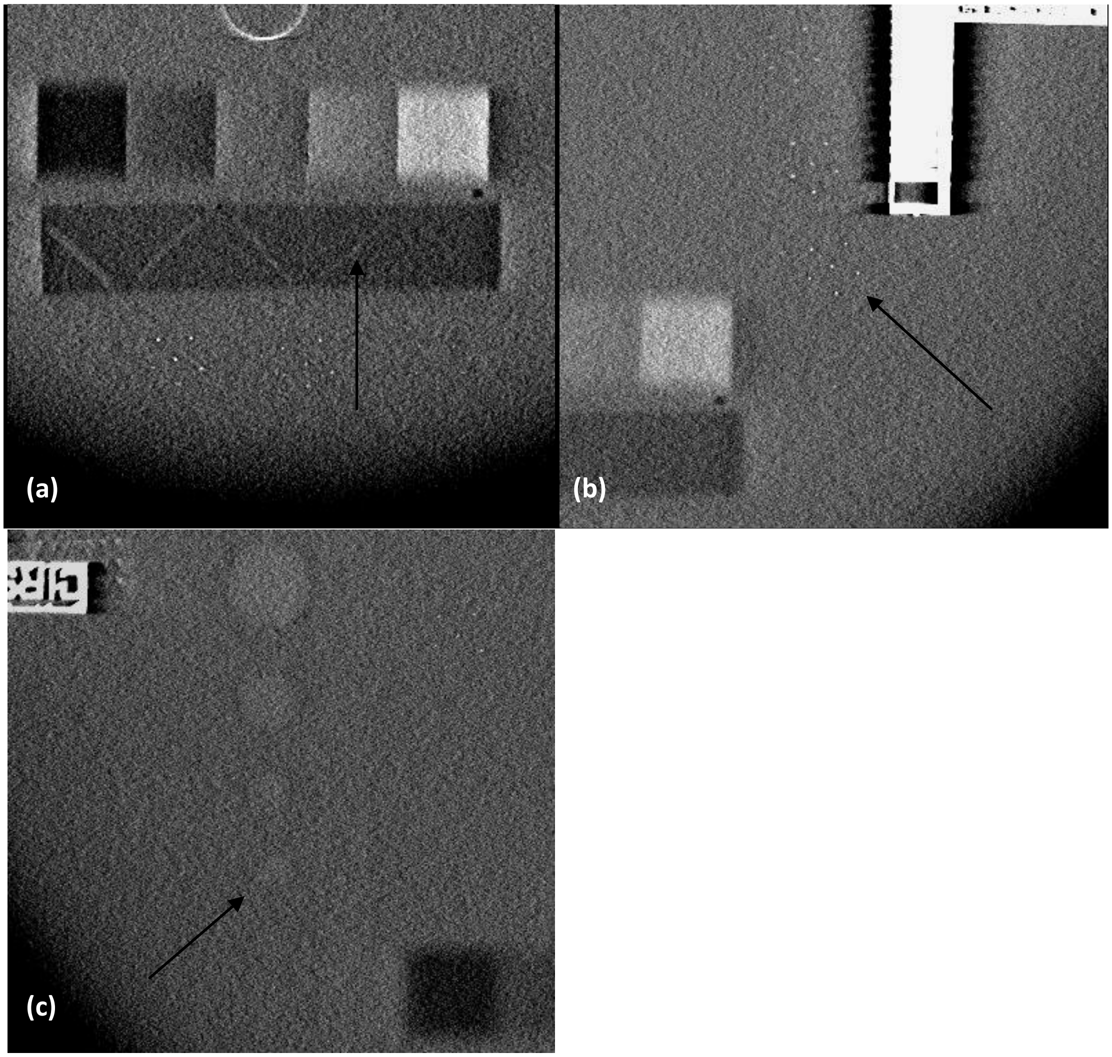

Figure 6-21: Smallest (a) fiber, (b) speck group, and (c) mass that are clearly visible in the 4.5 cm phantom, imaged with the W-Poly grid in the beam and with the gantry in motion during imaging. Arrows point to each of the smallest findings.

Since all features are not in a single plane of the phantom, the slices where they are most in focus are shown separately in Figure 6-21 for the (a) fibers, (b) speck groups, and (c) masses. The smallest visible object of each type is indicated by an arrow. Comparison with Figure 6-22 shows that these are the smallest features visible in the grid-out images of the 4.5 cm SNS-no grid images of the HMP-grid vs. SNS-no grid data set.

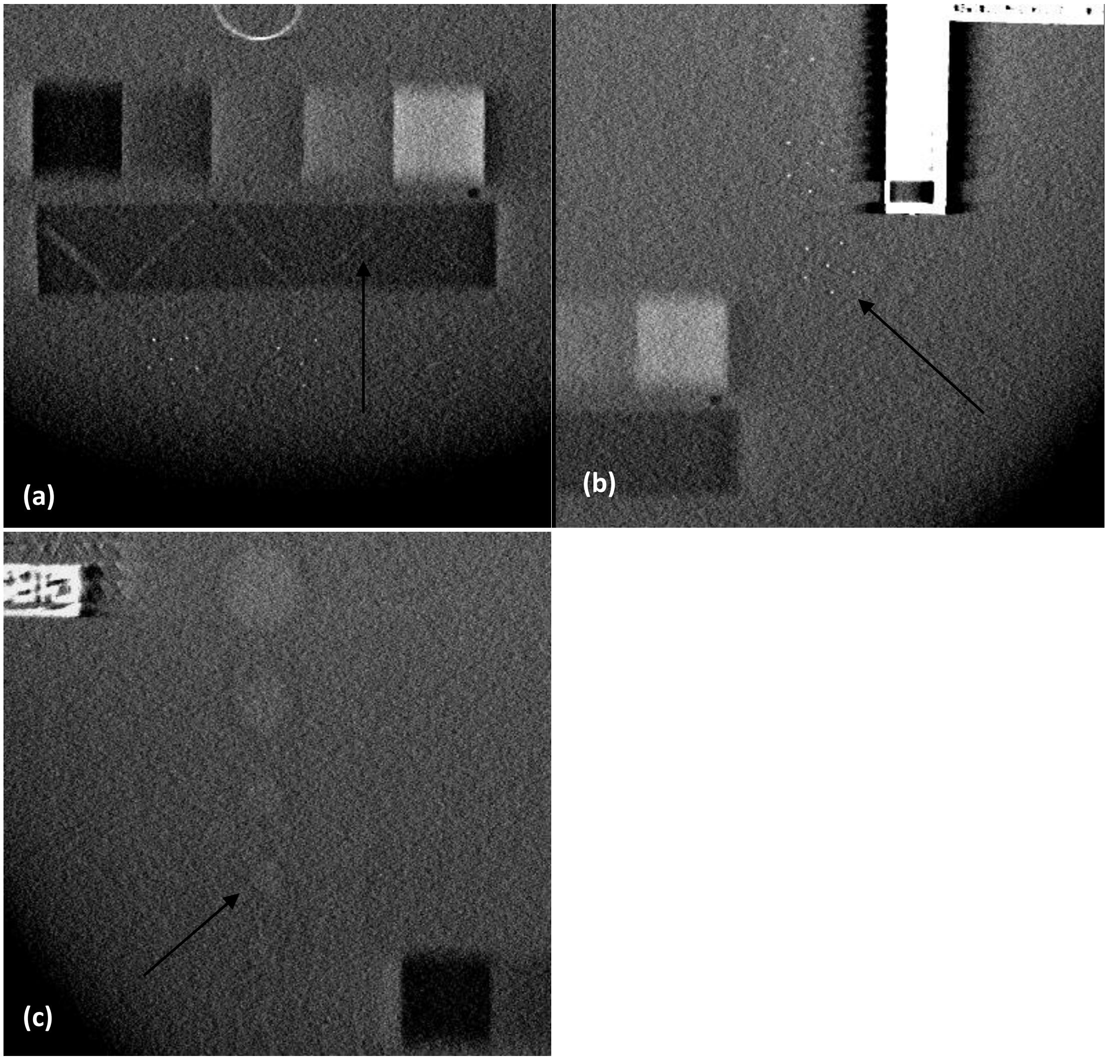

Figure 6-22: Smallest (a) fibers, (b) speck groups, and (c) masses that are clearly visible in the 4.5 cm phantom acquired without the grid and using 160 ms exposures with the SNS method. Arrows point to each of the smallest findings.

Table 6-6 contains the sizes of the smallest features visible in Figure 6-19 along with the sizes of the features in the ACR phantom that must be visualizable in DBT scans to meet Hologic QC requirements.

Table 6-6: Size [mm] of smallest visible features in grid-in HMP image along with passing feature sizes for the ACR phantom per Hologic DBT criteria

Feature	ACR	CIRS
fiber	0.75	0.53
speck group	0.32	0.196
mass (diameter)	5	1.98

Inclusion of the grid improved contrast over the grid-out acquisitions for all compressed thicknesses and tested blocks of the HMP-grid vs. SNS-no grid data set. Although the SDNR ratio (HMP-grid/SNS-no grid) for the HMP-grid vs. SNS-no grid data set for the 4.5 cm phantom was lower than the SDNR ratio (SNS-grid/SNS-no grid) for the SNS-grid vs. SNS-no grid data set (Figure 6-17(b)), all features that were clearly visible in the SNS-no grid image could still be discerned in the HMP-grid image. Thus at the level of the somewhat coarse detectability scale offered by the ACR accreditation phantom, HMP with the grid was equivalent to SNS with no grid for the case of a 4.5 cm phantom.

The ACR phantom was also imaged using the HMP and was compared to an SNS acquisition of the same phantom. There was no grid present for these acquisitions. Figure 6-23 is a focal slice from each reconstruction containing the speck groups, masses, and fibers from the (a) HMP and (b) SNS acquisitions. The smallest visible features within each phantom are boxed using dashed lines for the fiber, solid lines for the speck group, and dotted lines for the mass.

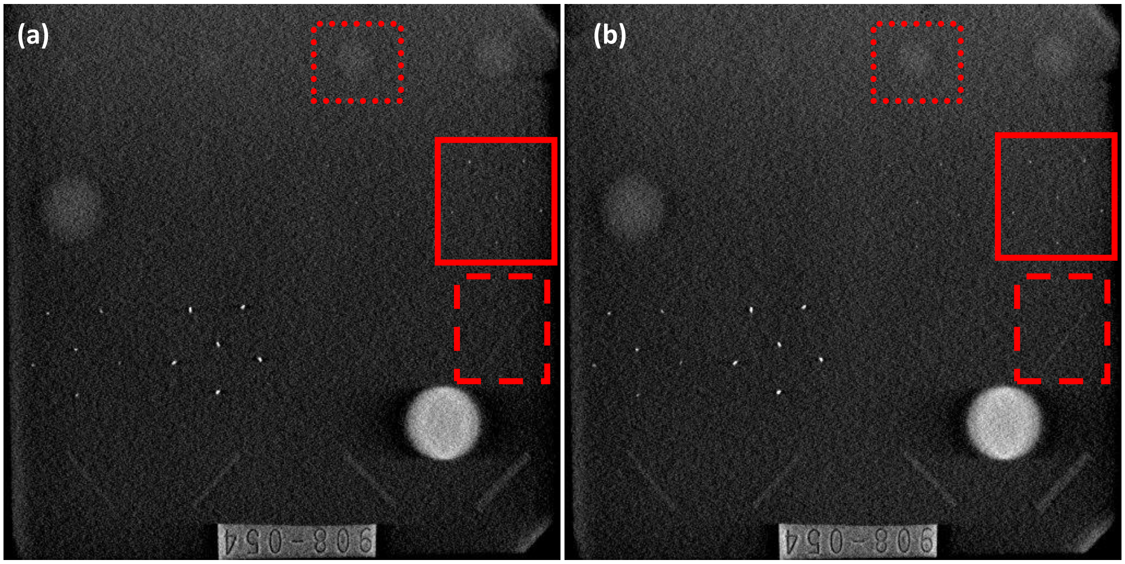

Figure 6-23: Reconstructed slices of the ACR phantom showing the feature slice from the (a) HMP-no grid acquisitions and (b) SNS-no grid acquisitions. Tube motion is in the left-to-right direction. The smallest features that are clearly visible in both images are boxed with dotted, solid, and dashed lines for the mass, a full speck group, and fiber, respectively.

Figure 6-24 shows the reconstructed slices that were used for calculation of SD, SDNR, and contrast and their HMP/SNS ratios of the acrylic disk located on the top surface of the phantom.

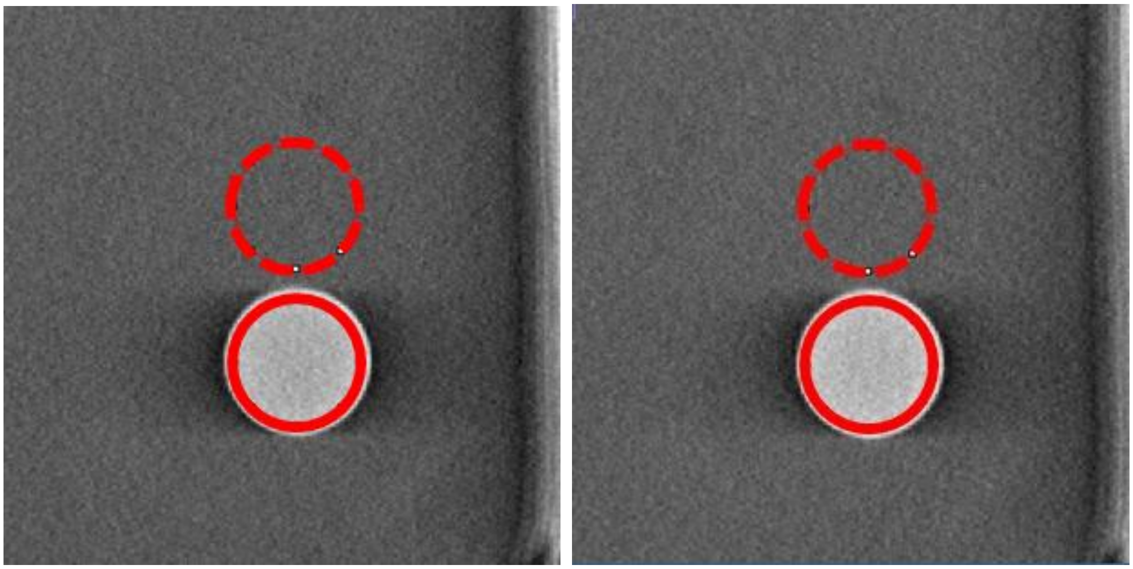

Figure 6-24: Reconstructed slice from which SD, SDNR, and contrast were measured for the (a) HMP and (b) SNS acquisition. The dashed circle shows the ROI chosen for the background and estimate of σ. The solid circle is the ROI drawn over the acrylic disk to calculate the mean voxel value of the signal.

Table 6-7 contains the SD, SDNR, contrast values and their HMP/SNS ratios.

Table 6-7: SD, SDNR, contrast and their HMP/SNS ratios of acrylic disk on ACR phantom

	HMP-no grid	SNS-no grid	HMP/SNS ratio
SD (Voxel value)	476	510	0.93
SDNR	11.31	12.03	0.94
Contrast	0.10	0.11	0.94

6.3 Discussion

6.3.1 Effects of Scatter Rejection

Despite the presence of an air gap of ~15 cm between the detector and the breast support, SPR data shows that there is still a large amount of scatter detected in DMT projection images for all phantom thicknesses and compositions evaluated. While scattered radiation dominates the image in the grid-out case for compressed thicknesses above ~7 cm, the grid prototype rejects the majority of the scatter. Grid-in SPRs are nearly constant (~0.2) over all tested thicknesses, with a magnitude approximately 17 - 20% of that with no grid for PMMA phantoms of 4 cm – 8 cm thickness.

Grid-in/grid-out ratios for SD and contrast (Figures 6-14(b) and 6-14(d), respectively) are well above unity for all tested compressed thicknesses. SDNR ratios (Figures 6-14(c) and 6-17(b)) show that inclusion of the grid resulted in essentially no improvement in SDNR for 4.5 cm thickness, with increasing degrees of improvement with increasing thickness. Since the radiation dose was held fixed for all scans of a given phantom thickness, and a large portion of the scattered radiation as well as some of the primary was removed by the grid, the total number of detected photons in the grid-in projection images is lower than for the grid-out images. This reduction in photon count makes the standard deviation of the voxel-to-voxel fluctuations in the reconstructed grid-in images noisier than that in the grid-out images (Figures 6-15 and 6-18) if the breast entrance exposure is held fixed. However, improvement in the signal difference (and contrast) afforded by the removal of the scattered photons results in improved SDNR for compressed thickness greater than ~5 cm. Furthermore, the fact that the intervals within the error bars in Figures 6-14 and 6-17 all lie above unity for both signal blocks for the 6.5 cm and 8.5 cm thick phantoms provides confidence that the grid improves SD, SDNR, and contrast for those thicknesses in both SNS-grid vs. SNS-no grid and HMP-grid vs. SNS-no grid data sets.

Figures 6-10, 6-11, and 6-16 illustrate the increasing non-uniformity of background voxel values and reduced visibility of fibers and the smaller speck groups as more scattering material is added to the 4.5 cm CIRS phantom in the grid-free images. With increasing phantom thickness, the variation in voxel value in the posterior-to-anterior dimension (going from the top of the image towards the bottom in Figure 6-10) increases, making it difficult to see the masses in the 8.5 cm phantom when the display setting is adjusted as in Figure 6-11(e). Voxel values in the left-right direction are nearly constant over the smaller region where the signal blocks are located. Inclusion of the anti-scatter grid results in more uniform voxel values in the anterior-posterior direction, permitting improved visualization of speck groups, fibers, and masses that are closer to the anterior side of the phantom as shown in Figures 6-10, 6-11, and 6-16.

Cupping artifacts in which higher μ values are observed at the periphery compared to central regions are characteristic effects of scatter observed in transaxial CT slices.

However, in the coronal DBT image slices of this study, cupping is not apparent and rather than an increase in voxel value around the skin line, there is a drop seen in estimated attenuation around the periphery of the breast phantom of the DMT grid-out reconstructions. Lower voxel values around the periphery of the breast were also observed in coronal DBT slices of a similar CIRS 011A phantom by Liu & Li, which they explain is due to an increase in scatter intensity in that region [121]. There is also a fat-simulating (0/100 glandular/adipose) layer that surrounds the 011A phantom resulting in a reduction in voxel value at the outer-most edges relative to those in the background (50/50) region of the phantom. Unlike CTBI, where the breast is more cylindrically shaped, the breast is compressed in DMT scans by a compression paddle and takes on a flattened shape, like the 011A phantom. The compressed shape and scatter from the compression paddle give rise to larger SPR values near the anterior periphery of the breast, as reported by Sechopolous et al [120]. The reason for the higher SPR in that region is the presence of scatter from the compression paddle that falls beneath the peripheral portion of the breast not in contact with the breast support [120]. Thus, while the presence of scatter always results in artifactual reduction in the estimated μ values, the spatial dependence of the voxel value non-uniformity is partially a function of the spatial distribution of the scatter radiation and thus on the particular breast (or phantom) shape [122].

A possible reason for the larger improvement of SDNR and relative voxel value accuracy for the 100/0 block compared to the 70/30 block is a difference in the SPR between the two blocks. Monte Carlo simulations performed by Boone et al. demonstrated that the SPR changed somewhat with glandularity, but not with a noticeable trend [137]. In contrast, Kwan et al. examined the dependence of SPR on glandularity in CTBI and found that SPR increased with increasing glandularity at the center of a 14 cm diameter phantom [173]. Shen et al. found the same trend with a slot-scanning digital mammography system where the SPR for the 8 cm phantom simulating a breast composition of 100% adipose tissue was 0.16 as opposed to an SPR of 0.19 for the 100% glandular phantom of the same thickness [174]. Similarly, Figures 4-4 and 4-6 show an increase in grid-out SPR with increasing glandularity, while grid-in SPRs for different compositions are nearly identical. Thus, scatter removal by a grid reduces the SPR by a larger fraction for higher glandularity blocks than for the lower glandularity blocks.

The difference in fractional improvement in the SPR by the grid may also account for why the correction by the grid of the estimated μ values for the 8.5 cm phantom are slightly lower than for the 6.5 cm phantom. The SPR of the 8 cm PMMA phantom in the presence of the W-poly grid is slightly higher than that of the 6 cm phantom. Even though the grid-out SPR for the 8 cm phantom is higher (1.36) than that for the 6 cm phantom (0.87), the resulting scatter rejection by the grid reduces the SPR by a factor of 5.8 for the 8 cm phantom and by a factor of 6.0 for the 6 cm phantom. The slightly larger fraction of scatter removed in the 6.5 cm case, could be part of the explanation for why the correction in μ by the grid was slightly better than for the 8.5 cm phantom.

The observed percent errors in image-based μ of 5% or more compared to theoretical values can be attributed partially to the polyenergetic beam and partially to DBT artifacts resulting from its incomplete angular sampling. The incomplete sampling results in the smearing of attenuation in the direction perpendicular to the planes of the reconstructed slices. Thus, unlike CT, in which voxel values are representative of the attenuation in a small volume centered on each voxel, in DBT, they are impacted by the attenuation in slices above or below the voxel in question. Figure 6-8 shows that, in the presence of scatter, the μ values of blocks with glandularities lower than that of the surrounding 50/50 background are artificially raised, while those with higher glandularity are lowered. This finding is consistent with the fact that slices above and below the block slices contain 50/50 material.

6.3.2 Effects of STR Combined with Scatter Rejection

As seen from analysis of the ACR phantom (HMP-no grid vs. SNS-no grid in Table 6-7), there is some loss in SD, SDNR, and contrast when using HMP alone. Gantry motion may also explain why grid-in SD and SDNR were lowered between SNS-grid and HMP-grid acquisitions of the 4.5 and 6.5 cm CIRS phantoms (Figures 6-19 and 6-20). The gantry’s servo motor was always tuned with the grid absent. Since the gantry motor requires proper tuning for the load it is moving, the additional mass of the grid and its hardware may have caused more perturbations during motion than if the grid and its hardware were not present. This could have lead to larger errors in the encoder angle measurements used for reconstruction. Mainprize et al have shown in simulation studies that inter-projection errors as small as 0.14° can reduce lesion intensity by 20% [102]. SD was reduced by 10% between the HMP-grid and SNS-grid acquisitions of the 4.5 cm and 6.5 cm phantoms for both the 100% and 70% glandular blocks. If errors in angles used for reconstruction caused this reduction, the gantry motor can be tuned to reduce perturbations and discrepancies in speed to improve contrast and SDNR of HMP-grid images.

The variations in SD, SDNR, and contrast measured over 5 trials for the SNS-grid vs. SNS-no grid data set are small for both the 70/30 and 100/0 blocks, but slightly larger for the 70/30 blocks. On the other hand, the trial-to-trial variations for the HMP-grid vs. SNS-no grid data are somewhat larger. A 60 x 60 voxel^2 ROI was used for measuring the signal, which included the edges of the blocks. The reconstruction algorithm creates non-uniformities over the block such that the left edge of the 70/30 block is brighter than and the right edge is darker than the center of the block in the reconstructed volume (Figures 6-16 and 6-21). If smaller ROIs were selected to just include the more uniform region of the signal blocks, this could reduce the trial-to-trial variations that caused the larger error bars of the 70/30 blocks in the 6.5 cm and 8.5 cm HMP-grid images of the HMP-grid vs. SNS-no grid data set (Figure 6-17).

The maximum individual view exposure time of 160 ms used in the HMP tested here, along with the maximum tube current of 180 mA, limits the maximum possible breast entrance fluence per view. This is especially important for larger compressed thicknesses, where the number of image photons could be less than optimal. In the cases where the dose applied in the clinical FFDM scan is higher than the HMP-limited dose, it would be recommended to use the grid-in SNS method for image acquisition using exposure times that are longer than 160 ms.

Acquisitions other than the HMP scheme tested here may also allow for a higher total number of DBT image photons. For example, exposure times could be varied between projections, with longer exposures used for the stationary views or a combination of longer exposures and slower gantry speed for the moving views. However, the Dexela x-ray detector used in these studies requires over 500 ms to process the command for setting the detector integration window. Therefore, it is possible that additional time would have to be programmed during the scan to allow for this change in the setting of the detector exposure time if the inter-view gap time was insufficient. Furthermore, because the current Dexela reconstruction algorithm assumes the same tube output for every projection view, some additional post-acquisition work would be required to scale the pixel values in each projection image individually to correctly normalize the pixel values under the breast to those that would be obtained from the unattenuated beam in the absence of detector saturation. Currently this normalization is the same for all projection images.

Another possible acquisition scheme to increase the total number of x-ray photons in the scan would be to add more projections to the scan. For an HMP acquisition these projections could be added between the more widely separated angles, which could increase overall scan time somewhat depending if the gantry comes to a stop for each additional view, or simply reduces its angular velocity sufficiently to obtain constant velocity moving views. Alternatively, these views could also be added between the more closely-spaced constant-velocity projections. Under any circumstances, the time required for the gantry to travel from one projection to the next must be long enough to allow for detector readout, repositioning of the grid, and preparation of all equipment for the next exposure.

Studies have shown that tomosynthesis imaging can benefit from the use of anti-scatter grids at the cost of increasing radiation dose for the smaller compressed thicknesses [175]. Our initial experience with the prototype 2D focused grid used with the investigational DMT scanner shows that DBT scans with isocentric systems can benefit from the addition of an anti-scatter grid. For the range of phantom thicknesses tested here, the SD, SDNR, and lesion contrast all either improved or remained approximately unchanged with the addition of the grid under conditions of fixed radiation dose. Observer studies can be performed to determine whether grid-in DBT scans of thinner breasts would be recommended in light of the relatively small amount of scatter to reject and the inevitable loss of primary photons. However, experimental results for the 6.5 cm and 8.5 cm phantoms imply that for thicker breasts an FFDM-equivalent dose may be sufficient to compensate for primary attenuation by the grid in order to maintain SDNR. For DBT scans of larger breasts where the system AEC is often programmed to increase the fluence at the detector surface compared to that for thinner breasts to overcome the effects of scatter [170], the use of a grid could reduce or eliminate this requirement and permit lower radiation dose for large breasts.

Chapter 7

Conclusion

7.1 Summary & Conclusion

To achieve scan time reduction (STR) of DMT DBT scans, gantry motion during imaging was explored for replacing the step-and-shoot (SNS) method, which had been employed for use with the outdated CCD detector of earlier DMT scans. A gantry angular speed limit ω_{limit} was calculated by placing a limit on the maximum allowable blur b, defined as the distance over which a single point projects onto the detector over a given exposure. It was determined that the exposure times for each projection image must be shortened to cut down the overall DBT scan time. The final selected exposure time for all projections was chosen to be 160 ms, a factor of 2 smaller than the 320 ms exposure time typical of DMT clinical trials.

MTF data showed a reduction of spatial resolution in the unbinned projection images that were acquired when the gantry was moving at a constant speed of ω_{limit} calculated for an exposure time of 160 ms. Since 2x2 binned images are used for image reconstruction, it permitted the use of double the value of ω_{limit} during image acquisition.

To reduce scan time further, acceleration was introduced between views separated by ≥ 2º. A hybrid motion profile (HMP) of the gantry was developed so that the gantry would be moving for seven of the thirteen exposures acquired for DMT DBT. The HMP was tested on phantoms consisting of 1.5 mm diameter BBs. Difference in BB widths of the HMP images and the SNS images was well below 5% and was imperceptible in the profiles drawn through the BBs. However, measurement of SDNR and contrast of an acrylic disk found on the ACR mammography phantom within the HMP reconstruction slices revealed that there is some loss in image contrast. Inaccuracies in projection angle measurements used in the reconstruction as well as motion blur could potentially be the cause.

Detector characterization in high dynamic range (HDR) and high sensitivity (HS) modes of the CMOS detector showed that the detector is capable of acquiring images over a large range of exposure levels, including the lower exposures required for STR, without degrading image quality from read noise. This result is of particular importance when considering a reduction in the total DMT DBT dose and the implementation of a scatter rejection method.

SPRs illustrated that there is a significant amount of scatter in DMT DBT projection images despite an air gap of ~15 cm. The SPR for an 8 cm phantom was found to be greater than unity, demonstrating that scatter radiation dominated the images of the average breast seen in DMT clinical studies. SPR experiments performed with the three grid prototypes showed that scatter can be significantly reduced from DMT DBT images through the integration of an anti-scatter grid. It was also confirmed that grid performance depended upon the grid parameters of height, spacing, septal thickness, and material used, where the tungsten-polymer (W-poly) grid provided the best scatter rejection of the three that were tested. Characterization of grid performance of the prototypes provided relations for determining optimal parameters for the final full-sized grid for use in future DMT clinical trials.

A novel anti-scatter grid reciprocation design was formulated, built, and tested for DMT DBT acquisitions. The described shift-and twist (ST) reciprocation scheme was found to allow nearly the same primary transmission as for the focused, stationary grid case, with a 2% reduction in intensity over the full active area of the grid. It was discovered that the ST motion scheme created grid line artifacts (GLAs) in the projection images, which were suppressed through flat-field correction (FFC). Artifacts in the reconstructed images that arose when residual lines were not corrected by FFC were reduced through image filtering in frequency space. The proposed motion scheme can provide efficient removal of scatter, potentially limiting the increase in radiation dose to the patient that may be necessary for maintaining the signal to the x-ray imager during grid-in acquisitions.

After building and integrating the grid reciprocation hardware into the DMT DBT system, phantom experiments were performed for analyzing grid-in image quality with and without the HMP of the gantry during imaging. Under conditions of fixed radiation dose to the breast, use of the 2D focused W-poly grid prototype increased contrast and accuracy of estimated linear attenuation coefficients μ of mass-simulating features with μ values that were greater than or equal to that of the surrounding tissue for the phantom thicknesses tested. The degree of improvement was found to be dependent upon material composition where more improvement was seen for compositions with higher percentages of glandular tissue. It was concluded that a 2D anti-scatter grid can be usefully incorporated in DBT systems that employ fully isocentric tube-detector rotation.

The utilization of a voice-coil positioning stage, capable of high force, oscillatory motion, made the use of a reciprocating 2D grid feasible when combined with the HMP for STR. However, it was determined that due to the limitations of the DMT x-ray tube, the described HMP using a 160 ms exposure time and 13 projection images would not be recommended for subjects whose clinical FFDM scan doses are much higher than the HMP-limited maximum achievable doses. In these cases, reverting back to grid-in SNS acquisitions with longer available exposure times or exploring other HMP motion schemes would be more beneficial to limit the relative image noise that increased with very low dose.

As a result of the change in the gantry motion profile and an upgrade of the x-ray detector, the scan time for the DBT portion of the DMT scan was effectively reduced from approximately two minutes to a 20 second scan for target dose levels that could be achieved using 160 ms exposures. In addition, with the introduction of the reciprocating grid and the use of HS mode, scatter rejection in DBT was found to improve upon grid-out acquisitions at the same exposure level as single-view mammography.

7.2 Future Work

7.2.1 Dose Optimization

In most clinical mammography and DBT units, automatic exposure control (AEC) is used for determining the exposure techniques to use for a given breast. For digital systems, AEC requires a low dose exposure, referred to as a pre-exposure, to determine optimal x-ray techniques [176]. For the DMT human subject clinical trials, the exposure techniques for the DBT scan are set to obtain approximately the same average glandular dose (AGD) as the subject's most recent clinical mammogram. These total doses are divided equally among thirteen projection images. However, with a more efficient scatter removal method made possible with the presented grid reciprocation design and better scatter rejection provided by a 2D grid [129], the applied DMT DBT radiation doses must be optimized to deliver the minimum dose necessary. Rather than using projection data for this optimization, an FOM optimization done upon reconstructed images where the accuracy of the estimated μ values are optimized can potentially be formulated to find the most favorable exposure techniques.

7.2.2 Human Subject Studies

Preliminary results of phantom studies done with the inclusion of an anti-scatter grid prototype show considerable improvement in SDNR and contrast in the grid-in reconstructed images of the thicker phantoms. There was also an improvement seen in the estimation of the linear attenuation coefficients for the same dose employed for grid-out acquisitions. Despite these promising results, it is yet to be seen whether this increase in contrast and SDNR will translate to an improvement in the detectability of subtle cancers and calcifications in a real human breast. For this analysis, findings from grid-in DMT DBT acquisitions must be compared to clinical images of the same breast, such as a clinical DBT scan. Hardware modifications are being made to accommodate a full-sized grid for the next phase of the DMT human studies.

Researchers are continually making strides in the development of existing imaging technologies to detect cancer in its earliest stages. Currently, there is no single imaging modality that can be applied universally for correctly diagnosing the presence or absence of cancer. However, scanners that combine modalities, such as the DMT, may provide better diagnostic tools for a wider range of breast types in the future.

APPENDIX A: CODE FOR PROGRAMMING HYBRID MOTION PROFILE (HMP)

```
//Setting acceleration as constant over entire profile

ExposureStruct[] sortedList = (ExposureStruct[])input;
Single speed_fast, AccelRate, DecelRate;
target = (Single)sortedList[numImages - 1].angle + padAngle;

Single term1, Range, NumStepsTemp = 0, next_term;
int waitTime = 100;

Single f_accel;       //fraction of gap time used for accelerating [seconds]
Single f_const_off;   //fraction of gap time used for constant speed when x-rays are off [seconds]
Single f_decel;       //fraction of gap time used for decelerating [seconds]

Single f_d = (Single)(1-(f_a + f_vc));
Single delThetaSteps = (Single)0;
int after_const_speed_interval = 0, m = 0;
Single firstRange, lastRange, stepSum = 0, timeSum = 0;

firstRange = (Single)MotorLogic.DegreesToSteps(sortedList[0].angle);
lastRange = (Single)MotorLogic.DegreesToSteps(sortedList[numImages - 1].angle);
if (firstRange < 0) firstRange *= -1;
if (lastRange < 0) lastRange *= -1;
if (lastRange > AngRangeLimit || firstRange > AngRangeLimit)
{
    VelProfFile.WriteLine("Angular range is too large");
    Console.WriteLine("Angular range is too large.  Returning...");
    continueSequence = false;
    goto ReturntoMain;
}
//Imaging speed:
speed = (Single)((delTheta) / ((sortedList[0].milliSeconds) / 1000));
//delTheta is angle traversed during x-ray on time. Images in milliseconds
//***This must be constant*** and exposure time chosen must be the same as the x-ray on time.
//Must keep all exposure times the same for all projections within a given acquisition to avoid
//detector initialization of new values for each projection (this takes a long time).

Single tempInterval;
Single padAngleTemp = (Single)0;
Single padAngleSteps = (Single)(MotorLogic.DegreesToSteps(padAngleTemp));
Add an extra degree to the end of the acquisition to keep from having jerky motion in the image

String MoveCommand;

//PROF1 is preprogrammed profile with 13 projection views from -12 to 12.
MotorLogic.SendCommandMotorDriveBy("DEL PROF3", false);  //Delete any data from previously
programmed profile #1
MotorLogic.SendCommandMotorDriveBy("DEF PROF3", false);  //Start new definition of profile #1
MotorLogic.SendCommandMotorDriveBy("MC0", false);  //Start new definition of profile #1
```

```
int m_before_const_v = -99;
for (int j = 1; j < numImages; j++)
{

    //Angle traveresed between x-ray on time intervals
    tempInterval = (Single)((sortedList[j].angle - sortedList[j - 1].angle));

    if (tempInterval > 3) AccelRate = 30; //Keep acceleration fixed throught motion
    else if (tempInterval <= 3 && tempInterval > 2) AccelRate = 25;//
    else if (tempInterval <= 2 && tempInterval > 1.5) AccelRate = 15;//
    else AccelRate = 5;

    DecelRate = (Single)(AccelRate * (f_a / f_d));  //Asymmetric trapezoidal velocity profile between
projection views

    if (j < numImages - 1) next_term = (Single)(sortedList[j + 1].angle - sortedList[j].angle);
    else next_term = 99;
    if (next_term < LimitingAngularInterval && m_before_const_v < 0) m_before_const_v = j+1;

    term1 = (Single)((sortedList[j].angle - sortedList[j - 1].angle));//

    if (term1 > LimitingAngularInterval && NumStepsTemp > 0 && DecelArray[j - 1] > 0) term1 -=
(Single)(0.5 * speed * speed / (DecelArray[j - 1] / 2));

//S-curve time:
    x_t[j] = (Single)(Math.Sqrt((double)(term1 / (0.5 * (AccelRate/2) * f_a * (f_a + 2*(f_vc + f_d))+ 0.5 * (-
DecelRate/2) * f_d * f_d ))) * 1000); //gap time between images

    f_accel = (Single)(x_t[j] * f_a / 1000);       //fraction of gap time
              used for accelerating [seconds]
    f_const_off = (Single)(x_t[j] * f_vc / 1000);   //fraction of gap time
              used for constant speed when x-rays are off [seconds]
    f_decel = (Single)(x_t[j] * (1- (f_a+f_vc)) / 1000);       //fraction of
              gap time used for decelerating [seconds]

    speed_fast = (Single)(AccelRate*f_accel/2);;//Speed between projections

    if (term1 > LimitingAngularInterval && NumStepsTemp > 0)
    {
        t_extra[j] = (Single)(speed * 1000 / (DecelRate));  //in milliseconds

      //Send  acceleration and deceleration rates to motor, which will be
              fixed for all subsequent images:
        MoveCommand = String.Format("A{0:F4}:AD{1:F4}", (AccelRate *
                convFactr), (DecelRate * convFactr));
        Console.WriteLine("{0}", MoveCommand);
        MotorLogic.SendCommandMotor(MoveCommand, false);
        //Wait a few hundred milliseconds for command to be processed otherwise it will cause an error.
        System.Threading.Thread.Sleep(waitTime);

                   MoveCommand = String.Format("V{0:F4}:D{1}", (speed * convFactr),
                   (NumStepsTemp));
        Console.WriteLine("{0}", MoveCommand);
        MotorLogic.SendCommandMotorDriveBy(MoveCommand, false);
```

```
        MotorLogic.SendCommandMotorDriveBy("VF0", false);
                MotorLogic.SendCommandMotorDriveBy("GOBUF1", false);   //Start motion for segment after
a pause for the exposure

        MoveCommand = String.Format("GOWHEN(T={0:F4})", sortedList[0].milliSeconds + delay_det);
        MotorLogic.SendCommandMotorDriveBy(MoveCommand, false);
        Console.WriteLine("{0}", MoveCommand);
//Increment total number of steps (encoder pulses) traversed
        stepSum += NumStepsTemp;

        NumStepsTemp = 0;
        after_const_speed_interval += 1;
        m = j;
    }
    t_extra[j] = (Single)(speed*1000 / DecelRate);  //in milliseconds
    accelTime = (Single)(speed_fast * 1000 / AccelRate);//in milliseconds
    Range = (Single)(MotorLogic.DegreesToSteps(term1));     //Angle traversed during acceleration
    if (speed_fast > 15.0 )
    {
        Console.WriteLine("Speed is too high.  Returning...");
        continueSequence = false;
        break;
    }
    if (term1 < LimitingAngularInterval && (j != numImages - 1))
    {
      gapTime[j] = (Single)(((sortedList[j].angle - sortedList[j - 1].angle) * 1000) / speed -
sortedList[j].milliSeconds);//
        if (NumStepsTemp == 0)
        {
MoveCommand = String.Format("A{0:F4}:AD{1:F4}", (AccelRate * convFactr), (DecelRate *
convFactr));
Console.WriteLine("{0}", MoveCommand);
MotorLogic.SendCommandMotor(MoveCommand, false);
System.Threading.Thread.Sleep(waitTime);
        }

           NumStepsTemp += (Single)MotorLogic.DegreesToSteps((sortedList[j].angle - sortedList[j -
1].angle));//(Range + delThetaSteps + padAngleSteps); //
        timeSum += gapTime[j];
        speed_fast = speed;

        continue;
    }
    else if (term1 < LimitingAngularInterval && j == numImages - 1)
    {

        //This if statement is set so that for differences between consecutive
        //angles > LimitingAngularInterval, the motor will accelerate between projection views and
        //NumStepsTemp is re-initialized.

        gapTime[j] = (Single)(((sortedList[j].angle - sortedList[j - 1].angle) * 1000) / speed -
sortedList[j].milliSeconds); //in milliseconds
        if (NumStepsTemp == 0) gapTime[j] -= accelTime;
```

```
    x_t[j] = gapTime[j];
NumStepsTemp += (Single)MotorLogic.DegreesToSteps((sortedList[j].angle - sortedList[j - 1].angle));

    MoveCommand = String.Format("D{0}", (NumStepsTemp));
    Console.WriteLine("{0}", MoveCommand);
    MotorLogic.SendCommandMotorDriveBy(MoveCommand, false);

    MoveCommand = String.Format("A{0:F4}:AD{1:F4}", (AccelRate * convFactr), (DecelRate *
convFactr));
    Console.WriteLine("{0}", MoveCommand);
    MotorLogic.SendCommandMotor(MoveCommand, false);
    System.Threading.Thread.Sleep(waitTime);

    MoveCommand = String.Format("V{0:F4}", (speed * convFactr));
    stepSum += NumStepsTemp;
    Console.WriteLine("{0}", MoveCommand);
    MotorLogic.SendCommandMotorDriveBy(MoveCommand, false);

    MotorLogic.SendCommandMotorDriveBy("VF0", false);
    MotorLogic.SendCommandMotorDriveBy("GOBUF1", false);   //Start motion for segment
    VelProfFile.WriteLine("GOBUF1");

    System.Threading.Thread.Sleep(waitTime);
    NumStepsTemp = 0;
  }
  else
  {
    gapTime[j] = (Single)(x_t[j] + t_extra[j]);

    MoveCommand = String.Format("D{0}", Range);  //Faster speed for non-imaging segment
    Console.WriteLine("{0}", MoveCommand);
    MotorLogic.SendCommandMotorDriveBy(MoveCommand, false);
    //Send  acceleration and deceleration rates to motor, which will be fixed for all subsequent :
    MoveCommand = String.Format("A{0:F4}:AD{1:F4}", (AccelRate * convFactr), (DecelRate *
convFactr));
    Console.WriteLine("{0}", MoveCommand);
    MotorLogic.SendCommandMotor(MoveCommand, false);

    System.Threading.Thread.Sleep(waitTime);

    MoveCommand = String.Format("V{0:F4}", (speed_fast * convFactr));  //Faster speed for non-
imaging segment
    Console.WriteLine("{0}", MoveCommand);
    MotorLogic.SendCommandMotorDriveBy(MoveCommand, false);
    stepSum += Range;
    MotorLogic.SendCommandMotorDriveBy("VF0", false);

    System.Threading.Thread.Sleep(waitTime);
    MotorLogic.SendCommandMotorDriveBy("GOBUF1", false);   //Start motion for segment

    MoveCommand = String.Format("GOWHEN(T={0:F4})", sortedList[0].milliSeconds + delay_det);
    MotorLogic.SendCommandMotorDriveBy(MoveCommand, false);
    Console.WriteLine("{0}", MoveCommand);
```

```
        if (j == 1) x_t[0] = (speed_fast / AccelRate) * 1000;  //in milliseconds
        // Refer to page 50 of Gemini Programmer's Reference pdf.

    }
}
// Slight adjustment in gaptime to allow for synchronization with detector and x-rays
gapTime[0] = (Single)0;  //
gapTime[1] -= (Single)(sortedList[0].milliSeconds);
x_t[1] -= (Single)(sortedList[0].milliSeconds);
gapTime[m_before_const_v] -= (t_extra[m_before_const_v]);
MotorLogic.SendCommandMotorDriveBy("END", false);           //End of profile
VelProfFile.WriteLine("END");

        ReturntoMain:
{
}
        }
```

APPENDIX B: DRAWINGS FOR GRID RECIPROCATION HARDWARE

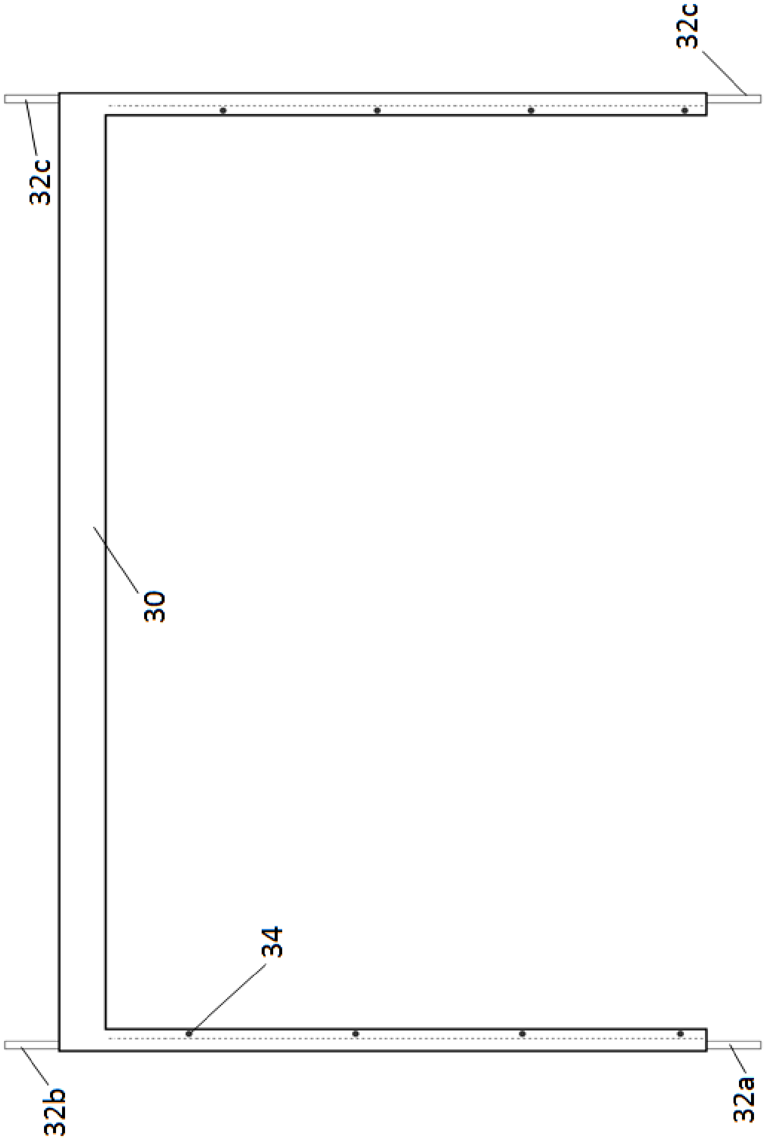

Figure 1: Bird's eye view of slotted frame alone. Slots in frame are shown with dotted lines. The focused anti-scatter grid is secured into the slots of the frame by set screws. Dowel pins are inserted into rod-end bearings that allow the grid to twist towards the x-ray focal spot (XFS) as it is shifted by the positioning stage.

30 – Slotted grid frame
32a,b, c, d – Dowel pins
34 – Example of threaded hole for set screws

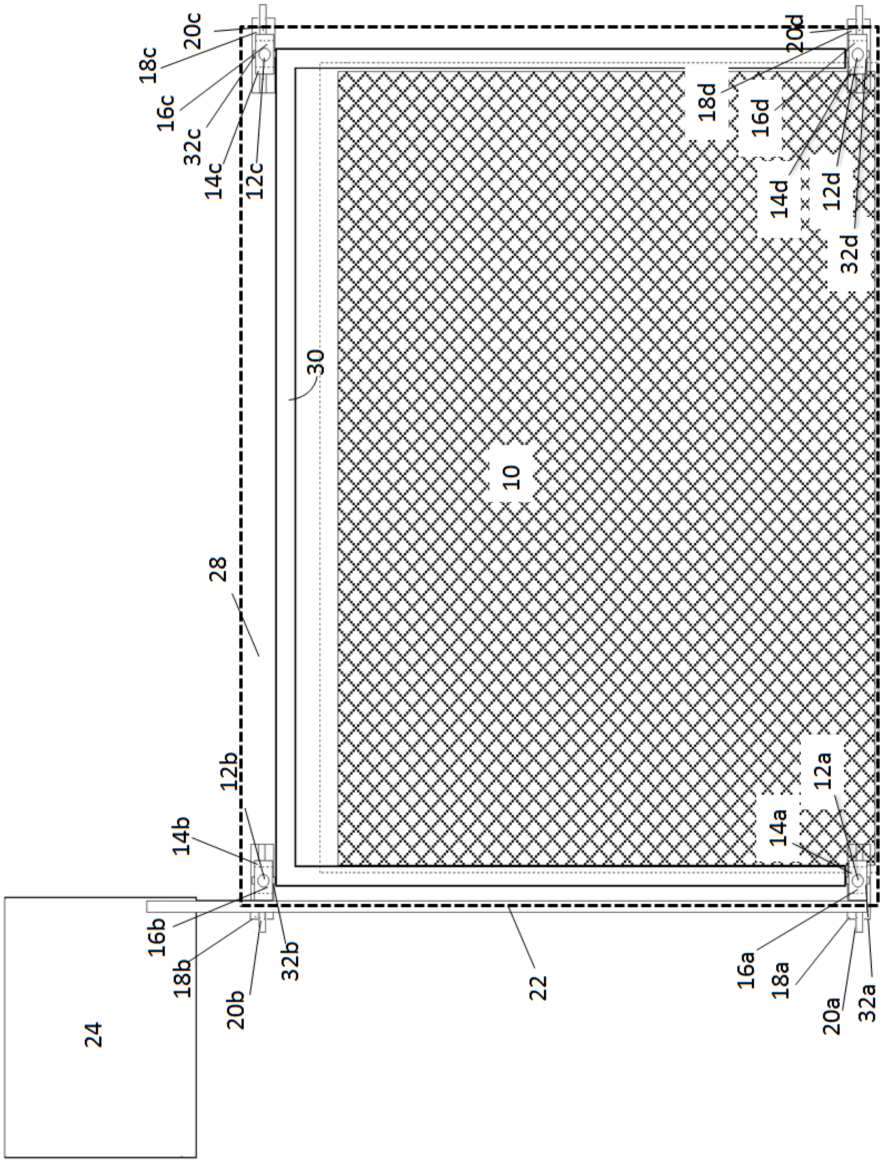

Figure 2: Bird’s eye view of design. Chest wall edge of the system is on the right side of this page.

10 – Anti-scatter grid
12a, b, c, d – Rod-end bearing
14a, b, c, d – C bracket for connecting rod end bearing to carriage
16a, b, c, d – Carriages that travels along linear track
18a, b, c, d – Wedge for mounting track at an angle
20a, d – Track
22 – Rod that connects positioning stage to C bracket
24 – Linear positioning stage
28 – X-ray detector
30 – Slotted grid frame
32a, d – Dowel pins

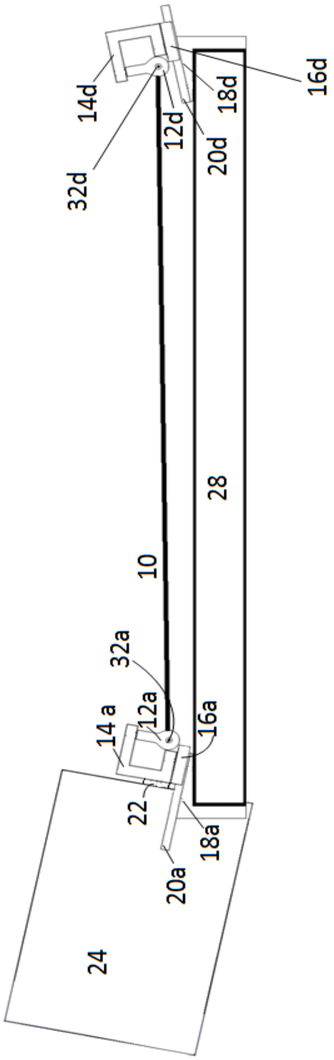

Figure 3: View from a patient’s perspective (sideways). The angle of tracks 20a and 20d, positioning stage 24, and wedges 18a and 18d can be seen from this view. The linear positioning stage 24 is mounted at the same angle as the tracks.

10 – Anti-scatter grid
12a, d – Rod-end bearing
14a, d – C bracket for connecting rod end bearing to carriage
16a, d – Carriage (with ball bearings) that travels along linear track
18a, d – Wedge for mounting track at an angle
20a, d – Track
22 – Rod that connects positioning stage to C bracket
24 – Linear positioning stage
28 – X-ray detector
30 – Slotted grid frame
32a, d – Dowel pins

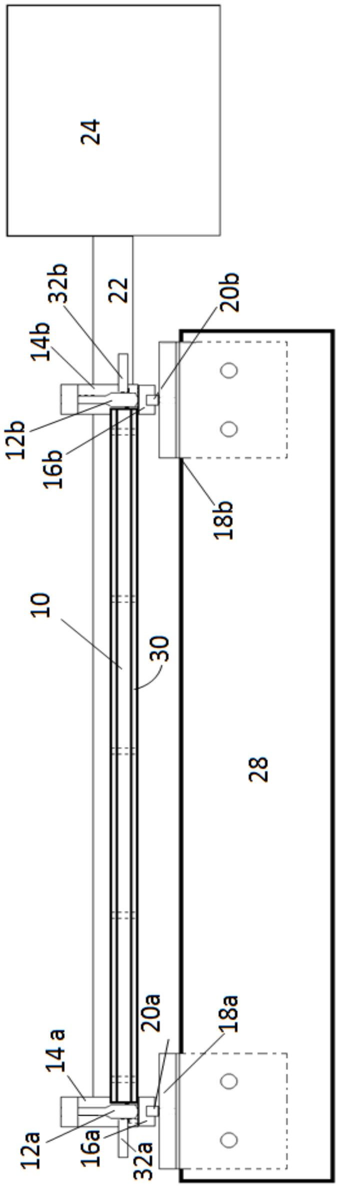

Figure 4: Cross-sectional view of the grid frame 30 and x-ray detector 28 as viewed from the right side of the detector
10 – Anti-scatter grid
12a, b – Rod-end bearing
14a, b – C bracket for connecting rod end bearing to carriage
16a, b – Carriage (with ball bearings) that travels along linear track
18a, b – Wedge for mounting track at an angle
20a, b – Track
22 – Rod that connects positioning stage to C bracket
24 – Linear positioning stage
28 – X-ray detector
30 – Slotted grid frame
32a,b – Dowel pins

APPENDIX C: CODE FOR PERFORMING HMP ACQUISITIONS WITH THE GRID

Subroutine written in C# that runs the grid positioning stage, x-ray generator, x-ray detector, and gantry arm motor. Code was modified from the original program written by Dexela, the manufacturer of the x-ray detector.

```
private Boolean PerformExposureDriveBy(ExposureStruct[] ExposureList, Boolean useXRay, Boolean
useMotor, Boolean isFlood)
    {
      Boolean ErrorOccured = true;
      continueSequence = true;
      SequenceCanceled = false;
      ScannerUtils.Canceled = false;
      errorString = "";
      Boolean oldAngles = true; //Use pre-programmed motion profile
(All DBT acquisitions will have the same projection angles)
      try
      {
        //Sort angles so 1st angle is most negative and gantry moves to most positive:
        numImages = ExposureList.Length;
        ExposureStruct[] sortedList = new ExposureStruct[numImages];
        SortAngles(ExposureList, ref sortedList);

        startAngle = (Single)(sortedList[0].angle);  //Start at initial angle w/o motion

        InfoLabel.ForeColor = Color.LimeGreen;
        errorString = "Load Technique";
        InfoLabel.Text = errorString;
        InfoLabel.Refresh();
//Check to make sure that all user-defined exposure parameters are valid and below limits. If not, return to
main GUI
        if ((!isFlood) && (!CheckTotalExposure(ExposureList)))
        {
          errorString = "total mAs too high ";
          continueSequence = false;
        }
        Boolean NoXRaySettings = true;
        for (int i = 0; i < ExposureList.Length; i++)
        {
          String reason;
          if (!CheckExposure(ExposureList[i], out reason))
          {
            errorString = "Exposure outside of " + reason;
            continueSequence = false;
          }
          if (!ExposureList[i].DarkImage) NoXRaySettings = false;
        }
        if (NoXRaySettings) useXRay = false;
        if (TestWithoutXRays) useXRay = false;
        if (ExposureList.Length < 1)
        {
          errorString = "No valid exposures ";
```

```
                continueSequence = false;
            }
            if (!continueSequence) goto Error;
//If all values check out, display an increase in the progress bar that shows how far through the acquisition process the program has gotten.
            progressBar1.Value = 5;

//Next, make sure that all hardware components are responsive and ready for executing commands:
            AngleLabel.Text = "Angle : " + TiltSerial.ArmAngleNow.ToString("F1");
            AngleLabel.Refresh();
            //TODO: what is scanner state
            ScannerState state = Scanner.State;
            compAngle = (Single)GantryLogic.SkinDegrees;
            if (useMotor)
            {
                errorString = "Motor";
                InfoLabel.Text = errorString;
                InfoLabel.Refresh();
                continueSequence = (state.Gantry == DeviceState.Ready);
                if (!continueSequence) goto Error;
                progressBar1.Value = 10;
                AngleLabel.Text = "Angle : " + TiltSerial.ArmAngleNow.ToString("F1");
                AngleLabel.Refresh();
            }

            if (!continueSequence)
            {
                errorString = "Speed or acceleration is too high or angular range is too large";
                stopwtch.Stop();
                goto Error;
            }

            errorString = "Detector";
            InfoLabel.Text = errorString;
            InfoLabel.Refresh();
            continueSequence = (state.Detector == DeviceState.Ready);
            if (!continueSequence) goto Error;
            PrepareImageBuffer(ExposureList);

            progressBar1.Value = 15;
            AngleLabel.Text = "Angle : " + TiltSerial.ArmAngleNow.ToString("F1");
            AngleLabel.Refresh();

            if (useXRay)
            {
                errorString = "Generator " + GeneratorLogic.ST;
                InfoLabel.Text = errorString;
                InfoLabel.Refresh();
                GeneratorLogic.SendCommand("ST");
                GeneratorLogic.WaitSt(2000);
                state = Scanner.State;
                continueSequence = (state.Generator == DeviceState.Ready);
                if (!continueSequence) goto Error;
                progressBar1.Value = 20;
```

```
            AngleLabel.Text = "Angle : " + TiltSerial.ArmAngleNow.ToString("F1");
            AngleLabel.Refresh();
//Push button to trigger generator to warm up:
            InfoLabel.Text = "Press Prep";
            errorString = "Prep error";
            InfoLabel.Refresh();
            continueSequence = Scanner.WaitPrepareButton(useXRay);
            if (!continueSequence) goto Error;
            progressBar1.Value = 25;
            AngleLabel.Text = "Angle : " + TiltSerial.ArmAngleNow.ToString("F1");
            AngleLabel.Refresh();

          }

         if (useMotor && !sortedList[0].DontMove)
          {
            GantryLogic.MotorMoveTo((Single)startAngle, WideAngleLimits);
          }

          int varProfile = 1, constGantryspeed = 0;// 1;
          System.Threading.Thread.Sleep(500);  //wait before sending commands for motion profile
          if (oldAngles) Profile_Available_Set_GapTimes(sortedList);
//If programming a new profile, set oldAngles to false.
          else SetupGantryProfile_Shorter(sortedList);


           if (useXRay)
           {
//Push button to initiate full DBT acquisition:

            InfoLabel.Text = "Press Expose";
            errorString = "Expose error";
            InfoLabel.Refresh();
            continueSequence = Scanner.WaitExposeButton(useXRay);
            if (!continueSequence) goto Error;
            progressBar1.Value = 30;
            AngleLabel.Text = "Angle : " + TiltSerial.ArmAngleNow.ToString("F1");
            AngleLabel.Refresh();
           }
//Update Progress bar and display:

          errorString = "Error in Loop";
          InfoLabel.Text = "Scanning";
          InfoLabel.Refresh();

          if (!continueSequence) goto Error;
          int remProgress = 100 - progressBar1.Value;
          progressBar1.Step = (remProgress) / ExposureList.Length;
          imgCount = 0;
          long ts;
          long StageWaitTime_ms = 50, x, timeNow;   //x is Used as a way of checking against stopwatch
for recording grid position
          long MGTimeNow, gridDelayTime, GenSetParamTime, extraGridTime;
```

```
        double RP_output = 0, TP_output = 0, TE_output = 0, TV_output = 0, TT_output = 0,
TimeOutput = 0, TP_init = 0;
        string XQCommand = "TP";

        GeneratorLogic.DoGenInput = false;
        DetectorLogic.GenReady = false;


//All images will  have to be taken with the same exposure time and mA
        SetupExposeNRead(sortedList[0]);    //Setup exposure time for detector expose_n_read mode
//If using x-rays set up exposure techniques by sending parameters to generator
        if (useXRay && !sortedList[0].DarkImage)
        {
          GenSet_ParamsDriveBy(sortedList[0], (int)sortedList[0].milliSeconds, 1000);
        }

        //Get current angle of gantry for angle calculations based on time image taken
        CurrentPosition = GantryLogic.ArmDegrees;

//Determine if there is any offset between the gantry motor encoder and the inclinometers for angle
calculations used in the reconstruction
        EncodrInclinoOffset = (double)(MotorLogic.CheckAngle() - CurrentPosition);

        Single GantryAngleDiff = 0, CurrentEncodrPos = 0;
        CurrentEncodrPos = (Single)MotorLogic.CheckAngle();
//Start a stopwatch for monitoring the times of all when all commands are sent to all hardware. This time is
used to synchronize all equipment

        stopwtch.Reset();
        stopwtch.Start();
        GenSetParamTime = stopwtch.ElapsedMilliseconds;

        for (int q = 0; q < numImages; q++)
        {
          imgCount = q;
          //Start thread for detector taking an image

          System.Threading.ParameterizedThreadStart SingleExp = new
System.Threading.ParameterizedThreadStart(SingleExposureDriveBy);
          System.Threading.Thread myt = new System.Threading.Thread(SingleExp);
          myt.Start((Object)(sortedList[q]));

//!!!!Gantry will not move and shoot x-rays unless generator triggered first before motor!!!!!
//Start moving for HMP after first exposure:
          if (q == 1 && useMotor && !sortedList[0].DontMove)
          {
            MovingThreadVariableSpeed("PRUN PROF3"); //Command
                              for variable velocity profile

            else MovingThread();

         GantryMoveStartTime = (int)stopwtch.ElapsedMilliseconds;

          }
```

```
            if (UseGrid && useXRay)
            {
              GridLogicExp.DBacq = true;
//Get current position of grid stage
              GridStageOut[q] = GridLogicExp.OutsideCommandRequest("TP");
//Get name of sub-routine that is programmed into the grid motor motion controller based upon the
exposure time (each exposure time has its own subroutine)
              XQCommand = "XQ #" +
GridLogicExp.Setup_Grid_Motion((Single)(sortedList[q].milliSeconds), StageWaitTime_ms,
(Single)(TiltSerial.ArmAngleNow));
//Calculate the amount of time required for accelerating the grid upto the correct speed for imaging (must
be constant)
              GridAccelTime[q] = (long)GridLogicExp.gridAccelTime;

            }

            timeNow = stopwtch.ElapsedMilliseconds;
//Determine how much wait time is required before initiating the next exposure
            if (q == 0) ts = (int)(GenSetParamTime + 500 - detWaitDelay);  //Wait 500 ms before taking
first exp.
            else if (q == 1) ts = (int)(GantryMoveStartTime + x_t[q] - (stopwtch.ElapsedMilliseconds));
            else ts = (int)((GenSetParamTime + gapTime[q]) - (stopwtch.ElapsedMilliseconds +
detWaitDelay));

            if (ts > 0) while (stopwtch.ElapsedMilliseconds < (timeNow + ts )) { };
//Set variable signaling program that generator is ready for the exposure
            DetectorLogic.GenReady = true;  //Ends while loop in SingleExposureDriveBy and snap
command sent to detector
            timeNow = stopwtch.ElapsedMilliseconds;
//Wait for detector to send ready signal
            while (!DetectorLogic.DetReady) { };
//Additional wait time to synchronize with gantry motion
              while (stopwtch.ElapsedMilliseconds < (timeNow + detWaitDelay)) { };

            timeVar[q] = (Single)(stopwtch.ElapsedMilliseconds);
            GenSetParamTime = (long)(stopwtch.ElapsedMilliseconds + sortedList[q].milliSeconds + 20);

            ExposureAngles[q] = (Single)MotorLogic.CheckAngle();
//If using grid, determine grid stage position to ensure that it starts off in the same position for all
exposures. If  it is not in the right position, move it to its starting place.
           if (UseGrid && GridLogicExp.StageProgramName != "No_Profile" && useXRay)
            {
              TP_init = Convert.ToDouble(GridLogicExp.OutsideCommandRequest("TP"));


              if (TP_init < 5000) motionSign = 1;
              else motionSign = -1;
              file.WriteLine("Initial Position {0}", TP_init);
              TP_output = Convert.ToDouble(GridLogicExp.OutsideCommandRequest("TP"));

If  it is still not in the right position, raise integrator gain to keep stage more rigidly at the right position.
              BGCommandSentTime[q] = stopwtch.ElapsedMilliseconds;
```

```
                  if (TP_output != 28000)
                  {
                    GridLogicExp.OutsideCommandRequest("KI 0.22");
                    TP_output = Convert.ToDouble(GridLogicExp.OutsideCommandRequest("TP"));
                  }
                  file.WriteLine("{0}, {1}", stopwtch.ElapsedMilliseconds, TP_output);

//Send command to execute grid motion for given gantry orientation, stroke direction, and exposure time
                   GridLogicExp.OutsideCommandRequest(XQCommand);
//Wait until grid is in the right position before shooting x-rays:
                  if (motionSign > 0)
                  {
                    GridStartPos = 100;
                    while ((TP_output < (GridLogicExp.accelDist * 1000 + dist_ext) + GridStartPos))
//2500//Wait until stage accels up to speed
                    {
                      TP_output = Convert.ToDouble(GridLogicExp.OutsideCommandRequest("TP"));
                      file.WriteLine("{0}, {1}", stopwtch.ElapsedMilliseconds, TP_output);
                    }
                  }
                   else
                   {
                    GridStartPos = 28000;
                    dist_ext = 5;
                    while ((TP_output > motionSign *(dist_ext) + GridStartPos))
                     {
                       TP_output = Convert.ToDouble(GridLogicExp.OutsideCommandRequest("TP"));
                       file.WriteLine("{0}, {1}", stopwtch.ElapsedMilliseconds, TP_output);
                     }
                   }

                }

x_rayOnTime[q] = stopwtch.ElapsedMilliseconds;


//Turn x-rays on once grid has accelerated up to correct speed:
                if (useXRay && !sortedList[q].DarkImage)
                {
                   MotorLogic.SendCommandMotor("OUT.1-1", false);

                    if (UseGrid)
                    {
//Wait for the duration of the programmed exposure time before issuing an off command to the generator
                        while (stopwtch.ElapsedMilliseconds < (x_rayOnTime[q] +
sortedList[q].milliSeconds+150))
                        {
                          TP_output = Convert.ToDouble(GridLogicExp.OutsideCommandRequest("TP"));
                        }
                    }
                    else System.Threading.Thread.Sleep((int)(sortedList[q].milliSeconds + 100));
//Turn x-rays off:
                   MotorLogic.SendCommandMotor("OUT.1-0", false);
```

```
                    }
//Get angle of gantry from encoder
                    ExposureAngleSmooth[q] = (Single) MotorLogic.CheckAngle();
//Send parameters for the next exposure to the generator
                    if (useXRay && !sortedList[0].DarkImage)
                    {
                        GenSet_ParamsDriveBy(sortedList[q], (int)sortedList[q].milliSeconds, 30);
                        if (UseGrid)
                        {
                            GridStagePostMove[q] = GridLogicExp.OutsideCommandRequest("TP");
                             positionError[q] = GridLogicExp.OutsideCommandRequest("TEA");
                        }
                    }
                    myt.Join();
                    DetectorLogic.GenReady = false;
                }
//Read images off of buffer
ReadDriveByBuffers(sortedList);
//Reset signal variables for next exposure
                GeneratorLogic.DoGenInput = true;
                DetectorLogic.GenReady = false;
                progressBar1.Value = 100;
                stopwtch.Stop();
//If no errors during image acquisition, continue. Else show error message.
                if (!continueSequence) goto Error;
                goto NoError;
            Error:
                {
                    InfoLabel.Text = "SCAN ABORTED  " + errorString;
                    InfoLabel.ForeColor = Color.Red;
                    InfoLabel.Refresh();
                    if (!SequenceCanceled) MessageBox.Show("Error " + errorString + " Occurred");
                    goto End;
                }
            NoError:
                {
                    if (!AutoSaveRawDriveBy(ExposureList))
                    {
                        InfoLabel.Text = "Failed to Save Raw data";
                        InfoLabel.ForeColor = Color.Red;
                        InfoLabel.Refresh();
                        MessageBox.Show("Error Saving\n" + "Please save image manually");
                    }
                    else
                    {
                        progressBar1.Value = 100;
                        AngleLabel.Text = "Angle : " + TiltSerial.ArmAngleNow.ToString("F1");
                        AngleLabel.Refresh();
                       ErrorOccured = false;
                   }
                if (CentrePostScan && useMotor) GantryLogic.MotorMoveTo((Single)0.00f,
WideAngleLimits);
                InfoLabel.Text = "Scan Complete";
```

```
                errorString = "";
                Console.WriteLine("Scan complete");
                InfoLabel.Refresh();
                }
            End:
                {}
            }
            finally
            {}
            return !ErrorOccured;
        }
```

Subroutine called by the previous code for sending commands to the grid positioning stage from Visual Studios.

```
using System;
using System.Collections.Generic;
using System.ComponentModel;
using System.Data;
using System.Drawing;
using System.Text;
using System.Windows.Forms;
using DexelaImageControls;
using DexelaRecon2;
using System.Diagnostics;
using System.IO;
using SCap;
using System.Runtime.InteropServices;

namespace Dexela.Scanner
{
    public partial class GridInitForm : Form
    {
        public GridInitForm()
        {
            InitializeComponent();
            g.address = "192.168.1.43";
            this.Text = g.connection();
        }
        private static GridInitForm fForm;
        private static Object lockObj = new Object();
        public static GridInitForm GridForm
        {
            get
            {
                lock (lockObj)
                {
                    if (fForm == null) fForm = new GridInitForm();
                }
                return fForm;
            }
        }

        Galil.Galil g = new Galil.Galil();
```

```
    string result;
    public double GridVelocity, GridAccel, AdjustedAccel, AdjustedTotDist;
    public double gridAccelTime;
    public static double r_d = 8.89;//(Full-sized grid repeat distance)
    public double r_d_microns = r_d*1000; //r_d in microns
    public static double Total_Distance = 27.9; // [mm] Amount of total distance available for grid to move
    static double StepsPer_mm = 1000;  //Encoder resolution = 1 micron, so 1000 counts = 1 mm
    public double exposureTime;
    Single desiredPosition;
    public string StageProgramName = "#LOAD3";
    public double CurrentPosition, accelDist;
    public long pos1 = 2500, pos2 = 27500, desiredPos;
    private static long Blimit = 50, Flimit = 28500;
    public Boolean DBacq = false;
    private void InitializeGridMotorForm_Load(object sender, EventArgs e)
    {
        try
        {

        }
        catch (System.Runtime.InteropServices.COMException ex)
        {
            Console.WriteLine(ex);  //print error message
            if (ex.Message.Contains("COMMAND ERROR"))
            Console.WriteLine("a command error occurred"); //special processing for command errors
        }
    }

    private string SendCommandToGridMotor(string command)
    {
        try
        {
            result = Convert.ToString(g.commandValue(command));
            g.onMessage += new Galil.Events_onMessageEventHandler(g_onMessage);
            return (result);
        }
        catch (System.Runtime.InteropServices.COMException ex)
        {
            Console.WriteLine(ex);  //print error message
            if (ex.Message.Contains("COMMAND ERROR"))
                Console.WriteLine("a command error occurred"); //special processing for command errors
            return ("Error");
        }
    }
    void g_onMessage(string message)
    {
        Console.WriteLine("{0}", message);
        //throw new Exception("The method or operation is not implemented.");
    }
    void g_onRecord(string message)
    {
                throw new Exception("The method or operation is not implemented.");
    }
```

```
    public static DialogResult ShowGridInit(string cmd)
    {
            return GridForm.ShowDialog();
    }

    private void button1_Click(object sender, EventArgs e)
    {
      //Turn off motor (This is actually just a way to turn off motion control to motor)
      Console.WriteLine("Turning off control to motor");
      SendCommandToGridMotor("MO");  //Turn motor off for now for debugging purposes
    }

    private void button2_Click(object sender, EventArgs e)
    { //Button used to test motion of stage
      Single CountsToMove;

      Console.WriteLine("Testing grid motor by moving 5000 steps backwards (negative counts)");
      SendCommandToGridMotor("AC 1024");
      SendCommandToGridMotor("DC 1024");
      SendCommandToGridMotor("SP 5000");

      Single currentPos = (Single)Convert.ToDecimal(SendCommandToGridMotor("RP"));  //Forward
software limit
      //Change the starting position of stage so that it starts at one of the extreme positions
      Console.WriteLine("Current Position = {0}", currentPos);
      if (currentPos < 5000) CountsToMove = 4500;
      else CountsToMove = -4500;
      String command = String.Format("PR {0}", CountsToMove);
      SendCommandToGridMotor(command);  //Forwards software limit
      SendCommandToGridMotor("BG");
      System.Threading.Thread.Sleep(5000); //Sleep for 5 seconds to wait for stage to be positioned

      //Then move stage back
      command = String.Format("PR {0}", (long)(-1*CountsToMove));
      SendCommandToGridMotor(command);  //Forwards software limit
      SendCommandToGridMotor("BG");
      Console.WriteLine(result);
    }

    private void button2_Click_1(object sender, EventArgs e)
    {
      //Done button
      //g.address = "";
      this.DialogResult = DialogResult.Cancel;
      this.Hide();
    }

    public string OutsideCommandRequest(string commandOut)
    {
      string resultOut = SendCommandToGridMotor(commandOut);
      return (resultOut);
    }
    public void Move_back_2_zero()
```

```
        {//Move stage back to starting position
            SendCommandToGridMotor("KD 140");
            SendCommandToGridMotor("KP 5");
            SendCommandToGridMotor("KI 0.01");
            SendCommandToGridMotor("AC 100000");
            SendCommandToGridMotor("DC 100000");
            SendCommandToGridMotor("SP 35000");
            SendCommandToGridMotor("PA 350");
            SendCommandToGridMotor("BG");
        }

        public string Setup_Grid_Motion(Single mSec, Single WaitTime_ms, Single GantryAngle)
        {
            string command;
            exposureTime = (double)mSec;
            double d_alpha = (double)((Total_Distance - r_d) / 2), speed160 = 121631;                    //Distance
available for acceleration
            CurrentPosition = Convert.ToDouble(SendCommandToGridMotor("TP"));    //Need to know
motor's current position to know if need to move grid left or right
            double t_exp = (double)(mSec / 1000);                          //convert exposure time to seconds
            long movePA;
//Call the appropriate subroutine from the stage's main program based upon the exposure time
            int selectTime = Convert.ToInt16(mSec);
            switch (selectTime)
            {
                case 1000:
                    GridAccel = 500;  //in mm/s^2
                    if (Convert.ToDouble(SendCommandToGridMotor("TP")) != 28000 && !DBacq)
SendCommandToGridMotor("XQ #GOMAX");
                    StageProgramName = "LD5D0";
                    break;
                case 500:
                    GridAccel = 1000;
                    if (Convert.ToDouble(SendCommandToGridMotor("TP")) != 28000 && !DBacq)
SendCommandToGridMotor("XQ #GOMAX");
                    StageProgramName = "LD3D0";
                    break;
                case 200:
                    GridAccel = 5600;
                    if (Convert.ToDouble(SendCommandToGridMotor("TP")) != 28000 && !DBacq)
SendCommandToGridMotor("XQ #GOMAX");
                    StageProgramName = "LD200";
                    break;
                case 160:

                   if (Convert.ToDouble(SendCommandToGridMotor("TP")) != 28000 && !DBacq)
SendCommandToGridMotor("XQ #GOMAX");

                    StageProgramName = "MV160BF";//"MV160BO";
                    GridAccel = 7501.824;
                    break;
                case 125:
                    GridAccel = 7000;
                    StageProgramName = "LD2D0";
```

```
                    break;
                case 100:
                    GridAccel = 20000;
                    StageProgramName = "LOAD1";
                    break;
                default:
                    StageProgramName = "No_Profile";//"MV";
                    if (t_exp > 300)
                    {
                        GridAccel = 10000;
                        SendCommandToGridMotor("KD 135");
                        SendCommandToGridMotor("KP 8");
                        SendCommandToGridMotor("KI 0.01");
                    }
                    else
                    {
                        GridAccel = 7000;
                        SendCommandToGridMotor("KD 150");
                        SendCommandToGridMotor("KP 7");
                        SendCommandToGridMotor("KI 0.01");
                    }
                    GridVelocity = (double)(r_d / t_exp); //required minimum velocity to blur grid lines in mm/s
                    DetermineNew1024Params(GridAccel, GridVelocity);
                    command = String.Format("DC {0}", (long)Dist_mmToSteps(AdjustedAccel)); //Set deceleration. Symmetric trapezoidal velocity profile
                    SendCommandToGridMotor(command);
                    command = String.Format("AC {0}", (long)Dist_mmToSteps(AdjustedAccel)); //Set acceleration in microns/s^2.
                    SendCommandToGridMotor(command);
                    command = String.Format("SP {0}", Math.Ceiling(Dist_mmToSteps(GridVelocity)));
                    SendCommandToGridMotor(command);
                    SendCommandToGridMotor("PA 26500");
                    goto noProfile;
                    break;
            }

            GridVelocity = (double)(r_d / t_exp); //required minimum velocity to blur grid lines in mm/s (See function below)
            DetermineNew1024Params(GridAccel, GridVelocity);   //all values should be in mm and s units
        noProfile:
            return (StageProgramName);
        }
        public void DetermineNew1024Params(double InitAccel, double speed)
        {
            //Function that changes motor acceleration to a factor of 1024 (this is an encoder characteristic;
            //it only takes long integer values that are a factor of 1024)
            //To make motion more accurate, must change acceleration room and time to match
            double factor, multiplier;
            factor = InitAccel*1000 / 1024;       //convert accel to microns/s
            multiplier = (double)(Math.Floor(factor));
            AdjustedAccel = (double)multiplier * 1024 / 1000;      //in mm/s^2
            accelDist = (speed * speed) / (2 * AdjustedAccel );    //in mm
            //Adjusted total distance to move:
            AdjustedTotDist = (double)(2 * accelDist + r_d);       //in mm
```

```
          //Adjusted time to wait for acceleration:
            gridAccelTime = (double)(1000 * GridVelocity / AdjustedAccel); //in milliseconds
        }

        public double Dist_mmToSteps(Double Dist_mm)
        {
            //Function that changes motor steps to physical distance
            return (double)(Dist_mm * StepsPer_mm);
        }
        static public Double StepsToDist_mm(Single steps)
        {
            //Function that changes physical distance to motor steps
            return steps / StepsPer_mm;
        }
        public void PrintPosition_and_Velocity(Single mSec)
        {
            //Print out actual velocity profile of grid
            string temp = @"C:\Users\Williamslab\Desktop\Anti-
scatter_grid\X_ray_Acq_GUI_output\1_30_14_angular_dependence\Gantry_+12deg_";
            string P_param = SendCommandToGridMotor("KP?"), I_param =
SendCommandToGridMotor("KI?"), D_param = SendCommandToGridMotor("KD?");
            string direction;
            string profileName;

            if (mSec == 125) profileName = "LOAD2";
            else if (mSec == 500) profileName = "LOAD3";
            else goto noProfile;

            double TimeDif;
            double RP_output, TP_output, TE_output, TV_output, TT_output;
            double final_pos = CurrentPosition + desiredPos, TimeOutput;
            TimeDif = 0;

            if (CurrentPosition > 5000) SendCommandToGridMotor("XQ #GoHome");
            System.Diagnostics.Stopwatch stopwtch = new System.Diagnostics.Stopwatch();
            stopwtch.Start();  //Start stopwatch before sending grid move command

            string command = String.Format("XQ #{0}", profileName);
            SendCommandToGridMotor(command);  //Execute 125 ms motion profile
            long RefTime = stopwtch.ElapsedMilliseconds;

            Object r = g.record("QR");
            double MGTimeNow = g.sourceValue(r, "TIME");
            //double x = 0;
            while (TimeDif < 3000)
            {
                r = g.record("QR");

                TimeOutput = g.sourceValue(r, "TIME") - MGTimeNow;
                RP_output = g.sourceValue(r, "_RPA");
                TP_output = g.sourceValue(r, "_TPA");
                TE_output = g.sourceValue(r, "_TEA");
                TV_output = g.sourceValue(r, "_TVA");
                TT_output = g.sourceValue(r, "_TTA");
```

```
                TimeDif = stopwtch.ElapsedMilliseconds - RefTime;
                while ((stopwtch.ElapsedMilliseconds - RefTime) <= (TimeDif + 5))
                {
                };
            }
        noProfile:
        }
//Code for commanding the stage to automatically record data to stage’s memory without sending a query to the stage to obtain it from Visual Studio
        public void GetQRData(double TimeOutput, double RP_output, double TP_output, double TE_output, double TV_output, double TT_output)
        {
            Object r = g.record("QR");

            TimeOutput = g.sourceValue(r, "TIME");
            RP_output = g.sourceValue(r, "_RPA");
            TP_output = g.sourceValue(r, "_TPA");
            TE_output = g.sourceValue(r, "_TEA");
            TV_output = g.sourceValue(r, "_TVA");
            TT_output = g.sourceValue(r, "_TTA");
        }

        public void StartRecord(long numPts)
        {
            SendCommandToGridMotor("DA *[]"); //Deallocate any pre-existing arrays
            string command = String.Format("DM TME[{0}], TPA[{0}], RPA[{0}]", numPts);
            SendCommandToGridMotor(command);  //Allocate arrays on controller
            SendCommandToGridMotor("RA TME[], TPA[], RPA[]");
            SendCommandToGridMotor("RD TIME, _TPA, _RPA");
            SendCommandToGridMotor("RC 3");
        }
//Save data from stage’s memory to a comma-separated file
        public void Save_to_CSV(string file)
        {
            g.arrayUploadFile(file, "TME TPA RPA");
        }
    }
}
```

Main Routine from which the grid positioning stage runs all subroutines. Stores all tuning, acceleration, deceleration, speed, and distance input parameters for multiple exposure times:

```
'VCS10-108-LB-01-MC
'UNIVERSITY OF VIRGINIA
'DMC-30012
'**************************************
#AUTO #MAIN
'**************************************
'AMP SETTINGS
AU 0;BR 1;AG 1;TM 1000;TL 6.0;TK 9.998

'GENERAL SETTINGS
```

```
ER 500;OE 1;MT 1;CE 0;CN-1

'PID PARAMETERS (Stage tuning)
KD 60;KP 5;KI 0;PL 0;SHX
WT 2500

JS#HOME REM //Jump to the subroutine for homing stage

WT 100;MG "WAIT OVER"
MG "STARTING OFFSET"
JS#GOMAX;MG "STAGE READY"
WT 500;SP 30000;AC 100000
DC 100000
EN
'****************************************
'SUBROUTINES
'****************************************
#HOME
TL 1.5
OE 0
JG -3000;BG
#JOG;JP#JOG,@ABS[_TEX]<1000
ST;AM
MG "HIT END"
MG "AXIS HOMED"
DP*=0
TL 6.0
OE 0
WT100
EN
'****************************************
#OFFSET
KI 0.01
PA 100;BG;AM
EN
'****************************************
#GoHome
KD 100 ;KP 7;KI 0.1
SP 10000;AC 15000;DC 15000
PA 100; BGX;AMX;TE
EN
'****************************************
#GOMAX
KD 100 ;KP 7;KI 0.22
SP 10000;AC 15000;DC 15000
PA 28000; BGX;AMX;TE
EN
'****************************************
#LD2D0
```

```
SP 72800;AC 8000000;DC 10000000;WT 10
KD 170 ;KP 7.5;KI 0
PA 26500; BGX;AMX;TE;WT 500
KD 140;KP 5;KI 0.01;
AC 100000;DC 100000;SP 35000
PA 250; BGX;AMX;TE
EN
'******************************************
#LD3D0
KD 135;KP 6;KI 0.01
SP 18200;'1024,8.89 rd
AC 1000000;DC 1000000
PA 100; BGX;AMX;TE;TT
WT 100
PA 28000; BGX;AMX;TE
KD 142;KP 5;KI 0.22;TT
EN
'******************************************
#LD4D0
'35.4 mm.s for 250 ms Exposure Time
KD 130;KP 10;KI 0
SP 35435; '1024,8.89 rd
AC 10000000;DC 10000000
PA 100; BGX;AMX;TE
TT;WT 100
PA 28000; BGX;AMX;TE
KD 142;KP 5;KI 0.22
EN
'******************************************
#LD5D0
'9.072 mm/s for 1000ms Exposure Time (1024 time scale)
KD 90;KP 6;KI 0.0098
SP 9072;AC 500000;DC 500000
PA 100; BGX;AMX;TE
TT;WT 100
PA 28000; BGX;AMX;TE
KD 142;KP 5;KI 0.22
EN
'******************************************
#LD200
'44.433 mm.s for 200ms Exposure Time
KD 151;KP 7.15;KI 0.01
AC 5600000;DC 5600000; SP 44433;
PA 100; BGX;AMX;TE
WT 500
KD 130;KP 5;KI 0.1
AC 100000;DC 100000;SP 35000
PA 28000; BGX;AMX;TE
KD 142;KP 5;KI 0.22
```

```
EN
'*************************************
#MV125 REM 125 ms exposure
SP 72800;PA 100; BGX;AMX;TE
WT 500
KD 130;KP 5;KI 0.1
AC 100000;DC 100000;SP 35000
PA 28000; BGX;AMX;TE
KD 142;KP 5;KI 0.22
EN
'*************************************
#MV500 REM 500 ms exposure
KD 130;KP 5;KI 0.1
SP 18200;AC 10000000;DC 10000000
PA 100; BGX;AMX;TE;TT
PA 28000; BGX;AMX;TE
KD 142;KP 5;KI 0.22;TT
EN
'*************************************
#MV160 REM 160 ms exposure
REMMoves using the last programmed AC, DC, SP, & PID parameters
SP 55542; '8.89
PA 28000; BGX;AMX;TE
WT 500
PA 100; BGX;AMX;TE
WT 500
EN
'*************************************
#MV160BF
REMMove for 160 ms exposure backward only and wait for next exposure where grid will
REMbe moved backward to go with gravity
AC 7501824;DC 7501824
KD 142;KP 8.88;KI 0.01
SP 56875 ; '8.89 mm r_d
PA 100; BGX;AMX;TE;TT
AC 7501824;DC 3750912;SP 195000
KD 130
PA 28000; BGX;AMX;TE
KD 142;KP 5;KI 0.22;TT
EN
'*************************************
```

APPENDIX D: GRID LINE ARTIFACT FILTERING ALGORITHM

The following code was written in Matlab for correction of grid line artifacts (GLAs) from both projection images and reconstruction slices

```
thresh_Value = 0.6 %GLA peaks must have an amplitude of >= 60% of 0^-1 mmm peak in PS to be
filtered
y_proj_box_locs = [183  206 229  275 298 321 327 302 277 227 202 177 251 250 256];%y-coordinate of
corner of ROIs where peaks are located
x_proj_box_locs = [177  202 227  277 302 326 183 206 229 275 298 322 125 301 205];%x-coordinate of
corner of ROIs where peaks are located
GLA_ROI_size = 8; %ROI size is 8 x 8 pixels^2 for filtering grid lines from projections
[scrap, numBoxes] = size(x_proj_box_locs);
 %Select file for correcting lines
[FileName,PathName] = uigetfile({'*.smv';'*.tif'},'Select the SMV or TIF file');
datatype=FileName(length(FileName)-2:length(FileName));
%Create two new files for the cropped original image and the filtered image
ext_string_1 = '_filtered.tif';
ext_string_2 = '_cropped_original.tif';
newFile = [PathName FileName(1:length(FileName)-4) ext_string_1];
cropFile = [PathName FileName(1:length(FileName)-4) ext_string_2];

%if it's an .smv file, open using the following format
if(strcmp(datatype,'smv'))
  file=fopen(strcat(PathName,FileName));
  wholefile=fread(file);
  binhead=(wholefile(1:512))';
  fclose(file);
  for i1=1:512
      strhead(1,i1)=native2unicode(binhead(1,i1));
  end
  [sm, sn] = size(strhead);
    totalHeadrString = strcat(strhead(1:sn));
  maxIntDim = 4; %maximum size of image will have 4 integer places (~1000)
  [hm, hn] = size(totalHeadrString);
%Get dimensions of image from file header
  k_loc_a_1 = strfind(totalHeadrString(1:hn), 'SIZE1');
  k_loc_a_2 = strfind(totalHeadrString(1:hn), 'SIZE2');
  k_loc_a_3 = strfind(totalHeadrString(1:hn), 'SIZE3');
  k_loc_b_1 = strfind(totalHeadrString(k_loc_a_1+6:k_loc_a_1+maxIntDim+6), ';');
  k_loc_b_2 = strfind(totalHeadrString(k_loc_a_2+6:k_loc_a_2+maxIntDim+6), ';');
  k_loc_b_3 = strfind(totalHeadrString(k_loc_a_3+6:k_loc_a_3+maxIntDim+6), ';');
   size1=str2num(char(totalHeadrString(k_loc_a_1+6:k_loc_a_1+5+k_loc_b_1)));
   size2=str2num(char(totalHeadrString(k_loc_a_2+6:k_loc_a_2+5+k_loc_b_2)));
   size3=str2num(char(totalHeadrString(k_loc_a_3+6:k_loc_a_3+5+k_loc_b_3)));   %now it's one big
string
  headarr=strsplit(strhead,{'=',';',' '});
   file=fopen(strcat(PathName,FileName));
   header2=fread(file,512);
end
%if it's a tiff image, do the following to open the entire image
   if(strcmp(datatype,'tif'))
```

```
        info = imfinfo(FileName);
        num_images = numel(info);
        size3=num_images;
    end
 for k1=1:size3
%If it is an .smv image file, read in each slice and correct individually
     if(strcmp(datatype,'smv'))
       binimage=fread(file,[size1,size2],'uint16');
     else
        binimage= imread(FileName, k1);
     end
%crop the image to get a reasonable ROI, and take fft
 if(k1==1)
    figure;
    imagesc(binimage);
    title('Choose area for filtering, then double click');
    rect=imrect;
    accept_pos = wait(rect);
    pos=rect.getPosition;
    x_min=round(pos(1)); %x-coordinate of corner of ROI
    y_min=round(pos(2)); %y-coordinate of corner of ROI
    x_crop=round(pos(3));%width of ROI
    y_crop=round(pos(4));%height of ROI
    disp('Coordinates of Location to Filter');
    disp([x_min, y_min,x_crop,y_crop]);
    imagesc(binimage);
    title('Choose ROI near worst gridlines or chest wall, then double click');

if (size1 == 3072) %If image is a projection view, use a larger ROI
        box_size = 512;
else %else use a 255 voxel x 255 voxel box for recon images
        box_size = 255; %mm^-1 %Reconstructed image has slightly different
                             %frequency than projection image due to
                             %binning
end
    rect2=imrect(gca,[100 100 box_size box_size]);
    setResizable(rect2,0);
    accept_pos = wait(rect2);
    pos=rect2.getPosition;
    x_min2=round(pos(1));
    y_min2=round(pos(2));
    x_crop2=round(pos(3));
    y_crop2=round(pos(4));
    disp('Coordinates of ROI used for Filter');
    disp([x_min2, y_min2, x_crop2, y_crop2]);
    disp('Filtering image slices...');
end

%Crop image
img_crop_final=imcrop(binimage,[x_min,y_min,x_crop,y_crop]);
original_mean = mean2(img_crop_final);
 %Find where there are background voxels in the image to remove GLA patterns
that will show up in the background after the filtering
```

```
if (size1 == 3072)
    zeroInds = find(img_crop_final>=16383);
else zeroInds = find(img_crop_final<=80);
end
imagefft=fftshift(fft2(img_crop_final));
img_crop_ps = imcrop(binimage,[x_min2,y_min2,x_crop2,y_crop2]);
I_0=mean(img_crop_ps(:));
 ps_orig=10*log10(abs(fftshift(fft2(img_crop_ps))).^2); %Calculate the power spectrum of the image (PS)
ps_mod= ps_orig;% Duplicate the PS to modify for filter creation
max_ps=max(ps_orig(:)); % find the max for threshholding

if (size1 == 3072) %Peaks are in slightly different locations in projections than in the reconstructed image

    for j=1:numBoxes
              %Find the peaks within the specific regions of the PS
      GLA_ROI =
              ps_orig(x_proj_box_locs(j):x_proj_box_locs(j)+GLA_ROI_size,y_proj_box_locs(j):y_proj_box_l
              ocs(j)+GLA_ROI_size);
        [row_ind,col_ind] = find(GLA_ROI >= thresh_Value*max_ps & GLA_ROI <=.9*max_ps);
                  %If arrays are negative (i.e. there were no pixels that matched the      condition), go to the next
                  ROI:
        TF = isempty([row_ind,col_ind]);
        if (TF == 0)
            [numpts,scrap] = size(row_ind);
            for k=1:numpts
                ps_mod((row_ind(k)+x_proj_box_locs(j))-1,(col_ind(k)+y_proj_box_locs(j)-1)) = 1; % Set
values equal to 1
            end
        end
    end
else %FOR RECONSTRUCTED IMAGES

    for i3=1:size(ps_mod,1)
        for i4=1:size(ps_mod,2)
            %Find grid peaks along diagonal lines in PS corresponding to grid pitches @
            %grid rotation angle

if(((i4<=46&&i4>=36)&&((i3<=35&&i3>=25)||(i3<=227&&i3>=217)))||((i4<=71&&i4>=61)&&((i3<=7
0&&i3>=60)||(i3<=194&&i3>=184)))||((i4<=106&&i4>=96)&&((i3<=103&&i3>=93)||(i3<=163&&i3>=1
53)))||((i4<=166&&i4>=156)&&((i3<=103&&i3>=93)||(i3<=163&&i3>=153)))||((i4<=196&&i4>=186)&
&((i3<=75&&i3>=65)||(i3<=194&&i3>=184)))||((i4<=224&&i4>=214)&&((i3<=35&&i3>=25)||(i3<=227
&&i3>=217))))
if(ps_mod(i3,i4)>= thresh_Value*max_ps&&ps_mod(i3,i4)<=.9*max_ps)
                    ps_mod(i3,i4)=1;
                    %set peak = 1
                end
            end  %Ends if statement for finding peaks in PS caused by peaks
                                  close to x-axis

if(((i4<=95&&i4>=85)&&((i3<=112&&i3>=102)||(i3<=155&&i3>=145)))||((i4<=134&&i4>=124)&&((i3
<=93&&i3>=83)||(i3<=173&&i3>=163)))||((i4<=173&&i4>=163)&&((i3<=112&&i3>=102)||(i3<=155&
&i3>=145))))
                %                   disp(i3);
```

```
                %                   disp(i4);
                if(ps_mod(i3,i4)>= thresh_Value*max_ps
                    %set peak=1
                                           ps_mod(i3,i4)=1;
                end
            end  %Ends if statement for finding peaks in PS caused by honeycomb pattern found in detector housing
            if((i3<=half_size_y+3&&i3>=half_size_y-3)&&((i4<=68&&i4>=63)||(i4<=194&&i4>=188)||(i4>=4&&i4<=8)||(i4>=249&&i4<=255)))
                if(ps_mod(i3,i4)>=lower_offax*max_ps)
                    ps_mod(i3,i4)=1;
                end
            end %Ends if statement for finding peaks close to x-axis of PS
        end %Ends loop over rows
    end %Ends loop over columns
    %honeycomb pattern removal
 end
%ps_mod now has peaks set to 1
filter=ps_mod./ps_orig;
%filter created with "holes" at peaks. The values in the filter where the GLA peaks were are now small fractional values.
%resize filter and multiply by orginial fft:
filter=imresize(filter,[size(imagefft,1) size(imagefft,2)]);
%Multiply filter with original image FFT in frequency space
mod_fft=imagefft.*filter;
%take inverse FFT to get the filtered image
new_image=abs(ifft2(ifftshift(mod_fft)));
%Remove grid artifacts from background of breast by reverting background
%voxels back to zero values as in the original image
if (size1 == 3072)
    new_image(zeroInds) = 16383;
else
    new_image(zeroInds) = 0;
end
%Convert image to 16-bit unsigned integer as the original image
new_image=uint16(new_image);
img_crop_final = uint16(img_crop_final);

%Write original cropped image and filtered cropped image slices to files
    if(k1==1)
        imwrite(new_image, newFile);%'lines filtered
        imwrite(img_crop_final, cropFile);%'original_with_lines
    else
        imwrite(new_image, newFile,'WriteMode','append');
        imwrite(img_crop_final, cropFile,'WriteMode','append');
    end
 end
%If original image file is a .smv file, close file
if(strcmp(datatype,'smv'))
fclose(file);
disp('Filtering complete. Files written to same folder as original image.');
end
```

APPENDIX E: DMT BEAM CHARACTERIZATION AND OPTIMIZATION

Table I: Half Value Layers (HVLs) of DMT

Tube Voltage [kVp]	Exposure [mR/mAs]	HVL [mm of Al]
22	0.91	0.49199
23	1.18	0.53028
24	1.45	0.55989
25	1.66	0.572
26	1.91	0.58196
27	2.16	0.59337
28	2.41	0.60143
29	2.64	0.60657
30	2.89	0.61549
31	3.13	0.62057
32	3.37	0.62848
33	3.62	0.63558
34	3.85	0.64056
35	4.09	0.64779
36	4.34	0.65621

Table II: Grid-in optimized tube voltages [kV] using the thickest calc step

Compressed Thickness [cm]	30% Adipose/70% Glandular	50% Adipose/50% Glandular	70% Adipose/30% Glandular
4	29	26	29
5	27	28	29
6	27	27	29
7	29	29	28
8	29	28	31
9	29	29	29

Table III: Grid-in optimized tube voltages [kV] using the thickest mass step

Compressed Thickness [cm]	30% Adipose/70% Glandular	50% Adipose/50% Glandular	70% Adipose/30% Glandular
4	24	26	28
5	28	28	29
6	27	29	27
7	29	27	29
8	27	31	26
9	27	24	24

Table IV: Grid-out optimized tube voltages [kV] using the thickest calc step

Compressed Thickness [cm]	30% Adipose/70% Glandular	50% Adipose/50% Glandular	70% Adipose/30% Glandular
4	26	28	28
5	29	28	29
6	28	28	29
7	27	29	28
8	31	29	29
9	35	33	37

References

[1] K. Saltsman, "Chapter 4: Cellular Reproduction: Multiplication by Division," U.S. Department of Health and Human Services, 22 April 2011. [Online]. Available: http://publications.nigms.nih.gov/insidethecell/chapter4.html. [Accessed 15 August 2015].

[2] C. M. O'Connor and J. U. Adams, Essentials of Cell Biology, Cambridge: NPG Education, 2010..

[3] "U.S. Breast Cancer Statistics," Breastcancer.org, 11 May 2015. [Online]. Available: http://www.breastcancer.org/symptoms/understand_bc/statistics. [Accessed 15 August 2015].

[4] C. H. Lee, D. D. Dershaw, D. Kopans, P. Evans, B. Monsees, D. Monticciolo, R. J. Brenner, L. Bassett, W. Berg, S. Feig, E. Hendrick, E. Mendelson, C. D'Orsi, E. Sickles and L. Burhenne, "Breast Cancer Screening With Imaging: Recommendations From the Society of Breast Imaging and the ACR on the Use of Mammography, Breast MRI, Breast Ultrasound, and Other Technologies for the Detection of Clinically Occult Breast Cancer," *J Am Coll Radiol,* vol. 7, pp. 18-27, 2010.

[5] B. A. Barnes, "Positioning in Mammography Unit 4," [Online]. Available: http://www.santarosa.edu/~xho/Mammo/Unit%204%20-%20Mammography%20Positioning.pdf. [Accessed 19 August 2015].

[6] W. E. Brant and C. A. Helms, Eds., Fundamentals of Diagnostic Radiology, Philadelphia: Lippincott Williams & Wilkins, a Wolters Kluwer business, 2007.

[7] D. Sullivan, C. Beam, S. Goodman and D. Watt, "Measurement of force applied during mammography," *Radiology,* vol. 181, no. 2, pp. 355-357, 1991 .

[8] A. Poulos, D. McLean, M. Rickard and R. Heard, "Breast compression in mammography: How much is enough?," *Australasian Radiology,* vol. 47, p. 121–126, 2003.

[9] D. R. Dance, J. Persliden and G. A. Carlsson, "Calculation of dose and contrast for two mammographic grids," *Phys. Med. Biol.,* vol. 37, pp. 235-248, 1992.

[10] P. S. Rezentes, A. Almeida and G. T. Barnes, "Mammography Grid Performance," *Radiology,* vol. 210, p. 227–232 , 1999.

[11] J. M. Boone, J. A. Seibert, C. Tang and M. Lane, "Grid and Slot Scan Scatter Reduction in Mammography: Comparison by Using Monte Carlo Techniques," *Radiology,* vol. 222, pp. 519-527, 2002.

[12] J. M. Boone, T. Yu and A. Siebert, "Mammography spectrum measurement using an x-ray diffraction device," *Phys. Med. Biol.,* vol. 43, p. 2569–2582, 1998.

[13] J. A. Siebert, "X-Ray Imaging Physics for Nuclear Medicine Technologists. Part 1: Basic Principles of X-Ray Production," *J Nucl Med Technol,* vol. 32, p. 139–147, 2004.

[14] F. Diekmann and U. Bick, "Tomosynthesis and contrast-enhanced digital mammography: recent advances in digital mammography," *Eur Radiol,* vol. 17, p. 3086–3092, 2007.

[15] M. Spahn, "Flat detectors and their clinical applications," *Eur Radiol,* vol. 15, p. 1934–1947, 2005.

[16] Konstantinidis, A. C., M. B. Szafraniec, R. D. Speller and A. Olivo, "The Dexela 2923 CMOS X-ray detector: A flat panel detector based on CMOS active pixel sensors for medical imaging applications," *Nuclear Instruments and Methods in Physics Research,* vol. A 689, p. 12–21, 2012.

[17] J. Rowlands and J. Yorkston, Flat Panel Detectors for Digital Radiography, Bellingham: SPIE Press, 2000.

[18] L. Bartella, N. Perry, K. Young, C. Lawinski and D. Evans, "Assessment of full field digital mammography (FFDM) detected microcalcification is not hindered by low spatial resolution," *Breast Cancer Res.,* vol. 4, p. 21, 2002.

[19] S. Ali and R. C. Coombes, "Endocrine-responsive breast cancer and strategies for combating resistance," *Nature Reviews Cancer,* vol. 2, pp. 101-112, 2002.

[20] V. A. McCormack and I. d. S. Silva, "Breast Density and Parenchymal Patterns as Markers of Breast Cancer Risk: A Meta-analysis," *Cancer Epidemiol Biomarkers Prev ,* vol. 15, pp. 1159-1169, 2006.

[21] Susan G. Komen, "Facts for Life: Breast Calcifications," April 2014. [Online]. Available: https://ww5.komen.org/uploadedFiles/_Komen/Content/About_Breast_Cancer/Tools_and_Resources/Fact_Sheets_and_Breast_Self_Awareness_Cards/BreastCalcifications.pdf. [Accessed 19 August 2015].

[22] R. Leborgne, "Diagnosis of tumours of breast by simple roentgenography: Calcifications in

carcinoma," *AJR,* vol. 65, p. 1–11, 1951.

[23] T. M. Kolb, J. Lichy and J. H. Newhouse, "Comparison of the performance of screening mammography, physical examination, and breast US and evaluation of factors that influence them: an analysis of 27,825 patient evaluations," *Radiology,* vol. 225, no. 1, pp. 165-175, 2002.

[24] R. D. Rosenberg, W. Hunt, M. Williamson, F. Gilliland, P. Wiest, C. Kelsey, C. Key and M. Linver, "Effects of age, breast density, ethnicity, and estrogen replacement therapy on screening mammographic sensitivity and cancer stage at diagnosis: review of 183,134 screening mammograms," *Radiology,* vol. 209, no. 2, pp. 511-518, 1998.

[25] W. Sickles, "Mammographic features of 300 consecutive nonpalpable breast cancers," *AJR,* vol. 146, pp. 661-663, 1986.

[26] "Draft Recommendation Statement: Breast Cancer: Screening," U.S. Preventive Services Task Force, May 2015. [Online]. Available: http://www.uspreventiveservicestaskforce.org/Page/Document/RecommendationStatementDraft/breast-cancer-screening1. [Accessed 15 August 2015].

[27] J. M. Park, E. A. Franken, M. Garg, L. L. Fajardo and L. T. Niklason, "Breast Tomosynthesis: Present Considerations and Future Applications," *RadioGraphics,* vol. 27, p. S231–S240, 2007.

[28] S. Friedewald, E. Rafferty, S. Rose, M. Durand, D. Plecha, J. Greenberg, M. Hayes, D. Copit, K. Carlson, T. Cink, L. Barke, L. Greer, D. Miller and E. Conant, "Breast cancer screening using tomosynthesis in combination with digital mammography," *JAMA,* vol. 311, pp. 2499-2507, 2014.

[29] A. McCarthy, D. Kontos, M. Synnestvedt, K. Tan, D. Heitjan, M. Schnall and E. Conant, "Screening outcomes following implementation of digital breast tomosynthesis in a general-population screening program," *Journal of the National Cancer Institute,* vol. 106, 2014.

[30] S. L. Rose, A. L. Tidwell, L. J. Bujnoch, A. C. Kushwaha, A. S. Nordmann and R. Sexton, "Implementation of Breast Tomosynthesis in a Routine Screening Practice: An Observational Study," *AJR,* vol. 200, pp. 1401-1408, 2013.

[31] M. A. Dennis, S. H. Parker, A. J. Klaus, A. T. Stavros, T. I. Kaske and S. B. Clark, "Breast Biopsy Avoidance: The Value of Normal Mammograms and Normal Sonograms in the

Setting of a Palpable Lump," *Radiology,* vol. 219, no. 1, pp. 186-191, 2001.

[32] K. Hardy, "Contrast-Enhanced Spectral Mammography — Adding the Power of Contrast to the Availability of Mammograms," *Radiology Today,* vol. 13, no. 2, p. 34, February 2012.

[33] S. Goergen, "Iodine-containing contrast medium (ICCM)," The Royal Australian and New Zealand College of Radiologists, 1 May 2009. [Online]. Available: http://www.insideradiology.com.au/pages/view.php?T_id=21#.VdelDflViko. [Accessed 21 August 2015].

[34] J. P. Gomilšek, I. Arcon, S. de Panfilis and A. Kodre, "X-ray absorption coefficient of iodine in the K edge region," *J. Phys. B: At. Mol. Opt. Phys.,* vol. 41, pp. 1-5, 2008.

[35] M. S. Jochelson, D. D. Dershaw, J. S. Sung, A. S. Heerdt, C. Thornton, C. S. Moskowitz, J. Ferrara and E. A. Morris, "Bilateral Contrast-enhanced Dual-Energy Digital Mammography: Feasibility and Comparison with Conventional Digital Mammography and MR Imaging in Women with Known Breast Carcinoma," *Radiology,* vol. 266, no. 3, pp. 743-751 , 2013.

[36] "Data Sheet: Ultravist," Bayer New Zealand Limited, 13 November 2012. [Online]. Available: http://www.medsafe.govt.nz/profs/datasheet/u/Ultravistinj.pdf. [Accessed 22 August 2015].

[37] V. Chan and A. Perlas, "Basics of Ultrasound Imaging," in *Atlas of Ultrasound-Guided Procedures in Interventional Pain Management*, Toronto, Springer Science + Business Media, LLC, 2011, pp. 13-19.

[38] "Ultrasound Imaging," U.S. Food and Drug Administration, 16 December 2014. [Online]. Available: http://www.fda.gov/Radiation-EmittingProducts/RadiationEmittingProductsandProcedures/MedicalImaging/ucm115357.htm. [Accessed 20 August 2015].

[39] "Negative Predictive Value of Sonography with Mammography in Patients with Palpable Breast Lesions," *American Journal of Roentgenology,* vol. 177, no. 5, pp. 1167-1170, 2001.

[40] S. Guhlke, "Radiochemistry and Radiopharmacy of the SPECT-Tracer Technetium-99m-Hexakis-2-methoxy-2-isobutyl isonitrile (99m-Tc-Sestamibi)," in *99mTc-Sestamibi: Clinical Applications*, New York, Springer-Verlag Berlin Heidelberg, 2012, pp. 2-5.

[41] P. A. Carvalho, M. L. Chiu, J. F. Kronauge, M. Kawamura, A. G. Jones, B. L. Holman and D. Piwnica-Worms, "Subcellular Distribution and Analysis of Technetium-99m-MIBI in Isolated Perfused Rat Hearts," *The Journal of Nuclear Medicine,* vol. 33, no. 8, pp. 1516-

1522, 1992.

[42] H. H. Barrett and K. J. Myers, Foundations of Image Science, Hoboken: John Wiley & Sons, Inc., 2004.

[43] S. Vallabhajosula, Molecular Imaging: Radiopharmaceuticals for PET and SPECT, New York: Springer-Verlag Berlin Heidelberg, 2009.

[44] K. M. Dallessio, "Breast-specific gamma imaging," *Applied Radiology,* pp. 34-36, 2007.

[45] F. Lumachi, F. G., M. Povolato and e. al., "Accuracy of technetium-99m sestamibi scintimammography and x-ray mammography in premenopausal women with suspected breast cancer," *Eur J Nucl Med,* vol. 28, p. 1776–1780, 2001.

[46] i. I. Khalkhal, J. Baum, J. Villanueva-Meyer and e. al., "99mTc-sestamibi breast imaging for the examination of patients with dense and fatty breasts: multicenter study," *Radiology,* vol. 222, p. 149–155, 2002.

[47] J. Cutrone, I. Khalkhali, L. Yosper and e. al., "Tc-99m sestamibi scintimammography for the evaluation of breast masses in patients with radiographically dense breasts," *Breast J,* vol. 5, p. 383–388, 1999.

[48] R. F. Brem, A. C. Floerke, J. A. Rapelyea, C. Teal, T. Kelly and V. Mathur, "Breast-specific Gamma Imaging as an Adjunct Imaging Modality for the Diagnosis of Breast Cancer," *Radiology,* vol. 247, no. 3, pp. 651-657, 2008.

[49] C. B. Hruska and M. K. O'Connor, "Nuclear imaging of the breast: Translating achievements in instrumentation into clinical use," *Med Phys.,* vol. 40, no. 5, p. 050901, 2013 .

[50] R. R. Edelman and S. Warach, "Magnetic Resonance Imaging (First of Two Parts)," *The New England Journal of Medicine,* vol. 328, no. 10, pp. 708-716, 1993.

[51] S. H. Heywang-Kobrunner, P. Viehweg, A. Heinig and C. Kiichler, "Contrast-enhanced MRI of the breast: accuracy, value, controversies, solutions," *European Journal of Radiology,* vol. 24 , pp. 94-108, 1997.

[52] E. Warner, D. B. Plewes, K. Hill and e. al, "Surveillance of BRCA1 and BRCA2 mutation carriers with magnetic resonance imaging, ultrasound, mammography, and clinical breast examination," *JAMA,* vol. 292, pp. 1317-1325, 2004.

[53] H. T. Le-Petross and M. K. Shetty, "Magnetic Resonance Imaging and Breast Ultrasonography as an Adjunct to Mammographic Screening in High-Risk Patients," *Seminars in Ultrasound CT and MRI,* vol. 32, pp. 266-272, 2011.

[54] I. Griebsh, J. Brown, C. Boggis and e. al, "Cost-effectiveness of screening with contrast enhanced magnetic resonance imaging vs X-ray mammography of women at a high familial risk of breast cancer," *Br J Cancer,* vol. 95, p. 801–810, 2006.

[55] C. Kuhl, S. Schrading, H. Bieling and e. al, "MRI for diagnosis of pure ductal carcinoma in situ: a prospective observational study," *Lancet,* vol. 370, p. 485–492, 2007.

[56] R. Schmutzler, K. Rhiem, P. Breuer and e. al, "Outcome of a structured surveillance programme in women with a familial predisposition of breast cancer," *Eur J Cancer Prev,* vol. 15, p. 483–489, 2006.

[57] M. Kriege, C. Brekelmans, B. C. and e. al, "Efficacy of MRI and mammography for breast cancer screening in women with a familial or genetic predisposition," *N Engl J Med,* vol. 351, p. 427– 500 , 2004.

[58] B. Hruska, A. L. Weinmann and M. K. O'Connor, "Proof of concept for low-dose molecular breast imaging with a dual-head CZT gamma camera. Part I. Evaluation in phantoms," *Med. Phys.,* vol. 39, p. 3466–3475, 2012.

[59] B. Hruska, A. L. Weinmann, C. M. Tello Skjerseth, E. M. Wagenaar, A. L. Conners, C. L. Tortorelli, R. W. Maxwell, D. J. Rhodes and M. K. O'Connor, "Proof of concept for low-dose molecular breast imaging with a dual-head CZT gamma camera. Part II. Evaluation in patients," *Med. Phys.,* vol. 39, p. 3476–3483, 2012.

[60] K. K. Lindfors, J. M. Boone, T. R. Nelson, K. Yang, A. L. C. Kwan and D. F. Miller, "Dedicated Breast CT: Initial Clinical Experience," *Radiology,* vol. 246, pp. 725-733, 2008.

[61] D. L. Parker, "Optimal short scan convolution reconstruction for fanbeam CT," *Med Phys,* vol. 9, no. 2, pp. 254-257, 1982.

[62] M. Goodsitt, H.-P. Chan, A. Schmitz, S. Zelakiewicz, S. Telang, L. Hadjiiski, K. Watcharotone, M. Helvie, C. Paramagul, C. Neal, E. Christodoulou, S. Larson and P. Carson, "Digital breast tomosynthesis: studies of the effects of acquisition geometry on contrast-to-noise ratio and observer preference of low-contrast objects in breast phantom images," *Phys. Med. Biol.,* vol. 59, p. 5883–5902, 2014.

[63] A. Karellas and J. Y. Lo, "Cone beam x-ray CT will be superior to digital x-ray tomosynthesis in imaging the breast and delineating cancer," *Med. Phys.,* vol. 35, pp. 409-411, 2008.

[64] M. B. Williams, P. G. Judy, S. Gunn and S. Majewski, "Dual-Modality Breast Tomosynthesis," *Radiology,* vol. 000, p. 1–8, 2010.

[65] W. Zhao, B. Zhao and Y.-h. Hu, "Latest Advances in Digital Breast Tomosynthesis," in *AAPM 51st Annual Meeting*, Anaheim, 2009.

[66] X. Liu, C. C. Shaw, T. Wang, L. Chen, M. C. Altunbas and S. C. Kappadath, "An accurate scatter measurement and correction technique for cone beam breast CT imaging using scanning sampled measurement (SSM)technique," *Proc. SPIE 6142, Medical Imaging 2006: Physics of Medical Imaging,* vol. 614234, 2006.

[67] M. C. Altunbas, C. C. Shaw, L. Chen, C. Lai, X. Liu, T. Han and T. Wang, "A post-reconstruction method to correct cupping artifacts in cone beam breast computed tomography," *Med. Phys.,* vol. 34, pp. 3109-3118 , 2007.

[68] P. M. Joseph and R. D. Spital, "The effects of scatter in x-ray computed tomography," *Med. Phys.,* vol. 9, p. 464–472, 1982.

[69] G. H. Glover, "Compton scatter effects in CT reconstructions," *Med. Phys.,* vol. 9, pp. 860-867, 1982.

[70] G. T. Barnes and I. A. Brezovich, "The intensity of scattered radiation in mammography," *Radiology ,* vol. 126, p. 243–247, 1978.

[71] R. Hendrick, E. Pisano, A. Averbukh and e. al., "Comparison of acquisition parameters and breast dose in digital mammography and screen-film mammography in the American College of Radiology Imaging Network Digital Mammographic Imaging Screening Trial," *AJR Am J Roentgenol,* vol. 194, no. 2, p. 362–369, 2010.

[72] R. Geise and A. Palchevsky, "Composition of mammographic phantom materials," *Radiology,* vol. 198, no. 2, p. 347–350, 1996.

[73] D. Grant, "Tomosynthesis: A Three-Dimensional Radiographic Imaging Technique," *IEEE Transactions on Biomedical Engineering,* vol. 19, no. 1, pp. 20-28, 1972.

[74] E. D. Pisano, C. Gatsonis, E. Hendrick, M. Yaffe, J. K. Baum, S. Acharyya, E. F. Conant, L. L. Fajardo, L. Bassett, C. D'Orsi, R. Jong and M. Rebner, "Diagnostic Performance of Digital versus Film Mammography for Breast-Cancer Screening," *New England Journal of*

Medicine, vol. 353, pp. 1773-1783, 2005.

[75] E. D. Pisano and M. J. Yaffe, "Digital Mammography," *Radiology,* vol. 234, pp. 353-362, 2005.

[76] Y. Zhang, H.-P. Chan, B. Sahiner, J. Wei, M. M. Goodsitt, L. M. Hadjiiski, J. Ge and C. Zhou, "A comparative study of limited-angle cone-beam reconstruction methods for breast tomosynthesis," *Med Phys,* vol. 33, pp. 3781-3794, 2006.

[77] T. Wu, R. H. Moore, E. A. Rafferty and D. B. Kopans, "A comparison of reconstruction algorithms for breast tomosynthesis," *Med Phys,* vol. 31, pp. 2636-2647, 2004.

[78] M. Defrise and R. Clack, "A cone-beam reconstruction algorithm using shift-variant filtering and cone-beam backprojection," *Medical Imaging, IEEE Transactions,* vol. 13, no. 1, pp. 186-195 , 1994.

[79] M. Levoy, Volume rendering using the fourier projection-slice theorem, Stanford University, 1992.

[80] R. J. Acciavatti, P. R. Bakic and A. D. A. Maidment, "Proposing a new velocity profile for continuous x-ray tube motion in digital breast tomosynthesis," in *Proc. SPIE 8668, Medical Imaging 2013*, Lake Buena Vista, 2013.

[81] I. Reiser and S. Glick, Eds., Tomosynthesis Imaging, Boca Raton: Taylor & Francis Group, LLC, 2014.

[82] R. J. Acciavatti and A. D. A. Maidment, "Optimization of continuous tube motion and step-and-shoot motion in digital breast tomosynthesis systems with patient motion," in *SPIE 8313, Medical Imaging 2012*, San Diego, 2012.

[83] R. Peng, R. Zeng, E. O'Bryan, C. Marini Bettolo, B. Sahiner, K. J. Myers and R. J. Jennings, "An Experimental Comparison of Continuous Motion and Step-and-Shoot Modes in Digital Breast Tomosynthesis," in *IWDM 2012*, Philadelphia, 2012.

[84] A. Smith, "Design Considerations in Optimizing a Breast Tomosynthesis System," *Imaging Science,* vol. Hologic.

[85] W. R. Hendee and E. R. Ritenour, Medical Imaging Physics, New York: Wiley-Liss, Inc., 2002.

[86] D. Kopans, "Digital tomosynthesis and other applications," *RSNA Program Book 2005,* vol.

130, 2005.

[87] M. A. Helvie, M. A. Roubidoux, L. M. Hadjiiski, Y. Zhang, P. L. Carson and H. P. Chan, "Tomosynthesis mammography vs conventional mammography: Comparison of breast masses detection and characterization," *RSNA Program Book,* vol. 381, 2007.

[88] Y. Zhang, H.-P. Chan, M. M. Goodsitt, A. Schmitz, J. W. Eberhard and B. E. Claus, "Investigation of Different PV Distributions in Digital Breast Tomosynthesis (DBT) Mammography," in *9th International Workshop on Digital Mammography*, Tucson, 2008.

[89] T. Mertelmeier, J. Ludwig, B. Zhao and W. Zhao, "Optimization of Tomosynthesis Acquisition Parameters: Angular Range and Number of Projections," in *9th Internation Workshop of Digital Mammography*, Tucson, 2008.

[90] F. Diekmann and U. Bick, "Breast Tomosynthesis," *Seminars in Ultrasound, CT and MRI,* vol. 32, no. 4, pp. 281-287, 2011.

[91] A. S. Chawla, J. Y. Lo, J. A. Baker and E. Samei, "Optimized image acquisition for breast tomosynthesis in projection and reconstruction space," *Med Phys,* vol. 36, no. 11, pp. 4859-4869, 2009.

[92] J. G. Mainprize, A. K. Bloomquist, M. R. Kempston and M. J. Yaffe, "Resolution at oblique incidence angles of a flat panel imager for breast tomosynthesis," *Med. Phys.,* vol. 33, pp. 3159-3164, 2006.

[93] A. Badano, I. S. Kyprianou, R. J. Jennings and J. Sempau, "Anisotropic imaging performance in breast tomosynthesis," *Med. Phys. ,* vol. 34, pp. 4076-4091, 2007.

[94] Y.-H. Hu and W. Zhao, "The effect of angular dose distribution on the detection of microcalcifications in digital breast tomosynthesis," *Med Phys,* vol. 38, no. 5, pp. 2455-2466, 2011.

[95] B.-H. Chang and Y. Hori, "Trajectory Design Considering Derivative of Jerk for Head-Positioning of Disk Drive System With Mechanical Vibration," *IEEE/ASME Transactions on Mechatronics,* vol. 11, no. 3, pp. 273-279, 2006.

[96] G. J. Whitman and T. Milner, Eds., Digital Mammography: A Practical Approach, New York: Cambridge University Press, 2013.

[97] W. Huda, A. M. Sajewicz, K. M. Ogden and D. R. Dance, "Experimental investigation of the dose and image quality characteristics of a digital mammography imaging system,"

Medical Physics , vol. 30, no. 3, pp. 442-448, 2003.

[98] A. K. Carton, D. Vandenbroucke, L. Struye, A. D. A. Maidment, Y.-H. Kao, M. Albert, H. Bosmans and G. Marchal, "Validation of MTF measurement for digital mammography quality control," *Med. Phys.,* vol. 32, no. 6, pp. 1684-1695, 2005.

[99] "MagicMaX Meters -mam," IBA Dosimetry, 2015. [Online]. Available: http://www.iba-dosimetry.com/magicmax-meters-imami. [Accessed 26 July 2015].

[100] C. W. E. van Eijk, "Inorganic scintillators in medical imaging," *Phys. Med. Biol.,* vol. 47, p. R85–R106, 2002.

[101] H. Helmers and M. Schellenberg, "CMOS vs. CCD sensors in speckle interferometry," *Optics & Laser Technology,* vol. 35, p. 587 – 595, 2003.

[102] J. Mainprize, A. Bloomquist, X. Wang and M. Yaffe, "Dependence of image quality on geometric factors in breast tomosynthesis," *Med Phys,* vol. 38, no. 6, pp. 3090-103., 2011 .

[103] G. D. Boreman, Modulation Transfer Function in Optical and Electro-Optical Systems, Bellingham: SPIE Press, 2001.

[104] H. Fujita, D.-Y. Tsai, T. Itoh, K. Doi, J. Morishita, K. Ueda and A. Ohtsuka, "A Simple Method for Determining the Modulation Transfer Function in Digital Radiography," *IEEE TRANSACTIONS ON MEDICAL IMAGING ,* vol. 11, no. 1, pp. 34-39, 1992.

[105] M. Goodsitt and H.-P. Chan, "History, Theory and Operation of Digital Breast Tomosynthesis Systems," [Online].

[106] M. Chang, Y. Xiao, Z. Chen, L. Li and L. Zhang, "Preliminary Study of Rotary Motion Blurs in a Novel Industry CT Imaging System," in *IEEE Nuclear Science Symposium*, Valencia, 2011.

[107] M. Piccoli and M. Yim, "Cogging Torque Ripple Minimization via Position Based Characterization," in *Proceedings of Robotics: Science and Systems*, 2014.

[108] S. M. Gruner, E. F. Eikenberry and M. W. Tate, "Comparison of X-ray Detectors," in *International Tables for Crystallography Vol. F*, Springer Netherlands, 2006, pp. 143-147.

[109] H. Illers, E. Buhr and C. Hoeschen, "Measurement of the Detective Quantum Efficiency (DQE) of Digital X-ray Detectors According to the Novel Standard IEC 62220-1," *Radiation Protection Dosimetry,* vol. 114, p. 39–44, 2005.

[110] International Electrotechnical Commission, "Medical electrical equipment–Characteristics of digital X-ray imaging devices-Part 1-2: Determination of the detective quantum efficiency-Detectors used in mammography," in *IEC 62220-1*, Geneva, IEC, 2006.

[111] M. B. Williams, P. A. Mangiafico and P. U. Simoni, "Noise power spectra of images from digital mammography detectors," *Med Phys,* vol. 26, no. 7, pp. 1279-1293, 1999.

[112] E. B. e. Podgorsak, Radiation Oncology Physics: A Handbook for Teachers and Students, Vienna: International Atomic Energy Agency, 2005.

[113] J. A. Seibert, J. M. Boone and K. K. Lindfors, "Flat-field correction technique for digital detectors," in *Proc. SPIE 3336, Medical Imaging 1998: Physics of Medical Imaging*, 1998.

[114] J. A. Seibert and J. M. Boone, "X-Ray Imaging Physics for Nuclear Medicine Technologists. Part 2: X-Ray Interactions and Image Formation," *J Nuc Med Technol,* vol. 33, p. 3–18, 2005.

[115] G. Wu, J. . Mainprize, J. M. Boone and M. J. Yaffe, "Evaluation of scatter effects on image quality for breast tomosynthesis," *Med. Phys.,* vol. 36, pp. 4425-4432, 2009.

[116] A. H. Baydush and C. E. Floyd, "Improved image quality in digital mammography with image processing," *Med. Phy.,* vol. 27, no. 7, p. 1503–1508, 2000.

[117] K. Nykänen and S. Siltanen, "X-ray scattering in full-field digital mammography," *Med. Phys.,* vol. 7, no. 30, p. 1864–1873, 2003.

[118] J. Xia, C. Floyd, J. Lo and B. Harrawood, "Improved signal to noise in full-field digital mammography by replacing the anti-scatter grid with nonlinear image processing," *roc. of the Radiological Society of North-America (RSNA),* 2004.

[119] C. E. Tromans, M. Cocker and S. M. Brady, "Digital scatter removel for mammography and tomosynthesis image aquisition," *Proc. of the 11th International Workshop on Digital Mammography (IWDM) 2012,* vol. 7361, p. 260–267, 2012.

[120] I. Sechopoulos, S. Suryanarayanan, S. Vedantham, C. J. D’Orsi and A. Karellas, "Scatter radiation in digital tomosynthesis of the breast," *Med. Phys.,* vol. 34, pp. 564-576, 2007.

[121] B. Liu and X. Li, "Effects of Scatter Radiation on Reconstructed Images in Digital Breast Tomosynthesis," *Proc. SPIE 7258,* vol. 7258, p. 72585Y, 2009.

[122] B. Liu, T. Wu, R. H. Moore and D. B. Kopans, "Monte Carlo Simulation of X-ray Scatter

Based on Patient Model from Digital Breast Tomosynthesis," *Proc. SPIE,* vol. 6142, p. 61421N, 2006.

[123] A. Krol, D. A. Bassano, C. C. Chamberlain and S. C. Prasad, "Scatter reduction in mammography with air gap," *Med. Phys.,* vol. 23, pp. 1263-1270, 1996.

[124] G. Bucky, "Method of and apparatus for projecting Röntgen images". Patent 1,164,987, 21 December 1915.

[125] W. E. Moore and D. J. Steklenski, "X-ray grid for medical radiography and method of making and using same". Patent 4951305 A, 21 August 1990.

[126] K. A. Fetterly and B. A. Schueler, "Experimental evaluation of fiber-interspaced antiscatter grids for large patient imaging with digital x-ray systems," *Phys. Med. Biol.,* vol. 52, p. 4863–4880, 2007.

[127] A. Carton, R. Acciavatti, J. Kuo and A. D. A. Maidment, "The effect of scatter and glare on image quality in contrast-enhanced breast imaging using an a-Si/CsI(Tl) full-field flat panel detector," *Med. Phys.,* vol. 36, no. 3, pp. 920-928, 2009.

[128] D. M. Gauntt and G. T. Barnes, "Grid line artifact formation: A comprehensive theory," *Med. Phys.,* vol. 33, no. 6, pp. 1668-1677 , 2006.

[129] J. E. Gray and J. A. Princehorn, "HTC Grids Improve Mammography Contrast," *White Paper,* 2004.

[130] J. M. Boone, O. V. Makarova, V. N. Zyryanov, C. Tang, D. C. Mancini, N. Moldovan and R. Divan, "Development and Monte Carlo Analysis of Antiscatter Grids for Mammography," *Technology in Cancer Research Treatment,* vol. 1, pp. 441-447, 2002.

[131] J. Siewerdsen and D. Jaffray, "Cone-beam computed tomography with a flat-panel imager: Magnitude and effects of x-ray scatter," *Med. Phys.,* vol. 28, p. 220, 2001.

[132] P. Johns and M. Yaffe, "Scattered radiation in fan beam imaging systems," *Med. Phys.,* vol. 9, p. 231, 1982.

[133] J. Boone, T. R. Nelson, K. K. Lindfors and J. A. Siebert, "Dedicated Breast CT: Radiation Dose and Image Quality Evaluation," *Radiology,* vol. 221, pp. 657-667, 2001.

[134] M. Endo, S. Mori, T. Tsunoo and H. Miyazaki, "Magnitude and effects of x-ray scatter in a 256-slice CT scanner," *Med. Phys.,* vol. 33, pp. 3359-3368, 2006.

[135] V. N. Cooper, J. M. Boone, J. A. Seibert and C. J. Pellot-Barakat, "An edge spread technique for measurement of the scatter-to-primary ratio in mammography," *Med. Phys. 27,* vol. 27, no. 5, pp. 845-853, 2000.

[136] E. Salvagnini, H. Bosmans, L. Struelens and N. W. Marshall, "Quantification of scattered radiation in projection mammography: Four practical methods compared," *Med. Phys.,* vol. 39, no. 6, pp. 3167-3180, 2012.

[137] J. M. Boone, K. K. Lindfors, V. N. Cooper and J. A. Seibert, "Scatter/primary in mammography: Comprehensive Results," *Med. Phys.,* vol. 27, no. 10, pp. 2408-2416, 2000.

[138] S. M. Leon, L. F. Brateman and L. K. Wagner, "Characterization of scatter in digital mammography from use of Monte Carlo simulations and comparison to physical measurements," *Med. Phy.,* vol. 41, no. 11, pp. 111914-1 - 111914-10, 2014.

[139] D. M. Cunha, A. Tomal and M. E. Poletti, "Evaluation of scatter-to-primary ratio, grid performance and normalized average glandular dose in mammography by Monte Carlo simulation including interference and energy broadening effects," *Phys. Med. Biol.,* vol. 55 , p. 4335–4359, 2010.

[140] D. R. Dance and G. J. Day, "The computation of scatter in mammography by Monte Carlo methods," *Phys. Med. Biol.,* vol. 29, no. 3, pp. 237-247, 1984.

[141] L. T. Niklason, J. A. Sorenson and J. A. Nelson, "Scattered radiation in chest radiography," *Med. Phys.,* vol. 8, p. 677–681 , 1981.

[142] C. E. Floyd, J. Y. Lo, H. G. Chotas and C. E. Ravin, "Quantitative scatter measurement in digital radiography using a photostimulable phosphor imaging system," *Med. Phys.,* vol. 18, p. 408–413, 1991.

[143] J. H. Siewerdsen, M. J. Daly, B. Bakhtiar, D. J. Moseley, S. Richard, H. Keller and D. A. Jaffray, "A simple, direct method for x-ray scatter estimation and correction in digital radiography and cone-beam CT," *Med. Phys.,* vol. 33, no. 1, pp. 187-197, 2006.

[144] K. A. Fetterly and B. A. Schuele, "Experimental evaluation of fiber-interspaced antiscatter grids for large patient imaging with digital x-ray systems," *Phys. Med. Biol.,* vol. 52, p. 4863–4880, 2007.

[145] Computerized Imaging Reference Systems, Inc. (CIRS), "Mammography Research Set, Model 012A," [Online]. Available:

http://www.cirsinc.com/file/Products/012A/012A_DS_092612.pdf. [Accessed 19 June 2015].

[146] H. Chan, K. L. Lam and Y. Wu, "Studies of performance of antiscatter grids in digital radiography: Effect on signal-to-noise ratio," *Med. Phys.,* vol. 17, no. 4, pp. 655-664, 1990.

[147] J. Prekeges, Nuclear Medicine Instrumentation, Sudbury: Jones and Bartlett Publishers, 2011.

[148] J. H. Hubbell and S. M. Seltzer, "X-Ray Mass Attenuation Coefficients," The National Institute of Standards and Technology (NIST), 17 September 2009. [Online]. Available: http://physics.nist.gov/PhysRefData/XrayMassCoef/tab3.html. [Accessed 13 July 2015].

[149] D. D. Dershaw, M. E. Masterson, S. Malik and N. M. Cruz, "Mammography using an ultrahigh-strip-density, stationary, focused grid," *Radiology ,* vol. 156, p. 541–544, 1985.

[150] C. Kimme-Smith, J. Sayre, M. McCombs, R. H. Gold and L. W. Bassett, "Mammography fixed grid versus reciprocating grid: Evaluation using cadaveric breasts as test objects," *Med. Phys.,* vol. 23, p. 141 , 1996.

[151] H. E. Potter, "The Bucky diaphragm principle applied to roentgenography," *Am. J. Roentgenol.,* vol. 7, p. 292–295, 1920.

[152] D. S. Kim and S. Lee, "Grid artifact reduction for direct digital radiography detectors based on rotated stationary grids with homomorphic filtering," *Med. Phys.,* vol. 40, p. 061905, 2013.

[153] A. J. Pellegrino, D. N. Lyke, D. P. Lieb, J. A. Buturlia and M. P. Appleby, "Air cross grids for mammography and methods for their manufacture and use". United States of America Patent 5814235, 29 September 1998.

[154] C.-M. Tang, "Two-dimensional, anti-scatter grid and collimator designs, and its motion, fabrication and assembly". United States of America Patent 6252938 B1, 26 June 2001.

[155] C. Lin, W. Lee, S. Chen, C. Tsai, J. Lee, C. Chang and Y. Ching, "A Study of Grid Artifacts Formation and Elimination in Computed Radiographic Images," *Journal of Digital Imaging,* vol. 14, pp. 351-361, 2006.

[156] D. R. Bednarek, S. Rudin and R. Wong, "Artifacts produced by moving grids," *Radiology,* vol. 147, p. 255–258, 1983.

[157] "FFT," [Online]. Available: http://imagejdocu.tudor.lu/doku.php?id=gui:process:fft. [Accessed 5 August 2015].

[158] Computerized Imaging Reference Systems, Inc. (CIRS), "BR3D Breast Imaging Phantom, Model 020," [Online]. Available: http://www.cirsinc.com/products/modality/51/br3d-breast-imaging-phantom/. [Accessed 28 June 2015].

[159] T. Cauley, W. Phillips, D. B. Kopans, R. H. Moore, J. W. Eberhard, B. Opsahl-Ong, L. Niklason and M. B. Williams, "Tomographic mammography using a limited number of low-dose cone-beam projection images," *Med. Phys. ,* vol. 30, pp. 365-380, 2003.

[160] The MathWorks, Inc., "imresize," 2015. [Online]. Available: http://www.mathworks.com/help/images/ref/imresize.html. [Accessed 25 October 2015].

[161] D. M. Gauntt and G. T. Barnes, "A novel technique to suppress grid line artifacts," *Med. Phys.,* vol. 33, p. 1654–1667, 2006.

[162] T. Maruyama and H. Yamamoto, "Elimination of gridlines in X-ray image," in *2008 IEEE Instrumentation and Measurement Technology Conference*, Victoria, 2008.

[163] L. E. Paulis, M. B. I. Lobbes, U. C. Lalji, N. Gelissen, R. W. Bouwman, J. E. Wildberger and C. R. L. P. N. Jeukens, "Radiation Exposure of Digital Breast Tomosynthesis Using an Antiscatter Grid Compared With Full-Field Digital Mammography," *Investigative Radiology,* vol. 00, pp. 1-7 , 2015.

[164] M. Williams, P. Raghunathan, M. J. More, J. A. Siebert, A. Kwan, J. Y. Lo, E. Samei, N. T. Ranger, L. L. Fajardo, A. McGruder, S. M. McGruder, A. D. A. Maidment, M. J. Yaffe, A. Bloomquist and G. E. Mawdsley, "Optimization of exposure parameters in full field digital mammography," *Med. Phys.,* vol. 35, no. 6, pp. 2414-2423, 2008.

[165] G. R. Hammerstein, D. W. Miller, D. R. White, M. E. Masterson, H. Q. Woodard and J. S. Laughlin, "Absorbed radiation dose in mammography," *Radiology,* vol. 130, no. 2, p. 485–491, 1979.

[166] J. A. Siebert and J. M. Boone, "X-Ray Imaging Physics for Nuclear Medicine Technologists. Part 2: X-Ray Interactions and Image Formation," *J. Nucl. Med. Technol.,* vol. 33, p. 3–18, 2005.

[167] J. M. Boone, "Glandular Breast Dose for Monoenergetic and High-Energy X-ray Beams:

Monte Carlo Assessment," *Radiology,* vol. 213, pp. 23-37, 1999.

[168] Computerized Imaging Reference Systems, Inc., "Tissue-Equivalent Phantom for Mammography, Model 011A," 2015. [Online]. Available: http://www.cirsinc.com/products/all/6/tissue-equivalent-phantom-for-mammography/. [Accessed 1 April 2015].

[169] E. Shaheen, N. Marshall and H. Bosmans, "Investigation of the effect of tube motion in breast tomosynthesis: continuous or step and shoot?," in *Proc. SPIE 7961, Medical Imaging*, Lake Buena Vista, 2011.

[170] S. S. J. Feng and I. Sechopoulos, "Clinical Digital Breast Tomosynthesis System: Dosimetric Characterization," *Radiology,* vol. 263, pp. 35-42, 2012.

[171] Hologic, Inc., *Quality Control Manual: Selenia Dimensions 2D FFDM, Selenia Dimensions DBT,* Bedford, 2011.

[172] Gammex, Inc., "Mammographic Accreditation Phantom," [Online]. Available: http://www.gammex.com/n-portfolio/productpage.asp?id=299&category=Mammography&name=Mammographic+Accreditation+Phantom%2C+Gammex+156. [Accessed 1 November 2015].

[173] A. L. C. Kwan, J. M. Boone and N. Shah, "Evaluation of x-ray scatter properties in a dedicated cone-beam breast CT scanner," *Med. Phys.,* vol. 32, pp. 2967-2975, 2005.

[174] S. Z. Shen, A. K. Bloomquist, G. E. Mawdsley, M. J. Yaffe and I. Elbakri, "Effect of scatter and an antiscatter grid on the performance of a slot-scanning digital mammography system," *Med. Phys.,* vol. 33, pp. 1108-1115, 2006.

[175] J. M. King, I. A. Elbakri and M. Reed, "Antiscatter grid use in pediatric digital tomosynthesis imaging," *Journal of Applied Clinical Medical Physics,* vol. 12, pp. 221-230, 2011.

[176] D. J. Dronker, J. H. C. L. Hendriks, R. Holland and G. Rosenbusch, The Practice of Mammography: Pathology, Technique, Interpretation, Adjunct Modalities, New York: Georg Thieme Verlag, 2002.